THE UNIVERSITY OF NOTTINGHAM

Department of Electrical and Electronic Engineering

Faculty of Engineering

High Performance, Direct Drive Machines for Aerospace Applications

Michael Galea, B.Eng.(Hons.), M.Sc.(Elec.)

Submitted to the University of Nottingham for the degree of Doctor of Philosophy,

February 2013

ABSTRACT

For aerospace related electric systems, torque/force density, reliability and fault tolerance are of the utmost importance. A method by which high figures of reliability can be achieved is by eliminating any mechanical gearing or interconnection elements between the electrical machine and its mechanical load. This means that direct drive, electrical machines must be employed. However, to implement such solutions (without any mechanical advantages), electrical machines with excellent torque density (for rotational machines) and force density (for linear machines) performances are required.

In this work, the main aim is to propose and investigate possible methods for extending and improving the torque/force density capabilities of high performance, state of the art, electrical machines (both rotational and linear). This is done in order to be able to meet the performance requirements while lacking the mechanical advantages synonymous with gearing and/or mechanical interconnections. Novel electro-magnetic and thermal management structures, detailed design and optimisation procedures for electrical machines are presented in this thesis. As vehicles to investigate these novel concepts, a tubular linear, permanent magnet motor and a rotational, synchronous permanent magnet motor are designed, built and experimentally tested. These machines which are both for aerospace related applications serve to show and validate the worthiness of the proposed, performance enhancement measures.

ACKNOWLEDGMENTS

I must express my thanks to all those who helped in realising and implementing the projects described in this work.

Heartfelt gratitude goes to Professor Chris Gerada for his constant help, guidance and support. I must also thank Professor Pat Wheeler, Dr. Tsarafidy Raminosoa and Dr. Mohand Hamiti for their interventions and help whenever required.

Thanks to all the friends and colleagues that were part of the long and difficult journey towards the completion of the objectives outlined in this work, with special thanks going to Luca Papini and Paolo Giangrande.

Mikiel

2013

TABLE OF CONTENTS

LIST OF FIGURES

LIST OF TABLES

ACRONYMS

BLAC	Brushless AC
BLDC	Brushless DC
BkEnv	Back Envelope
CFD	Computational Fluid Dynamics
CoFe	Cobalt Iron
DD	Direct Drive
EHA	Electro-Hydraulic Actuator
EMA	Electro-Mechanical Actuator
EMC	Electro-Magnetic Clutch
EMF	Electro-Motive Force
FCS	Flight Control Surface
FE	Finite Element
FrEnv	Front Envelope
GT	Green Taxiing™
IM	Induction Motor
IPM	Inset Permanent Magnet
MEA	More Electric Aircraft
NdFeB	Neodymium Iron Boron
PEMC	Power Electronics, Machines and Control
PM	Permanent Magnet
PMSM	Permanent Magnet Synchronous Machine
QI	Quality Indicating
SiFe	Silicon Iron
SmCo	Samarium Cobalt
SMC	Soft Magnetic Composite
SMPM	Surface Mount Permanent Magnet
TLPM	Tubular Linear Permanent Magnet
UoN	University of Nottingham

GLOSSARY OF SYMBOLS

A_h	Hydraulic cross-sectional area of coolant flow in water-jacket (m^2)
A_{mov}	Total surface area of the mover of TLPM motor (m^2)
A_{rms}	RMS value of the electric loading (*kA/m*)
A_{rot}	Total surface area of the rotor of rotational motors (m^2)
A_{slot}	Area of one slot of TLPM motor (m^2)
B_{demag}	Demagnetisation value in terms of flux density of a PM material (*T*)
B_g	No-load air-gap flux density (*T*)
B_{g1}	Fundamental of the no-load air-gap flux density (*T*)
B_{prox}	Demagnetisation proximity field in terms of *B* (*T*)
B_{rem}	PM residual flux density (*T*)
d_h	Hydraulic diameter of water-jacket (*m*)
f_s	Synchronous frequency (*Hz*)
F_{cog}	Electro-magnetic cogging force for linear motors (*N*)
F_{cog_end}	Cogging force component due to finite stator length (*N*)
F_{cog_sl}	Cogging force component due to slotting (*N*)
F_{cog1}	Left side cogging force component due to finite stator length (*N*)
F_{cog2}	Right side cogging force component due to finite stator length (*N*)
F_{lin}	Electro-magnetic thrust force for linear motors (*N*)
F_{rip}	Ripple on electromagnetic thrust force of linear motors (*%*)
F_{sc}	Braking force (*N*)
h	Overall heat transfer coefficient
H	PM energy field (*kA/m*)
H_c	PM coercive force (*kA/m*)
H_{ci}	Intrinsic coercive force (*kA/m*)
h_{cv}	Convection heat transfer coefficient (W/m^2K)
H_{prox}	Demagnetisation proximity field in terms of *H* (*kA/m*)
I_d	Current along the direct *d-axis* (*A*)
I_{pk}	Peak value of the phase current (*A*)

I_q	Current along the quadrature *q-axis* (*A*)
I_{rms}	RMS value of the phase current (*A*)
I_{sc}	Short circuit current (*A*)
J_{pk}	Peak value of the copper current density (A/mm^2)
J_{rms}	RMS value of the copper current density (A/mm^2)
k_{Al}	Thermal conductivity of aluminium (*W/mK*)
k_{cu}	Thermal conductivity of copper (*W/mK*)
k_{eq}	Equivalent thermal conductivity of the slot area (*W/mK*)
k_{Fe}	Thermal conductivity of typical silicon steel (*W/mK*)
k_{lin}	Thermal conductivity of typical slot liner insulation material (*W/mK*)
k_{wat}	Thermal conductivity of water (*W/mK*)
K_{fill}	Slot fill factor in terms of copper area to total slot area
K_F	Force constant (*N/A*)
K_{lam}	Lamination fill factor/ratio of sunshine structure to ideal tubular structure
K_T	Torque constant (*Nm/A*)
K_w	Fundamental winding factor
l_{ax}	Axial length (*m*)
l_{wat}	Peripheral length through which coolant flows in ducts (*m*)
L	Self-inductance of a coil or phase (*mH*)
L_a	Self-inductance of a Phase A of TLPM motor (*mH*)
L_a	Self-inductance of a Phase A of GT motor (*mH*)
L_b	Stator yoke thickness of TLPM motor (*m*)
L_b	Stator back iron thickness of GT motor (*m*)
L_d	Inductance along the direct *d-axis* (*mH*)
L_e	External length of TLPM motor (*m*)
L_g	Air-gap length (*m*)
L_{g_eff}	Effective air-gap length (*m*)
L_{ext}	Extra added length to stator yoke of TLPM motor (*m*)
L_q	Inductance along the quadrature *q-axis* (*mH*)
M	Magnetisation vector of a field

N	Number of turns
N_s	Angular synchronous speed (*rpm*)
N_{slots}	Number of slots
N_u	Nusselt number
P	Number of pole pairs
P_{cu}	I^2R copper loss (*W*)
P_{cu_tot}	I^2R copper loss for whole machine (*W*)
P_{ed_HP}	Eddy currents loss in the HP (*W*)
P_h	Perimeter that has contact with coolant fluid in water-jacket (*m*)
P_r	Prundtl number
$\mathfrak{R}$	Reluctance (*A/Wb*)
R_a	Resistance of Phase A of TLPM motor (Ω)
R_a	Resistance of Phase A of GT motor (Ω)
R_e	External radius of TLPM motor (*m*)
R_e	External radius of GT motor (*m*)
R_{ey}	Reynolds number
R_{hc}	Radius at height of centre of slot of TLPM motor (*m*)
R_{hc}	Radius at height of centre of slot of GT motor (*m*)
R_{in}	Stator bore radius of TLPM motor (*m*)
R_{pit}	Pitch ratio of TLPM motor
R_{rot}	Radius of the rotor of rotational motors (*m*)
R_{spl}	Split ratio of TLPM motor
R_{stat_bore}	Stator bore radius of GT motor (*m*)
R_{ts}	Tooth to slot pitch ratio of TLPM motor
T	Torque (*Nm*)
T_{amb}	Ambient temperature (°*C*)
T_{cog}	Electro-magnetic cogging torque (*Nm*)
T_m	Magnet span of TLPM motor (*m*)
T_m	Magnet span of GT motor (°)
T_{max}	Maximum allowable winding temperature (°*C*)

T_{pm}	Temperature of the PMs (*°C*)
T_{rip}	Ripple on electro-magnetic torque (*%*)
T_s	Slot pitch of TLPM motor (*m*)
T_s	Slot pitch of GT motor (°)
T_{sc}	Braking torque (*Nm*)
T_t	Tooth thickness of TLPM motor (*m*)
T_t	Tooth thickness of GT motor (*m*)
T_{t_uw}	Unwound tooth thickness of GT motor (*m*)
T_{t_w}	Wound tooth thickness of GT motor (*m*)
T_p	Pole pitch of TLPM motor (*m*)
T_{wat}	Temperature reference set by cooling fluid (*°C*)
v_{sc}	Kinematic viscosity of water (m^2/s)
V_{air}	Velocity of forced air for cooling (*m/s*)
V_d	Voltage across the direct *d-axis* (*V*)
V_{lin}	Linear mechanical velocity (*m/s*)
V_q	Voltage across the quadrature *q-axis* (*V*)
V_s	Synchronous speed (*m/s*)
V_{wat}	Velocity of cooling fluid (*m/s*)

ΔT	Temperature rise (*°C*)
δ_g	Electro-magnetic shear stress in air-gap (N/m^2)
θ_{lin}	Linear mechanical position (*m*)
θ_{el}	Angular electrical position (*elec.°*)
θ_m	Angular mechanical position (*mech.°*)
μ_0	Permeability of free space (*H/m*)
μ_{rrec}	PM relative recoil permeability (*H/m*)
ρ_{Al}	Electrical resistivity of aluminium (*Ωm*)
ρ_{cu}	Electrical resistivity of copper (*Ωm*)
ϕ_g	No-load air-gap flux (*Wb*)
ϕ_m	No-load PM flux (*Wb*)

Ψ_0	No-load flux linkage (*Wb*)
Ψ_{HP}	Flux linked by HP (*Wb*)
ω_{el}	Angular electrical speed (*elec. rad/s*)
ω_{mec}	Angular mechanical speed (*mech. rad/s*)
1ϕ	Single phase
3ϕ	Three phase

Chapter 1
Introduction

In accordance with the on-going more electric aircraft (MEA) initiative, the Power Electronics, Machines and Control (PEMC) research group at the University of Nottingham (UoN) is actively involved with research in the field of aerospace related electrical systems.

A major project currently being undertaken by the research group involves the use of electro-mechanical actuators (EMA) to control the swash-plate of rotary aircraft. A parallel endeavour to this project was also initiated to study and investigate the possibility and feasibility of using electro-magnetic actuators (linear machines) for the same application. To this end, a major part of this thesis will investigate the design and analysis of a tubular, linear, permanent magnet (TLPM) motor for high force density applications.

Another challenging program that is also underway within the PEMC group considers the concept of using in-wheel electric motors for aircraft traction during the taxiing phase, without using any form of mechanical gearing. The main research effort in this application is towards reducing mass. This indicates the adoption of a machine with permanent magnets (PM) due to the inherent stored energy in the PMs, however issues with peak torque capability (demagnetising armature reaction), fault current and field weakening need considering. The topology selection, design, analysis and implementation of a traction motor for this application makes up another major part of this work. Within this part of the work, a novel machine design is developed, adopting an out-runner, Halbach array rotor and open slot stator with concentrated coils. The machine is force ventilated and achieves a peak torque of $7kNm$.

The main novelties in this thesis are a structured methodology for the improvement of torque density capability of electrical machines and a technique that improves the effective current loading a machine can handle. The latter (a novel thermal management technique based on integrated, high conductivity, thermal paths in the windings) is presented and investigated through an experimental instrumented setup. It is then implemented for both the above applications. It is shown that this method significantly enhances the torque/force density performances that electrical machines can achieve.

1.1 The role of electrical machine technology in the MEA

Force and torque transmission in aircraft is achieved by combining four main power distribution systems, namely mechanical, hydraulic, pneumatic and electrical. The general move towards more electrically based generation and distribution systems resulting from the MEA initiative [1-3], gives a natural preference towards having more electric loads. Thus, recent years have seen electrical drives gain an ever increasing role of importance in aircraft systems. The MEA concept which seeks to reduce or remove the presence of traditional hydraulic, pneumatic and mechanical systems has been around for the past few decades [1]. One major aspect of the MEA trend is to replace the well-established 'fly by wire' technology, by the 'power by wire' concept [4]. Nowadays, linear force actuation such as required for the control of the primary and secondary flight control surfaces (FCS), can be achieved by the use of EMAs and electro-hydraulic actuators (EHA). Their wide-spread use is still limited mainly due to their reliability. A major bottleneck is the probability of jamming, which can be alleviated by the elimination of screws and gearboxes. This pushes research towards direct drive (DD) actuation where the torque/force requirements from the electro-magnetic device are considerably higher. Apart from mechanically geared actuation, high performance, rotational machines can also be adopted for applications such as aircraft taxiing [5], environmental conditioning systems, tail rotor drives and electrical generation [6, 7].

For the aerospace industry, torque/force density, reliability and fault tolerance are of high importance. A wealth of literature [3, 8-10] exists that examines which machine topologies are best suited for such requirements. All this indicates that especially for aerospace applications, the need for improvement in terms of size, efficiency and cost is a main issue which the electrical machine designer has to consider through all the design stages [11].

1.2 Electrical linear actuation in aerospace

In aircraft, high force density, linear actuation is often achieved by the use of electrically powered actuators. These fall in to two main categories, namely EHAs and EMAs. In an EHA, a hydraulic pump driven by an electric motor, pumps hydraulic fluid contained in the actuator itself to a piston to which a mechanical joint is usually connected [12]. On the other hand, an EMA usually takes the form of a roller or ball screw driven by an electrical motor through an intermediate gearbox [13]. The use of EMAs in aircraft is highly desirable due to the lack of any hydraulic fluid [13]. The removal of the fluid and all its necessary accessories considerably improves system efficiency, lowers the overall system mass and reduces the overall system maintenance requirements. In addition, the intrinsic mechanical advantages synonymous with EMAs result in small, compact actuators ideal for aerospace applications. Such actuators are widely used for industrial, automotive and aerospace applications [2, 12, 14].

There are however a number of limiting factors or barriers which to date still prevent the complete takeover of the industry by EMAs, most important of which are the possibility of jams in the mechanical drive train [9, 13] and when a low inertia is highly desirable [15, 16]. The presence of mechanical components represents a considerable reduction in the reliability figures of any system, mainly due to the afore-mentioned possibility of jams. For safety critical applications such as the control of primary FCSs, this could lead to catastrophic failures unless complex mechanical disconnect systems are used in junction with redundant actuators, which in turn results in heavy and complex systems.

An interesting but highly challenging solution to these problems is to replace the mechanically geared EMA with a DD, electro-magnetic device such as a linear motor. This introduces a considerable simplification factor in terms of the above issues, mainly through the absence of any mechanical gearing and/or ball or roller screws [17], which makes a linear motor virtually jam-free.

The main drawback with linear motors is however their inherent inability to achieve the required performance in terms of force-to-mass and force-to-volume ratios as is expected from their mechanically geared, rotational counterparts [18]. Even so, there are some application scenarios that do make linear motors an attractive solution. These include applications where for example pulsed actuation is required such as for locks or in environments where fluid cooling is acceptable (such as for rotorcraft platforms). In these cases, it is the electro-magnetic limitations of the motor itself that represent the major barrier to force density rather than thermal limitations.

1.2.1 The helicopter swash-plate actuation application

To date, the primary FCSs of rotary aircraft are still controlled with conventional hydraulic actuators for heavy weight helicopters and with simple mechanical lever systems for light to medium weight helicopters. Due to the MEA efforts outlined above, a number of organisations such as the European Union's Clean Sky initiative [19] are interested in replacing these old but tested systems with new electric schemes [20-22] that incorporate EMA actuators. One of the systems under consideration is that of the swash-plate assembly, whose position commands the angle of the pitch of the main rotor blades. In general for a helicopter, lift is produced by the main rotor. In order to do this, the angle of the rotor blades needs to be adjusted with each revolution they make and this is achieved by the use of a swash-plate assembly. As shown in Figure 1.1a, the 'traditional' swash-plate assembly is made up of two main parts, namely the fixed assembly and the rotating assembly, mounted to each other by means of a main bearing. The stationary part is usually mounted on the main rotor mast and via lever and pushrod connections, is allowed to tilt in all directions and move vertically. It is these movements on the stationary part that actually produce the required adjustments on the angle of the blades of the main rotor [23].

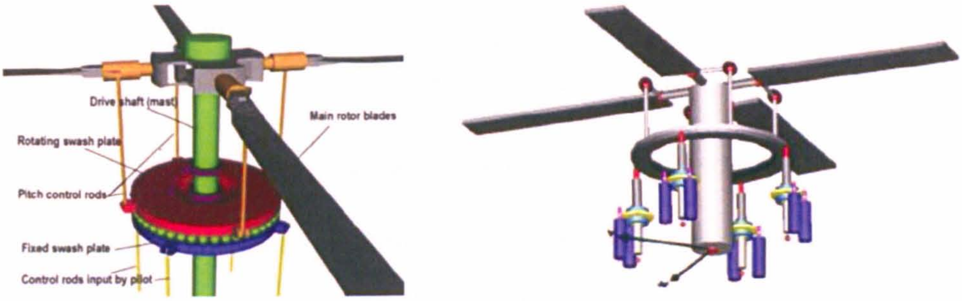

a) Typical swash-plate b) Proposed EMA-actuated swash-plate

Figure 1.1 Helicopter swash-plate systems

As described in [20-22], it is possible to replace the 'traditional' swash-plate assembly (that comprises mechanical and hydraulic levers and/or pushrods) with a system operated by EMAs. An example of a such a potential system is shown in Figure 1.1b, which is proposed in [21]. Along with other project partners, the UoN is currently involved in a similar initiative [22] to replace 'traditional' swash-plates with EMA-controlled systems and is investigating EMA design and general system concepts in order to achieve a high torque density performance coupled with satisfactory system fault-tolerance to counter any possible jams. For rotorcraft this represents a major challenge as this particular flight control system is safety critical and thus the actuation system must be able to support both jamming and free-wheeling fault conditions. Table 1.1 tabulates some general, specification requirements (for each EMA) for such a system, while Figure 1.2, whose source is [22] shows the typical, operating duty cycle required from each EMA, for this particular application.

	EMA specification
Peak linear force (*kN*)	15
Mass (*kg*)	45
Maximum velocity (*mm/s*)	100
Maximum stroke (*mm*)	100

Table 1.1 General EMA specifications for proposed EMA system

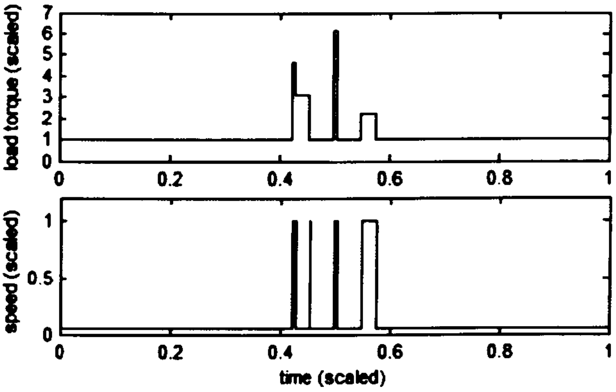

Figure 1.2 Typical duty cycles for proposed EMA system

Considering that a linear motor is virtually jam free, then a parallel project was also initiated to investigate the feasibility of utilising TLPM motors for the same application. The DD characteristics (high controllability, low inertia and jam-free nature) of a TLPM motor are the main 'attractions' for implementing such a device for the system presented above. With reference to the previously mentioned, force density concerns synonymous with linear motors, a perceived advantage of this particular application with respect to other linear motor implementations is the physical proximity of the main rotor lubrication system, which would thus enable the use of fluid cooling for the implemented motor. A major part of this thesis is thus concerned with the design and analysis of a high force density, DD, fluid-cooled, TLPM motor for a helicopter, swash-plate application.

1.3 Rotational electrical machines in aerospace

The role of the electrical machine in aircraft is not limited exclusively for linear actuation with EMAs. Applications which require high performance, rotational torque transmission in aircraft include the main electric generator systems [6, 7, 24], cabin pressurisation systems [25, 26] and propulsion on small aircraft [27, 28]. Recent years have seen the MEA initiative create new and exciting challenges, such as the use of electrical motors for the main propulsion of rotary aircraft and the afore-mentioned aircraft traction during taxi phase concept.

1.3.1 The aircraft traction application

The reduction of fuel consumption and carbon emissions is a main objective of the MEA initiative. The Clean Sky initiative is investing heavily in the study and implementation of schemes that would result in more environmentally responsible operation at all stages of aircraft utilisation. One of the main initiatives that is currently capturing a lot of attention is the concept of using electrical machines to provide traction during the taxi phase. This scheme proposes to offer the possibility to manoeuvre an aircraft on the ground without having to utilise the main engines or the traditional airport tow trucks [5]. A major multi-national company involved with the Clean Sky organisation has launched Green Taxiing™ (GT) in 2008 [29]. This scheme projects a 4-5% reduction in fuel burning and carbon emissions, whilst other advantages include lower noise pollution in airports and reduction of wear on the landing gear brakes, which would no longer need to counter residual thrust from the main engines.

The UoN as a project partner of the above-mentioned company is involved in this GT project as the main responsible for the design and construction of a DD, electrical machine to be used for this application and which will be located in the main landing gear. Apart from the challenging performance requirements, the electrical machine has also to deal with the high heat generated from the neighbouring brakes and with the take-off and landing speeds which can be more than ten times the operational speed of the machine. As explained in later chapters (considering the high torque density and fault tolerance requirements), the initial studies and investigations [30] indicate an AC, PM synchronous machine (PMSM) with a full Halbach array located on an outer rotor as the most promising topology for this project. The design, analysis and implementation of this machine are presented in this thesis.

1.4 PMSMs

In general, PM machines have a higher force/torque density, are more efficient and have lower losses than any other type of machine [31]. The torque/force density capabilities [9, 17, 30] and the fault tolerance performances [32, 33] ensuing from using PM technology for electric motors are very well documented. This indicates why PM motors have the fastest growing machine/drive market share, even when considering recent developments in the commercial prices of rare-earth materials and magnets. The main disadvantages with PM machines are the natural intolerance of PMs to high temperatures, the economic burden related to PM material and the always present no-load flux because a PM cannot be simply 'switched off' [4].

PM machines can be generally classified into three main branches, namely DC commutator motors, DC brushless motors (BLDC) and brushless AC (BLAC) synchronous motors [31]. The DC commutator motor is a conventional DC motor with the field excitation winding replaced by PMs. The BLDC and the BLAC machines, which are both PMSMs, are practically the same except for the nature of the excitation voltage. The BLDC is fed with a trapezoidal waveform and uses a switching pattern synchronised with the rotor angular position, thus only two phases conduct at any given moment. On the other hand, sinusoidal waveforms that produce a travelling magnetic field are used to operate a BLAC machine.

The similarity between BLDC and BLAC machines also extends into their performance and general characteristics. Table 1.2 whose source is [34] presents a simplistic comparison indicating the main differences between the two technologies' characteristics, where obviously the '+' sign represents a merit and a '-' sign represents a disadvantage. It is important to note that the information in Table 1.2 does not consider the variations due to specific applications and to specific design and optimisation techniques, but generalises its survey as much as possible. It can be noted how the main advantages of the BLAC are torque smoothness and the field weakening capability at the cost of an extra economic effort. These advantages are crucial for an aerospace application such as mentioned in Section 1.3.1, therefore the rest of the discussion will mainly focus on BLAC machines, which for convenience will henceforth be referred to as PMSMs.

	BLDC	**BLAC**
Motor Efficiency	+++	+++
Torque Smoothness	+	+++
Torque Density	+++	+++
Open Loop control	-	-
Closed Loop Simplicity	+++	+
Minimum Control Sensors	+++	+
Machine Design Flexibility	++	+++
Extended Speed Range	+	+++
Motor Robustness	+	++
Cost - Motor	££	££
Cost – Converter, Sensors & Control	£	£££

Table 1.2 General comparison of BLDC and BLAC machines

PMSMs are usually classified into two main categories. The first is surface mount PM (SMPM) machines with the PMs located in the air-gap on the rotor surface area, while the second is interior PM (IPM) machines where the PMs are buried into the rotor. Figure 1.3 whose source is [35] shows cross-sectional views of a SMPM machine and an IPM machine.

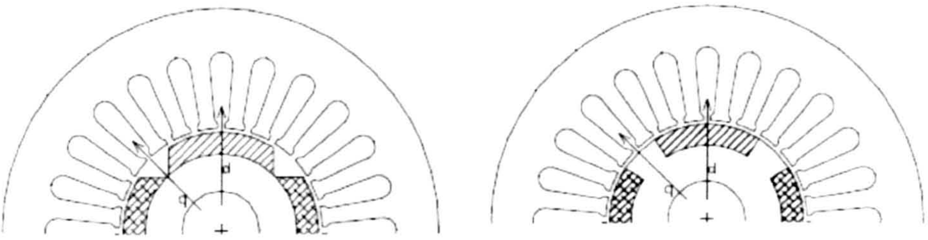

a) SMPM machine b) IPM machine

Figure 1.3 Rotor structures of PMSMs

Comparisons of these two topologies have been widely reported in literature [35-41]. The SMPM topology enables the use of larger air-gaps [42], thus reducing construction tolerances but more importantly permits a better utilisation of PM material, which automatically improves torque density. Machine volume and mass is also more readily minimised in SMPM machines which can result in further enhancements of torque density [36]. Because of its construction, an

SMPM machine in general enjoys a better efficiency, mainly due to the lower rotor losses [34, 43]. The main demerits of this configuration are the higher risk of PM demagnetisation, the lower inductance [35] and the need for a retaining sleeve for the PMs especially for high speed machines [42, 43].

On the other hand, the dissymmetry or saliency that characterises IPM machines results in a saliency (reluctance) torque component [35] and a higher magnetic inductance [31, 44]. This makes the IPM machine the better option for fault tolerance applications because of the better handling of short circuit current whilst it also enhances its field weakening capabilities [34]. A further, ensuing advantage is the difference in the values of the direct or *d-axis* inductance L_d and the quadrature or *q-axis* inductance L_q which simplifies and enhances the implementation of advanced control techniques such as sensor-less control [45]. The rotor of an IPM machine is obviously more robust and easier to manufacture than for the SPM configuration, however it also leads to more elevated rotor losses [38] which reduces machine efficiency and can also result in higher armature reaction effects [34].

Considering all the above and keeping in mind that it is always difficult to achieve a general comparison (i.e. without considering the application and the design procedures), the main merits and disadvantages of the two topologies relative to each other, can then be simplistically tabulated as shown in Table 1.3.

	SMPM	**IPM**
Motor Efficiency (Rotor Losses)	+++	+
Torque Density & Smoothness	+++	+
Extended Speed Range	+	+++
Fault Tolerance	++	+++
Rotor Robustness	+	++
Cost - Motor	££	££

Table 1.3 General comparison of SMPM and IPM machines

1.4.1 High torque density PMSMs

Considering that the main challenge for the application mentioned in Section 1.3.1 is achieving the specified levels of torque required while keeping the overall actuator mass to a minimum, then the intrinsic advantages in terms of torque density, torque smoothness and efficiency of the SMPM machine indicate this topology as a better option. While the aircraft is flying, the wheel actuator system will have to be carried (i.e. dead weight) and so the torque density must be maximised in all possible ways. Maximising of torque density for PMSMs is a well-documented and researched subject where various techniques and procedures exist to for its optimisation.

1.4.1.1 Torque density limitations

Despite the vastness of the range of electrical machines available today, in general all machines are subject to the constraints imposed by the materials (copper, insulation, soft and hard magnetic materials) from which their main components are constructed [46]. For PM machines in particular, the constraints can be considered to fall into two main categories, namely the electro-magnetic limit and the thermal limit [47]. These two limits can be said to define the main boundaries of the air-gap shear stress δ_g capability of any machine, a value which can be used to simplistically size electrical machines. An important aspect of PM machines is PM demagnetisation, a possibility which can be prevented by operating safely 'in respect' to both limits. In conjunction with other boundaries set by other limitations (for example mechanical constraints) then these limits quantify what force/torque and therefore force/torque density can be obtained from a particular machine.

The relationship between δ_g and the electro-magnetic limit for different PM machine topologies is investigated in [48]. Table 1.4, the source of which is [48] presents a number of PM machines that are studied in order to achieve an understanding of this limit. Figure 1.4, the source of which is also [48] compares the δ_g of these machines in relation to the electrical current loading A_{rms}. From Figure 1.4, it can be observed how distributed wound machines with a high number of slots, result in a higher δ_g indicating a better performance in terms of the electro-magnetic limit.

Machine	**Topology**			**Slot/Pole**	**Winding**
Mach1	Traction PMSM	IPM	Rotational	18/6	Distributed
Mach2	Traction PMSM	SMPM	Rotational	24/28	Concentrated
Mach3	Low Speed PMSM	SMPM	Rotational	18/14	Concentrated
Mach4	High Speed PMSM	Segmented SMPM	Rotational	24/4	Distributed (5/6 Pitch)
Mach5	PM, Flux Switching	IPM in Stator	Rotational	6/7	Concentrated
Mach6	TLPM	IPM	Linear	12/10	Concentrated

Table 1.4 PM machines for δ_g analysis

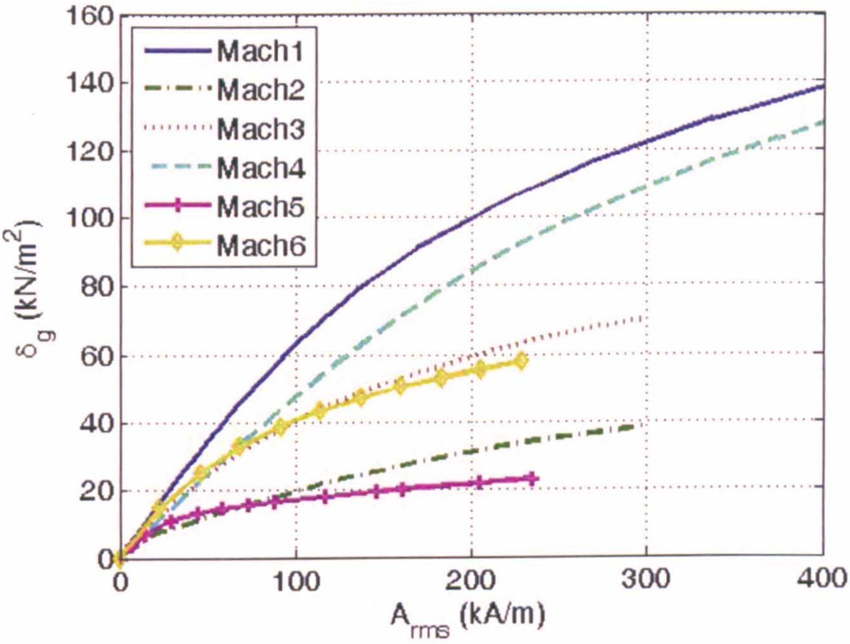

Figure 1.4 Results of δ_g analysis

However, as stated in [48], this does not necessarily mean a better performance overall. Typically the copper loss P_{cu} for such machines is higher than for concentrated wound machines, while a higher δ_g usually indicates a better torque per rotor volume capability and not torque per overall volume. This last point is also proven in [48], where it is shown how it is actually Mach3 (concentrated winding) that exhibits the best performance in terms of torque per total machine volume. All this indicates that while a higher δ_g indicates a general improvement in the electro-magnetic limit, a better torque density performance can also be achieved by considering other parameters such as presented below in Section 1.4.1.2.

1.4.1.2 Torque density improvements

A main advantage associated with the use of concentrated wound, PMSMs is the possible use of fractional slot per pole configurations. This winding technology while offering a considerable performance in terms of fundamental winding factor K_w [49-51], has the added merits related to the use of concentrated windings. Such advantages include improvements in terms of the slot fill factor K_{fill} [50, 52], shorter end-windings [50, 53] thus reducing the amount of non-torque-productive copper and the overall total copper mass and other design related advantages such as efficiency and fault tolerance [50, 53]. Further improvements on K_w, torque density, torque ripple and on fault tolerance capability have also been shown to be obtainable by implementing the use of unequal widths of the stator teeth [30, 54, 55]. The adoption of an outer rotor configuration automatically increases the radius of the air-gap, thus resulting in a higher torque capability for any machine. It can be argued that this is true for any machine [56] and has been shown in [57] to improve considerably the performance of PM machines.

An interesting but very challenging variation of the SMPM and IPM configurations is the use of Halbach arrays [58]. The air-gap flux density and thus the torque capability of a PMSM can benefit greatly from the use of such arrays [59, 60]. Various works [61-63] document how adopting such a configuration enhances the sinusoidal shape of the air-gap flux density, thus improving the ratio of the fundamental air-gap flux component to the total air-gap flux. Having a high value of this ratio ameliorates the torque capability of the machine [30], as it is the fundamental component of the air-gap flux density that actually produces the torque, whilst the total air-gap flux has other effects such as the saturation levels in the stator.

The torque/force capability improvements resulting from the use of Halbach arrays are documented in several comparative studies [58, 62, 64, 65], however these arrays also present a number of issues that must be taken into account. The major problem is mainly the higher risk of demagnetisation, synonymous with Halbach arrays [66, 67]. In a Halbach array, each complete pole is assembled out of segments that are magnetised in different directions. The proximity of a segment to another intrinsically creates reverse magnetic fields that can demagnetise parts (usually the corners) of the segment next to it [66], even at no-load. The demagnetisation phenomenon is more of an issue when quasi-Halbach arrays are preferred to full-Halbach arrays.

Quasi-Halbach arrays [62] are popular because of the reductions in costs, manufacturing and assembly procedures when compared to a full-Halbach array. Therefore safety factors and careful analyses [66] are required when a Halbach array is to be implemented. Another demerit of Halbach arrays arises from the fact that while they can improve the torque capability of a PMSM, it is also true that with Halbach, more PM material is used which increases the mass of the machine. It is however also important to point out that adopting a Halbach array will minimise the need of back iron as a return magnetic path. Thus for an application with focus on torque density, careful comparative studies must be carried out to confirm whether the torque improvement gained by the use of the Halbach array outweighs the extra cost and weight due to the added PM material.

Other issues with Halbach arrays include the reduced robustness of the rotor and the more difficult assembly procedures. However, the fact that the back iron is minimised and does not need to fill the role of a return magnetic path can be highly beneficial as non-magnetic rotors can be adopted. The rotor can then either be of very low weight (aluminium or carbon fibre composites) or of very high strength material (stainless steel, titanium etc...).

The use of high grade soft magnetic material such as cobalt iron can also be implemented as a measure to improve torque density capabilities as this permits an increase in the magnetic loading limits of the machine. In [30], the merits of applying such materials to machine design are highlighted relative to traditional, lower grade materials such as silicon iron. This however comes at the cost of a slightly higher mass density and a considerably higher economic factor.

The information gathered in the above sections, indicates the PMSM topology as a candidate for the application of Section 1.3.1. As discussed and presented in later chapters, the above points to maximise the torque density performance of the machine are all taken into consideration and careful studies are carried out to confirm the validity of the schemes. By combining these schemes into a structured methodology, considerable improvements in terms of torque density can be achieved.

1.5 Linear machines

If a multi-phase, alternating current (AC) rotational machine has its stator 'unrolled' such as shown in Figure 1.5, then instead of producing a torque about a centre of rotation, it will produce a force along the length of the 'unrolled' material. Such a configuration is in general called a linear machine and it can drive a linear motion load without intermediate gears, screws or crank shafts [68].

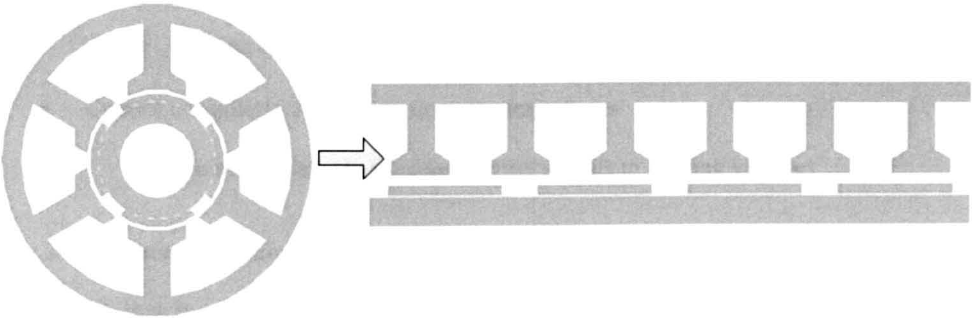

Figure 1.5 Visualisation of rotational to linear motor conversion

By rolling a flat, linear motor around the axis parallel to the direction of the travelling magnetic field (i.e. parallel to the direction of thrust), a tubular (cylindrical), linear machine can be obtained. Figure 1.6 shows the hypothetical evolution from a rotational motor to its tubular counterpart.

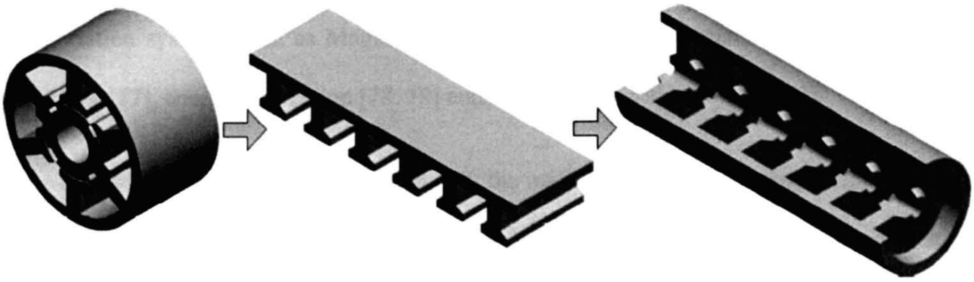

Figure 1.6 Evolution from rotational to tubular concept

Linear motors can be used anywhere that requires linear actuation or movement. They can serve as an effective alternative to mechanically dependant devices such as chain and belt based conveyer systems, hydraulic actuators, and lead screw drives amongst others. The use of a linear motor instead of the devices mentioned above results in a number of advantages, amongst which are

- Increased reliability
  - Less components subject to wear
  - Virtually independent of friction issues
- Improved performance
  - Improvements in speed, acceleration, efficiency
  - Better position control
- Freedom in direction of motion
  - Motion can be in any slope including vertical
- Control of multiple vehicles on complex trajectories
  - No need of communication/control signals to moving vehicles

Any linear motor can be considered as an unrolled version of its more conventional rotational counterpart, thus it can be said that the range of linear machine types available today almost matches the available range of rotational machines [18]. This vast range makes possible the utilisation of linear motors in various fields and sectors so as to satisfy a wide range of performance requirements. The levels of efficiency, reliability and accuracy that can be achieved have made them indispensable to the industrial automation sector, such as for pick and place [69] and translational carriage [70, 71] systems. Other examples of documented applications are for the automotive and electric vehicle industries [72], high speed transportation systems such as Maglev trains [73, 74], elevator systems [75, 76], household appliances [77], energy conversion [78, 79] and for defence applications [80-83].

However, as already mentioned in Section 1.2, the main challenge concerning linear motors is always to achieve satisfactory force density performances. When faced with an application where weight and volume play an important, vital part such as for aerospace, the machine designer must be careful and come up with a project strategy that will increase the possibility of maximising the force density performance. A look at the available literature indicates that the correct choice of a machine topology that would permit the maximum performance should always be the initial step of this strategy. In the next sections, a look at what has been reported in literature in order to achieve and/or maximise high force density in linear machines is presented.

1.5.1 High force density linear machines

The various technologies and topologies of electrical machines available today give the user/designer of machines a vast range from which to choose according to the application required. In the case of linear machines, published literature reveals that of the various technologies and topologies, it is when combining PM technology with a tubular topology that one can achieve the highest efficiency levels and more importantly the better torque/force/power densities possible [62, 65, 84, 85]. This is mainly due to the lack of end-windings, which permits the full utilisation of the current carrying conductors and automatically removes the end-winding hot-spot, thermal problem. Authoritative reviews of traditional, single air-gap TLPM motors with focus on high force outputs are presented in the reference publications of [65, 84].

However, in recent years there has also been an interest in advanced, more complex, multi air-gap concepts such as proposed in [79, 86-88]. An initial study of these last topologies [89] indicates attractive advantages in terms of force density and fault tolerance however at the cost of increased complexity and manufacturing difficulties. In fact, probably this excessive, increased complexity is keeping these technologies from a more prominent role in linear actuation systems.

In the next sections, a qualitative comparison of these different topologies, investigates recent high force linear machines documentation and reviews recent single air-gap and multi air-gap linear/tubular machines. In general, the relationship between the force capability of a linear machine and its air-gap can be described by (1.1), where F_{lin} is the mean of the thrust force achieved and A_{mov} is the surface area of the moving part of a linear machine, henceforth called the mover. Equation (1.1) indicates how the force capability is proportional to δ_g and to the surface area of the mover, which is virtually the same area as that of the air-gap.

$$F_{lin} = \delta_g \times A_{mov} \tag{1.1}$$

As previously mentioned, it is widely accepted that PM machines usually achieve the best performances in terms of force density and therefore this review will mainly focus on such machines.

1.5.1.1 Single air-gap machines

The performances of different, single air-gap, TLPM motor configurations are investigated in [65, 84] with comparisons between IPM and SMPM and slotted and slot-less configurations being conducted. In both papers, the authors stress the importance of the relationship between the force capability and the PM mass, i.e. they relate performance to the weight and cost of the machine. From these studies, it emerges clearly that excellent force density performances can be obtained by the use of a slotted motor with axially magnetised IPMs. Figure 1.7 shows such a configuration, where the reduced PM mass results in a reduction in weight and cost. The main disadvantages of this configuration are the slightly higher cogging effects and the increased radial attractive forces due to any eccentricity [89]. The use of Halbach arrays for tubular motors is investigated in [62, 64]. However as already mentioned in Section 1.4.1, this technology must be studied carefully before being implemented, mainly because of the impact it can have on the overall weight of the machine.

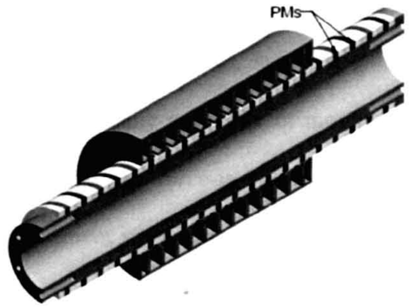

Figure 1.7 Single air-gap, TLPM motor with IPMs

The authors of the above publications all stress the importance of the design and optimisation procedures used during the conception of a particular project. As highlighted in [17, 89], the main parameters to address for optimisation are mainly the split ratio R_{spl} and the pitch ratio R_{pit} which will be discussed in later chapters. The pitch ratio in particular has an important effect not only the force-to-mass ratio but also on the force ripple and the machine back-EMF.

A method to maximise the force density of a TLPM motor via a thermal management technique is introduced in [17]. This technique permits higher current densities to be used without increasing the thermal limit of the machine, thus automatically increasing the force-to-mass ratio. This concept is also presented and discussed in ensuing chapters.

1.5.1.2 Multi air-gap machines

As mentioned in Section 1.4.1.1, any electrical machine can be simplistically sized using its δ_g value. Thermal constraints at steady state and magnetic saturation in terms of instantaneous peaks usually define the main limits of this value. As stated in (1.1), for a given, maximum allowed δ_g, the force produced for a particular machine volume can be maximised simply by maximising the air-gap area per unit volume. A method by which to obtain this increase in A_{mov} is to have a number of active surface areas utilising all the available space within the volume of the machine. This is termed as a multi air-gap structure, where the increased active area implies an improvement in the generated force/torque [89].

Whilst mainly focusing on the force-to-volume ratio, an indicative but somewhat application-restricted comparison between single and multi air-gap topologies is reported in [86], indicating the superior performance of the multi air-gap concept. The authors also investigate different methods of splitting the active zone. Better performances are claimed when the winding coils are kept whole (global coils). The results of this investigation are used by the same authors to design and implement a tubular, multi air-gap prototype presented in [87]. Active zone splitting is achieved by using a number of moving rods with axially magnetized IPMs. The authors report an achieved force-to-volume ratio of 1 N/cm^3 for continuous operation, an impressive improvement when comparing to the typical force-to-volume ratio of a classical, single air-gap TLPM motor of approximately 0.3 N/cm^3.

The multi air-gap principle is used in [88] for the design and implementation of a linear, high force density, fault tolerant actuator. A number of moving plates equipped with magnetic teeth, stationary plates and a global coil are the main components used for this prototype. The output force is generated by the interaction of the longitudinal field created by the global coil and the field due to the PMs on the fixed plates. Very encouraging results are reported with a force-to-volume ratio of 4.8 N/cm^3, a force-to-mass ratio of 923 N/kg and an air-gap shear stress of 3.73 N/cm^2. It is however important to note that these values are reported for the actuator in short-pulse operation. From this publication, a perceived disadvantage of multi air-gap arrangements is their effective thermal management and construction complexity.

The double air-gap, TLPM machine presented in [79], makes a very efficient use of the space in the available exterior envelope of the machine, by creating two co-axial air-gaps. Different set-ups of the PM arrays are investigated whilst an investigation on the mechanical aspects of the construction and assembly is also given. The reported force-to-volume ratio of this machine is approximately 0.3899 N/cm^3.

1.5.1.3 Single air-gap vs. multi air-gap

As is clear from the above, these multi air-gap concepts all exhibit very good high performance results in terms of force density whilst they are also shown to be excellent fault tolerant devices. Thus, from the referenced literature, it can be concluded that the multi air-gap technology is a very promising technology, highly adequate for the aerospace industry, in terms of force density. However, all the authors report that the high degree of conceptual complexity makes the realisation and implementation of these machines extremely difficult. The higher number of active components and the difficult manufacturing and assembly procedures result in the initial capital costs and reliability penalty to be very elevated.

In [89], two TLPM machines having the same volume but one with a single air-gap and one with two co-axial air-gaps are designed and compared in terms of force, force density and temperature performances. The double air-gap concept demonstrates considerable improvement over its single air-gap counterpart at the cost of extra mass and components (active and non-active). This improvement is much reduced when the whole machine assembly and not just active components is considered. Main concerns emerging from this paper are the issues of rigidity, robustness and concentricity as the space available for necessary mechanical components such as bearings, and guiding rails is limited by the spatial location of the stationary parts. On top of this, thermal management of the coils can be a significant challenge due to the structure having PMs on both sides of the air-gap. The multi air-gap technology, when considering overall, complete systems, loses a lot from its 'appeal', as it requires a considerable effort for effective implementation. Simultaneous mechanical, thermal and electro-magnetic design is probably the only feasible way to go about the successful design and implementation of such technologies. Thus, a single air-gap, TLPM motor is the technology of choice as the main contestant for the application mentioned in Section 1.2.1.

1.6 Objectives, aims and thesis structure

As already partly revealed in the above literature review, the main objective of this thesis is to make a marked improvement in the torque/force density performance that state-of-the-art electrical machines can achieve. This is done through novel electro-magnetic and thermal management structures, detailed design and optimisation considering both the performance requirements and the manufacturing constraints. As vehicles to investigate these novel concepts the two applications mentioned above are considered, i.e. a TLPM motor for the helicopter swash-plate application described in Section 1.2.1 and a PMSM for the GT application described in Section 1.3.1. To achieve these objectives the general methodology used for the machines follows the four steps outlined below:

- Principles and theoretical evaluation
    - An extensive literature investigation that reviews the state of-the-art in the respective research field.
    - Identification of key topologies and technologies to investigate.
    - A theoretical explanation that culminates in practical, analytical models (thermal, electro-magnetic) to predict quickly the performance of both the machines.
    - Building of finite element (FE) models to accurately perform analysis of the required models.
- Design and optimisation
    - Using the analytical and FE models the identified possible configurations are simulated.
    - The best performing arrangements are then subjected to specific optimisation techniques structured in a well organised methodology.
    - The use of a thermal management technique for the phase windings is investigated and tested in an effort to yet gain further improvements in performance.
- Manufacture and construction
    - The final designs are used to build prototypes of the machines.

  - In-house equipment and manufacturing tools in conjunction with specialised assembly procedures are used to manufacture and construct the machines.
- Experimental testing and results verification
  - The TLPM motor and the PMSM are set up in appropriate rigs and tested accordingly. Results are presented and compared to validate the analytical and FE models.

The thesis consists of six chapters that are designed to logically report and present all the work done in order to reach the objectives above.

Chapter 1 serves firstly as an introduction to the projects and the required applications and secondly as a literature review that reports recent advancements in high performance electrical machines related to the required applications.

The knowledge gained from the literature review is used to build analytical and FE models of the TLPM motor. These models are presented in Chapter 2 which also includes comparisons between the analytical and FE results for the TLPM motor. The same is repeated in Chapter 3 for the PMSM for the GT application.

In Chapter 4, a novel thermal management technique for the phase windings of electrical machines is introduced. Analytical and FE models are used to investigate this technique. The effects of implementing this concept to the TLPM machine and the GT motor are investigated and documented.

Manufacturing, construction and experimental validation of the thermal management technique set-up, the TLPM motor and the GT motor are tackled in Chapter 5. The specialised manufacturing procedures, the materials and the assembly procedures used in the realisation of the set-ups/prototypes are reported. Brief considerations for the test rigs are also given. This chapter also deals with the experimental validation of the machines and set-ups. Experimental results are presented and compared with the analytical and FE results, with everything being rounded up with qualitative discussions and analyses. Chapter 6 finishes off this thesis by presenting general conclusions, overall discussions and further work to be done.

Chapter 2
The TLPM Motor

This chapter deals with the design and optimisation of the TLPM motor with IPMs. Considering the elevated, force density requirements and the nature of the application as described in Section 1.2.1, it was decided to take advantage of the proximity of the rotor lubrication system by incorporating fluid cooling into the design.

The literature review of Section 1.5 identifies a TLPM motor with IPMs as the topology that guarantees the better force density performances. An initial verification exercise is done where a number of possible topologies and possible designs are proposed and investigated. Analytical and FE techniques are used to build electro-magnetic, electrical and thermal models that cater for a naturally cooled motor and also for a water-based, fluid cooled motor. Design and optimisation procedures are explained in this chapter. The performance and results of the models are then compared and discussed, thus validating any choices made.

More specifically, this chapter starts off by validating the choice of an IPM configuration over a SMPM topology. This is done by building and testing, analytical and FE models of the two options. The models are then used to identify the optimum slot-pole combination for the better configuration. Tools for thermal design and analysis are then created, taking the form of a lumped parameter, thermal network model, complemented by a thermal, FE model. Having set the design environment, this chapter then investigates in detail the optimisation process for the TLPM motor with main focus on geometrical optimisation and the reduction of cogging effects relative to the stator finite length. The chapter concludes by presenting the optimal design of the TLPM motor.

2.1 Linear PMSM basic relationships

Considering the linear and tubular concepts as shown in Figure 1.6 and Figure 1.7, then the mechanical position θ_{lin} of the moving part (henceforth called the mover) of a linear motor and the angular electric position θ_{el} are related as described in (2.1), where T_p is the pole pitch in *mms* and θ_{el} is in electrical radians.

$$\theta_{lin} = \frac{T_p}{\pi}\theta_{el} \tag{2.1}$$

Thus, the linear mechanical speed V_{lin} of the mover can be expressed relative to the equivalent angular electrical speed ω_{el} by (2.2).

$$V_{lin} = \frac{T_p}{\pi}\omega_{el} \tag{2.2}$$

A basic relationship between the linear electromagnetic thrust force F_{lin} and the equivalent torque T of a rotational counterpart is described by (2.3) where P is the number of pole pairs.

$$F_{lin} = \frac{\pi T}{P T_p} \tag{2.3}$$

The angular mechanical speed ω_{mec} is related to ω_{el} by

$$\omega_{mec} = \frac{\omega_{el}}{P} \tag{2.4}$$

This thesis is concerned with a linear PMSM, however (2.1) - (2.4) are valid for any topology and type of linear motor. For linear PMSMs the mechanical linear motion of the mover is synchronized with the armature field [68]. For a motor with the armature on the stator, the force F_{lin} is generated due to the interaction of the travelling magnetic field produced by the poly-phase windings and the PM array on the mover.

Considering the principle of the travelling magnetic field, then V_{lin} can be expressed as (2.5) where V_s and f_s are the synchronous speed and frequency.

$$V_{lin} = V_s = 2 f_s T_p \tag{2.5}$$

2.2 Choice of topology

From the literature review of Section 1.5.1, it is clear that there are a number of feasible PMSM topologies adequate for the required application presented in Section 1.2.1. An evaluation and comparison of different configurations is done in order to identify the best suited topology. This also serves to confirm the reported findings of the mentioned publications when applied to the application requirements of this work. For the following comparisons, a TLPM motor with the PMs on the mover is considered as this has the advantage of having space fixed coils.

The investigation is done by considering a set of quantifiable, quality indicating (QI) parameters that reflect the performance of the machines, amongst which are the output thrust force generated (i.e. F_{lin}), the force-to-mass ratio, the no-load induced back-EMF, the force ripple F_{rip} and the total machine copper loss P_{cu_tot}.

The force capability F_{lin} of a linear PMSM is a function of the electric loading A_{rms}, the magnetic loading and the mover surface area. Fixing the machine dimensions, the force capability can be expressed at various values of electrical and magnetic loading, giving a clear indication of the quality of the topology. A direct consequence of the force capability is the value of the force density (i.e. the force-to-mass or force-to-volume ratio). As the application is for aerospace, this parameter is one of the main criteria that must be addressed during all of the design process.

For a PM machine, the quality and value of the induced back-EMF on no-load, indicate how controllable and feasible the machine is. This makes the back-EMF a highly appropriate parameter from which to take a measure of the “goodness” factor of any machine. In general the machine designer tries to achieve a smooth a force/torque as possible. A high F_{rip} can result in vibrations and acoustic noise. A component of F_{rip} is the cogging force F_{cog}, thus the models investigated are also studied in terms of these two parameters. Another important parameter that defines the quality of the machine is the copper loss P_{cu_tot} that has a direct impact on the thermal and electrical limits of the machine. Most of the following comparisons are done by designing for similar values of P_{cu_tot} so as to have the ‘fairest’ comparisons possible.

2.2.1 SMPMs vs. IPMs

The PMs on a TLPM motor are usually configured with either a SMPM or an IPM configuration or as Halbach arrays. However, considering the cost and demagnetisation problems associated with Halbach arrays, it was decided to focus the following comparison between the former two configurations. As shown in the cross-sectional views of Figure 2.1, the SMPM configuration is achieved by employing radially magnetised PMs whilst the IPM configuration utilises axially magnetised PMs.

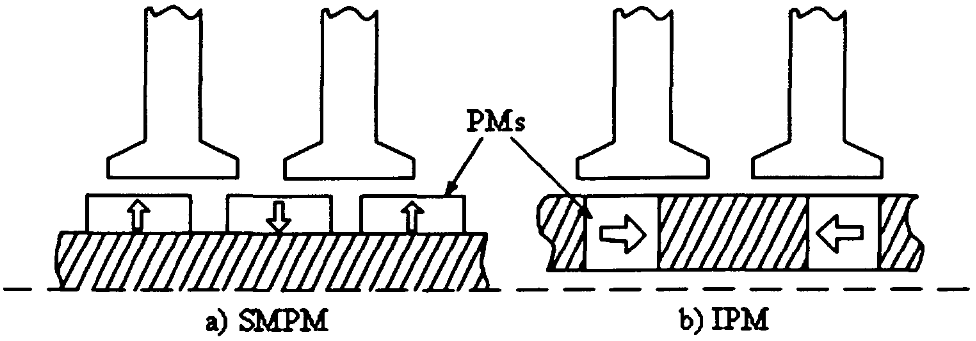

Figure 2.1 TLPM motor with a) SMPMs and b) IPMs

The operation of a linear SMPM machine is similar to a rotational PM machine with surface mount PMs, whilst a TLPM motor with an IPM configuration is similar to a machine with interior PMs. The comparisons presented in [65, 84] claim a better performance in terms of force density for the IPM configuration.

2.2.1.1 Magnetic models

In order to investigate the respective performances, mathematical models for both configurations are built using the reluctance model approach [68]. The derivations and procedures of the analytical magnetic models are presented in Appendix A. For these models, the following assumptions were considered necessary for the idealisation of the TLPM models.

1) Infinite iron permeability in both stator and mover, such that iron losses are null.
2) A balanced 3ϕ supply giving a sinusoidal electric loading.
3) Leakage flux through the mover is negligible.
4) Armature reaction due to current in stators is negligible.
5) An infinite length of the motor such that the cogging end effect is null.

6) A_{rms} is constrained by the thermal limit of the machines and not by the magnetic limit. Since modern PMs have high coercive field values, even at relatively high temperatures then the thermal limit results to be more restrictive [84] than the magnetic limit that usually defines the demagnetisation limits of the PMs.

A. The SMPM configuration

The use of SMPMs in a TLPM motor, results in a large effective air-gap with a relatively small magnetic saliency. A common feature of such arrangements is the resulting small inductance with little or no difference between L_d and L_q. Figure 2.2 shows the geometrical description of a TLPM motor with a SMPM configuration using radially magnetised PMs.

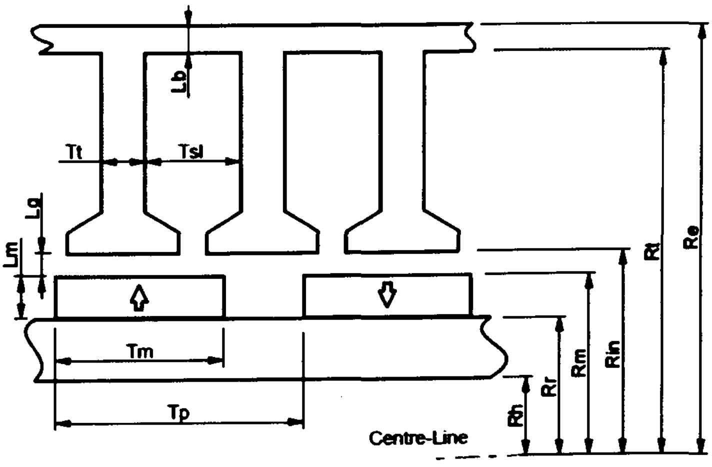

Figure 2.2 Structure of TLPM motor with SMPMs

Considering the geometry in Figure 2.2, and the assumptions above, then the no-load air-gap flux density B_g can be described by (2.6), whose derivation is given in Appendix A.2 and where B_{rem} is the PM residual flux density and μ_{rrec} is the PM relative recoil permeability. The fundamental component B_{g1} of B_g, which is directly proportional to the no-load flux linkage Ψ_0 and to F_{lin} is obtainable through a Fourier series expansion and is as described in (2.7).

$$B_g = B_{rem} \times \frac{1}{\frac{(R_{in} + R_m)}{(R_m + R_r)} + \left(\frac{\mu_{rrec}}{L_m}\right) L_g} \tag{2.6}$$

$$B_{g1} = \frac{4}{\pi} B_g \sin\left(\frac{\pi T_m}{2T_p}\right) \tag{2.7}$$

B. The IPM configuration

TLPM motors employing an IPM configuration usually have a higher magnetic saliency and a better flux weakening capability. Figure 2.3 shows the geometrical description of a TLPM motor with an IPM configuration. The air-gap, flux density B_g is given by (2.8), where $T_c = T_p - T_m$ and whose derivation is given in Appendix A.3, whilst B_{g1} is described by (2.9).

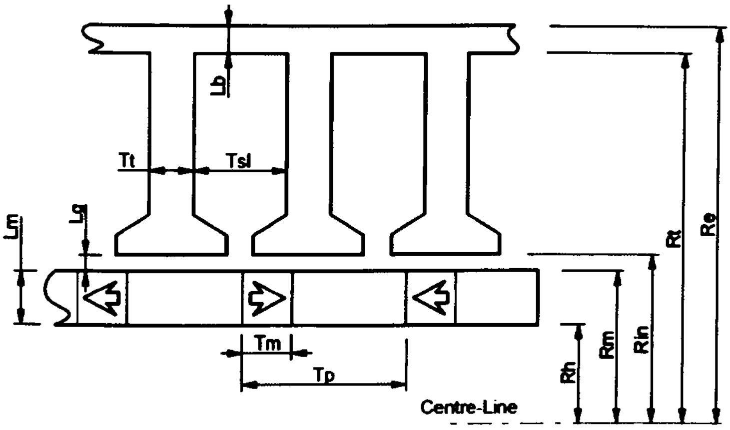

Figure 2.3 Structure of TLPM motor with IPMs

$$B_g = B_{rem} \times \frac{\frac{T_m}{\mu_{rrec}}(R_m^2 - R_h^2)}{L_g(R_m^2 - R_h^2) + \left(\frac{T_m}{\mu_{rrec}}\right)\left(\frac{T_c}{4}\right)(R_{in} + R_m)} \tag{2.8}$$

$$B_{g1} = \frac{4}{\pi} B_g \sin\left(\frac{\pi T_c}{2T_p}\right) \tag{2.9}$$

2.2.1.2 Electrical models

The electric models of the machines are based upon the physical geometry and the electric properties of the coils. In general, the maximum temperature rise ΔT experienced by the windings defines the limits for A_{rms} and for the maximum copper current density J_{rms}. For this analysis, the following assumptions are considered for the electrical models.

1) The only source of heat is due to the I^2R losses with negligible stator iron losses.
2) Stator iron is a perfect thermal conductor.
3) The length of any turn of a stator winding is always calculated as if it was geometrically placed in the centre of the slot.
4) Only natural cooling is present at the external surface of the machines.

Considering these assumptions then as a first approximation, the total machine loss can be described by (2.10), whose derivation is given in Appendix B.1 and where ρ_{cu} is the electrical resistivity of copper and N_{slots} is the number of slots.

$$P_{cu\_tot} = \frac{\pi}{2} \times \rho_{cu} N_{slots} \times J_{rms}^2 \times T_{sl} K_{fill} (R_t - R_{in})(R_t + R_{in}) \tag{2.10}$$

Since at this stage of the design only natural cooling is considered, any loss generated in the machine can be said to be dissipated into the environment through the external surface area of the stator at a rate dependent on the temperature difference between the windings and the ambient temperature T_{amb} and on the overall heat transfer coefficient h, as shown in (2.11).

$$P_{cu\_tot} = h \times \Delta T \times (4\pi R_e P T_p) \tag{2.11}$$

By combining (2.10) and (2.11), then the maximum ΔT in the windings is found from (2.12). Using (2.12), the maximum values of J_{rms} and A_{rms} for safe operation of the machine, can then be identified.

$$\Delta T = J_{rms}^2 \frac{N_{slots}}{8P} \rho_{cu} T_{sl} K_{fill} \left[\frac{(R_{in} + R_t)(R_t - R_{in})}{h R_e T_p} \right] \tag{2.12}$$

2.2.1.3 Generated force

Considering assumptions 2 and 4 of Section 2.2.1.1, then F_{lin} developed by the machines can be expressed by (2.13). The force is mainly dependant on the interaction between the flux density fundamental component B_{g1}, the electric loading A_{rms} and A_{mov} defined by $(4\pi R_{in} P T_p)$.

$$F_{lin} = B_{g1} A_{rms} \times (4\pi R_{in} P T_p) \tag{2.13}$$

2.2.1.4 Design procedure

The analytical models based on the above equations are built to provide adequate starting points for more accurate FE models. The design is initiated by considering any parameters that are fixed either by the application requirements or by material properties. Thus, the maximum external length L_e and the maximum external radius R_e of the machine are fixed by the available envelope, whilst such parameters as B_{rem} and μ_{rrec} are set by the PM properties. The SMPM vs. IPM comparison was decided to be investigated on a 12-slot/10-pole combination.

For fixed external dimensions, this automatically sets the slot pitch T_s and the pole pitch T_p to specific values. Typical values of the magnet span T_m and the stator bore radius R_{in} provide reasonable initial values. Setting typical values of B_g, then (2.6) and (2.8) can be used to find the remaining geometry values, including the tooth thickness T_t and the stator yoke thickness L_b. Electrical properties of the machines are mainly dependant on the thermal characteristics resulting from (2.10) – (2.12). The values of A_{rms} and J_{rms} obtained from these, define the values of the rated current of the machines. The fill factor K_{fill} is initially set to a typical value of 0.5, and a maximum temperature for the windings T_{max} is assumed to be 180 °C.

2.2.1.5 Modelling with FE

The initial values achieved from the analytical analysis are used to build FE models for the TLPM motor with SMPMs and also with IPMs.

A. Design and results

The FE models are geometrically optimised in an effort to achieve the best performances possible. A 'fair' comparison between the two configurations is achieved by considering performances relative to P_{cu_tot} and maintaining the overall weight of the mover (PM material, flux focusing pieces) the same for both topologies. The same stator geometry and winding configuration is used for both models as the only difference resides in the mover. Figure 2.4 shows the final FE models of the two configurations, both of which were tested with "transient with motion component" simulations. The values of the main QI parameters mentioned in Section 2.2 for the two TLPM configurations are compared in Figure 2.5, where θ_{lin} is the linear mechanical position in *mm*.

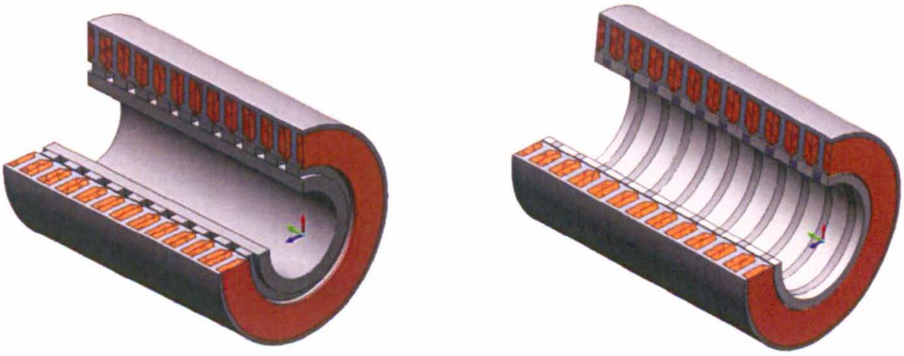

a) SMPM FE model b) IPM FE model

Figure 2.4 FE models of a) SMPM and b) IPM configurations

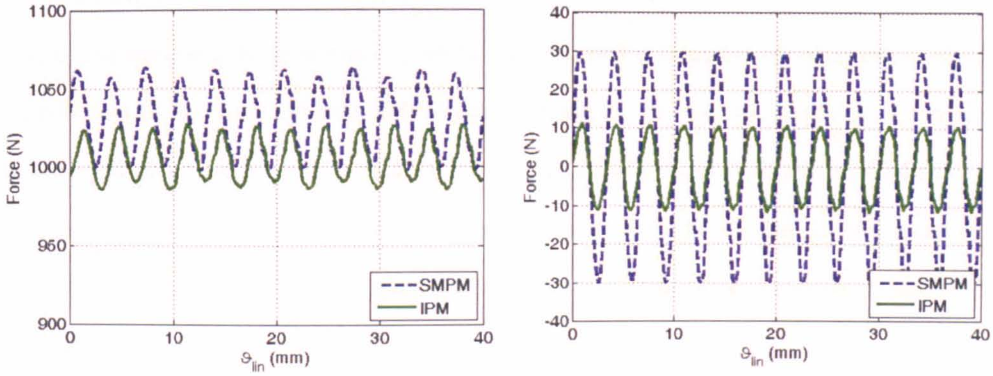

a) Force

b) Cogging force

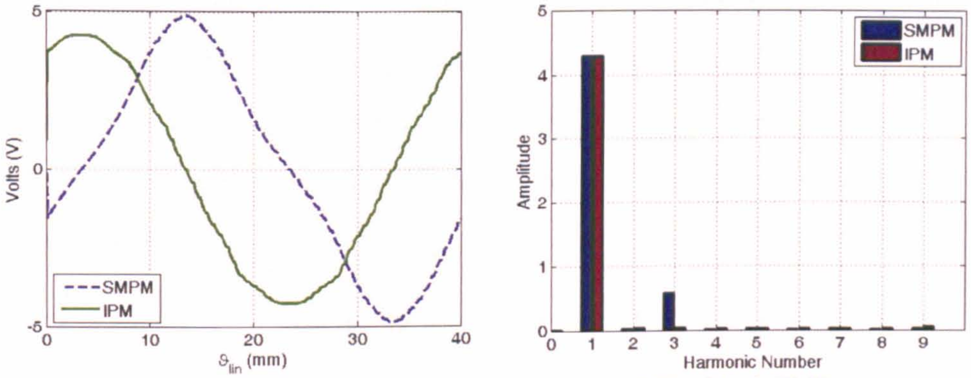

c) Back-EMF

d) FFT of Back-EMF

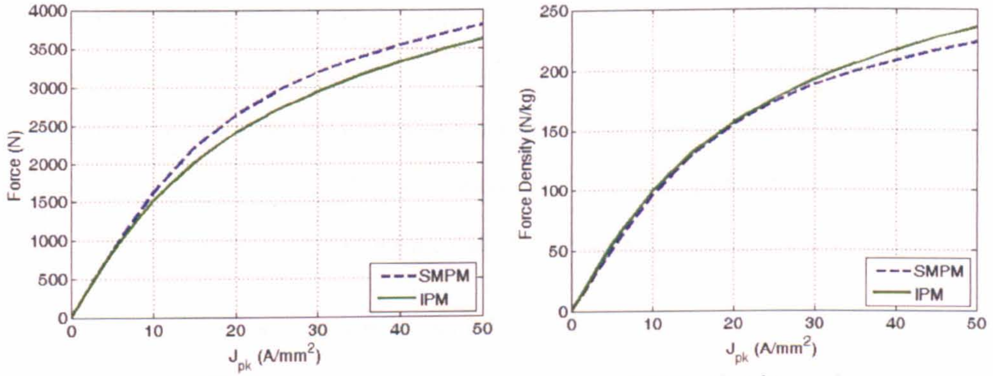

e) Force vs. J_{pk}

f) Force density vs. J_{pk}

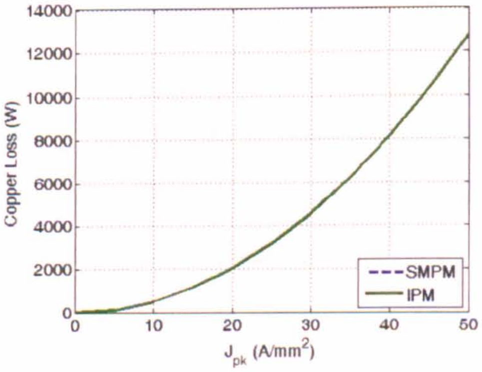

g) Copper loss vs. J_{pk}

Figure 2.5 SMPM vs. IPM performance comparisons

B. Discussion

Figure 2.5a compares the generated F_{lin} whilst Figure 2.5b illustrates the corresponding F_{cog} of the two models. In Figure 2.5a, the SMPM configuration can be observed to achieve a slightly higher mean force, however at the cost of a higher F_{rip}. This is partly due to the higher F_{cog} that is usually present for all SMPM configurations. For the case of this comparison, it can be observed from Figure 2.5b that the SMPM model has a F_{cog} that is three times that of the IPM configuration.

The no-load back-EMFs for a rated V_{lin} of the two models are presented in Figure 2.5c, whilst Figure 2.5d shows their harmonic spectrum obtained via a Fourier analysis. The same fundamental can be observed for both models; however Figure 2.5d clearly shows how the SMPMs result in a higher degree of the 3rd harmonic which slightly distorts the back-EMF of this configuration.

Figure 2.5e and Figure 2.5f compare the response of the models (in terms of F_{lin} and force density) to the current density J_{pk}, where it is important to note that J_{pk} represents the ratio of the peak value of the phase current I_{pk} to the cross-sectional area of one copper wire turn A_{1cop}. The superiority in terms of generated F_{lin} of the SMPM configuration can be observed, however when one considers the total mass of the active components of the machines, then it is clear from Figure 2.5f that the IPM configuration gives the better performance, especially for higher loads. Finally, Figure 2.5g confirms that all the tests were done for the same P_{cu_tot}.

From the above results, one can note that while the SMPM topology shows a slight superiority in terms of F_{lin}, the IPM configuration offers advantages in terms of force density, better quality back-EMF and a smaller F_{rip}. An important feature resulting from the above comparative study can be glimpsed by considering Figure 2.5f. The force-to-mass ratio of the IPM configuration is seen to improve relative to the SMPM configuration, as the electric loading is increased. This fact represents an important potential when the possibility of implementing a fluid-based cooling system is considered, as this would automatically allow the use of higher current loadings. Apart from the above findings, there exist other general benefits in using the IPM configuration. As reported in literature and largely practiced in industry, the implementation of the IPM configuration for motors is in general less costly to produce and considerably facilitates assembly procedures. The investigation of this section thus indicates the TLPM motor with an IPM configuration to be the most promising topology for such an application as presented in Section 1.2.1.

2.2.2 Slot-pole combinations

Having decided on an IPM configuration, the next step of the design process involves the choice of the most beneficial slot-pole combination for the application. The slot-pole combination has a considerable effect on the design and performance of any machine, so the specific application and its requirements must always be kept 'in mind' when investigating for this feature. For example, if the force-to-mass ratio is a major constraint (as is the case for most aerospace applications) then it is beneficial to consider that an increase in the number of poles may result in an increase in force density [90]. This is due to the fact that an increase in P reduces the stator back iron thickness, thus increasing the air-gap area. The speed, at which the machine will be required to operate at, is also important when choosing N_{slots} and P, as it is generally known that high speed applications usually require a low P and vice-versa.

A. Design and results

The analytical models presented in Section 2.2.1 and explained in Appendix A.3, are used to study a number of feasible combinations with IPMs that all comply with the basic geometry of Figure 2.3. The same procedure as explained in Section 2.2.1.4 is used to build adequate initial analytical models. From this analytical analysis, the most promising arrangements for the required application are found to be for combinations that feature a number of slots in the region of between 9 and 12 slots and the number of poles ranging from 8 to 10. Considering this, then FE models are built to accurately test and compare the performances for 12-slot/10-pole, 9-slot/10-pole and 9-slot/8-pole combinations.

The tests for the three slot-pole combinations are again done assuming a naturally cooled set-up, with no extra forced cooling. A 'fair' comparison is achieved by considering the same value of P_{cu_tot} for all three models at steady state. The same A_{rms} is maintained by adjusting the number of turns when different combinations are tested, whilst care is taken to keep the overall mass of PM material constant. The values of the main QI parameters mentioned in Section 2.2 for the three configurations are presented and compared in Figure 2.6.

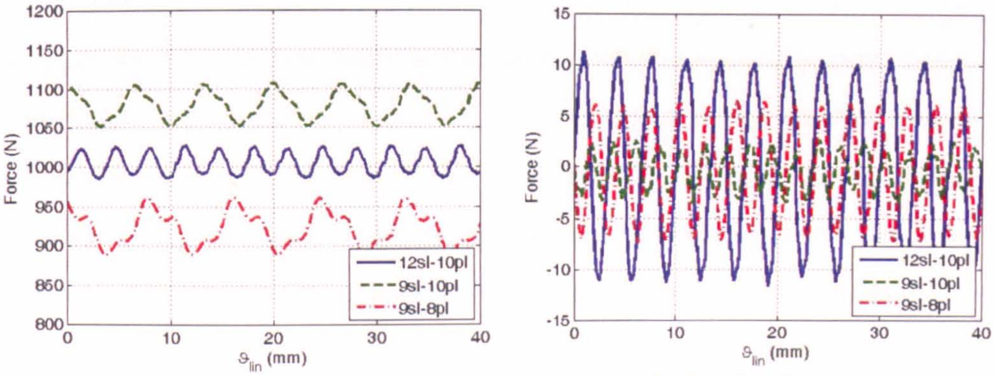

a) Force b) Cogging force

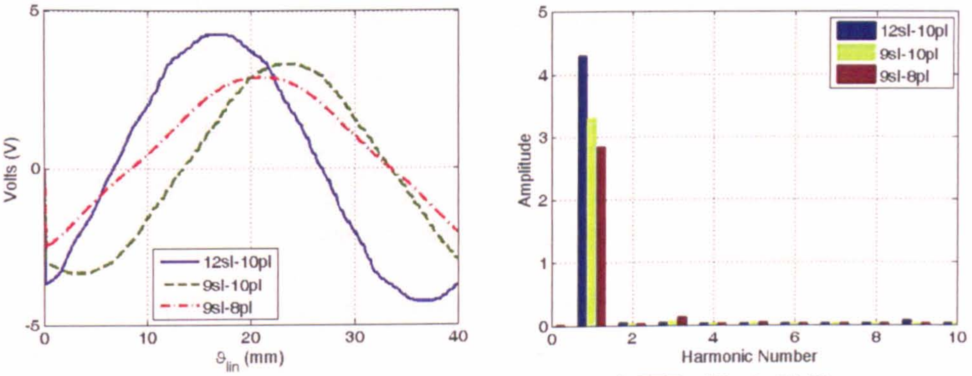

c) Back-EMF d) FFT of Back-EMF

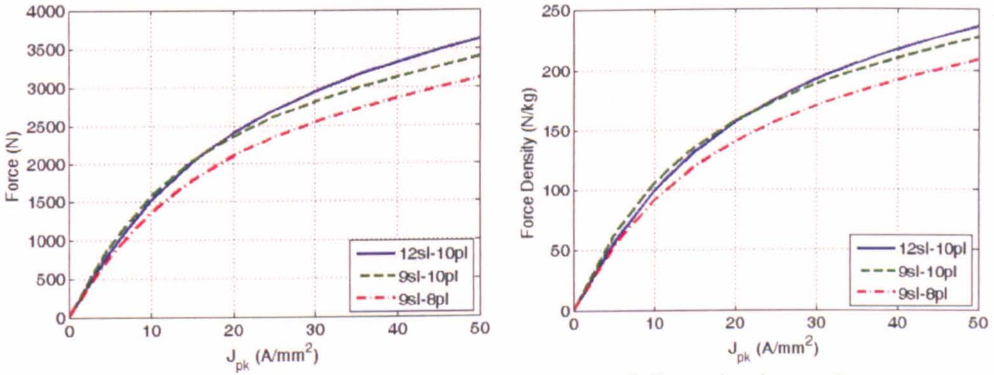

e) Force vs. J_{pk} f) Force density vs. J_{pk}

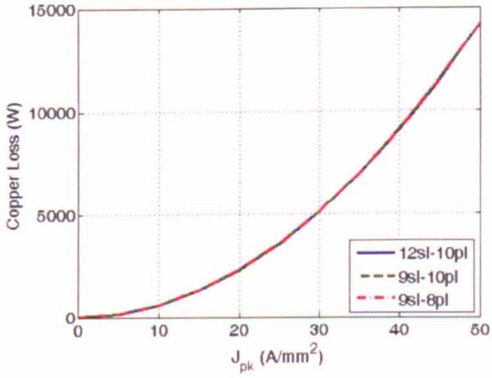

g) Copper loss vs. J_{pk}

Figure 2.6 IPM slot-pole combination performance comparisons

B. Discussion

The generated F_{lin} of the three models is achieved for a safe operating J_{pk} of approximately $6A/mm^2$, which respects the thermal limit T_{max} of 180°C. At this loading, the three slot-pole combinations achieve a F_{lin} as shown in Figure 2.6a. Table 2.1 lists the δ_g, the force density values and the F_{rip} of the three models for this condition, from which it is clear that at this particular loading the best force density performance is achieved by the 9-slot/10-pole combination.

	δ_g **(kN/m²)**	**Force density (N/kg)**	F_{rip} **(%)**
12-slot/10-pole	16.94	65.39	4.09
9-slot/10-pole	18.18	69.06	5.17
9-slot/8-pole	15.57	61.69	7.99

Table 2.1 Slot-pole combinations comparison at $J_{pk}=6A/mm^2$

Figure 2.6b shows the cogging forces of the three models with the 12-slot/10-pole model exhibiting the highest cogging force. In fact the 9-slot/10-pole model demonstrates a F_{cog} that is only 25% of that of the 12-slot/10-pole model. However when considering the actual F_{rip} values presented in Table 2.1, it is the 12-slot/10-pole model which achieves the least overall force ripple.

The back-EMFs and their harmonic spectra are shown in Figure 2.6c and Figure 2.6d. There is little or no difference between the quality of the three induced voltages. The slight difference in amplitudes is due to the modified number of turns, so as to keep A_{rms} constant which results in a constant P_{cu_tot} as shown in Figure 2.6g.

The superiority of the 9-slot/10-pole combination in terms of generated F_{lin} and force density, shown in Figure 2.6a and Table 2.1 is however only true for low values of J_{pk}, i.e. with natural cooling and at rated current. In fact, it can be observed from Figure 2.6e and Figure 2.6f that as J_{pk} is increased, the 9-slot/10-pole combination is slightly inferior to the 12-slot counterpart. As mentioned in the previous section, this factor can be exploited to maximum advantage when fluid cooling is considered. Considering all the above and the possibility of fluid cooling, then it was decided to focus the rest of the investigation and design on a 12-slot/10-pole model.

2.2.3 The fractional slot topology

The investigation of the previous sections has shown that for the required application, a 12-slot/10-pole TLPM motor with IPMs represents the most promising topology. This slot-pole combination is in general known as a fractional slot per pole per phase configuration. Fractional slot combinations have a number of advantages amongst which are reduction of manufacturing costs [91], reduction of the end-winding lengths [50, 53, 92] and a low torque/force ripple [51, 93]. Another main advantage of fractional slot configurations is their inherent fault tolerance capability [90, 94, 95]. For a tubular machine the end-winding length is not an issue, however in order to have a good utilisation of the magnetic paths, a high P is desirable, whilst a reasonable slot size ensures a high K_{fill}.

A wealth of literature exists that investigates winding configurations and winding layouts for fractional slot machines [90, 94-99]. Table 2.2, the source of which is [57], tabulates the winding layout for a number of combinations of slots and poles, while Table 2.3, the source of which is also [57] lists K_w for a number of double layer, fractional slot combinations. Exclusively for these two tables, q is the number of slots per pole per phase, Q_s is the number of slots and p is the number of poles. Using these tables, it is possible to achieve the winding layout for the double layer, 12-slot/10-pole TLPM motor, whilst K_w is found to be 0.933.

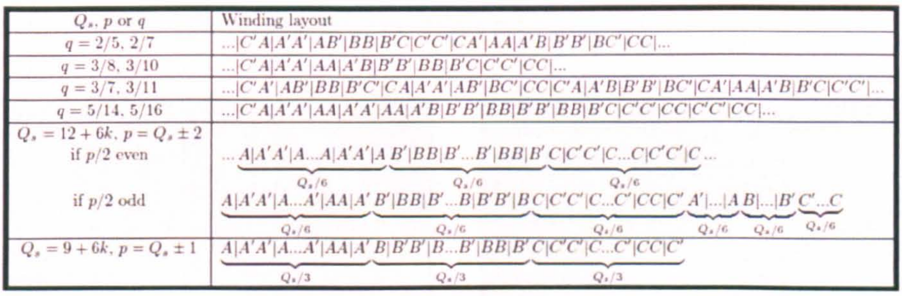

Q_s, p or q	Winding layout
$q = 2/5, 2/7$	$\ldots\vert C'A\vert A'A'\vert AB'\vert BB\vert B'C\vert C'C'\vert CA'\vert AA\vert A'B\vert B'B'\vert BC'\vert CC\vert\ldots$
$q = 3/8, 3/10$	$\ldots\vert C'A\vert A'A'\vert AA\vert A'B\vert B'B'\vert BB\vert B'C\vert C'C'\vert CC\vert\ldots$
$q = 3/7, 3/11$	$\ldots\vert C'A'\vert AB'\vert BB\vert B'C'\vert CA\vert A'A'\vert AB'\vert BC'\vert CC\vert C'A\vert A'B\vert B'B'\vert BC'\vert CA'\vert AA\vert A'B\vert B'C\vert C'C'\vert\ldots$
$q = 5/14, 5/16$	$\ldots\vert C'A\vert A'A'\vert AA\vert A'A'\vert AA\vert A'B\vert B'B'\vert BB\vert B'B'\vert BB\vert B'C\vert C'C'\vert CC\vert C'C'\vert CC\vert\ldots$
$Q_s = 12 + 6k$, $p = Q_s \pm 2$ if $p/2$ even	$\ldots\ \underbrace{A\vert A'A'\vert A\ldots A\vert A'A'\vert A}_{Q_s/6}\ \underbrace{B'\vert BB\vert B'\ldots B'\vert BB\vert B'}_{Q_s/6}\ \underbrace{C\vert C'C'\vert C\ldots C\vert C'C'\vert C}_{Q_s/6}\ \ldots$
if $p/2$ odd	$\underbrace{A\vert A'A'\vert A\ldots A'\vert AA\vert A'}_{Q_s/6}\ \underbrace{B'\vert BB\vert B'\ldots B\vert B'B'\vert B}_{Q_s/6}\ \underbrace{C\vert C'C'\vert C\ldots C'\vert CC\vert C'}_{Q_s/6}\ \underbrace{A'\vert\ldots\vert A}_{Q_s/6}\ \underbrace{B\vert\ldots\vert B'}_{Q_s/6}\ \underbrace{C'\ldots C}_{Q_s/6}$
$Q_s = 9 + 6k$, $p = Q_s \pm 1$	$\underbrace{A\vert A'A'\vert A\ldots A'\vert AA\vert A'}_{Q_s/3}\ \underbrace{B\vert B'B'\vert B\ldots B'\vert BB\vert B'}_{Q_s/3}\ \underbrace{C\vert C'C'\vert C\ldots C'\vert CC\vert C'}_{Q_s/3}$

Table 2.2 Winding layouts for some fractional slot combinations

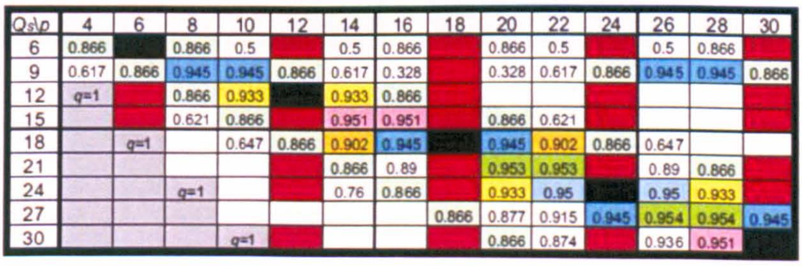

Qs\p	4	6	8	10	12	14	16	18	20	22	24	26	28	30
6	0.866	⬛	0.866	0.5	🟥	0.5	0.866	🟥	0.866	0.5	🟥	0.5	0.866	🟥
9	0.617	0.866	0.945	0.945	0.866	0.617	0.328	🟥	0.328	0.617	0.866	0.945	0.945	0.866
12	q=1	🟥	0.866	0.933	⬛	0.933	0.866	🟥			🟥			🟥
15		🟥	0.621	0.866	🟥	0.951	0.951	🟥	0.866	0.621	🟥			🟥
18		q=1		0.647	0.866	0.902	0.945	⬛	0.945	0.902	0.866	0.647		
21					🟥	0.866	0.89	🟥	0.953	0.953	🟥	0.89	0.866	🟥
24			q=1		🟥	0.76	0.866	🟥	0.933	0.95	⬛	0.95	0.933	🟥
27								0.866	0.877	0.915	0.945	0.954	0.954	0.945
30				q=1	🟥			🟥	0.866	0.874	🟥	0.936	0.951	⬛

Table 2.3 Fundamental winding factors

2.3 Thermal management with fluid cooling

As stated in assumption 4 of Section 2.2.1.2, all the above studies are done assuming that only natural cooling is present. However, as seen from Figure 2.5 and Figure 2.6, considerable improvements in performance can be achieved if higher current loadings and current densities are used. To be able to increment these parameters while still respecting the thermal limit, a forced cooling arrangement is incorporated into the design.

Natural cooling of electrical machines [100, 101] has traditionally been enhanced by the use of fins and ducts [102, 103] on the outer housing of the machines. This is usually done in order to improve the convection and radiation heat transfer. Forced air cooling methods such as [104, 105] can result in better cooling but at the cost of extra components and complexity. A high performance method of cooling involves the use of liquids [17, 106, 107], especially for environments where a cooling circuit is readily available.

A common and convenient way to apply fluid cooling is through the use of a stator jacket, thus avoiding the implications represented by rotating seals and potential viscous drag. Stator jacket arrangements, of which some general examples are shown in Figure 2.7, are known to function reasonably well for machines with relatively small rotor losses such as with PM brushless motors. Such arrangements are usually designed to maintain a 'safe', motor winding temperature for when the cooling fluid temperature is typically in the range of 20 to 50*°C*.

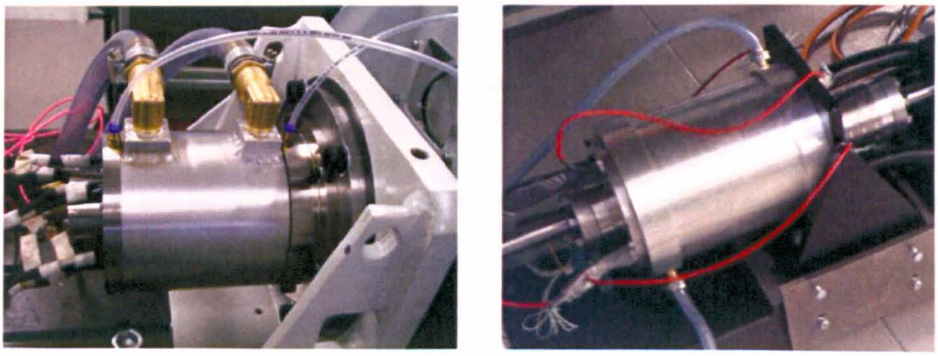

Figure 2.7 Stator water-jacket examples

2.3.1 The stator water-jacket

To correctly model, design and implement a stator water-jacket, the correct calculation of the thermal conduction and convection parameters of the system, especially the convection heat transfer coefficient h_{cv} is critical [107]. The cooling fluid in the water-jacket ducts is able to carry away heat from the stator housing mainly because of its flow/velocity on which h_{cv} is completely dependent.

Figure 2.8 shows part of the cross-sectional view along the axial length of a tubular motor fitted with a stator water-jacket, where P_h is the perimeter of the ducts in contact with water and A_h is the hydraulic cross-sectional area of the coolant flow.

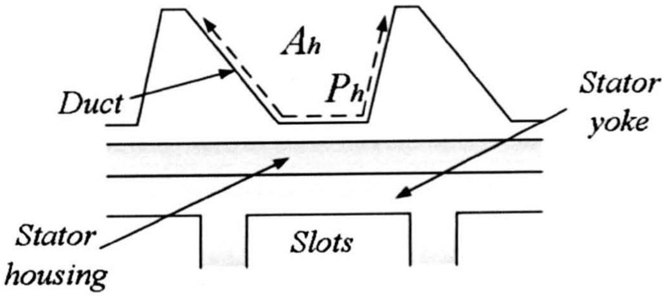

Figure 2.8 Tubular motor water-jacket coolant ducts

Considering Figure 2.8, then h_{cv} can be described by (2.14), whose derivation is given in Appendix B.2.1 and where k_{wat} is the thermal conductivity of water, N_u is the Nusselt number of the system and d_h is the hydraulic diameter of the water-jacket.

$$h_{cv} = \frac{k_{wat} N_u}{d_h} \tag{2.14}$$

As seen in the next sections, the importance of the value of h_{cv} resides in the fact that it defines the value of the thermal resistance that represents the ability of the whole system to dispel heat from the stator windings. The low speed nature of the application results in the windings copper losses to be the main source of heat and thus it is very important to note that it is this particular loss, which practically sets the thermal limit of the whole machine.

2.3.2 Thermal modelling

Equations (2.11) and (2.12) are only valid if the machine housing temperature is allowed to increase to values, which are much higher than T_{amb}, which is the case when natural cooling is employed. For systems making use of fluid cooling, this is not possible as the housing temperature will be at a temperature reference T_{wat} set by the cooling fluid.

A lumped parameter model of one slot pitch section of the TLPM motor must then be used to achieve an estimate of the temperature distribution in the machine. Using the traditional, lumped parameter, thermal networks approach [108, 109], the slot area of the TLPM motor is modelled as a number of thermal resistances from the centre of the slot to the cooling agent. With the exception of assumptions 2 and 4, this model is also constrained with the assumptions of Section 2.2.1.2, to which the following are annexed.

5) Predominant thermal dissipation in the machine is in the radial direction.
6) Maximum hot-spots are approximately in the centre of the coils, at height R_{hc}.

Considering the above, then the slot pitch of the double layer, TLPM motor can be modelled as shown in Figure 2.9, where $R_1 - R_{12}$ are the thermal resistances and R_{wat} and R_{hc} are defining radii for the thermal calculations. The slot is longitudinally divided into three equal parts and for clarity only the resistive elements are shown. Capacitors representing thermal masses can easily be added at each node, when transient behaviour needs to be evaluated. The derivations of the thermal resistances and the heat sources are given in Appendix B.2.2.

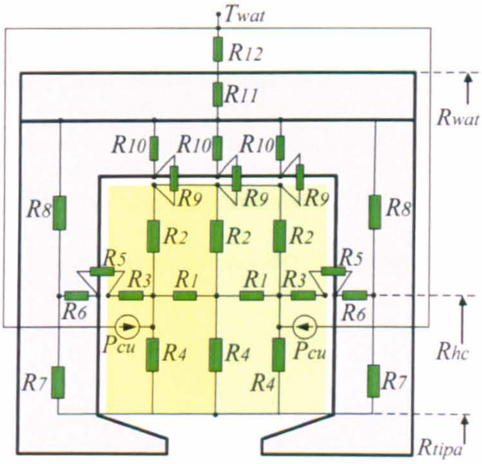

Figure 2.9 Lumped parameter model for one slot pitch

Knowing the maximum permissible ΔT, which is dependent on the imposed T_{max} of the windings, then using the thermal model of Figure 2.9, the maximum allowable values of P_{cu} for each coil can be found. The maximum value of the copper current density J_{rms} that will respect the thermal limits of the machine is then obtained from (2.15).

$$P_{cu} = \pi \times T_{sl} R_{hc} K_{fill} \times \rho_{cu} \left(R_t - R_{tipa} \right) J_{rms}^2 \qquad (2.15)$$

In previous sections, one of the main equalising factors to obtain 'fair' comparisons was assumed to be the thermal limit imposed by the windings T_{max}. Using the thermal model of Figure 2.9 in conjunction with (2.15) permits that the analysis and optimisation procedures presented in the next sections will keep to this adopted, design trend, even when fluid cooling is considered.

2.4 Optimisation of the 12-slot/10-pole TLPM motor

Having established a slot-pole combination, a winding configuration and a cooling arrangement, the next step in the design is the optimisation of the machine with respect to the principal design geometrical dimensions that have considerable effects on the machine in terms of the quality indicating QI parameters mentioned in Section 2.2. Considering the application, the main objective of this design procedure is to focus on the force density capability of the machine, within the given space constraints and performance requirements. The computationally efficient, analytical models are used in conjunction with the more accurate, FE models in order to minimise computational resources without jeopardising model accuracy.

2.4.1 Geometrical optimisation

Considering a TLPM motor with IPMs such as shown in Figure 2.3, where the external dimensions L_e and R_e are fixed by the application envelope, then the main dimensions that are most influential on the force-to-mass performance of the machine [17, 78] are the PM thickness L_m, the air-gap length L_g and the geometrical ratios R_{ts}, R_{spl} and R_{pit}, as given in (2.16).

$$R_{ts} = \frac{T_t}{T_s} \qquad R_{spl} = \frac{R_{in}}{R_e} \qquad R_{pit} = \frac{T_m}{T_p} \qquad (2.16)$$

A. Design and results

For the purpose of this study, L_g is fixed to be constant at 1mm, which is a typical value for PM machines of such a size as that dictated by the application space limits of L_e and R_e. Although a smaller air-gap would in general improve performance, the minimum size is always limited by mechanical and manufacturing tolerances and thus a 'safe' 1mm value is assumed to facilitate manufacturing and assembly procedures.

Performance of the machine is also highly dependent on the amount of PM material used, thus in general any increase in L_m automatically improves performance. This however increases the cost of the PMs required and more importantly the net weight of the machine due to the high mass density value of rare-earth PM material. Special attention to the effects on force density capability must therefore be given to the dimensioning of L_m. As an initial, starting dimension a value of L_m that sets B_g to approximately 0.8T is chosen.

The analytical and FE models built and explained in Section 2.2 are used to study the effects of the above parameters on the performance of the double layer, 12-slot/10-pole TLPM motor. The analytical model is used (via an iterative approach) to quickly determine general, optimum values of these parameters, which are then more accurately "fine-tuned" via the FE model. For these tests, a fluid cooling arrangement is assumed according to the thermal model shown in Figure 2.9, where T_{max} is again set at 180°C. The FE model including the housing and water-jacket is shown in Figure 2.10. The effects of the above design parameters on the force and the force capability performance of the TLPM motor are shown in Figure 2.11.

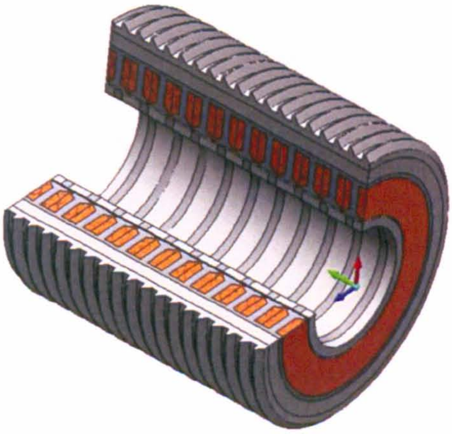

Figure 2.10 FE model with stator housing and water-jacket

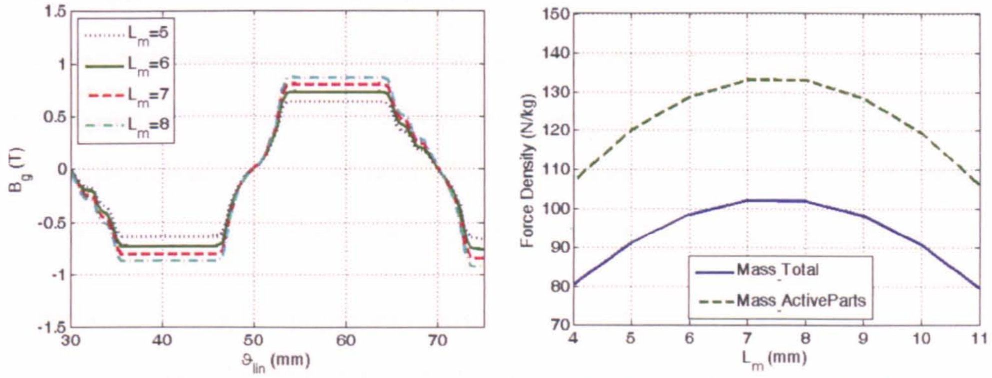

a) Effect of L_m on B_g b) Effect of L_m on force density

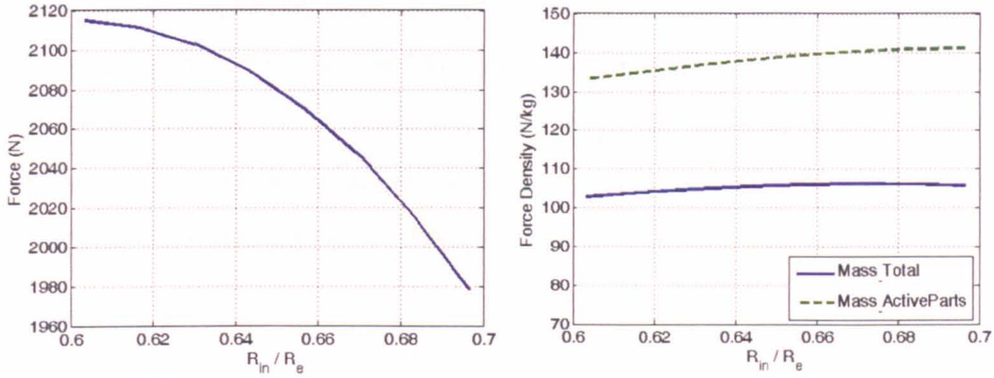

c) Effect of R_{spl} on force d) Effect of R_{spl} on force density

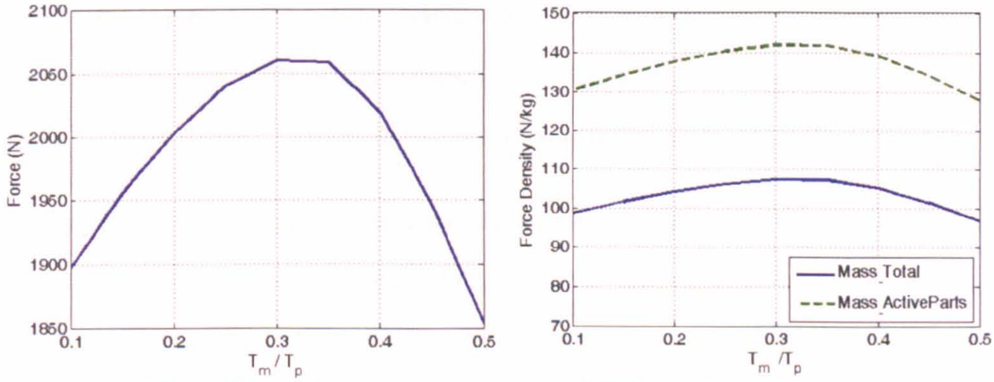

e) Effect of R_{pit} on force f) Effect of R_{pit} on force density

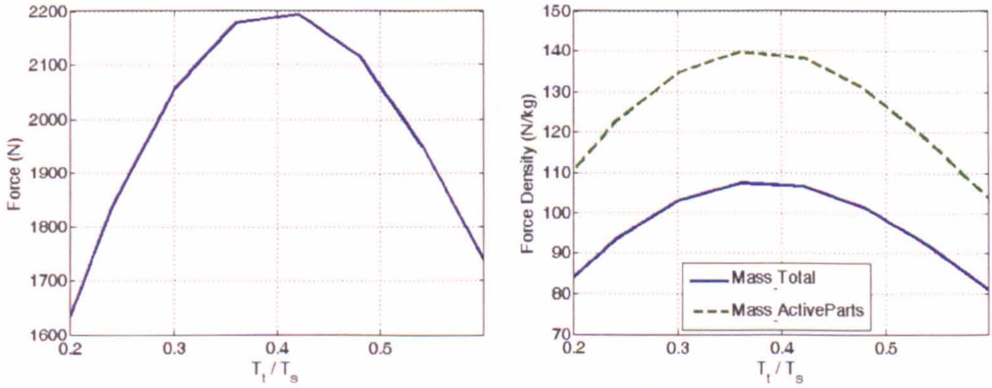

g) Effect of R_{ts} on force h) Effect of R_{ts} on force density

Figure 2.11 TLPM optimisation comparisons

B. Discussion

The optimisation procedures, the results of which are shown in Figure 2.11 are done by considering a safe operating J_{pk} of approximately $16A/mm^2$, which due to the fluid cooling, respects the thermal limit T_{max} of 180°C. This is reconfirmed for each iteration, with special attention when the slot area is modified (as is the case for example during optimisation of T_t).

As previously mentioned, the generated force is proportional to the PM thickness L_m. The air-gap flux densities for an increasing L_m are plotted in Figure 2.11a. Since the particular silicon steel utilised for the stator, saturates at approximately 1.6T, then for this study it was decided to settle on an L_m that sets B_g at around 0.8T. Figure 2.11b shows how the force density varies with respect to L_m when only the active parts are considered and also when the stator housing and water-jacket are included as the total mass. The value of L_m that corresponds to the optimal force density values shown in Figure 2.11b corresponds to the value of L_m that sets B_g at 0.8T.

The effects of R_{spl} on the force and force density performance of the machine are shown in Figure 2.11c and Figure 2.11d. For a set thermal limit as is the case in this investigation (T_{max} = 180°C), R_{spl} represents the balance between the electrical and magnetic loadings of the machine. An optimal value of approximately 0.66 yielding the maximum force density is shown to exist in Figure 2.11d, thus this value is chosen, automatically setting the value of R_{in}.

A value of R_{pit} representing an optimal condition for maximum force capability for a given T_{max} is also shown to exist in Figure 2.11e and Figure 2.11f. This establishes the magnet span T_m and it can be shown that this optimal value does not depend on the pole pitch T_p [78]. Finally, Figure 2.11g and Figure 2.11h show the effect that T_s has on the machine performance via the ratio of the tooth thickness to the slot pitch R_{ts}.

Even though the above variables can be considered as the major geometry defining parameters, the 12-slot/10-pole TLPM model can be further improved by the optimisation of other dimensions such as L_b and the slot opening dimensions. These are also investigated in a manner similar to that explained above where the optimisation procedure is always carried out for the maximum force density possible.

2.4.2 Optimisation to reduce cogging effects

As mentioned in the introduction of Section 2.2, one of the QI parameters being considered in this investigation is the cogging force F_{cog} and its effects on F_{rip} and F_{lin}. Having large values of F_{cog} and F_{rip} usually results in vibrations and acoustic noise, can compromise the positional accuracy and can cause oscillations and instabilities. In addition, holding torque in stationary position will imply a larger converter current rating roughly proportional to the ratio of the maximum torque to average torque values. While the effects of cogging can be minimised by efficient control strategies, it is always desirable to eliminate or reduce these effects by appropriate design of the machine itself.

Cogging forces in PM machines are mainly due to the tendency of the moving PMs to align themselves in specific stable positions where minimum magnetic energy is experienced for an unexcited state [110]. In the case of TLPM machines, cogging forces are made up of two main components, namely

1) The interaction F_{cog_sl} between the PMs and the stator teeth (i.e. due to slotting)
2) The interaction F_{cog_end} between the PMs and the stator finite length (i.e. end effects),

However for machines with a fractional slot configuration (such as explained in Section 2.2.3 for the 12-slot/10-pole TLPM motor) the force due to F_{cog_sl} is of a minimum, inconsequential value [111]. This small component which can however still be observed in Figure 2.5b and Figure 2.6b can be even further minimised by standard techniques used for the reduction of cogging force in PM machines such as [93, 112]. Thus for the purpose of this investigation, it can safely be assumed that the total F_{cog} produced is mainly due to F_{cog_end} and it is this component which needs to be addressed.

However, for all the above studies and results, F_{cog_end} has been neglected due to the need of adhering to assumption 5 of Section 2.2.1.1 (so as to be able to neglect any fringing and cogging end effects related to the interaction between the mover and the finite length of the stator). The main disadvantage of having such a set-up is that no indication of these end effects is reflected on F_{cog} and also on F_{lin}, which as seen below can be quite considerable.

2.4.2.1 The effects of the finite length

For the FE models used above, the mentioned assumption 5 is implemented by utilising a periodic boundary condition at both ends of the stator and mover. As shown in Figure 2.4 and Figure 2.10, this results in the added benefit of having the same L_e for both the mover and the stator, which reduces the simulation time. In order to consider the effects of the machine finite lengths, this boundary condition is removed and the model is modified so as to have a configuration with a longer mover (as would be necessary in practice). Figure 2.12 shows the modified FE model whilst the resulting effects on F_{cog} and F_{lin} are plotted in Figure 2.13.

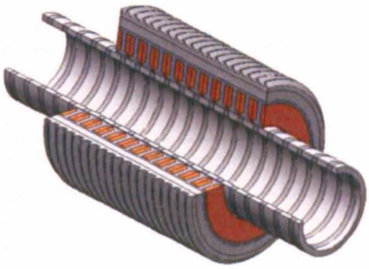

Figure 2.12 FE model with extra mover length and no periodic boundary

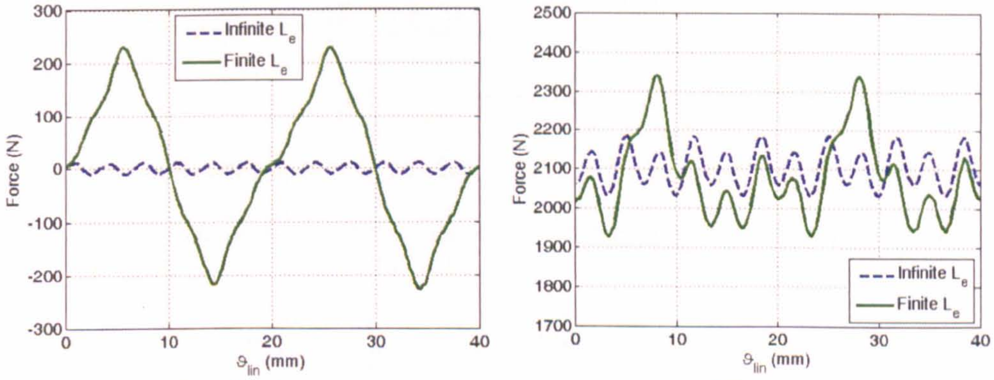

a) Cogging force b) Force

Figure 2.13 TLPM finite length comparisons

With the removal of the periodic boundary, the FE model becomes much more representative of what really happens in practice. The effects due to the stator finite length on F_{cog} can be observed in Figure 2.13a where F_{cog} manifests a considerable amplitude. As shown in Figure 2.13b, this in turn has a considerable effect on the ripple of the generated F_{lin}. Such values of F_{cog} and F_{rip} as shown above are too large to be considered acceptable and therefore specific techniques need to be implemented so as to reduce them as much as possible.

2.4.2.2 Reduction of F_{cog_end}

The machine flux travelling the magnetic path of the stator experiences an abrupt change in the material permeance at the finite ends of the stator. As illustrated in Figure 2.14, a cogging force at each end of the stator is thus created, due to the normal force developed on the end faces of the stator yoke, These forces F_{cog1} and F_{cog2} are unidirectional and opposite in direction to each other [113]. Assuming that L_e is long enough such that no magnetic interference between one end and the other exists, then the resulting cogging force F_{cog_end} is the algebraic sum of F_{cog1} and F_{cog2}. As shown further on, the F_{cog1} and F_{cog2} components at each end can be made to effectively cancel each other out, by optimising the finite L_e of the stator to a specific length [111, 113], thus achieving important reductions in the values of F_{cog_end}, F_{cog} and F_{lin}.

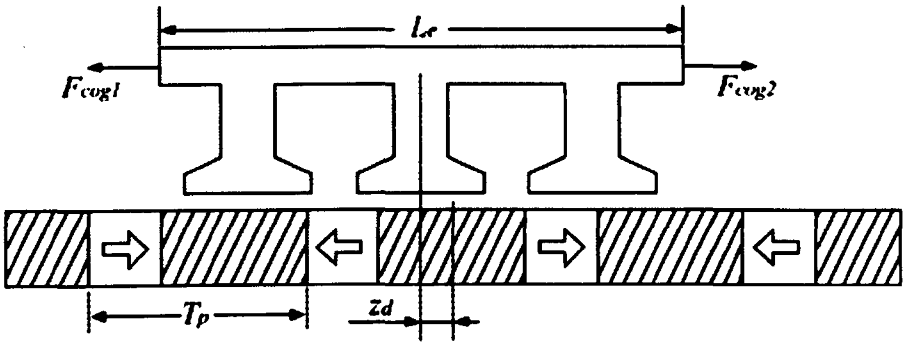

Figure 2.14 Forces due to finite L_e

The cogging force component F_{cog_end}, whose derivation is given in [113] is described by (2.17), where z_d is the distance from the midpoint of L_e to the centre point of the nearest pole.

$$F_{cog\_end} = \sum_{n=1}^{\infty} 2F_{n\_cog\_end} \times \sin\left(\frac{2n\pi}{T_p} z_d\right) \tag{2.17}$$

As shown in [111, 113], F_{cog_end} can be drastically minimised by setting L_e to be an exact multiple of T_p plus an optimal incremental length L_{ext}, as shown in Figure 2.15. The value of L_{ext} can be described by (2.18), where $F_{s\_cog\_end}$ and $F_{c\_cog\_end}$ are the sine and cosine terms of F_{cog_end} respectively. The derivation of (2.18) and the equation for the optimal L_{ext} are also given in [113].

$$L_{ext} = \frac{T_p}{n\pi} \times \tan^{-1}\left(-\frac{F_{s\_cog\_end}}{F_{c\_cog\_end}}\right) \tag{2.18}$$

A. Design

The method is applied to the 12-slot/10-pole TLPM motor as shown in Figure 2.15, where the extra material (applied to each end of the stator yoke) is shown as shaded. The analytical model described by (2.17) and (2.18) is used to find a first approximation of the optimal L_{ext}, which is then more accurately optimised by the FE model. For simplicity, the initial analytical and the ensuing FE analyses are done whilst maintaining the depth of the extra material L_{ext_d} at a constant, maximum value, as described by (2.19).

$$L_{ext\_d\_max} = R_t - R_{in} \tag{2.19}$$

Having achieved an optimal L_{ext}, the FE model is then used to study more in detail the effect that L_{ext_d} has on the performance of the machine. The effects of the above design parameters on the F_{cog}, F_{rip} and F_{lin} performances of the TLPM motor are shown in Figure 2.16.

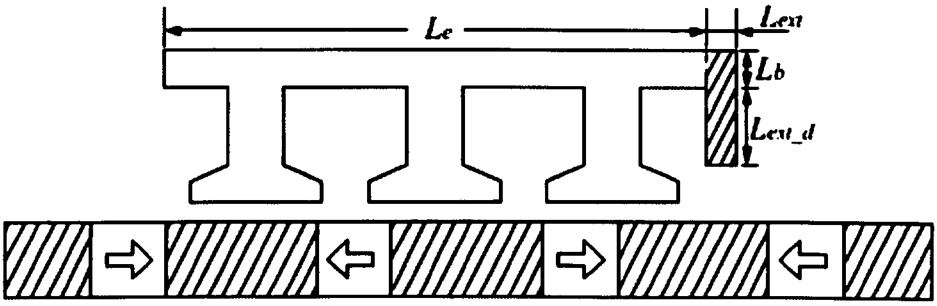

Figure 2.15 Optimising the finite L_e by adding L_{ext}

B. Results and discussion

The effect that the value of L_{ext} has on the cogging force of the TLPM motor is illustrated in Figure 2.16a, where F_{cog} is plotted for a set of L_{ext} values, with L_{ext_d} constant. From this figure, an optimal L_{ext} that results in the minimum F_{cog} can be observed to exist. Plotting the values of F_{rip} as a percentage of the generated F_{lin} as shown in Figure 2.16b, indicates the close relationship that exists between F_{cog} and F_{rip}, as the same optimal value is found for both figures. To investigate the importance of L_{ext_d}, further tests are done. Figure 2.16c and Figure 2.16d compare F_{cog} and F_{rip} respectively for a set of L_{ext_d} values, while L_{ext} is kept constant at its newly found optimal value. As can be observed, the best performances recorded by the machine are found when the value of L_{ext_d} is constrained by (2.19).

The optimal values of L_{ext} and L_{ext_d} are then applied to the final FE model of the TLPM motor. A considerable improvement in the machine performance can be observed in Figure 2.16e and Figure 2.16f, which respectively compare F_{cog} and F_{lin}, before and after the optimisation technique is applied to the stator finite length. The use of the technique shows that a reduction of approximately 82% for F_{cog} and a reduction of approximately 9% for F_{lin} can be achieved.

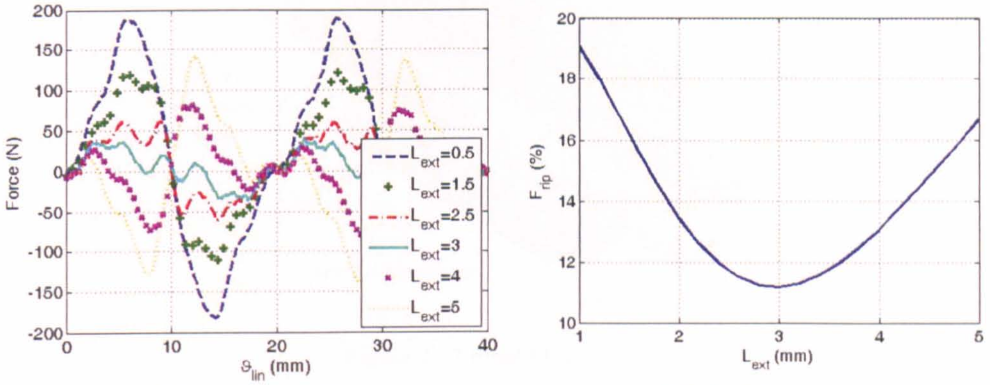

a) Effect of L_{ext} on F_{cog} b) Effect of L_{ext} on F_{rip}

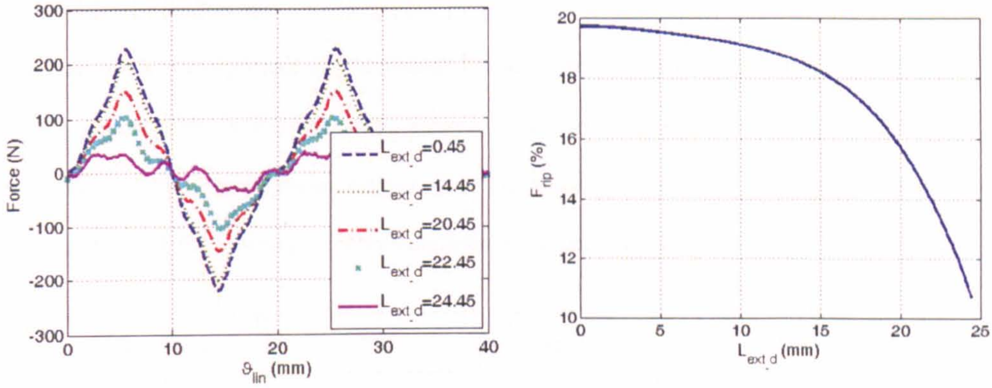

c) Effect of L_{ext_d} on F_{cog} d) Effect of L_{ext_d} on F_{rip}

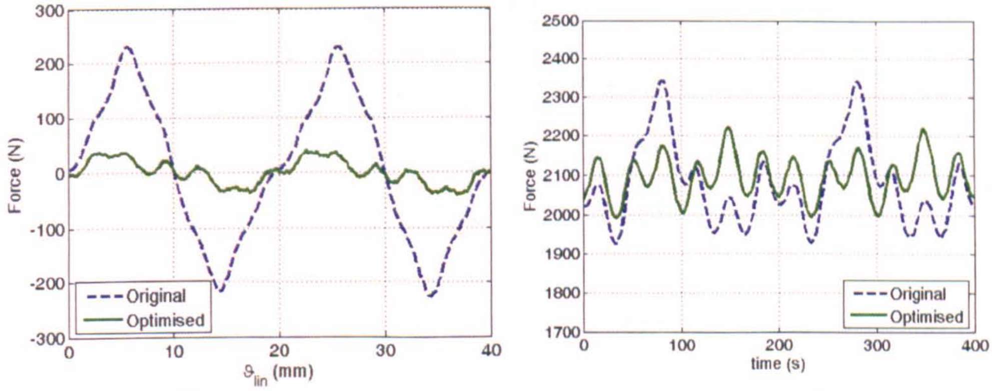

e) Comparing F_{cog} f) Comparing F_{lin}

Figure 2.16 Cogging forces optimisation comparisons

2.5 Conclusion

The information obtained from the investigation outlined above is used to build and test a final FE model of the double layer, fluid cooled, 12-slot/10-pole, TLPM motor with IPMs, as shown in Figure 2.17.

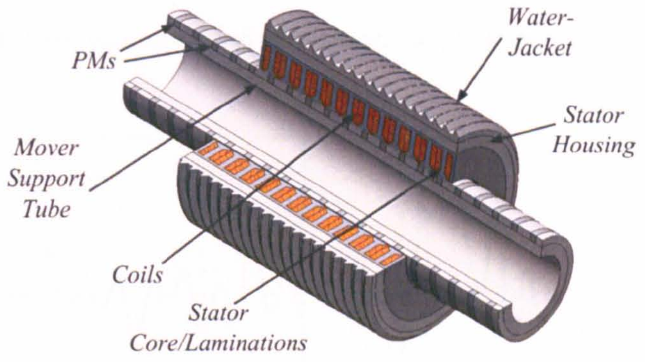

Figure 2.17 Final FE model

A. Final design and results

The final model incorporates an aluminium PM support tube, which while not being required electro-magnetically is mechanically indispensable, so it is included so as to obtain an indication of any ensuing losses related to it. The main specifications used for the model as obtained through the design procedures outlined in the previous sections are listed in Table 2.4.

Slots/Poles	12/10
L_e (mm)	199.8
R_e (mm)	75
L_g (mm)	1
R_{spl}	0.66
R_{pit}	0.3
R_{ts}	0.375
N	23
K_{fill}	0.5
K_w	0.933

Active mass (kg)	18.58
Total mass (kg)	25.79
Active volume (m^3)	0.0035
Total volume (m^3)	0.0057
V_{wat} (m/s)	1
T_{wat} $(°C)$	40
T_{max} $(°C)$	180
I_{rms} (A)	31.07
A_{rms} (kA/m)	85.83
J_{rms} (A/mm^2)	11.31

Table 2.4 TLPM motor final model data

The temperature T_{wat} of the cooling, water-based fluid, which acts on the external surface area of the stator, is set to 40°C, reflecting a typical and readily available water-based cooling system. The rated values of currents and temperatures, along with the resulting electrical parameters are shown in Table 2.4. The performance of the machine relative to the main QI parameters mentioned in Section 2.2 is illustrated in Figure 2.18, where Figure 2.18f plots the force density in terms of the total mass of the machine, including non-active elements.

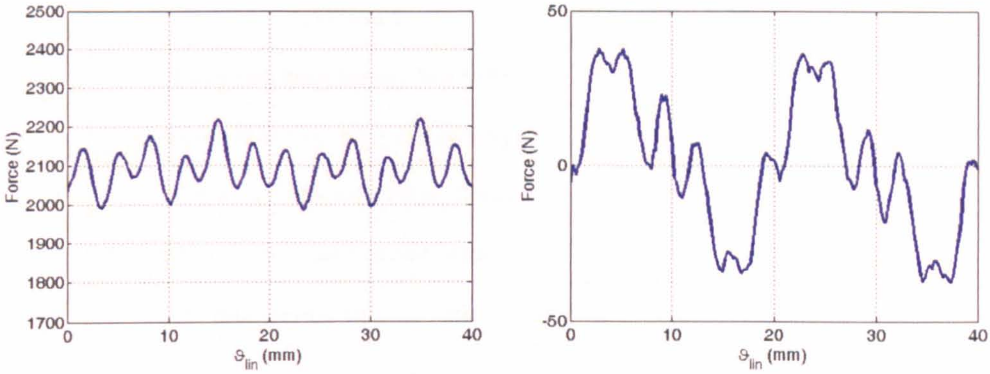

a) Force b) Cogging force

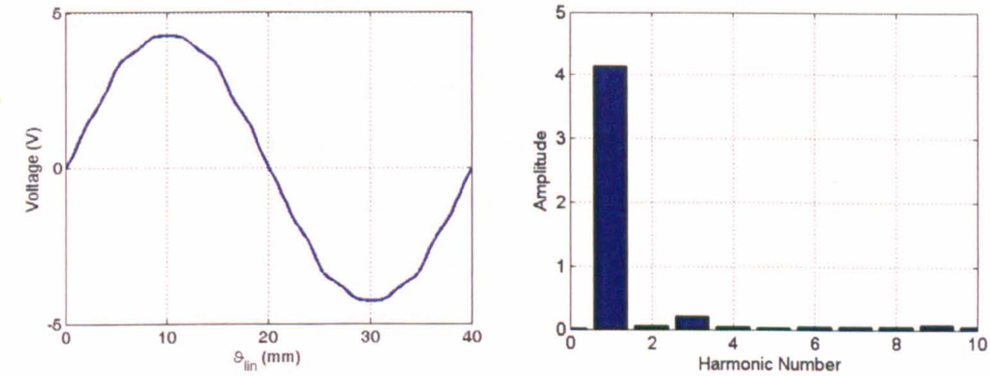

c) Phase back-EMF d) FFT of Back-EMF

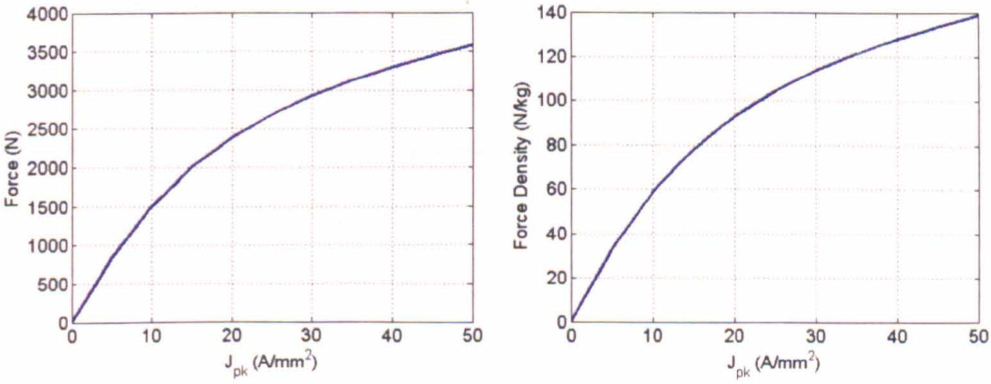

e) Force vs. J_{pk} f) Force density vs. J_{pk}

Figure 2.18 TLPM motor final model performance

B. Performance

The performance capability of the modelled, TLPM motor, at the rated values given in Table 2.4 is presented in tabulated form in Table 2.5.

Mean of F_{lin} (kN)	2.09
Peak of cogging force (N)	37.4
F_{rip} (%)	11.08
δ_g (kN/m^2)	35.3
Total machine copper loss (kW)	1.3
Force to active-mass ratio (N/kg)	112.65
Force to total-mass ratio (N/kg)	81.14
Force to active-stator-volume ratio (kN/m^3)	598
Force to total-stator-volume ratio (kN/m^3)	367

Table 2.5 TLPM motor final model performance chart

C. Conclusion

In this chapter, in detail procedures on the design and modelling of the TLPM motor are presented. The final results illustrated in this final section of the chapter, show the excellent performance achievable by adopting the analytical and FE models presented above. An excellent F_{lin} of approximately $2kN$ is achieved for a J_{rms} of $11.3A/mm^2$ and a A_{rms} of $85.83kA/m$, when the total mass of the whole machine is approximately $25kg$. The force density values of $81.14N/kg$ and $376kN/m^3$ compare excellently to results published in available literature such as [78, 84].

It can be argued that the main weakness of this design is that a F_{rip} of 11% over a force of approximately $2kN$ cannot be safely considered as relatively low. This value of F_{rip} is mostly due to spatial harmonics resulting from the high A_{rms} associated with the rated, continuous operation of the machine. However, considering that the application requires the TLPM motor to operate mostly as a locking device (i.e. a stand-still actuator where $V_{lin} = 0$), then it is safe to assume that such a value of the force ripple will not have a major effect on the operation of the motor.

As a final thought, it is important to note that all the above design and modelling procedures are based on a number of specific, design assumptions, the most important of which are the value of the slot filling factor K_{fill} and the velocity of the cooling fluid V_{wat}. For example, in the design stages, K_{fill} is always assumed to have a value of 0.5, whilst V_{wat} is set to a typical value of surface velocity of water based, cooling fluid. These values have an important impact on the practical performance of the machine, so as shown in later chapters, practical tests and measurements are performed in order to achieve more realistic values of these parameters. As a final step during the comparisons between model and experimental results (shown in Chapter 5), these 'more realistic' values are imported and used in the models, so as to achieve more reliable and accurate modelling results.

Chapter 3
The GT Motor

This chapter deals with the design and optimisation of a PMSM for the aircraft taxiing application mentioned in Section 1.3.1. The nature, size, importance and complexity of this project prohibits it from being an individual project but is the result of a collaboration between the electrical, thermal and mechanical departments of the UoN, involving a number of researchers/engineers from the mentioned fields. However for the scope of this thesis, the main focus is of course on the electro-magnetic design with references to thermal and mechanical issues when necessary.

The procedures utilised for the design of the GT motor, follow the general, design methodologies that are also operated in the design of the TLPM motor of Chapter 2. However, the more varied technical expertise and the much higher budget available for this project resulted in the possibility to employ high specification materials such as cobalt iron (CoFe) laminations, in an effort to achieve the highly challenging requirements set by the application performance specifications. In this chapter such choices are investigated and validated.

In more specific terms, this chapter starts off by introducing to some detail, the specifications required from the application of Section 1.3.1. The space available in the two possible locations on the main landing gear where the machine can be housed and the required performance specifications are presented.

The chapter continues with an initial trade study so as to identify the most suitable topology for the application. A number of machine types and possible topologies are considered. This is achieved by building analytical and FE models (electro-magnetic and thermal) in order to study the performances of the chosen topologies. As an initial objective, the required torque is set to $5kNm$ for the peak load condition.

Having decided on a machine technology and a space where to implement the motor, then an innovative methodology that combines a series of performance enhancing strategies into a well-defined structure is used in order to improve the machine performance with main focus on torque density enhancement. The methodology starts from the design mentioned above and then applies a number of performance improvement techniques in a logical 'journey' towards the optimum design. As seen later, the methodology investigates a sequence of techniques (such as the use of an outer rotor, the use of CoFe laminations, the use of Halbach arrays and the use of open slots) , where for each step it manages to 'build up' on the advantages of the previous technique. In other words, the methodology improves performance by simultaneously addressing both the thermal and electro-magnetic limits of the machine.

Using all the information achieved from these methods, the process towards the final design is initiated. The final torque requirement of $7kNm$ is considered as the main objective of a general comparative study to choose the best slot-pole combination for the space indicated. Further performance improvements are achieved by investigating a number of winding configurations in order to achieve better mean torque and torque ripple at peak load condition. Considering the risk of demagnetisation, synonymous with PM machines, a detailed demagnetisation analysis is then performed which shows the elevated possibility of demagnetisation that characterises the use of quasi-Halbach arrays. An innovative solution for the practical implementation of a full-Halbach array is presented.

The chapter continues by introducing an electro-magnetic clutch system used during the 'take-off' and 'landing' of the aircraft, while a validation of the thermal performance of the machine, operating under a typical, taxiing, duty cycle (including take-off) is performed. The chapter concludes by presenting the optimal design of the GT motor.

3.1 Introduction

As mentioned in Section 1.3.1, the main objective of the GT project is to implement a DD, machine onto the main landing gear of a medium range aircraft in order to achieve smart taxiing operation on the ground. In general the main requirements of such a machine are

1. Highest torque density in terms of torque-to-mass and torque–to-volume ratios, as possible. A low mass is imperative as the machine needs to be carried during flight while a low volume is necessary in order to be able to fit the machine and all its accessories in the space available on the landing gear.
2. Sinusoidal back-EMF, low harmonic distortion and general good quality of voltage and current in order to minimise time harmonic losses. The machine has to operate within the converter VA rating and must be able to safely operate at the maximum voltage produced at higher speeds (landing and take-off).
3. The ability to support an electro-magnetic clutch system that comes into action, once the jet engines are started for take-off and landing. In simplistic terms this system takes the form of a short circuiting of all the phases of the machine, resulting in that the machine requires the ability to electro-magnetically and thermally withstand the considerable braking currents generated at the elevated landing and take-off speeds.
4. Reliability and robustness in order to be able to survive the harsh conditions associated with the landing gear of an aircraft. These include the expected, high levels of shocks and vibrations (the wheel of a typical, medium range aircraft experiences a deflection of approximately 8 to 10cm at the moment of landing), the wide range of ambient temperatures (-10°C to 70°C), the proximity of the aircraft brakes (a considerable generation of heat (up to 500°C) almost adjacent to the machine) etc...

The requirements of 1) and 2) are synonymous with the QI parameters outlined in Section 2.2, so the same set of indicators (applied to torque instead of linear force, where appropriate) are used during all the investigational comparisons of this chapter.

3.1.1 Initial specifications and objectives

In relation to 1) above, the main constraint is the issue of the available space for the machine. The typical aircraft indicated for the GT application has a front landing gear and two rear landing gears. Each rear landing gear is equipped with two wheels. Figure 3.1 shows the cross-sectional, general view of one wheel of one of the rear landing gears. The two different space envelopes (i.e. the back envelope (BkEnv) and the front envelope (FrEnv) spaces) indicated in Figure 3.1 and whose dimensions in *mms* are given in Figure 3.2, were identified by the project partners as possible locations for the integration of the GT motor.

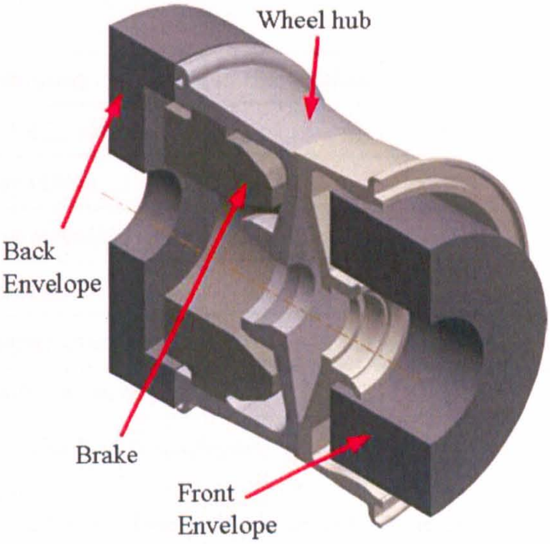

Figure 3.1 Typical main landing gear of a medium range aircraft

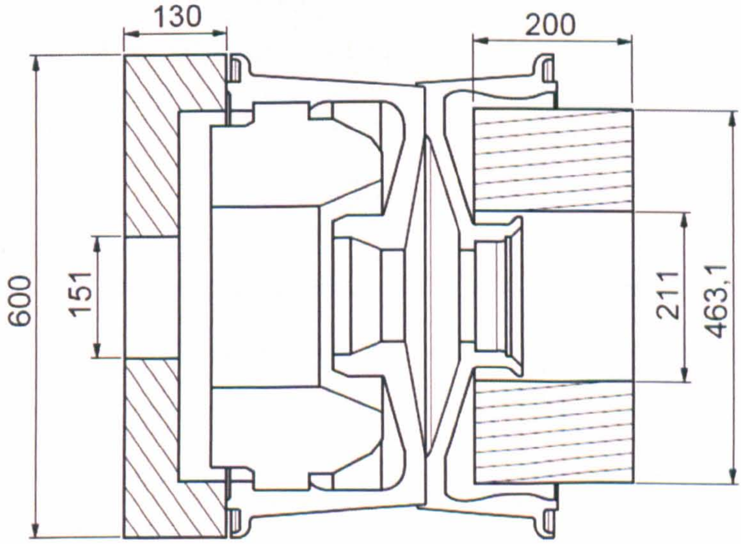

Figure 3.2 Dimensions of possible envelopes

The torque performance required from each rear landing gear system of the aircraft depends on a specific torque duty cycle, which will be discussed later on. One of the main challenges perceived from these duty cycles is the requirement of peak toque at peak load condition. Originally the torque requirement per landing gear was set to $10kNm$ (in fact as shown later the initial trade-off study investigates the possible use of having two $5kNm$ motors per landing gear). During the course of the project, it was however found that realistically the peak torque requirement is $7kNm$ per landing gear. Considering this value as the final, peak load torque requirement, then the torque capability performance required from both envelopes can be tabulated as shown in Table 3.1.

Specification	**BkEnv**	**FrEnv**
Converter VA_{max} ratings	$I_{pk} = 225\text{A}$, $V_{dc} = 525\text{V}$	
Torque (kNm)	7	
Maximum mass (kg)	130	
Volume (m^3)	0.0368	0.0337
Torque density (Nm/kg)	53.84	
Torque density (kNm/m^3)	190.22	207.72

Table 3.1 GT application specification requirements

The initial, trade-off studies are done for both the BkEnv and the FrEnv spaces. As explained in Section 1.4.1.1, any machine can be simplistically sized by using a value of δ_g which depends on the surface area of the air-gap which in turn depends on the radius of the rotor R_{rot}. For a rotational motor, the torque capability T can be described by (3.1), where l_{ax} is the axial length of the rotor.

$$T = 2\pi \times \delta_g \times l_{ax} \times R_{rot}^2 \tag{3.1}$$

Considering (3.1) and the larger external diameter of the BkEnv, then from an electro-magnetic point of view it can be said that the BkEnv has a much better potential for torque. This is reflected in the lower torque density requirement shown in Table 3.1. However, it must also be mentioned that a strong preference towards the FrEnv space was shown by the system developers because this would result in extensive simplifications concerning inter-connection issues with the rest of the system.

3.2 Initial studies of machine topologies

As part of the initial trade off study, different machine types are investigated. The initial investigations [30, 114] include a technology comparison between PM based topologies and a more economic and robust solution that considers a field wound, flux switching (FWFS) machine [56].

From this study, it is perceived how FWFS machines can offer high flexibility in terms of limiting the converter, peak *kVA* requirements and are ideal to adopt in view of mitigating faults and the high voltages generated during take-off and landing. This is mainly due to the complete control on the excitation field, synonymous with technologies that have a field winding. On the other hand, the study shows that the torque density performance in terms of torque-to-mass ratios of FWFS machines is incomparable to what can be achieved by PM machines. Considering this and the fact that the space constraints shown in Figure 3.2 were proclaimed by the project partners as non-negotiable and also that any extra converter *kVA* does not necessarily mean extra weight (in aircraft, converters are usually placed in air-conditioned, pressurised zones), it was decided to choose a PM topology for the GT application. To this aim, a number of PM machine topologies are investigated for both envelopes in order to determine the better suited technology.

3.2.1 The FrEnv space

The initial, comparative exercises performed within the spatial limits of the FrEnv are aimed at assessing the performance of different PM machine topologies. The investigational studies are presented in detail in [30, 114], where the comparative exercise between topologies is based on radial and axial geometries.

3.2.1.1 Machine topologies

Figure 3.3, which is sourced from [114] shows the general concepts of some machine topologies that yielded the best results from the range of technologies investigated in [114], where Figure 3.3c shows a double air-gap machine with extra PMs whose purpose is to interact with the end-windings in order to achieve more torque. Figure 3.4 shows the lumped parameter thermal network developed in order to estimate the thermal performance of the machines when driven by a set, worst case duty cycle (shown in Figure 3.28). The derivations of the thermal resistances are given in Appendix B.3.1, while the heat sources P_{cu} are dependent on the torque duty cycle given in Figure 3.20a and derived by the calculations shown in Figure 3.28. For the purpose of this study, the thermal model is constrained with the assumptions listed in Section 2.2.1.2 (less assumptions 2 and 4). In addition it is assumed that a uniform temperature distribution, either in the axial or radial direction (depending on the machine topology) exists.

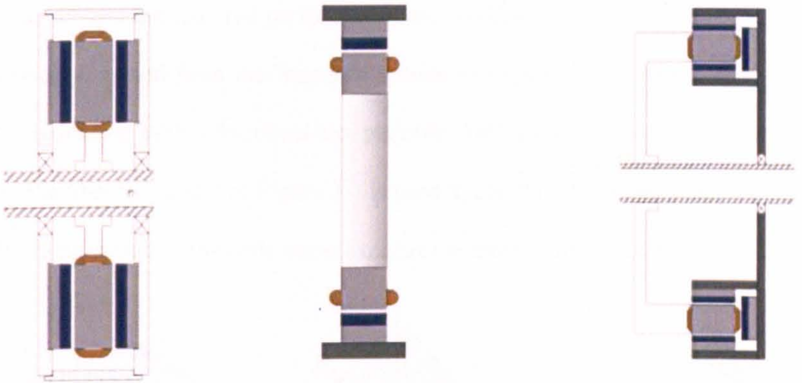

a) Axial machine with double air-gap

b) Radial machine with outer stator

c) Radial machine with double air-gap and extra end-winding PMs

Figure 3.3 Initial topologies considered for FrEnv

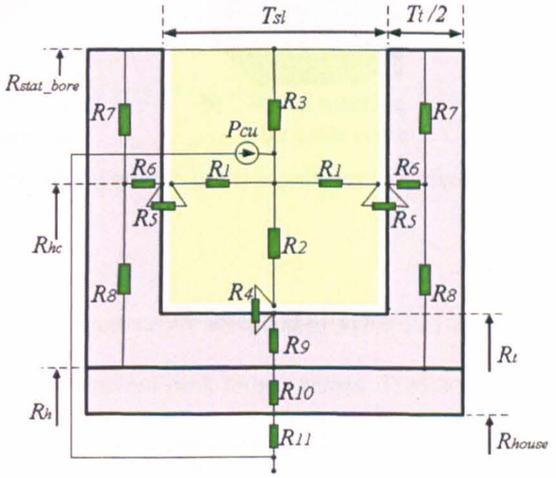

Figure 3.4 Initial thermal network

A. Design

FE based designs for each of the machine topologies mentioned above are built and geometrically optimised and are shown in Figure 3.5. The optimisation procedures, detailed in [114] consider the available space envelope and the required peak torque specification as the main design constraints. Having a fixed, maximum external radius R_e, a number of geometrical dimensions such as the split ratio, tooth width and depth and back iron thickness are varied in order to obtain optimal values in terms of torque capability. As explained above, at this stage of the design, the required peak torque is set to $5kNm$ and thus the models are optimised in order to reach the required torque performance in the smallest volume possible. A perceived challenge from this study is that the main limitation of the machines (for the space limitations shown) is represented by the electro-magnetic limit (due to saturation).

In order to achieve the required performance, the models are designed to reflect the guidelines and knowledge gained from the literature review of Section 1.4.1, thus where possible outer rotor configurations with a fractional slot per pole combination and a SMPM configuration are adopted. The thermal model of Figure 3.4 is used to confirm that even under a worst case duty cycle, the temperature in the coils never exceeds the thermal limit, set by T_{max} to 220 °C.

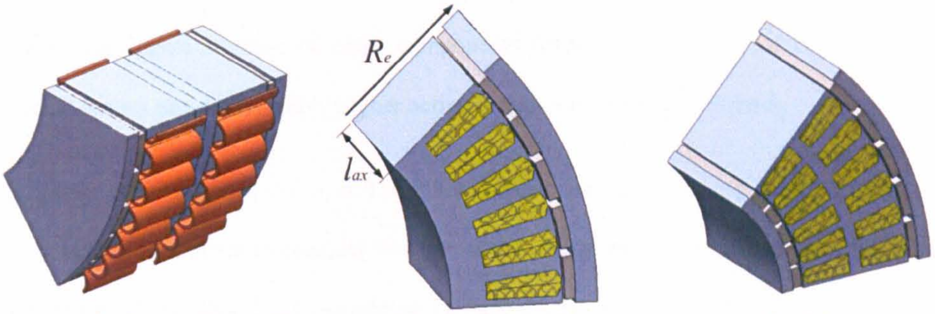

a) Axial machine with double air-gap
b) Radial machine with outer stator
c) Radial machine with double air-gap

Figure 3.5 FE models of the topologies considered for FrEnv

B. Results and discussion

The results of the above comparison are tabulated in Table 3.2, showing the incapability of the axial machine to reach the required peak torque values. Traditionally axial flux machines are considered an attractive solution for applications requiring a high torque to volume ratio [115, 116]. This can also be glimpsed from Table 3.2, which shows that the optimised model of the axial flux machine has a shorter l_{ax} than its single air-gap, radial counterpart. However, Table 3.2 also highlights the deficiency of the axial flux motor in terms of the torque capability, where it is clear that for the maximum possible R_e, the magnetic limit has been reached and no increase in l_{ax} could serve to improve the torque density performance any further, unless a further stage is added.

	Axial machine	Radial machine	Radial machine with double air-gap
R_e (mm)	231.55	231.55	231.55
l_{ax} (mm)	156	200.2	151.5
Active mass (*kg*)	105	120	131
J_{pk} (A/mm^2)	/	36	36
T (*kNm*)	2	4.8	4.8
Torque density (*Nm/kg*)	19.04	40	36.64
K_{fill}	0.5	0.5	0.5
Comment	Completely saturated	Possible further mass and volume reduction	Possible further mass and volume reduction

Table 3.2 Results of machine topology study for FrEnv

On the other hand, the *5kNm* required can be seen to be achieved by the radial topologies. For the required torque, the double, air-gap option results in an axially, more compact model however the higher number of extra components (especially in terms of copper and PM material) results in a considerably higher active mass, even when l_{ax} is shorter.

The torque density values given in Table 3.2 indicate the single air-gap model as the better option, but it is important to consider that the values shown are for the minimum l_{ax} possible to reach *5kNm*. If the same l_{ax} is considered for both the radial air-gap models, than the double air-gap model shows a better torque density performance. However, it is also important to note that Table 3.2 only considers active material. The insight and information gained from the comparative exercise between single and multi air-gap linear motor topologies presented in Section 1.5.1.3 also holds for rotational machines. The mentioned exercise indicates that any advantage in terms of force/torque-to-mass ratio, gained by a multi air-gap topology, reduces considerably when all the extra components and not just the active material are considered. For electrical machines, benefits in terms of torque performance are dependent on the size and aspect ratios of the machines, ratios which can be influenced by the presence of the extra components required for multi air-gap technologies. Other major disadvantages of multi air-gap machines are the elevated conceptual complexity and mechanical and robustness issues. Considering all the above, it was decided to focus the next steps of the study on a single air-gap, outer rotor PMSM with a SMPM configuration.

3.2.1.2 Slot-pole combinations

Having decided on a machine topology, the next step of the design process involves the choice of the most beneficial slot-pole combination for the application. As already discussed in Section 2.2.2 the slot-pole combination has a considerable effect on the design and performance of any machine, and thus a careful study is done to determine a suitable combination. FE models for each combination are built and geometrically optimised with the same criteria as described in Section 3.2.1.1. The specification for the required torque is again set at $5kNm$. The final FE models of the most interesting combinations are shown in Figure 3.6, where it can be noticed that the models are implemented with single layer windings, thus offering advantages in terms of K_{fill} and P_{cu_tot}. The results of these optimised models are tabulated in Table 3.3, the source of which is [114].

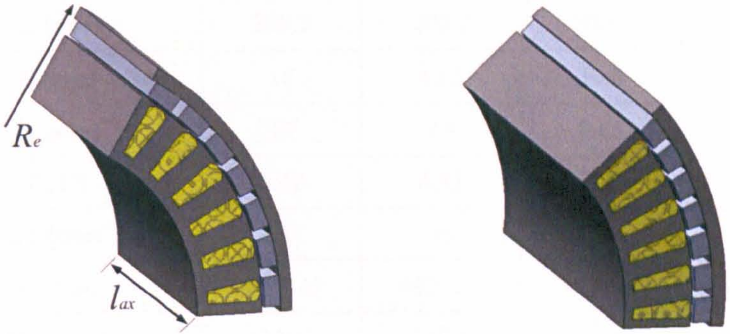

a) 36-slot/42-pole b) 48-slot/56-pole

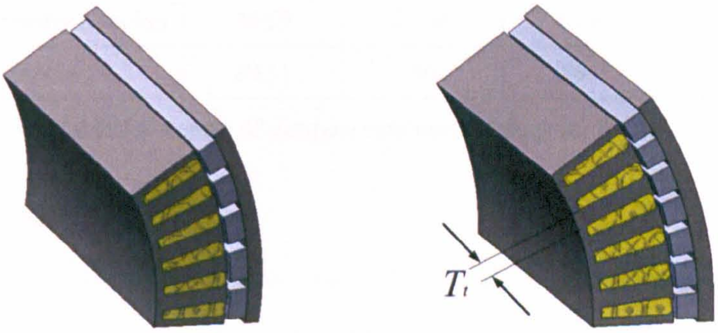

c) 60-slot/50-pole d) 60-slot/70-pole

Figure 3.6 FE models of the slot-pole combinations considered for FrEnv

From Table 3.3, the first thing that can be noticed is that the models shown (chosen as giving the better results from the range of combinations that were investigated) are all based on the 12-slot/10-pole or 12-slot/14-pole combination. As discussed in Section 2.2.3, the fractional slot per pole configuration ensures a high K_w and automatically reduces cogging forces. The MMF harmonic content and any magnetic radial forces are also very much reduced for these configurations. The best torque capability performance for the FrEnv is achieved by the 48-slot/56-pole combination. This results from the fact that this slot-pole combination enables a reduction in the thickness of the back-iron L_b which for a machine with a fixed R_e automatically increases the air-gap radius. This is also true for the combinations with a higher number of slots and poles, but these combinations result in a thinner stator teeth thickness T_t and much smaller PM spans which elevate the slot leakage and the PM interpole leakage and fringing values. Considering all the above, it is thus confirmed that at this stage of the design, the best machine topology for the FrEnv is an outer rotor, SMPM machine with a 48-slot/56-pole combination.

	36-slot / 42-pole	**48-slot / 56-pole**	**60-slot / 50-pole**	**60-slot / 70-pole**
R_e (*mm*)	231.55	231.55	231.55	231.55
l_{ax} (*mm*)	200.2	200.2	200.2	200.2
T_t (*mm*)	18	13.5	10.8	10.8
L_b (*mm*)	10	8.9	8.85	8.44
T_m (°)	6.42	4.82	5.4	3.86
J_{pk} (*A/mm²*)	36	36	36	36
T (*Nm*)	4801.45	4827.31	4543.99	4375.97
Mass (*kg*)	124.43	120.8	110.85	110.85
Torque density (*Nm/kg*)	38.59	39.96	40.99	39.47
δ_g (*kN/m²*)	89.51	90	84.7	81.58

Table 3.3 Results of slot-pole combination study for FrEnv

3.2.2 The BkEnv space

The initial, comparative investigation in order to find the best machine topology and slot-pole combinations within the spatial limits of the BkEnv follows closely the procedures outlined above for the FrEnv in Section 3.2.1.2, such that the information gained from the FrEnv investigation serves as a background for the BkEnv investigation. Due to this, the comparative exercise is just focused on geometrically optimising the 'final' models identified for the FrEnv (i.e. the FE models shown in Figure 3.6) to the new envelope dimensions of the BkEnv. The results from these newly optimised models are tabulated in Table 3.4, where it is clear that it is the 36-slot/42-pole combination that results in the better torque capability.

	36-slot / 42-pole	48-slot / 56-pole	60-slot / 50-pole	60-slot / 70-pole
R_e (*mm*)	300	300	300	300
l_{ax} (*mm*)	100	100	100	100
T_t (*mm*)	21.58	16.18	12.95	12.95
L_b (*mm*)	10	9.8	9.8	9.2
T_m (°)	6.42	4.82	5.4	3.86
J_{pk} (A/mm^2)	30	30	30	30
T (*Nm*)	4326	4240	4080	3940
Mass (*kg*)	75.24	74.4	73.95	73.95
Torque density (*Nm/kg*)	57.49	56.98	55.17	53.27
δ_g (kN/m^2)	89.73	87.95	84.63	81.73

Table 3.4 Results of slot-pole combination study for BkEnv

3.2.3 FrEnv vs. BkEnv

A simple, visual comparison between the results shown in Table 3.3 and Table 3.4 is enough to immediately recognise the superiority of the machines in terms of torque to mass ratios when implemented in the BkEnv. This is mainly due to the fact that a larger R_e permits a larger air-gap radius (i.e. a larger R_{rot}), thus increasing A_{rot} in the air-gap, where the electro-magnetic force is actually produced. As this force is acting on a larger radius R_{rot}, then considering (3.1), this implies a higher torque T.

Thus the conclusions that can be deduced from this initial, trade-off study are namely that a radial machine with an outer stator is the most suited to offer the highest torque and torque density performances, and the larger diameter BkEnv would be better suited to increase the torque capability. However as seen and addressed later on, inter-connecting issues and customer requirements remain to be considered.

3.3 Torque density improvements

In order to maximise the performance of the machines mentioned above, a number of measures as previously presented in Section 1.4.1 can be adopted and implemented. In this section, four main strategies that offer the possibility to improve performance are proposed and investigated. Comparisons in terms of the QI parameters of Section 2.2 are made between the original models and the modified ones. The purpose of this investigation is to establish a logical sequence by which the torque density performance of electrical machines can be improved, and thus at this design stage, these comparisons are performed for the 36-slot/42-pole combination in the BkEnv space, which shows the best torque density performance from the results tabulated in Table 3.3 and Table 3.4.

3.3.1 The use of cobalt iron laminations

The electrical steel used for all the above models is a typical, readily available silicon steel (SiFe) such as M330-35, which has a silicon component of approximately 3% [117]. Figure 3.7 compares the BH curve of this material with that of a high performance, much more expensive CoFe lamination steel.

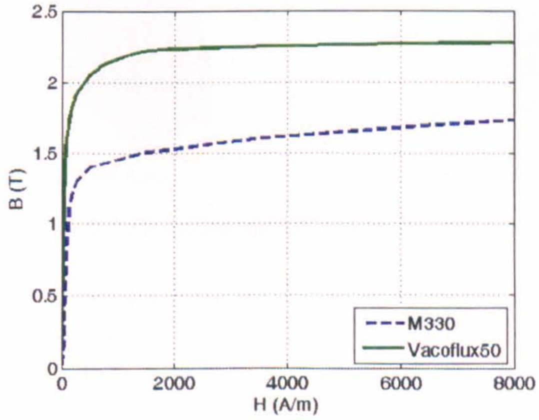

Figure 3.7 Comparing BH curves of M330 and Vacoflux50

The CoFe material shown in Figure 3.7 has a 49% cobalt composition and goes by the name of Vacoflux50^{TM} [117]. For this comparison, the lamination thickness is assumed to be 0.35*mm*. The superiority of the Vacoflux50 lamination steel in terms of the magnetic performance can be observed in Figure 3.7. While the traditional SiFe reaches its magnetic limit at around 1.6*T*, the CoFe can be driven to much higher values, approximately up to 2.2 or 2.3*T*.

The main setback regarding CoFe laminations apart from the considerably higher economic factor is that its mass density ($8120kg/m^3$) is a little higher than that of the SiFe ($7800kg/m^3$). The forthcoming comparative exercise investigates whether the advantage gained by the magnetic performance due to the CoFe laminations outweighs the higher mass density.

A. Design and results

As mentioned above, the study to investigate the effect of using CoFe laminations as opposed to SiFe is carried out by considering the 36-slot/42-pole combination in the BkEnv. The FE model of this combination (as used in used in Section 3.2.2) is redesigned with these CoFe laminations to the same optimisation criteria as described above. The details of the design and optimisation procedures are given in [114]. Figure 3.8 shows the two, optimised FE models, while Figure 3.9, where θ_m is the mechanical position in degrees, compares the results in terms of the more relevant, QI parameters of the two models.

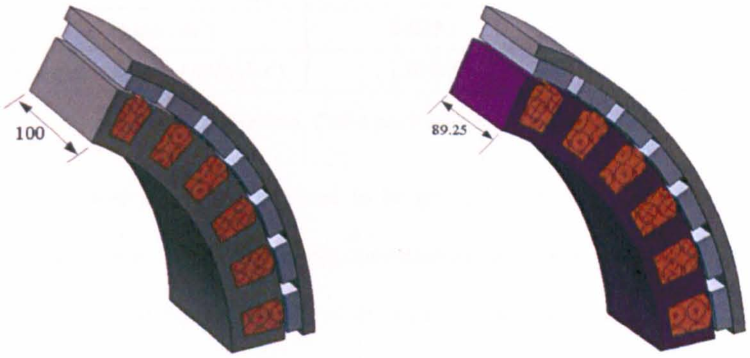

a) SiFe laminations b) CoFe laminations

Figure 3.8 FE models for SiFe vs. CoFe comparison

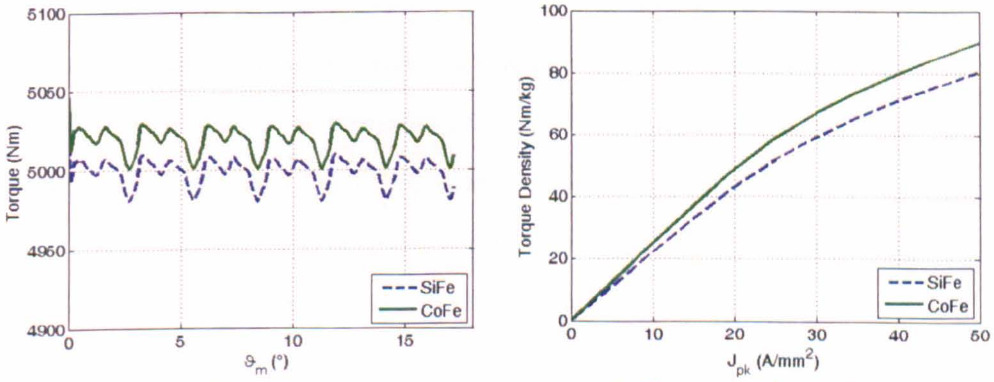

a) Torque b) Torque density vs. J_{pk}

Figure 3.9 SiFe vs. CoFe performance comparisons

B. Discussion

The performance of the two configurations with different stator material laminations in terms of the torque and the torque density are compared in Figure 3.9a and Figure 3.9b respectively. The torque is practically the same for both configurations (*5kNm*) as it is this parameter that is set as the equalising factor. In order to build on the results shown above, Table 3.5 tabulates and compares the main performance parameters of the two models, where the volume is calculated considering only l_{ax} (i.e. not considering the space needed for the end windings).

	SiFe	CoFe
R_e (*mm*)	300	300
l_{ax} (*mm*)	100	89.25
T_t (*mm*)	21.58	19
J_{pk} (*A/mm²*)	36	36
δ_g (*kN/m²*)	103.71	116.2
Mass (*kg*)	74.93	66.52
Torque density (*Nm/kg*)	66.735	75.18
Volume (*m³*)	0.0283	0.0252
Torque density (*kNm/m³*)	176.68	198.41

Table 3.5 SiFe vs. CoFe performance comparisons

Considerable advantages can be perceived to be possible with the implementation of CoFe laminations for the stator. The results of the optimised models show the net superiority in terms of the volume, mass and torque density of the CoFe model, where the objective of a *5kNm* torque is achieved by the CoFe model with a mass reduction of 11.22% and a volume reduction of 10.77% when compared to its SiFe counterpart. Considering all this, it was decided to continue the rest of the design and investigation while implementing CoFe laminations.

The main disadvantage associated with this type of laminations is of course the economic effort involved. At the time of writing, the price of CoFe laminated material is approximately five times as much as that of typical SiFe material. However, the price of the raw material does not necessarily reflect the price of the finished machine. Using CoFe material means a shorter l_{ax}, therefore less soft magnetic iron, less PM material and less copper. From a predicted calculation, this means that the adoption of CoFe laminations would increase the total cost of the machine by approximately a third of the original price. This is a reasonable penalty to pay when considering the improvement gained in terms of peak torque density capability.

3.3.2 The use of open slots

An important feature of using open slots (i.e. stator teeth that are straight all the way from the stator yoke to the air-gap) is the possibility of using pre-formed coils, i.e. the ability to manufacture, varnish and pot the coils before the actual assembly onto the teeth. The main advantage resulting from this is the possibility to achieve a compact and consistent winding lay-out and high values of K_{fill} [47, 52], especially if pressure is applied to the coils before assembly. On the other hand, the removal of the tooth tips as shown in Figure 3.10b increases the cogging torque T_{cog} and therefore the torque ripple T_{rip}. Another effect of having an open slot configuration is that the increase in the slot opening also serves to reduce the phase inductance L_a and the L_d and L_q of the motor, due to the higher effective air-gap length L_{g_eff}.

A. Design

The comparative exercise to assess the benefits and/or demerits of having an open slot configuration is carried out by comparing the results of the model of Figure 3.8b (here called the tooth tips model) with a similar, re-designed model (no tooth tips), as shown in Figure 3.10.

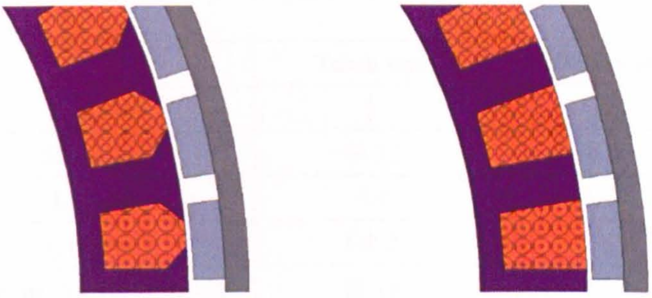

a) Tooth tips b) Open slot

Figure 3.10 FE models for tooth tips vs. open slot comparison

B. Results and discussion

Figure 3.11 compares the performance of the two models in terms of the QI parameters that are most relevant to this comparative exercise, while Table 3.6 tabulates and compares the main characteristics of the two models. The $5kNm$ is achieved by both models with the open slot model showing a slight increase in T_{rip} and T_{cog} as can be observed in Figure 3.11a and Figure 3.11b respectively. From Figure 3.11c and Figure 3.11d, a slightly higher distortion in the back-EMF waveform due to more harmonic content can be observed when the open slot model is implemented.

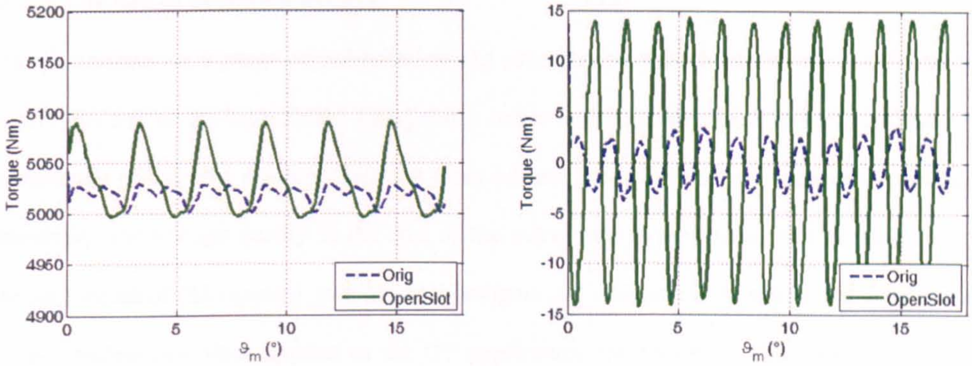

a) Torque b) Cogging torque

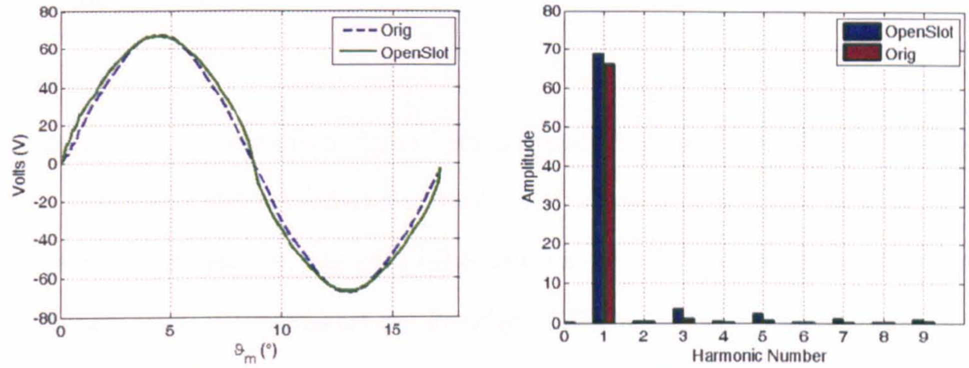

c) Back-EMF d) FFT of Back-EMF

Figure 3.11 Tooth tips vs. open slot performance comparisons

	Tooth tips	**Open slot**
T (kNm)	5	5
Mass (kg)	66.52	66.05
L_a (mH)	5.5	4.78
δ_g (kN/m^2)	116.2	116.2
Torque density (Nm/kg)	75.18	75.7
Torque density (kNm/ m^3)	198.41	198.41
T_{rip} (%)	0.89	1.9

Table 3.6 Tooth tips vs. open slot comparisons

All the above results indicate that the open slot configuration deteriorates the performance of the machine by a very small factor. The main disadvantages perceived from this analysis are the increase in T_{rip} and the small reduction in L_a. Both changes are however very small and the effect of the reduced L_a on the converter kVA rating is minimal. A perceived benefit is the lower mass but again the improvement is also minimal. Considering all the above and the advantages to be gained in terms of a lower P_{cu_tot} when K_{fill} is high, then it was decided to continue the design and analysis of the GT motor using an open slot configuration.

3.3.3 The use of Halbach arrays

As documented in a range of published works presented in the literature review of Section 1.4.1, the use of Halbach arrays can greatly improve the performance in terms of the QI parameters of any PM machine with the main advantages being the improvements in torque capability and voltage quality at the cost of the extra mass synonymous with the high mass density values of PM material. In order to investigate and compare these merits and demerits of such a technology when applied to the GT application, the following investigative study is carried out.

A. Design

Starting from the model shown in Figure 3.10b, a quasi-Halbach array is implemented instead of the conventional SMPM configuration. Due to some of the reasons given in Section 1.4.1 such as complexity and cost, then as an initial design a quasi-Halbach array (as opposed to a full Halbach array) is implemented and investigated. The new model containing the quasi-Halbach array is generally optimised in order to achieve a 'fair' a comparison as possible. It is beyond the scope of this stage of the design to go into the details of the optimisation procedure as here the objective is only to achieve a measure and an understanding of the possible advantages associated with the use of Halbach arrays. However it is important to note that special care is taken to find the optimum ratio between the span of the axially magnetised and the radially magnetised PMs. Figure 3.12 shows the FE models used for the comparison with Figure 3.12a being the same model of Figure 3.10b, whilst Figure 3.12b illustrates the concept of the quasi-Halbach PM array. For visualisation reasons, the magnetisation direction of the PMs is indicated by the red arrows.

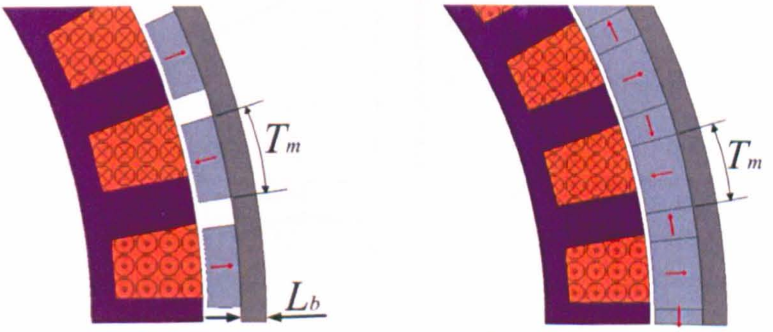

a) SMPM array b) Quasi-Halbach PM array

Figure 3.12 FE models for SMPM vs. quasi-Halbach comparisons

B. Results and discussion

In an effort to understand and confirm the effects that entail from the implementation of a quasi-Halbach array, the performance results of the two above models in terms of the QI parameters are illustrated in Figure 3.13, with the most important points to note being the quality of the back-EMF waveforms for both models, the slight improvement in T_{cog} for the quasi-Halbach configuration and the superiority of the same model in terms of torque density.

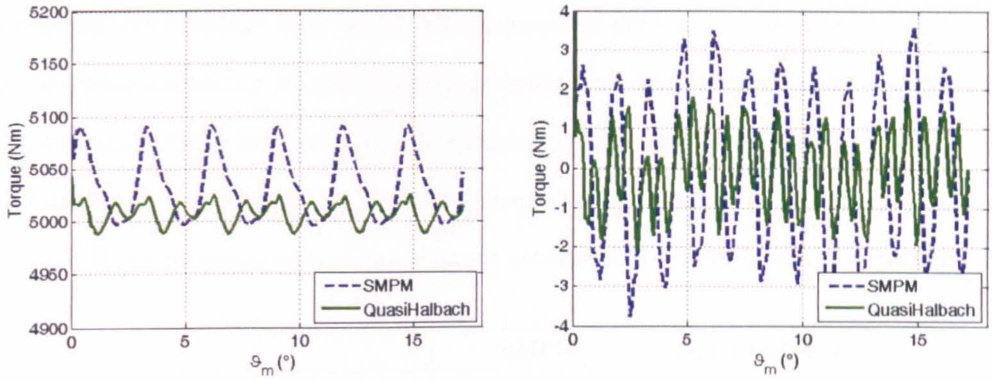

a) Torque b) Cogging torque

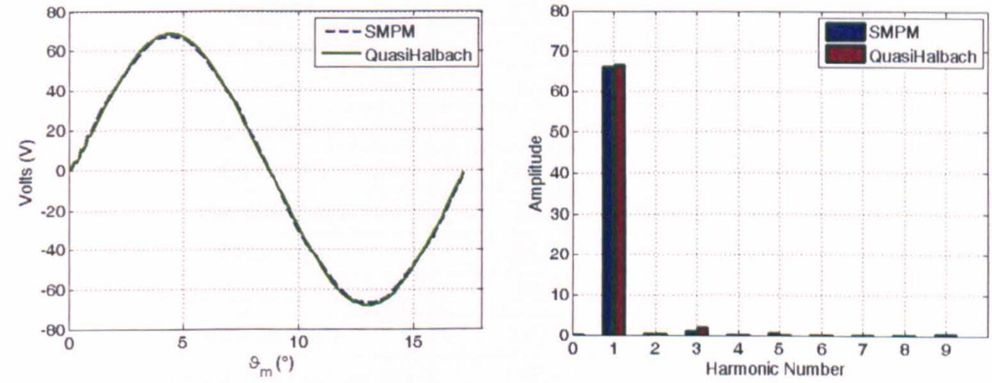

c) Back-EMF d) FFT of Back-EMF

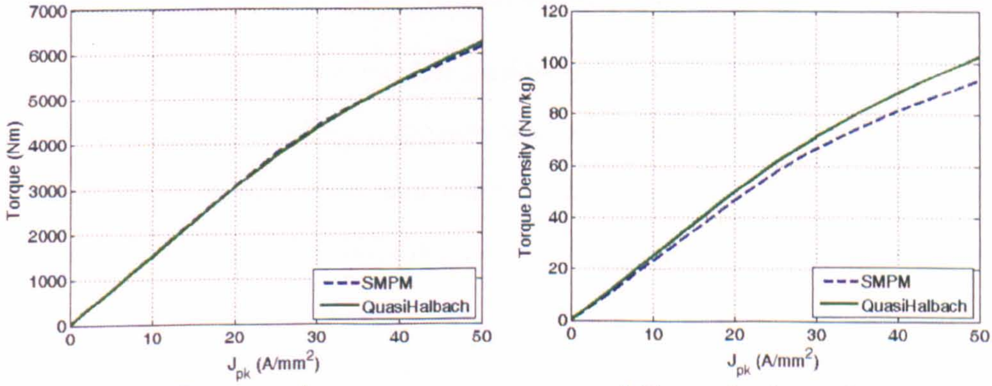

e) Torque vs. J_{pk} f) Torque density vs. J_{pk}

Figure 3.13 SMPM vs. quasi-Halbach performance comparison

The torque requirement of 5*kNm* is shown in Figure 3.13a to be achievable by both models, however as can be glimpsed from Figure 3.13f, the quasi-Halbach array configuration gives considerable advantages in terms of torque density performance capability. Table 3.7 tabulates the performance parameters of the two models. From Table 3.7, where T_m represents the span of the radially magnetised PMs, it can be observed how the total PM mass for the quasi-Halbach model is increased by approximately 35%, which means that further improvement could be achieved by reducing the PM height. However, the objective here is to confirm the superiority of the Halbach array for the 5*kNm* requirement and not to go into a detailed design. In fact, when considering the total machine active mass, the quasi-Halbach model results in a 7.5% reduction. Other improvements, due to this configuration are a reduction of 21.6% for l_{ax} and 21.52% for the stator volume. These improvements in turn result in enhancements of 7.5% and 21.53% for the torque-to-mass and torque-to-volume ratios (no end windings) respectively.

	SMPM	Quasi-Halbach
R_e (*mm*)	300	300
l_{ax} (*mm*)	89.25	70
L_b (*mm*)	10	10
T_m (°)	6.42	5.9
J_{pk} (A/mm^2)	36	36
δ_g (kN/m^2)	116.2	155.94
PM mass (*kg*)	12.86	20.4
Mass (*kg*)	66.05	61.13
Torque density (*Nm/kg*)	75.7	81.79
Volume (m^3)	0.0252	0.0198
Torque density (kNm/m^3)	198.41	252.53

Table 3.7 SMPM vs. quasi-Halbach comparisons

From the above, a general superiority of the quasi-Halbach arrangement is perceived, while an extra advantage of this technology is the potential for improvement if as shown later different configurations of Halbach arrays with different number of stages are considered. The advantage gained in terms of the torque density performance (both torque to mass and torque to volume) is too important to overlook especially when considering the high performance requirements of the application. Thus considering all the above it was decided that the implementation of Halbach arrays is of merit for the application and therefore the ensuing design steps will incorporate the use of such arrays.

3.3.4 The use of unequal stator teeth

All the models from Section 3.2.1.2 onwards are implemented with single layer, concentrated windings whose merits have already been described in the literature review of Section 1.4.1. The single layer configuration means that the coils are wound only on alternate teeth which for convenience will hence forth be called the wound tooth with the other tooth being called the unwound tooth. Apart from the K_{fill} related advantages, other benefits of such an arrangement include lower mutual inductances, higher self inductances and the magnetic, electrical and thermal separation of the coils from each other [118]. Further benefits can be reaped for machines with a similar number of poles and slots, by making the coil pitch approximately equal to the pole pitch, which is achieved by employing unequal tooth widths for the wound and the unwound teeth [30, 54, 55]. A visualisation of this concept is given in Figure 3.14 whose source is [54] and where the thickness of the wound teeth T_{t_w} can be seen to be different from the thickness of their unwound counterparts T_{t_uw}.

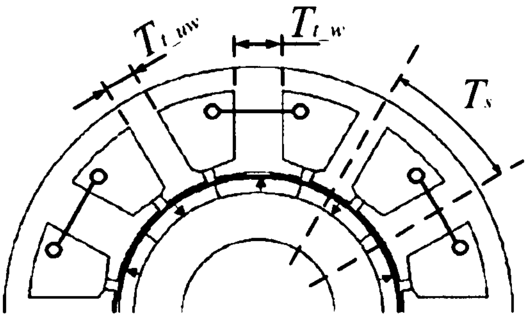

Figure 3.14 Unequal tooth widths concept

A. Design and general optimisation

The model of Figure 3.12b is modified to incorporate the concept of the unequal tooth widths for the wound and the unwound teeth as shown in Figure 3.14. A series of optimisation tests are carried out on the FE model in order to achieve the optimal dimensions for the teeth and back iron of the stator. The effect that the relative width of the stator teeth (i.e. when $T_{t\_uw} = T_{t\_w}$) has on the performance of the machine is first investigated, with Figure 3.15a and Figure 3.15b illustrating its effect on the torque and the torque density capabilities respectively and where T_t is the general tooth thickness and T_s is the slot pitch.

The effects of the ratio of T_{t_uw} to T_{t_w} are studied, with Figure 3.15c and Figure 3.15d illustrating how the torque and the torque density capabilities of the machine are affected by this ratio. From Figure 3.15 it can be observed how optimal values exist for each of the parameters mentioned above. Comparing the optimal values given in Figure 3.15b and Figure 3.15d confirms that by modifying T_{t_uw} in relation to T_{t_w} an improvement of 2.14% in the torque density capability of the machine can be achieved.

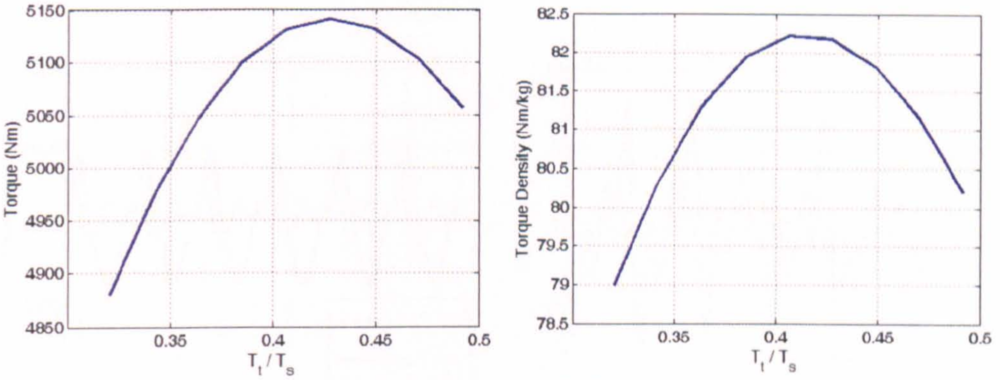

a) Effect of relative T_t on torque b) Effect of relative T_t on torque density

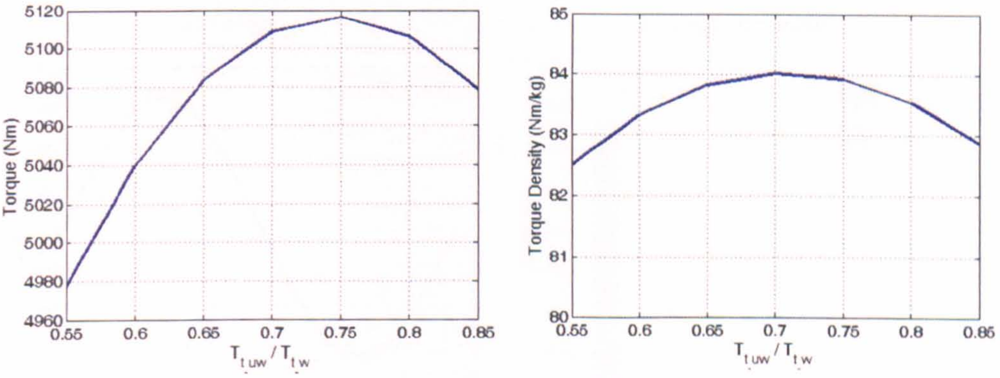

c) Effect of T_{t_uw} on torque d) Effect of T_{t_uw} on torque density

Figure 3.15 Tooth widths optimisation comparisons

B. Comparison and discussion

In order to understand and visualise any merits and demerits of the newly implemented technique, the optimal design corresponding to the results shown above and to the 5*kNm* requirement is then run and compared to the model of Figure 3.12b. The two models used for comparison are shown in Figure 3.16, with Figure 3.16a being the same model of Figure 3.12b and Figure 3.16b is the model with the optimal dimensions for unequal tooth widths. Figure 3.17 compares the results of the two models in terms of the afore-mentioned QI parameters.

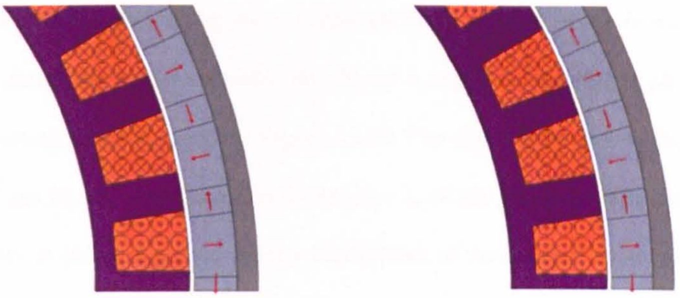

a) Equal tooth widths b) Unequal tooth widths

Figure 3.16 FE models for equal vs. unequal tooth widths comparisons

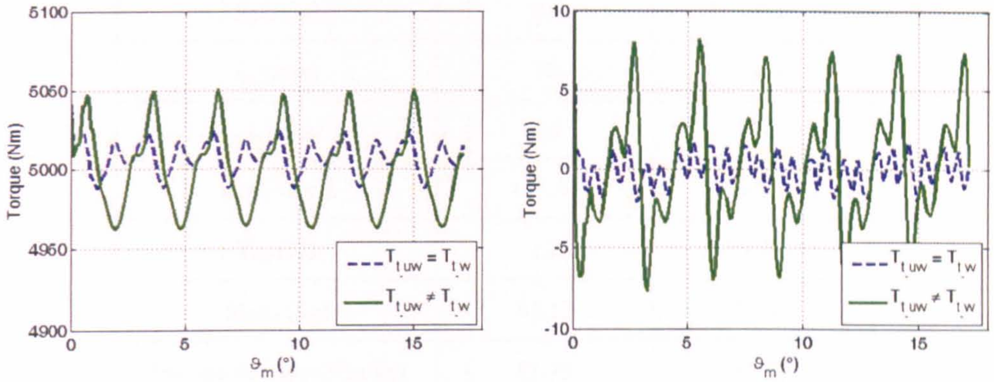

a) Torque b) Cogging torque

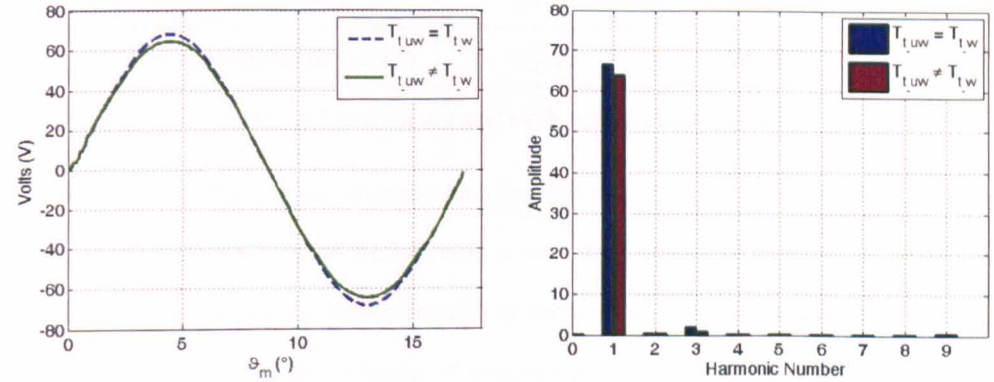

c) Back-EMF d) FFT of Back-EMF

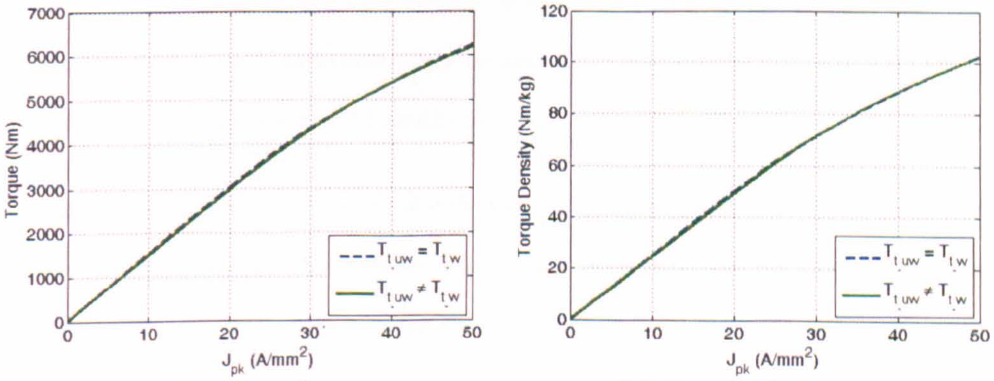

e) Torque vs. J_{pk} f) Torque density vs. J_{pk}

Figure 3.17 Equal vs. unequal tooth widths performance comparisons

From the results shown above, the most important point to note is the higher T_{cog} that the unequal tooth thickness model exhibits, this being a result of the larger physical distance between the tooth tips for the model of Figure 3.16b. The slight difference in the amplitudes of the back-EMF can be safely attributed to the smaller l_{ax} of the unequal tooth width model. The small superiority in terms of torque density capabilities of the unequal tooth width model can also be appreciated in Table 3.8 which tabulates the main characteristics of the two models.

	$T_{t\_uw} = T_{t\_w}$	$T_{t\_uw} \neq T_{t\_w}$
R_e *(mm)*	300	300
l_{ax} *(mm)*	70	68.07
J_{pk} *(A/mm^2)*	36	36
δ_g *(kN/m^2)*	155.94	160.36
T_{rip} *(%)*	1.2	1.77
Mass *(kg)*	61.13	60.68
Torque density *(Nm/kg)*	81.79	82.39
Volume *(m^3)*	0.0198	0.0192
Torque density *(kNm/ m^3)*	252.53	260.04

Table 3.8 Equal vs. unequal tooth widths comparisons

The main message that can be perceived from the results of this investigation is that for this particular GT application in the BkEnv, only a very small advantage in terms of mass and volume can be gained by the implementation of the unequal tooth width technique. This is mainly due to the fact that the technique of modulating the teeth thicknesses gives very good performance improvements when the machine is operating under linear conditions. However the improvement is much attenuated when the machine is heavily saturated, as is the case of the GT motor when under peak load conditions.

Considering all the above and the fact that the utilisation of the $T_{t\_uw} \neq T_{t\_w}$ technique does not involve any excessive effort to implement, then it was decided to continue the process of the design of the GT motor while incorporating this technique for any proposed, single layer model.

3.4 General summary and project updates

Towards achieving a successful implementation of a motor for the GT application, at this point in the design process, it is important to summarise all the information achieved from the above investigations. From the methodology presented in Section 3.3, at this point of the design, the investigation indicates that the best torque, torque density and general performances possible can be achieved by implementing a PM, BLAC motor that comprises the following features

1) A single air-gap, radial configuration
2) An outer rotor arrangement
3) Single layer windings
4) CoFe stator laminations
5) An open slot stator teeth structure
6) Unequal widths of wound and unwound teeth
7) The use of Halbach arrays for the rotor PMs

It is generally indicative that by adopting the above measures, a torque density performance of 82.39*Nm/kg* and 260.04*kNm/m*^{3} can be achieved. Considering that the target values for the BkEnv, shown in Table 3.1 are 53.84*Nm/kg* and 190.22*kNm/m*^{3}, then this indicates the potential synonymous with the methodology with which the above techniques are applied.

To re-cap all the above, and update the design with the improvement procedures outlined above a new comparative exercise [119] is done for both envelope spaces. For each envelope, FE models comprising all the above features are built and geometrically optimised. Considering that most of the investigations in the previous sections were done on one particular, slot-pole combination then the main aim of this new comparative exercise is to compare, identify and actually confirm the slot/pole combination that results in the better performance possible for both envelopes. Due to the large number of possible combinations, the investigation is mainly focused on finding and confirming the maximum possible torque for each combination and for the moment sets aside the other QI parameters. For this exercise, the main constraints that limit the operation of the machines are considered to be the maximum available space (set by the particular envelope being investigated) and a set J_{pk} (set as a safe value by the thermal model of Figure 3.4).

3.4.1 BkEnv updated comparisons

Figure 3.18, sourced from [119] compares the torque performance for the BkEnv machines at a J_{pk} of $28A/mm^2$. This current density is chosen according to Figure 3.4 as the J_{pk} that guarantees a safe thermal limit for all the slot-pole combinations considered. As already mentioned, to gain a measure of simplicity, this part of the investigation only focuses and compares the maximum achievable torque.

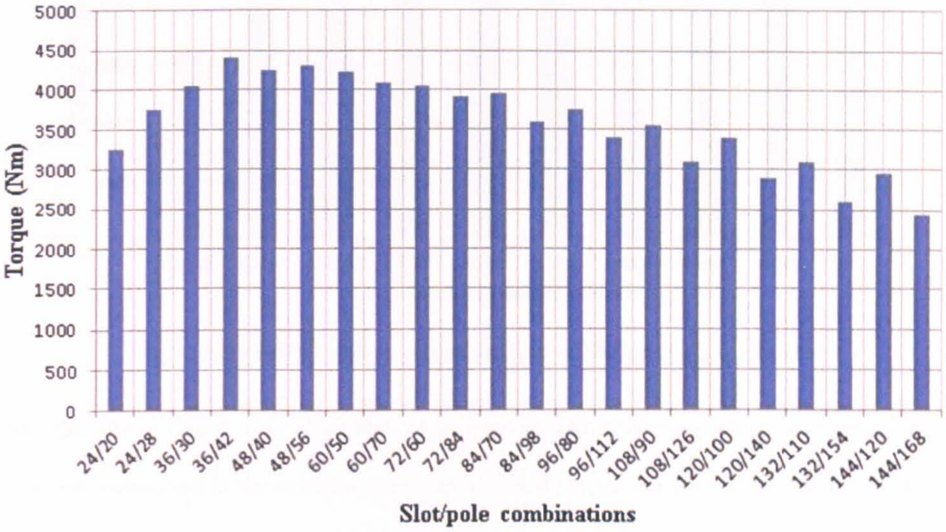

Figure 3.18 BkEnv slot/pole combination influence at $J_{pk} = 28A/mm^2$

From the above figure, it is clear that when implementing all the performance improvement measures mentioned in the previous sections, the best torque capability is given by the 36-slot/42-pole combination. This compares nicely with the initial slot-pole investigation results given in Table 3.4 which had also previously indicated the same slot-pole combination as the better option for the BkEnv.

As a small side note, regarding this comparison between Figure 3.18 and Table 3.4, it is important to look back and note that for Table 3.4, the J_{pk} used was $36A/mm^2$ and not the $28A/mm^2$ used here. Also the mass of the 36-slot/42-pole combination is $75.24kg$ in Table 3.4, whilst it is approximately $61kg$ for Figure 3.18. All this clearly indicates the considerable improvements achieved by the implementation of the measures presented in Section 3.3.

3.4.2 FrEnv updated comparisons

Figure 3.19 which is sourced from [114] compares the torque performance for the FrEnv machines at a J_{pk} of $32A/mm^2$. This current density is chosen according to Figure 3.4 as the J_{pk} that guarantees a safe thermal limit for all the slot-pole combinations considered.

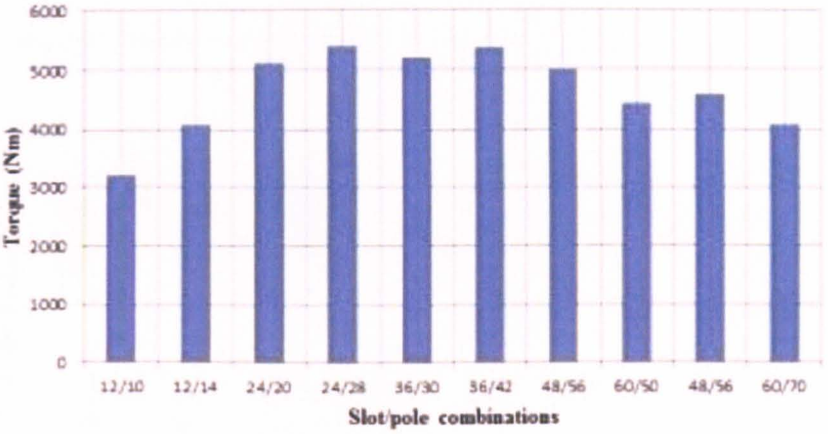

Figure 3.19 FrEnv slot-pole combination influence at $J_{pk} = 32A/mm^2$

From the above figure, it is clear that when implementing all the performance improvement measures mentioned in the previous sections, the best torque capabilities are given by the 24-slot/28-pole and 36-slot/42-pole combinations. This indicates that *au contraire* to the BkEnv situation, the best performance combinations are different from those indicated by the initial studies illustrated in Table 3.3 of Section 3.2.1.2. For that study the best performance had been found to be that of the 48-slot/56-pole combination. This indicates that for the FrEnv space the implementation of the performance improvement measures (for this particular J_{pk}) has resulted in the 24-slot/28-pole and 36-slot/42-pole combinations showing a better performance, thus implying a higher design potential.

3.4.3 Customer specifications and requirements updates

As reported in [114, 119, 120] the design process of the GT motor was done in parallel with work done on the landing gear structure, requirements specifications from typical taxi cycles and predicted aircraft weight. In fact in [119], studies involving indirect drives with gear-boxes, different load values, different machine topologies etc... are presented; studies which however go beyond the scope of this work and are thus not included in this thesis.

Having done the above studies with indicative requirements, the requirements were frozen so that the final design could be initiated. The available options in terms of the machine design (as presented above) were presented and discussed in detail with all the partners involved in the project. Following these discussions, the final required performance characteristics given in terms of the required torque and speed duty cycles as shown in Figure 3.20a and Figure 3.20b respectively, were indicated as the main specifications for the GT application.

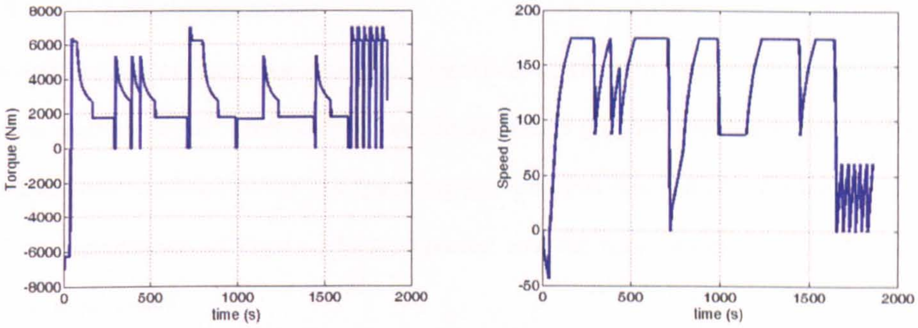

a) Torque duty cycle b) Speed duty cycle

Figure 3.20 Customer supplied performance duty cycles

After careful considerations regarding inter-connection and compatibility issues with the rest of the aircraft, aircraft regulations etc… and more importantly the required specifications shown in Figure 3.20, a decision was finally reached that the most appropriate space for the implementation of the GT motor is the FrEnv space with one motor per landing gear. The peak torque value (per landing gear) was reduced from 10*kNm* to 7*kNm*, as in [119] it had been shown that a 10*kNm* torque capability could only be reached with mechanical gearing. However the condition of one motor per landing gear excludes the possibility of having two 3.5*kNm* motors, which means that one motor in the FrEnv space must be able to provide the 7*kNm* requirement. This decision, taken with the approval of the author and other colleagues, thus settles the question of which envelope is to be used, but however sets the requirement of torque capability to a highly challenging threshold.

In the next sections, the development of the motor in the FrEnv space with the 7*kNm* requirement will be addressed. Special attention will now start to be given to thermal design as in these latter stages of the design, the issues regarding this factor start to have a considerable weight in the composition of the machine.

3.5 Towards the final design

Using the information presented in the previous sections, the next step of the design process focuses on the realisation of the torque requirement for the space indicated. For this reason, an evaluation and comparison of different configurations is done in order to identify the best suited topology. The following investigations are again done by considering the QI parameters mentioned in Section 2.2.

3.5.1 Slot-pole combinations

Having decided on the space envelope dimensions as given in Figure 3.2 and on the peak torque requirement of $7kNm$, the next step in the design process is to decide and confirm the best slot-pole combination for the specifications. Towards this purpose, the most promising FrEnv combinations of Figure 3.19 are updated with the main objective being to reach the torque requirement.

A. Design

The FE models of four slot-pole combinations (chosen from Figure 3.19) are updated and re-optimised in detail in order to achieve the best performances possible for the allowed space. The design is initiated by considering any parameters that are fixed either by the application requirements or by material properties. Thus, the maximum l_{ax} and R_e of the machine are fixed by the dimensions of the FrEnv, whilst such parameters as B_{rem} and μ_{rrec} are set by the PM properties. For fixed external dimensions, each slot-pole combination automatically sets the slot pitch T_s and the pole pitch T_p to specific values. Typical values of T_m and the stator bore radius R_{stat_bore} are set to provide reasonable initial values. The optimal dimensions for each combination are derived via a FE, optimisation procedure. Figure 3.21shows the final models.

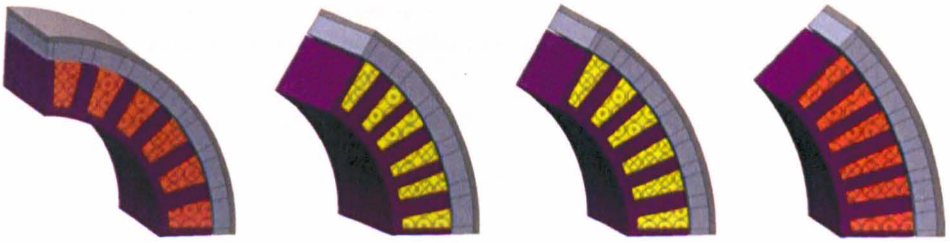

a) 24-slot/ 28-pole

b) 36-slot/ 30-pole

c) 36-slot/ 42-pole

d) 48-slot/ 56-pole

Figure 3.21 FE models of the updated slot-pole combinations considered for FrEnv

The tests for the slot-pole combinations comparisons are done assuming a force air cooling system with an air velocity V_{air} of 1m/s. A 'fair' comparison is achieved by considering the same value of P_{cu_tot} for all the models at steady state. The same A_{rms} is maintained by adjusting the number of turns when different combinations are tested. For this exercise l_{ax} is assumed to be 160*mm* in order to allow 20*mm* of space for the end-windings on each side. The thermal model of Figure 3.4 is used to confirm that even under the specified duty cycle, the temperature in the coils never exceeds the thermal limit, that is set by T_{max}.

B. Results and discussion

Following the general trend adopted throughout this thesis, the values of the main QI parameters mentioned in Section 2.2 for the different slot-pole combinations are compared and discussed below.

The generated torque of the four models is achieved for a J_{pk} of 36*A/mm*^{2}, at which loading, the slot-pole combinations investigated achieve a mean torque at peak load condition as shown in Figure 3.22a. Table 3.9 lists the torque, mass, torque density and the T_{rip} of the models for this condition, from which it is clear that at this particular loading the best torque and torque density performance is achieved by the 36-slot/42-pole combination.

	Torque (*Nm*)	**Mass (*kg*)**	**δ_g (*kN/m*^{2})**	**Torque Density (*Nm/kg*)**	**T_{rip} (%)**
24-slot/28-pole	6752.8	113.75	159.1	59.36	7.17
36-slot/30-pole	6790	119.22	163.1	56.95	2.02
36-slot/42-pole	6984.7	113.85	162.93	61.35	5.37
48-slot/56-pole	6299.2	108.42	144.14	58.1	5.36

Table 3.9 Updated slot-pole combinations comparison at J_{pk}=36*A/mm*^{2} with l_{ax} =160*mm*

Figure 3.22b shows the cogging torques of the four models with the 36-slot/30-pole model exhibiting the highest T_{cog}, while the lowest value of T_{cog} is achieved by the 24-slot/28-pole. However from Table 3.9, it is clear that it is actually the latter combination which exhibits the worst performance in terms of T_{rip}, with the 36-slot/42-pole showing a T_{rip} of 5.37%.

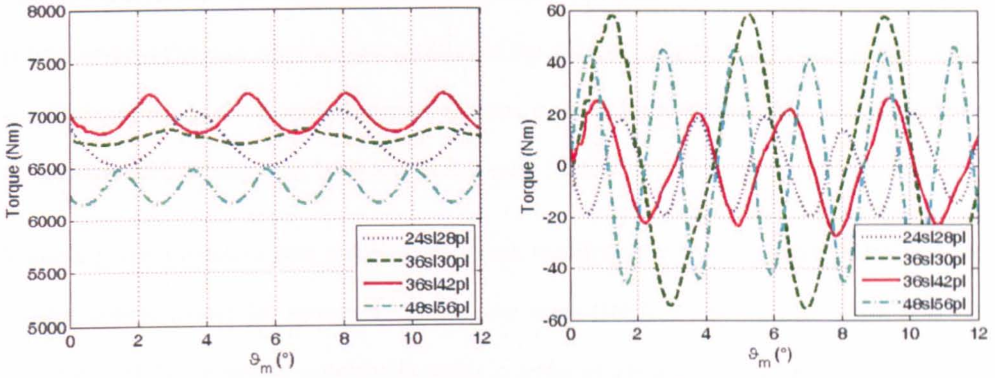

a) Torques b) Cogging torques

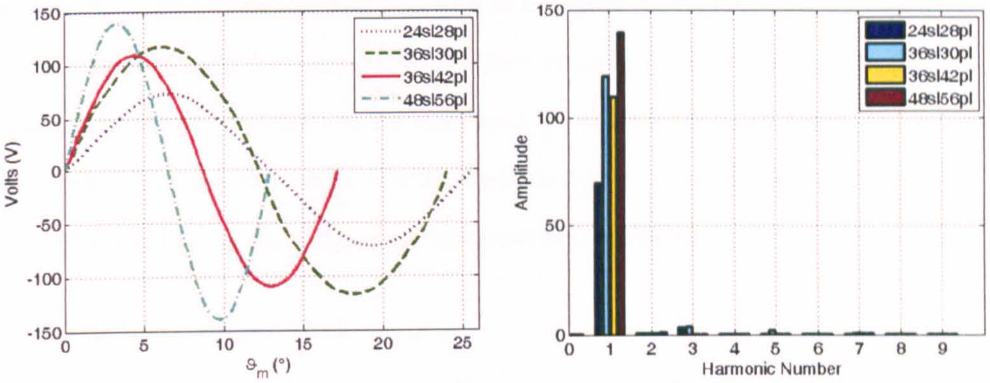

c) Back-EMFs d) FFT of Back-EMFs

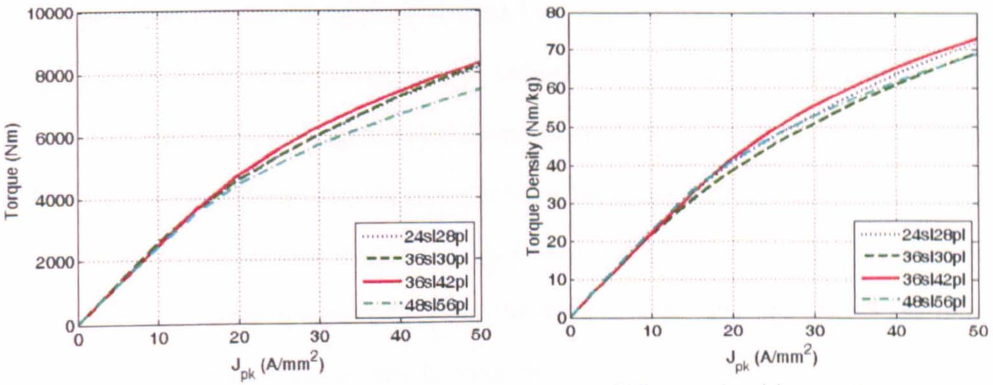

e) Torques vs. J_{pk} f) Torque densities vs. J_{pk}

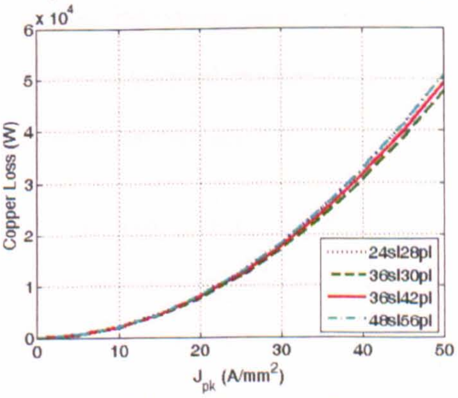

g) Copper losses vs. J_{pk}

Figure 3.22 Updated slot-pole combinations performance comparisons with l_{ax} =160*mm*

The back-EMFs and their harmonic spectra are shown in Figure 3.22c and Figure 3.22d. There is little or no difference between the qualities of the induced voltages. The slight difference in amplitudes is due to the modified number of turns, so as to keep A_{rms} constant which results in an approximately constant P_{cu_tot} as shown in Figure 3.22g.

While it is the 36-slot/30-pole combination which manifests the best T_{rip} performance and the 24-slot/28-pole model the lowest active material mass (for l_{ax} = 160*mm*), however it is the superiority of the 36-slot/42-pole combination in terms of generated torque and torque density that has the highest 'attraction' factor for such an aerospace application as the GT motor. The main factor of choice is the motor version that gives the highest minimum value of torque. This is critical as this can potentially be the exact point at which the GT motor has to start at zero speed while requiring peak torque. It is therefore this that influences the decision to focus the rest of the investigation and design on the 36-slot/42-pole combination.

3.5.2 Winding configurations

From Figure 3.22a and Table 3.9, it can be observed that for the chosen motor, the mean torque for the peak load condition at $36A/mm^2$ is 6984.7*Nm* with a T_{rip} of 5.37%. As stated above, these values are achieved considering a l_{ax} of 160*mm*. After experimental tests on purposely built, dummy slots (shown in Figure 5.20a) it was observed that to ensure enough space for the end-windings while still respecting the spatial limits of the FrEnv, the maximum permissible l_{ax} is 151*mm*. Henceforth all modelling and design is done using this value of l_{ax}. This however results in a considerable reduction of torque. In fact as shown later in Figure 3.29a (plot labelled as single layer), with the new l_{ax} value the mean torque is 6621.8*Nm* with a T_{rip} of 5.87%. In an effort to increase the torque whilst reducing T_{rip}, two different winding configurations, are proposed and investigated, the first being a double layer equivalent of the above motor and secondly a double star configuration.

The advantages of a double layer configuration include a lower copper mass [97, 121], a shorter l_{ax} and a considerable reduction in space harmonics when compared to a single layer arrangements [51]. The resulting, higher fundamental B_{gl} can ameliorate the torque capability and reduces T_{rip}. The main demerits of double layer windings are the lower K_w [51] and the lower fault tolerant performance.

The improvements due to double layer windings can be enhanced by applying the concept of a double star configuration [122-124]. In this section, an introduction onto the concepts of the double layer and double star is given while an investigative study to compare the performance of the above machine with that of its double layer and double star equivalents is presented.

3.5.2.1 The double layer and double star concepts

It is common knowledge that concentrated windings in a single layer configuration cannot achieve the high value of K_w synonymous with distributed windings [51]. However, this can be considerably improved by the use of a fractional slot configuration, in fact for a standard, 36-slot/42-pole motor it is shown in [97] that K_w is 0.966 and this can be achieved both by a single layer and arguably also by a double layer configuration.

A. The double layer configuration

Apart from the reduction of spatial harmonics in the air-gap, an added advantage of a double layer winding is the shorter end-windings [121]. The nature of a concentrated winding with the benefit of having pre-formed coils is also maintained. However, this new configuration means that the number of coils is doubled and the concept of the alternate teeth winding is nullified. Thus if the use of different teeth thicknesses as presented in Section 3.3.4 is implemented then two different sets of coils (in terms of geometrical size and shape) are required which increases the complexity of the coil manufacturing. For this reason, in the case of the double layer machines the uneven tooth thickness technique is not utilised.

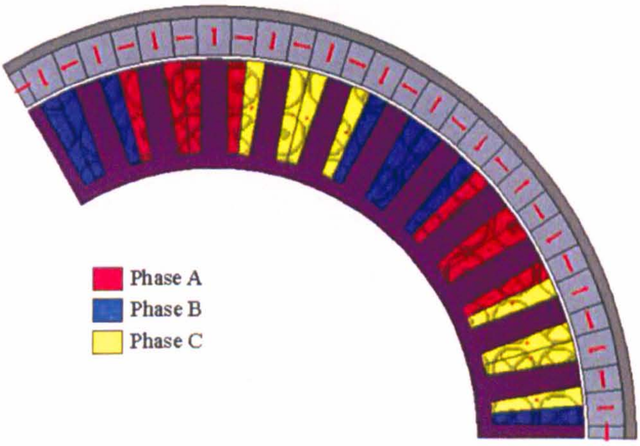

Figure 3.23 FE model of the double layer, 36-slot/42-pole machine

A FE model of a double layer equivalent of the single layer, model (shown in Figure 3.21c) is built and geometrically optimised. This is shown in Figure 3.23 where the equal tooth thicknesses can be observed and the three different colours indicate the three different phases.

B. The double star concept

The double star concept involves the use of two sets of 3ϕ windings fed by two separate converters. Thus the coils available in the double layer motor are separated into two individual sets or star points with an individual converter for each star as shown in Figure 3.24.

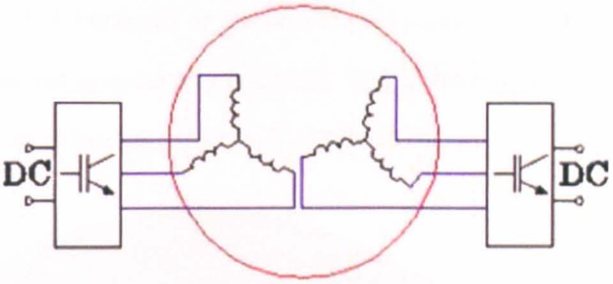

Figure 3.24 The double star concept

The winding structure of the double star arrangement is shown in Figure 3.25, where M_{1a2a} is the mutual inductance between the two stars and θ_{1a2a} is the phase shift angle between the two stars, whose optimum value is usually of 30°.

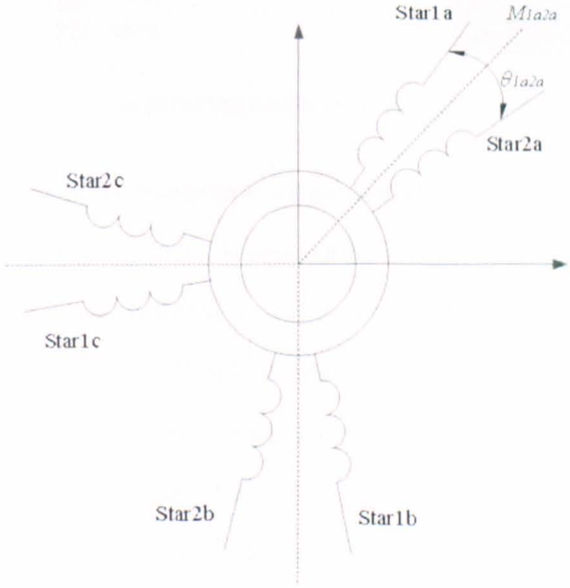

Figure 3.25 The double star winding arrangement

The main advantages of this configuration are the reduced dc-link, voltage/current ripple [122], an improved K_w relative to a single star, double layer equivalent [125, 126] and the elimination of the sixth harmonic torque pulsation [124]. This pulsation is mainly dependent on θ_{1a2a}. A perceived advantage of this configuration is the fault tolerance potential [127]. In case of a critical fault in one star, the machine should theoretically still be able to supply half the torque via the other star. The double star configuration's main setbacks are the electro-magnetic coupling between the two stars [128] and the potential risk of excitation of the 5th and 7th harmonics due to the reduced impedance in their current paths resulting from harmonics in the input voltages [127]. A FE model of a double star equivalent of the double layer, model of Figure 3.23 is built and geometrically optimised. This is shown in Figure 3.26 where all the phases corresponding to any star are shown in a different colour.

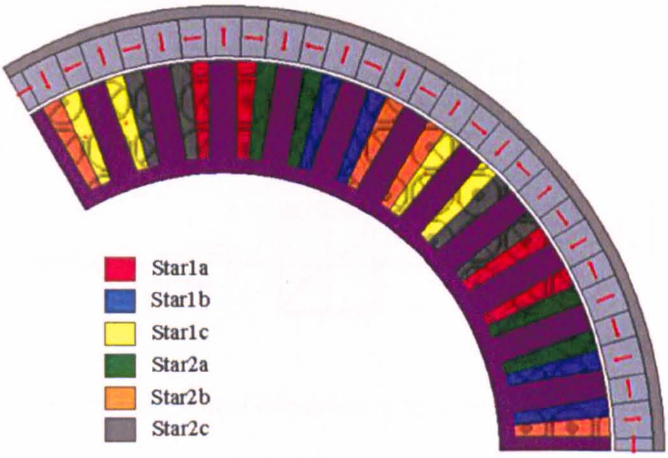

Figure 3.26 FE model of the double star, 36-slot/42-pole machine

3.5.2.2 Thermal modelling for double layer arrangements

The thermal model shown in Figure 3.4 is designed for a single layer winding and thus is not suitable for double layer arrangements. To this purpose a thermal model for double layer arrangements as shown in Figure 3.27 is built, where $R_1 - R_{12}$ are the thermal resistances and R_{wat}, R_{hc}, R_t, R_{stat_bore} and R_{house} are the defining radii for the thermal calculations. The concepts behind the thermal model and the derivations of the thermal resistances are given in Appendix B.3.2, while the heat sources P_{cu} are dependent on the torque duty cycle given in Figure 3.20a and derived by the calculations shown in Figure 3.28, where $R_{coilside}$ is the resistance of the part of the coil that is in any one half of a slot.

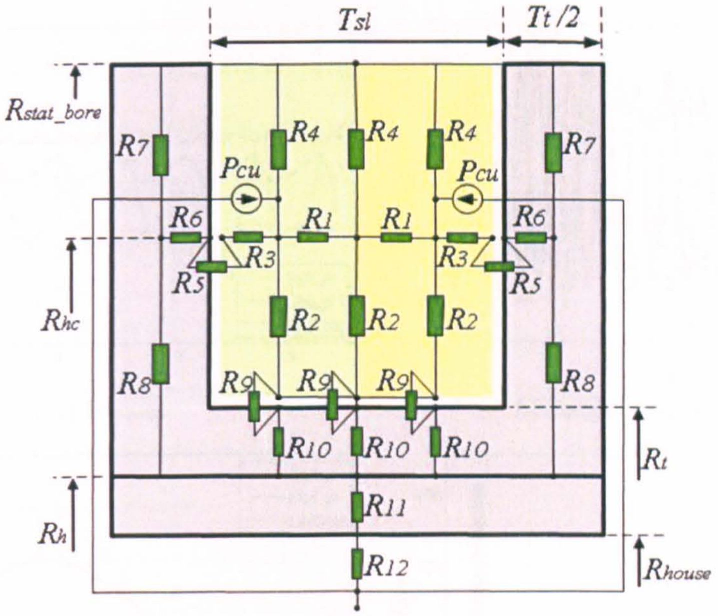

Figure 3.27 Lumped parameter model for one slot pitch with double layer windings

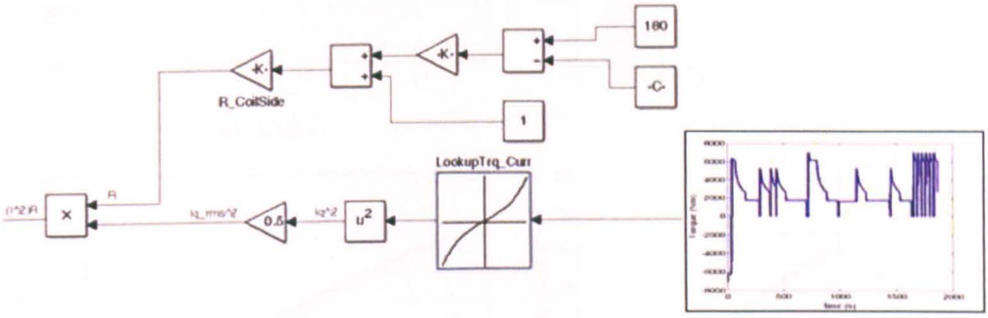

Figure 3.28 Heat sources calculation as for given torque duty cycle

3.5.2.3 Comparative exercise

A comparative investigation in terms of the QI parameters between the single layer model of Figure 3.21c, its double layer equivalent shown in Figure 3.23 and the double star model shown in Figure 3.26 is done. Figure 3.29 illustrates the results of this exercise.

A. Results and discussion

The generated torque of the three winding configurations is achieved for a J_{pk} of $36A/mm^2$, which according to the thermal model of Figure 3.27 guarantees safe operation. At this loading, the three models achieve a torque at peak load condition as shown in Figure 3.29a. Figure 3.29b shows the cogging torques of the three models where it can be observed that a minimal difference in terms of this QI parameter exists between the three models.

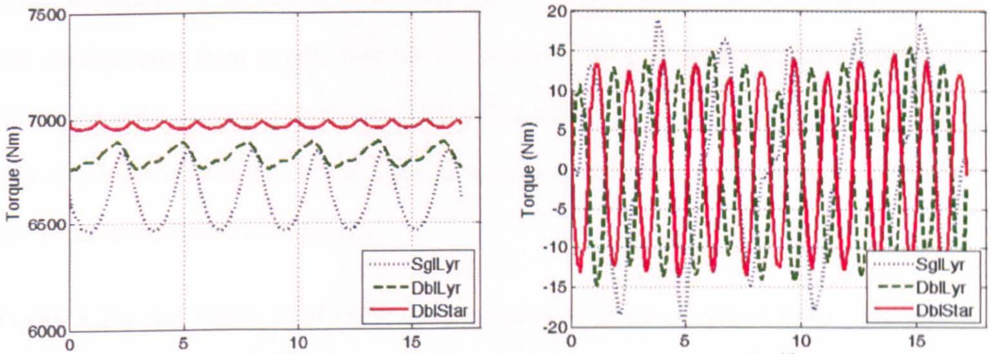

a) Torques b) Cogging torques

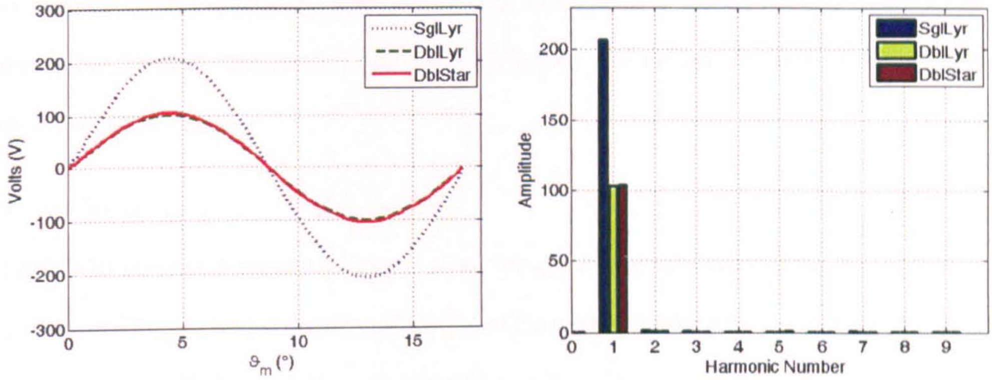

c) Back-EMFs d) FFT of Back-EMFs

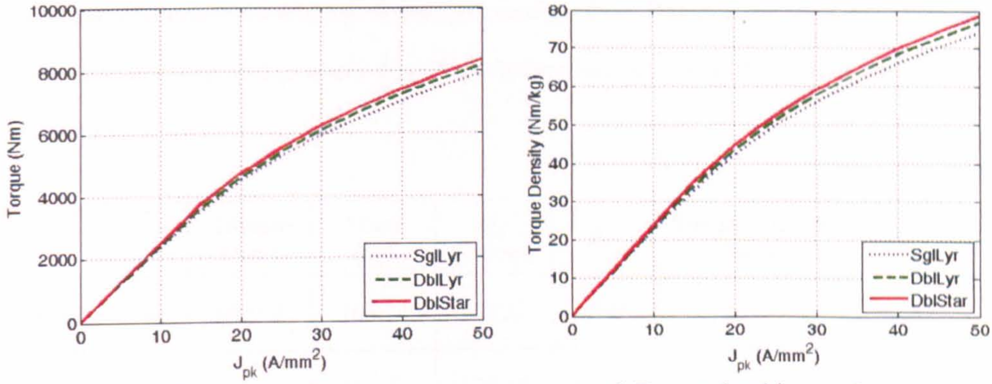

e) Torques vs. J_{pk} f) Torque densities vs. J_{pk}

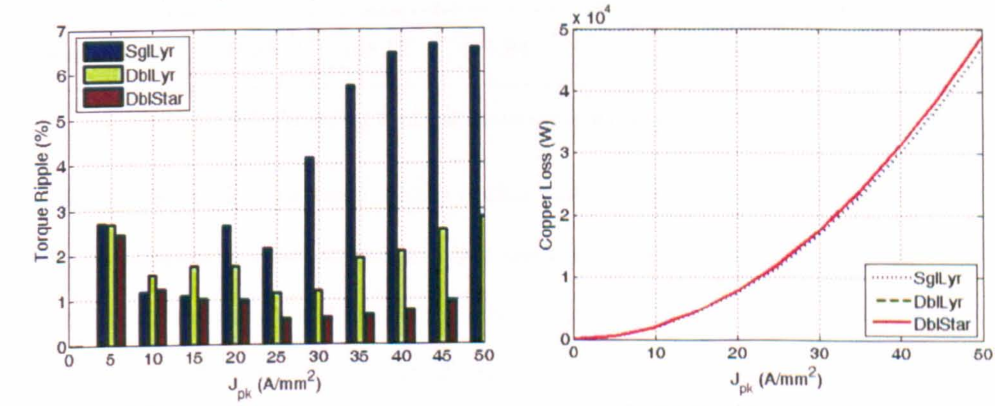

g) Torque ripples vs. J_{pk} h) Copper losses vs. J_{pk}

Figure 3.29 Winding configurations performance comparisons

When implementing the double layer models, the number of turns N has to be halved as with this configuration there is only half the slot available for each coil-side. This explains the difference in the amplitude of the back-EMF of the single layer model, shown in Figure 3.29c. The double star model indicates a slight improvement in the quality of the back-EMF when compared to the double layer model.

Figure 3.29e and Figure 3.29f show the superiority in terms of torque and torque density capability of the double star machine, while Figure 3.29g illustrates the considerable advantage in terms of T_{rip} that is achieved when considering the double star model. Finally, Figure 3.29g shows that the above comparative exercise is performed with the main equalising factor being that of the same P_{cu_tot}.

B. Conclusion

Table 3.10 presents a general overview of all the above and tabulates the torque, mass, the fundamental K_w, the torque density and the T_{rip} of the models for the peak load condition. Table 3.10 illustrates a 5% increase in terms of torque and also of torque density when comparing the double star machine to the original, single layer configuration. However the main improvement is achieved in terms of T_{rip} where this QI parameter can be seen to have been reduced by almost 10%.

	Torque ***(Nm)***	**Mass** ***(kg)***	δ_g (kN/m^2)	K_w	**Torque Density** ***(Nm/kg)***	T_{rip} (%)
Single layer	6621.8	106.74	165.27	0.966	62.04	5.87
Double layer	6818.2	106.12	170.17	0.933	64.25	1.97
Double star	6965	106.12	173.84	0.966	65.64	0.56

Table 3.10 Winding configurations comparison at $J_{pk}=36A/mm^2$

Considering Figure 3.29 and Table 3.10, it is clear that the best peak load, torque and torque density performance is achieved by the double star configuration. A main point in favour of this winding combination is also shown to be the relative smoothness of the generated torque, where an optimal T_{rip} of 0.56% is achieved. Due to all the above, it was decided to adopt this concept as the winding configuration for the GT motor.

3.5.3 The PMs, the Halbach array and demagnetisation issues

Having decided on the slot-pole combination and the winding arrangement to be used, a careful investigation building up on the studies of Section 3.3.3 is initiated in order to achieve a better understanding of the behaviour, merits and demerits of the PM configurations used.

As stated in Section 1.4.1.2, the aim of utilising Halbach arrays is to obtain advantages in the torque capabilities and the quality of the back-EMF. These usually come at the cost of added weight, added expenses, reduced robustness and more importantly the risk of demagnetisation. Due to the reasons mentioned in Section 3.3.3, such as simpler assembly and manufacture procedures, the studies presented above all make use of a PM structure in a quasi-Halbach configuration. From the above studies a perceived 'weakness' of this configuration is the potential risk of irreversible demagnetisation of the PMs, which complies with the general idea that this particular configuration is always more at risk of demagnetisation than other configurations [66].

Thus, in this section the PMs being used for the GT motor and their properties are presented and studied. The quasi-Halbach array presented previously is also thoroughly studied and compared to a possible alternative.

3.5.3.1 The PMs

The harsh environments associated with the aircraft taxiing application and the expected elevated temperatures serve as an indication of the high quality of the PM material required for this GT application. The main constraints influencing the choice of the material are the high level of B_{rem} required in order to reach the high torque requirements and a high operating temperature T_{pm}.

The last two or three decades have seen the advent of rare-earth magnet materials such as Samarium Cobalt (SmCo) and Neodymium Iron Boron (NdFeB). Figure 3.30, the source of which is [129] summarises the most common materials that are considered relatively 'modern', where H_{ci} is the intrinsic coercive field, $(BH)_{max}$ is the maximum energy product and the years indicate the date of the start of commercialisation for the respective PM material.

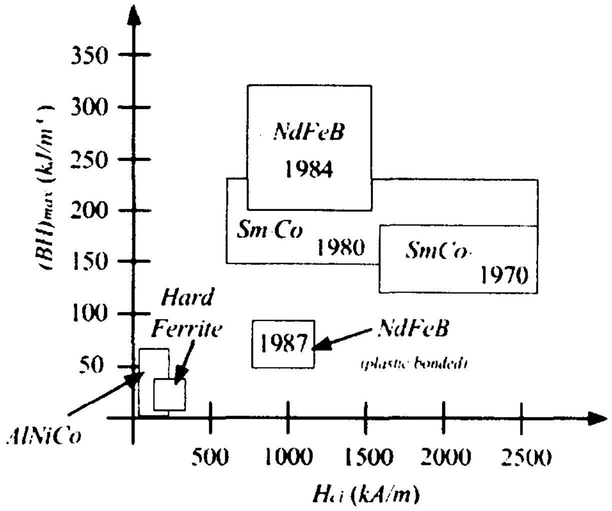

Figure 3.30 Modern PM materials

For high performance machines, today only the SmCo and NdFeB materials are widely utilised, due to the obvious reasons of high values of $(BH)_{max}$, H_{ci} and T_{pm}. As can be observed from Figure 3.30, PMs constructed from SmCo have exceptionally high H_{ci} values and relatively low temperature coefficients of B_{rem} thus ensuring a very good thermal stability. The T_{pm} associated with SmCo is typically 250°C for $SmCo_5$ and 350°C for Sm_2Co_{17}. Another advantage of this technology is that there is no need of corrosion protection. On the other hand the main disadvantages are the lower $(BH)_{max}$ when compared to the NdFeB materials and its inherent, elevated brittleness [129]. The main advantages of NdFeB magnets when compared to SmCo materials are the higher $(BH)_{max}$ and B_{rem}. In fact, NdFeB offers the highest possible values of these parameters from all the commercially available PM products. However their poor corrosion resistance and relatively low working temperatures (maximum is approximately 200°C) tend to be the main points in their disfavour.

To satisfy the torque requirements specified by the duty cycle of Figure 3.20a, it can be observed from Figure 3.29e that high values of J_{pk} and therefore of the phase currents will be required, especially for the peak load condition. This automatically results in elevated motor temperatures during operation. Thus, as a precaution it was decided to select the SmCo material, which ensures a safe T_{pm} even for the worst case scenarios (including a hefty safety factor). The material chosen is a 26/10 grade of Sm_2Co_{17} whose demagnetisation curves and properties are shown in Figure 3.31 and Table 3.11 respectively.

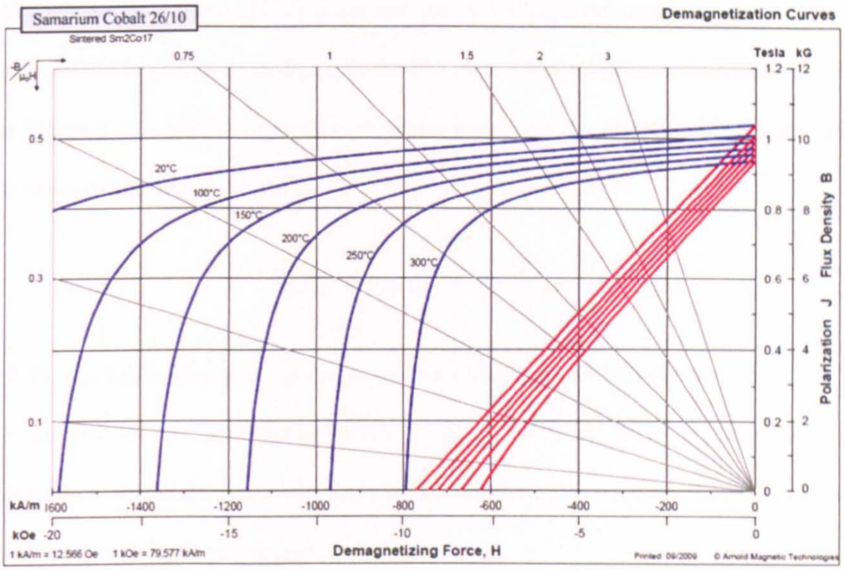

Figure 3.31 Sm_2Co_{17} demagnetisation curves

Maximum T_{pm} (°C)	350
$(BH)_{max}$ (kJ/m^3)	205
B_{rem} (T)	1.04
H_{ci} (kA/m)	2000

Table 3.11 Sm_2Co_{17} material properties

3.5.3.2 Demagnetisation analysis

Irreversible demagnetisation occurs when the PM operating point goes below the knee value of the closed loop curve (shown in red in Figure 3.31). As the operating T_{pm} increases, this knee-limit in terms of B increases, in fact for the lower temperature curves, this knee point is negative and does not appear in Figure 3.31, whilst for a T_{pm} of 300°C it is situated at approximately $0.2T$. This means that for a PM operating temperature that is equal to or under 250°C, demagnetisation would occur only when the flux density field B at any point in the PM material has been completely reversed in its direction.

On the other hand, as a worst case scenario, if the operating T_{pm} is 300°C, and the flux density in the direction of the PM magnetisation goes below $0.2T$, then irreversible demagnetisation occurs and the PM involved or part of it will be 'magnetically lost', in other words the demagnetised part of the PM simply becomes dead weight.

The demagnetisation analysis [130] is carried out by setting a demagnetisation proximity field B_{prox} as described in (3.2), where B_{demag} is the PM material demagnetisation value (i.e. the knee point in Figure 3.31), $\underline{M}$ is a magnetisation vector indicating the direction of magnetisation and M is the norm of the vector $\underline{M}$.

$$B_{prox} = B_{demag} - \underline{B} \cdot \underline{M}/M \tag{3.2}$$

From (3.2), a reliable demagnetisation prediction technique can be achieved. If $B_{prox} \leq 0$, then there is no risk of demagnetisation while if $B_{prox} > 0$ then there is a risk of potential demagnetisation. It can be perceived from (3.2), that the more positive B_{prox} is, then the more important (irreversible) the demagnetisation is.

Equation (3.2) can also be expressed in terms of the energy field H, as described in (3.3) whose derivation is given in Appendix A.4 and where H_{prox} is the demagnetisation proximity field in terms of H. The two fields described, can then be used to predict the possible demagnetisation of the PMs for various temperatures.

$$H_{prox} = H_{ci} - \underline{H} \cdot \underline{M}/M \tag{3.3}$$

A. Demagnetisation on no load

In a Halbach array, each complete pole is assembled out of segments that are magnetised in different directions relative to each other. The proximity of a segment to another intrinsically creates reverse magnetic fields that can demagnetise parts (usually the corners) of the segment next to it, even when under no load. The demagnetising fields are typically very strong near the corners of the PMs and these can be analysed by looking first at the radially magnetised PMs alone (not considering the axially magnetised PMs) and then at the axially magnetised PMs alone.

Figure 3.32a shows the flux distribution due to the radially magnetised PMs at no load (windings open circuit). The field highlighted by the dotted line is acting in the physical space of the axially magnetised PMs (disabled in Figure 3.32a) and thus can act as a demagnetising field for these axially magnetised PMs. The same phenomenon can be observed for the radially magnetised PMs in Figure 3.32b.

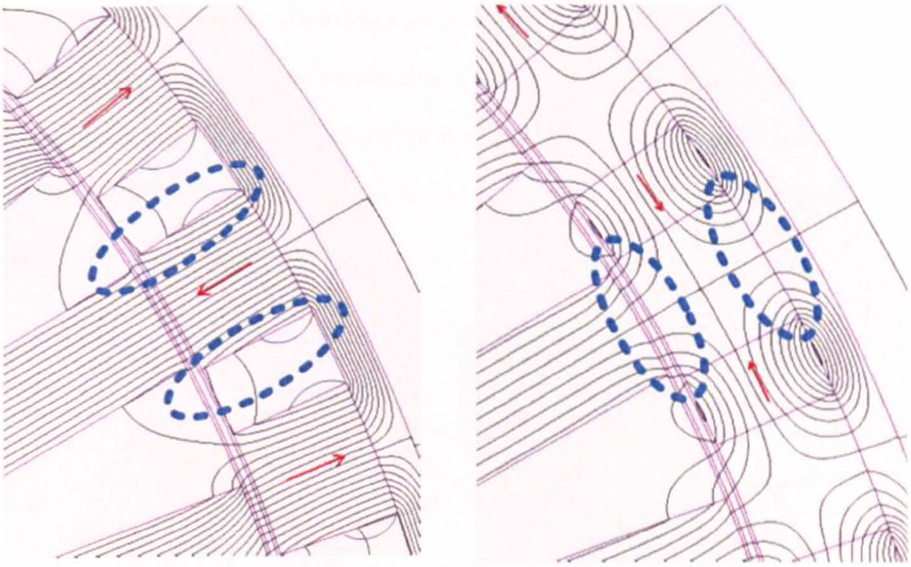

a) Field due to radial PMs b) Field due to axial PMs

Figure 3.32 Flux distributions on no load

Having illustrated the fields that are created by each set of PMs, then the no load analysis is furthered by investigating what happens when all the PMs of the Halbach array are present. Figure 3.33 and Figure 3.34 show plots taken from the FE software at different temperatures that illustrate the flux maps in the PM array vicinity. Using (3.2) and (3.3), a prediction of where demagnetisation is most likely to happen in the regions of the PMs can be achieved. The colour red is used to show complete demagnetisation.

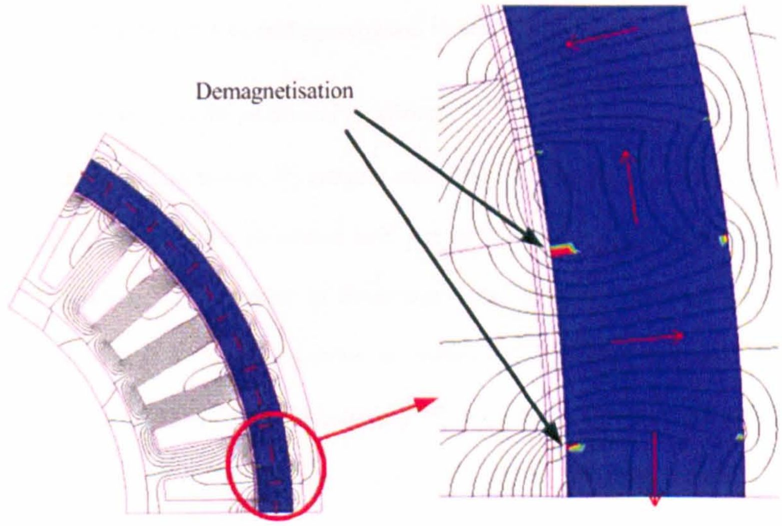

Figure 3.33 No load demagnetisation prediction at ambient temperature

Figure 3.33 illustrates the demagnetisation prediction for an ambient temperature, while Figure 3.34 predicts demagnetisation for a worst case T_{pm} of 300°*C*. Thus for the no load case, a very small, negligible demagnetisation is manifested when the motor is at ambient temperature, but for the worst case T_{pm}, it can be observed how almost one third of the axially magnetised PMs is magnetically lost.

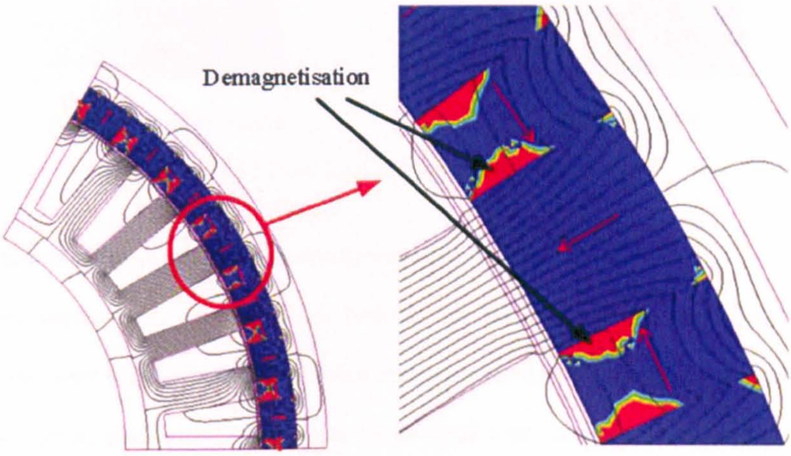

Figure 3.34 No load demagnetisation prediction at $T_{pm} = 300°C$

At this point, it is important to note that it is very improbable that the GT motor will ever be operating at 300°*C* for the obvious reason that at such a temperature, not only the PMs would be in danger of damage but also other vital components such as the windings etc… However, the above (i.e. for the max T_{pm} scenario) does indicate the general weakness of the quasi-Halbach configuration in terms of demagnetisation issues.

B. Demagnetisation analysis for peak load condition

The risk of demagnetisation is actually greatest when the machine is operating at the maximum current loading. Apart from the generated heat due to the copper losses which automatically increases the operating T_{pm}, a number of fields due to the armature windings also come in to play. This is even truer if field weakening is implemented by applying finite values of I_d current along the d-axis. However for this stage of the investigation it is assumed that the phase currents are in phase with the back-EMF. Figure 3.35a shows the demagnetisation prediction for the peak load condition assuming an ambient temperature whilst Figure 3.35b shows the same assuming a worst case T_{pm} of 300°*C*. As for the previous figures, the colour red represents the irreversibly demagnetised areas of the PMs.

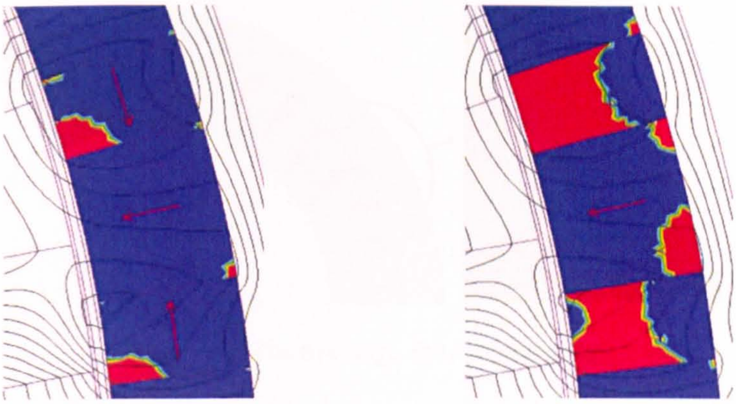

a) Ambient temperature b) $T_{pm} = 300°C$

Figure 3.35 Peak load demagnetisation prediction

C. Conclusions about quasi-Halbach demagnetisation issues

The results shown in the above figures both for the no load and the peak load condition, evidence the very elevated demagnetisation risk associated with the use of a quasi-Halbach array. Considering the Figure 3.35a results for the peak load condition at ambient temperature, the loss in PM material in the axially magnetised PMs is about 16.67%. The loss for the T_{pm} = 300°C case is approximately 16.67% for the radially magnetised PMs and a staggering 66.67% for the axially magnetised PMs. In general this means that after the first run at peak condition, the torque performance of the machine will be drastically reduced. This reveals the situation as completely unacceptable and a solution to the problem is thus investigated.

3.5.3.3 The full-Halbach array arrangement

For a quasi-Halbach array configuration such as shown in Figure 3.12b, a pole is practically made up in only three stages. This implies that the angle of the direction of the PM magnetisation changes abruptly (90° for quasi-Halbach) from one PM to its successive neighbour. As shown in Figure 3.32, this creates very strong fields which as illustrated by Figure 3.35 can be very detrimental in terms of demagnetisation of the PMs.

A. First Solution

As a solution to this problem, a five-stage, full-Halbach PM array is implemented in order to replace the quasi-Halbach version. The main reason for this is that with a full-Halbach array, the transition between the magnetisation directions of the PMs is smaller due to the increased number of stages. The concept of the five stage array is illustrated in Figure 3.36.

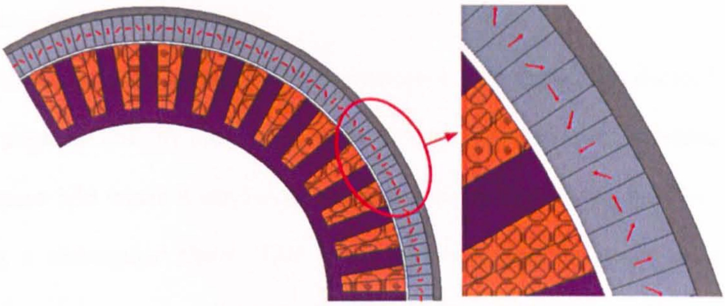

Figure 3.36 The five stage, full-Halbach array

Figure 3.37a shows the demagnetisation prediction for the no load condition assuming an ambient temperature whilst Figure 3.37b shows the same assuming a worst case T_{pm} of $300°C$. By comparing Figure 3.37b with Figure 3.34 then a considerable improvement in terms of demagnetisation risk can already be glimpsed from these no load tests. However, some demagnetisation in the top corners of the main radially magnetised PMs is still present for the worst case temperature case. As mentioned before, it is when the machine is operating at peak current load, that the risk is highest and so Figure 3.37c and Figure 3.37d show the demagnetisation prediction for the peak load condition assuming an ambient temperature and a worst case T_{pm} of $300°C$, respectively. By comparing Figure 3.37c and Figure 3.37d with Figure 3.35, it is clear that considerable improvement is obtained. However for the worst case scenario shown in Figure 3.37d, a loss of approximately 20% in the main radially magnetised PMs is predicted. This level of possible material loss is not deemed satisfactory and so further improvement procedures are investigated.

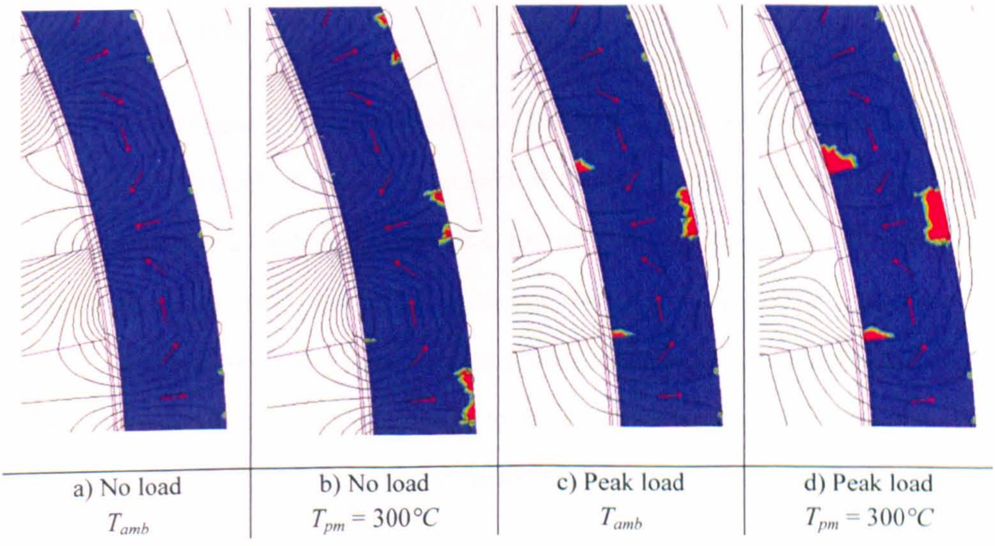

a) No load T_{amb}

b) No load $T_{pm} = 300°C$

c) Peak load T_{amb}

d) Peak load $T_{pm} = 300°C$

Figure 3.37 Full-Halbach, demagnetisation prediction

B. Improvement and practical solution

In order to reduce the continued risk of demagnetisation seen above, it is decided to physically separate the adjacent PMs by introducing small air-gaps between each individual PM. This is shown in Figure 3.38 where it can be observed how the space between the PMs results in the PMs having a rectangular shape. This is also an advantage in terms of manufacturing strategies. The square shape of the PMs reduces the amount of wasted material, limits manufacturing time and simplifies assembly procedures, thus scaling down the traditionally elevated costs of such a full-Halbach arrangement by a considerable factor.

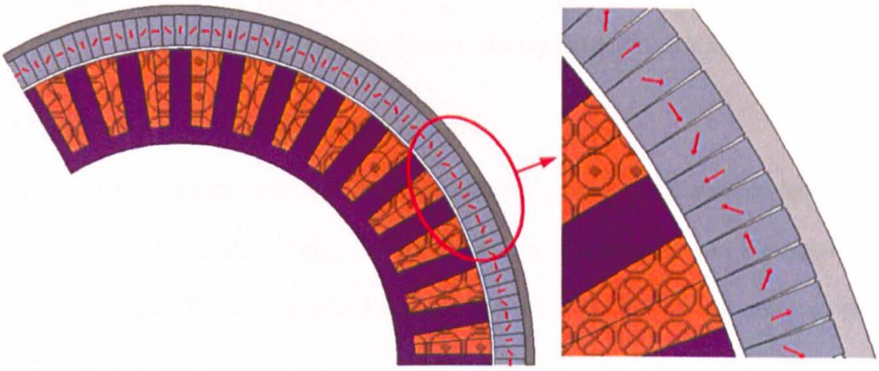

Figure 3.38 Practical solution for the full-Halbach array

The results of the demagnetisation analysis for this full-Halbach, practical solution are illustrated in Figure 3.39. As indicated, this solution represents the best performance in terms of minimisation of demagnetisation risk. The no load condition for maximum T_{pm} shown in Figure 3.39b shows the small, negligible amount of inevitable demagnetisation present in the top corners of the PMs.

Figure 3.39c and Figure 3.39d show the effects of the fields created by the armature at the peak load condition especially at the bottom corners of the main, axially magnetised PMs. This means that if during peak load conditions, the rotor of the machine ever operates at temperatures near to 300°*C*, then a small amount of material (less than 3% for each individual PM) would be lost. As a safety precaution this possible material loss is considered in the next section where comparisons with this solution to the quasi-Halbach arrangement are presented. As shown in Section 3.5.3.4, the effect of the lost material on the torque performance can be considered negligible.

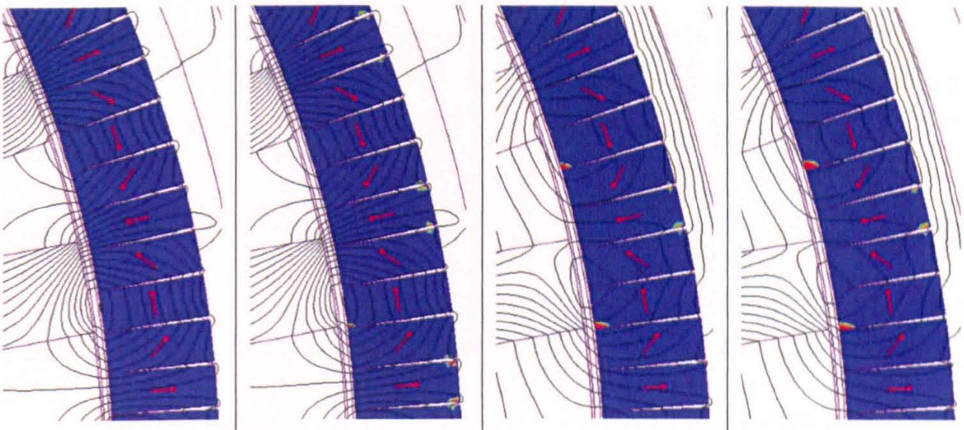

a) No load T_{amb} | b) No load $T_{pm} = 300°C$ | c) Peak load T_{amb} | d) Peak load $T_{pm} = 300°C$

Figure 3.39 Full-Halbach solution, demagnetisation prediction

3.5.3.4 Full-Halbach solution vs. quasi-Halbach

In order to confirm the performance of the more practical, full-Halbach solution in terms of the QI parameters, the FE model of Figure 3.38 is tested and compared with the quasi-Halbach model of Figure 3.26. The demagnetised corners shown in Figure 3.39d are removed from the full-Halbach model and assigned as air, so as to simulate the worst case scenario of irreversible demagnetisation of approximately 3% material from the corners of the main, axially magnetised PMs.

A. Results

Assuming a peak load J_{pk} of $36A/mm^2$ then Figure 3.40 shows the results of the comparative exercise. The generated torque of the two models is shown in Figure 3.40a, with the full-Halbach array demonstrating an improvement in the average torque reached. From Figure 3.40b, the cogging torque of the full-Halbach solution can be observed to have been reduced by approximately 50%. The full-Halbach array also results in a better quality back-EMF, shown in Figure 3.40c, which as can be observed from Figure 3.40d, for exactly the same stator, there is a slight increase in the amplitude of the fundamental. The mentioned, small, torque capability improvement seen in Figure 3.40a, can also be observed in Figure 3.40e and Figure 3.40f for higher values of J_{pk}. In terms of T_{rip}, it is shown in Figure 3.40g how the full-Halbach model gives a better performance at lower J_{pk} values. However for the peak load value of $36A/mm^2$, the two models exhibit almost identical T_{rip} values.

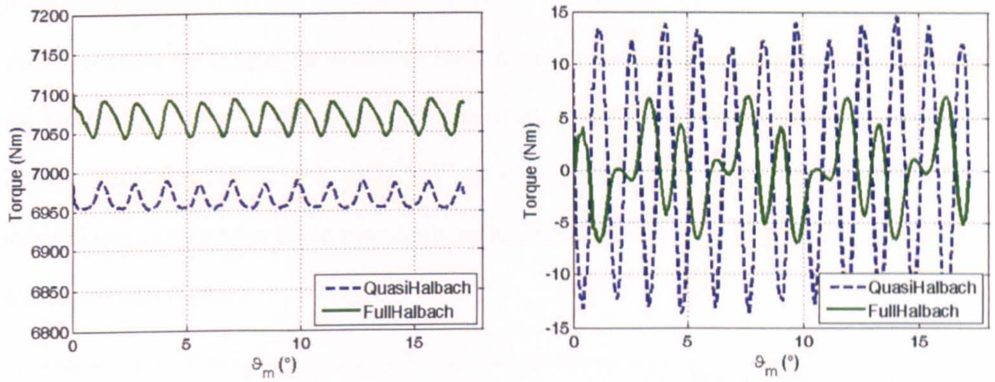

a) Torques b) Cogging torques

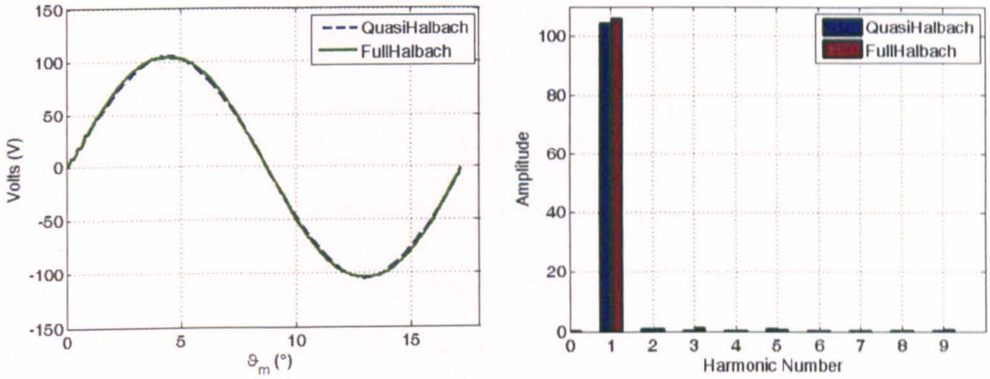

c) Back-EMFs d) FFT of Back-EMFs

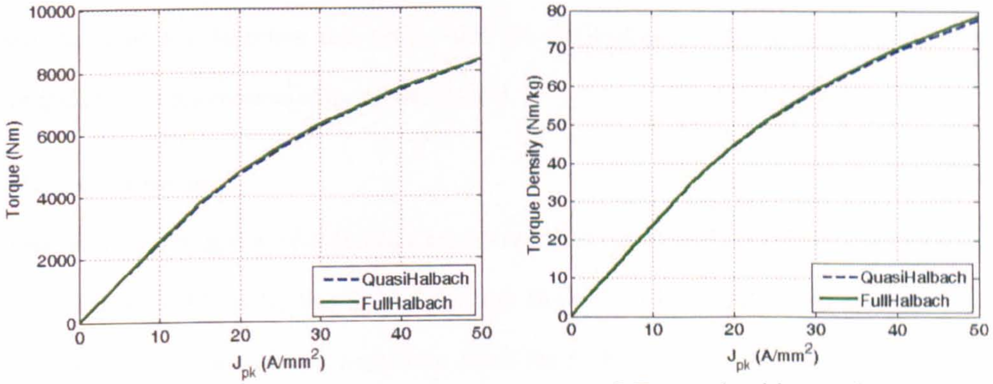

e) Torques vs. J_{pk} f) Torque densities vs. J_{pk}

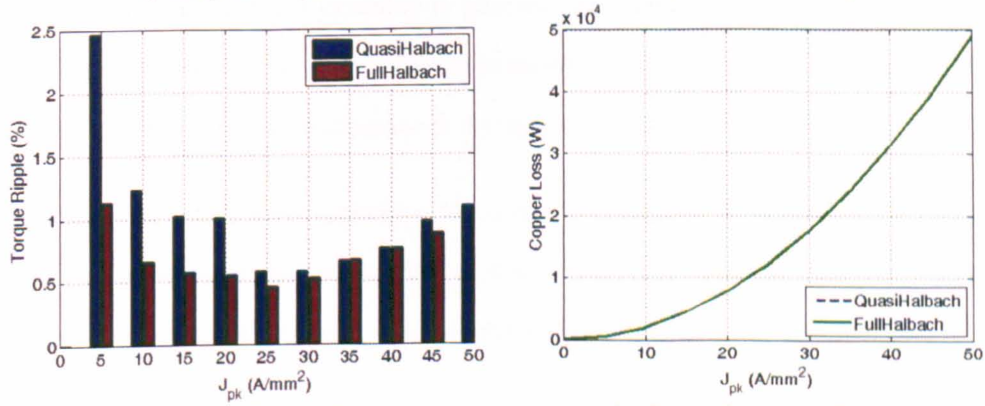

g) Torque ripples vs. J_{pk} h) Copper losses vs. J_{pk}

Figure 3.40 Quasi-Halbach vs. practical, full-Halbach performance comparisons

B. Discussion

Table 3.12 lists the torque, the total PM mass, the total machine mass, the torque density and the T_{rip} of the models for the peak load value of $J_{pk} = 36A/mm^2$, so as to illustrate clearly the improvements that can be achieved by the use of the full-Halbach array. A comparison of the material (per magnet) that could potentially suffer irreversible demagnetisation under peak load and T_{max} is also shown.

	Torque (*Nm*)	**PM mass (*kg*)**	**Mass (*kg*)**	**T_{rip} (%)**	**δ_g (kN/m^2)**	**Worst case demagnetisation (%)**	**Torque Density (*Nm/kg*)**
Quasi-Halbach	6965	33.94	106.12	0.56	173.84	66.67	65.64
Full-Halbach	7069.3	32.34	108	0.59	176.44	3	65.5

Table 3.12 Quasi vs. full-Halbach solution, comparison at $J_{pk}=36A/mm^2$

As can be seen from the above, the main improvement in terms of the QI parameters due to the use of the full-Halbach array instead of the quasi-Halbach arrangement is the that the torque capability improves by approximately 1.5%. The remaining QI parameters are all more or the less the same and therefore this proves that the full-Halbach, practical solution satisfies completely the requirements of the QI parameters.

3.5.3.5 Conclusions

Apart from the fact that the full-Halbach solution reduces and virtually nullifies the irreversible demagnetisation risk, in Section 3.5.3.4 it is also shown how a practical solution of the full-Halbach arrangement does not negatively affect the performance of the machine. In fact a slight improvement in torque capability is achieved. As mentioned before, the main issue regarding full-Halbach arrays is the difficulty in manufacturing and elevated costs, which are however somewhat mitigated with the use of the square shaped PMs, shown in Figure 3.38.

Considering the nature of the application, the necessity to achieve the required performance without demagnetisation risks dictates that such an arrangement be adopted and thus it was decided to employ the full-Halbach, practical solution for the rotor PM arrangement.

3.5.4 The electro-magnetic clutch system

For an application such as presented in Section 1.3.1, the most demanding condition that the motor must be able to withstand is probably the short time periods during which the aircraft is performing take-off or landing. During these periods (typically 40 seconds), high rotating speeds of approximately 1800*rpm* are experienced by the aircraft wheels. Due to the inherent properties of any PM motor, this could result in severe damage to the GT motor and its drive system. Acceptable values of voltages for an aerospace drive are typically in the range of 600 *V*, while stresses on the insulation of the motor and the converter should not exceed 1.6*kV/mm*. One method by which to eliminate this problem is to incorporate a mechanical clutch system that acts as a disconnecting device during take-off/landing. In this case the motor would not be rotating with the aircraft wheel and thus is not concerned with any ensuing effects. However, additional mechanical components reduce the system reliability figures and increase the overall weight which is unfavourable especially for the aerospace industry. Thus, it is decided to investigate the possibility of using an electro-magnetic clutch (EMC) system [120], which permits that the motor be directly coupled to the wheel even at high speeds. This capitulates on the fault tolerant properties of the motor and as seen below requires low values of short circuit current I_{sc} and braking torque T_{sc}.

3.5.4.1 Concept

To assess the feasibility of an EMC system during the take-off and landing stages, an analysis comprising analytical and FE methods is done on the FE model shown in Figure 3.38. Simplistically speaking, the concept is that when the aircraft wheels are rotating at high speed then all the phases are either completely open circuit, by keeping T_1 - T_6 open in Figure 3.41(showing one star), or completely short circuit (T_1, T_3 and T_5 closed in Figure 3.41).

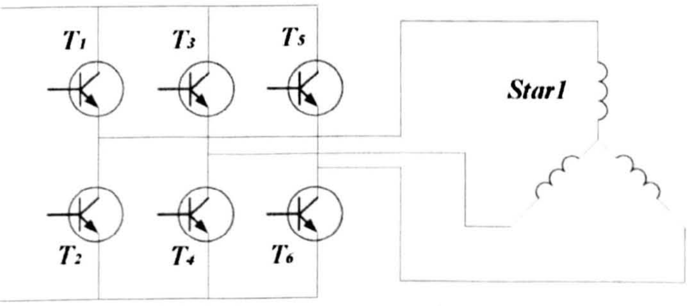

Figure 3.41 EMC concept for one star

3.5.4.2 EMC system on open circuit

The FE model of Figure 3.38 is tested with all the phases on open circuit and a rotating speed of the rotor of 1800*rpm*. With these conditions it is found that the induced voltages result in a terminal voltage across each phase of approximately 4.2*kV*. This immediately rules out the open circuit possibility as that kind of voltage would be impossible to support both from the motor and from the drive point of view. It was thus decided to focus the analysis on the short circuit arrangement.

3.5.4.3 EMC system on short circuit

In general, I_{sc} can analytically be expressed as described in (3.4), whose derivation is given in Appendix A.5 and where ϕ_m is the PM flux and L_{ph} is the self-inductance of a phase of the motor. Equation (3.4) states that as the speed increases, I_{sc} is bound to the ratio of ϕ_m to L_{ph}.

$$\lim_{\omega \to \infty} I_{sc} = \frac{\phi_m}{L_{ph}} \tag{3.4}$$

This analytical model is used to calculate how I_{sc} and T_{sc} behave with speed and Figure 3.42 shows the results. From Figure 3.42a it can be observed that a I_{sc} of approximately 160*A* per phase is predicted after the initial ramp from zero speed. The main concern with this I_{sc} is of course the resulting increase in winding temperatures. The effect of this is investigated by the thermal model of Figure 3.27 and it is shown later that the GT motor temperature still remains at acceptable levels. Figure 3.42b calculates a braking torque peak at around 11*rpm* which (peak being for such a short duration) can easily be overcome by the jets.

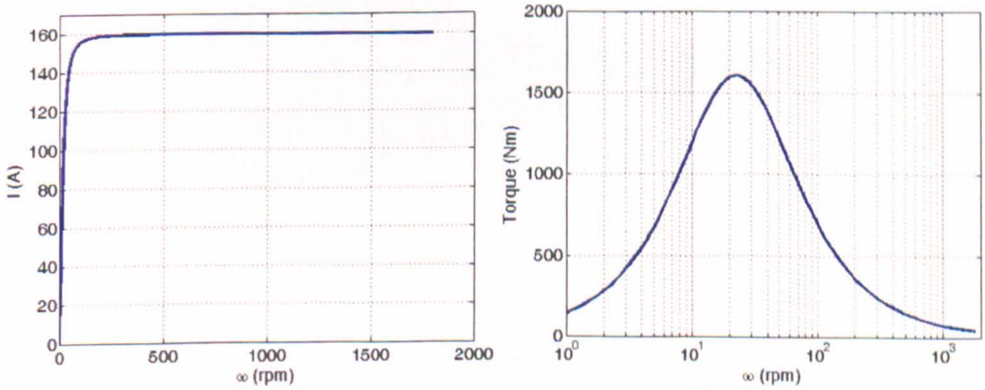

a) I_{sc} b) T_{sc}

Figure 3.42 Calculated short circuit results

The FE model of Figure 3.38 is also tested with all the phases on short circuit and a rotating speed of the rotor of 1800*rpm*. Figure 3.43 and Figure 3.44 show the FE model results for this condition, where the I_{sc} can be seen to be stabilising towards a 160*A* peak in Figure 3.43, thus almost exactly agreeing with the calculated result shown in Figure 3.42a. The braking torque at 1800*rpm* can be observed in Figure 3.44 to be gradually reducing itself towards zero which also agrees with the calculated T_{sc}.

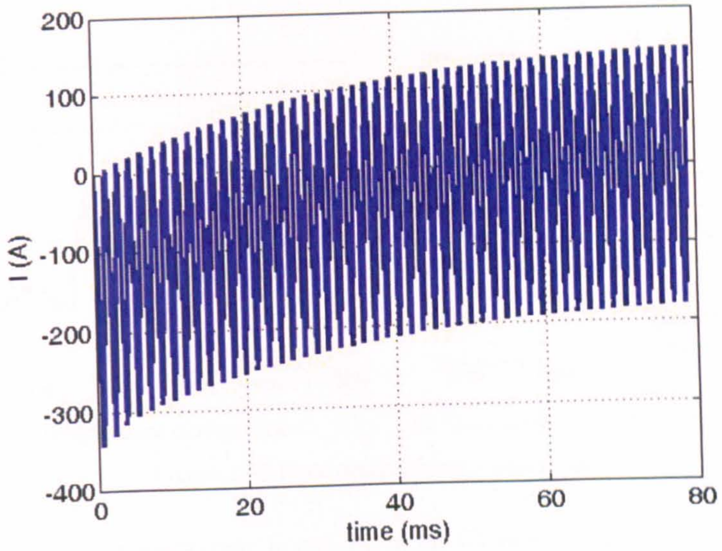

Figure 3.43 FE model: I_{sc} at 1800*rpm*

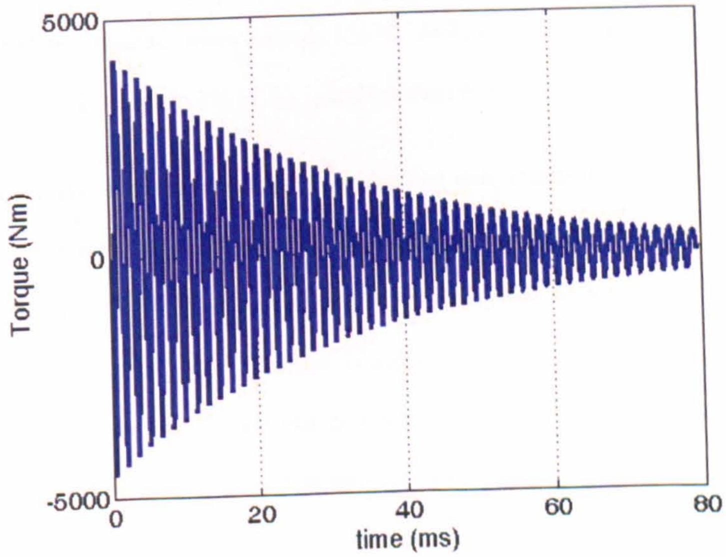

Figure 3.44 FE model: T_{sc} at 1800*rpm*

3.5.5 Thermal verification for the final design

The thermal model of Figure 3.27 is used in conjunction with the torque duty cycle requirement shown in Figure 3.20a to verify the thermal performance of the machine. The thermal model is constrained by the assumptions given in Section 2.2.1.2 and in Section 2.3.2. For the verification exercise a forced air cooling system is assumed with an air velocity V_{air} of $1 m/s$. The ambient temperature T_{amb} is assumed to be $50°C$ and at time = 0, the motor is assumed to have been idle for an extended period of time.

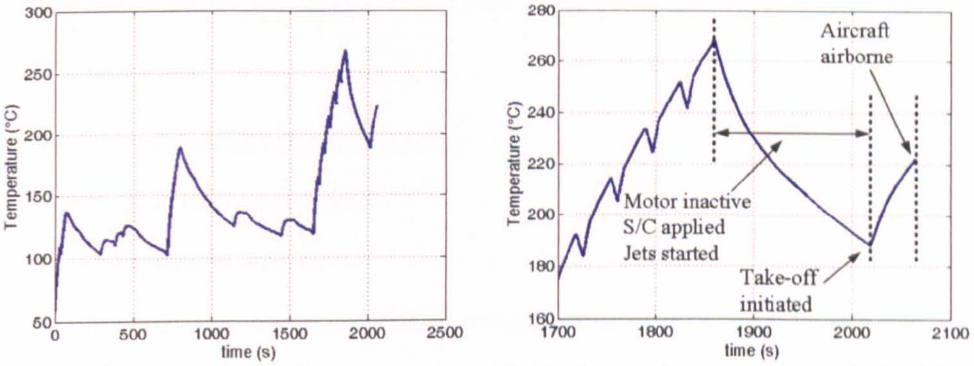

a) Slot temperature performance b) Slot temperature performance during S/C

Figure 3.45 Final design thermal performance

Figure 3.45a plots the temperature in one coil of the GT motor, over the whole required duty cycle, plus a transition period and the time required for the aircraft to take off. A zoomed view of this last part is illustrated in Figure 3.45b. It is important to note that throughout the whole cycle, the PM temperature never exceeds $150°C$, while iron losses at the maximum speed of $1800 rpm$ amount to less than 2% of P_{cu_tot} and are therefore assumed negligible.

It can be observed in Figure 3.45, how the winding temperature increases from T_{amb} until it reaches approximately $260°C$ at the end of the required duty cycle (1860 seconds). A drop of motor temperature (to $190°C$) is then registered which equates to the period of time labelled as 'Motor inactive', in which the GT motor is switched off, the phases short circuited and the aircraft jet engines started. The aircraft then starts its run-up towards take-off during which time the GT motor is in short circuit mode. The time taken for the aircraft to reach take-off speed from standstill is approximately 40 seconds. From Figure 3.45b, it can be observed that after 45 seconds of operation with the EMC on short circuit mode, the winding temperature reaches approximately $220°C$.

The results shown in Figure 3.45 demonstrate the high temperatures experienced by the stator windings. At the end of the taxi duty cycle a peak of 260°*C* is obtained. Considering the thermal limit of 220°*C* (typical class of wire insulation), then it is clear that the results exceed this limit. A solution to this problem and comparisons between Figure 3.45 and the results of the proposed solution is investigated later in Section 4.5.2.

3.6 Conclusion

From the investigational studies outlined and presented above, it is decided that the final machine chosen for the GT application is a PM, BLAC motor that comprises the following features

1) A single air-gap, radial configuration
2) An outer rotor arrangement
3) CoFe stator laminations
4) A double layer, double star winding arrangement with one converter for each star
5) A full-Halbach arrangement in a practical configuration

A. The final design

The FE model for such a machine is shown in Figure 3.38, where all the above features can be observed. The results of this final model can be observed in Figure 3.40 (for the plots labelled as full-Halbach), Table 3.12 and Figure 3.43 - Figure 3.45, so it is unnecessary to repeat them in this concluding section. However for the sake of clarity and for completeness, the main specifications used for the model as obtained through the design procedures outlined in the previous sections are listed in Table 3.13, where A_{rms} and J_{pk} are the values at which the peak load requirement is achieved and the volume recorded only considers l_{ax} (i.e. not the space required for the end windings).

Slots/Poles	36/42
l_{ax} ***(mm)***	151
R_e ***(mm)***	231.5
L_g ***(mm)***	2
N	33

Active mass (*kg*)	108
Active volume (m^3)	0.0254
T_{amb} **(°C)**	50
A_{rms} ***(kA/m)***	189.631
J_{pk} ***(A/mm²)***	36

Table 3.13 GT motor final model data

B. Performance

The performance capability of the modelled, GT motor, at the load values given in Table 3.13 is presented in tabulated form in Table 3.14, where it can be observed that the main requirement of a peak load torque of 7*kNm* is achieved while respecting the spatial limits set by the FrEnv and also respecting the thermal and demagnetisation limits of the motor.

Mean of generated torque at peak load condition (*Nm*)	7069.3
Peak of cogging torque (*Nm*)	7.06
δ_g at peak load condition (kN/m^2)	176.44
T_{rip} at peak load condition (%)	0.59
P_{cu_tot} at peak load condition (*kW*)	25.31
Torque density at peak load condition (*Nm/kg*)	65.5
Torque density at peak load condition (kNm/m^3)	278.32

Table 3.14 GT motor final model performance chart

C. Conclusion

In this chapter, the evolution of the GT motor from the first concepts and ideas to the present, final design of the first prototype is presented. Exhaustive and in detail procedures on the design and modelling of the GT motor are given, highlighting the efforts made to improve the electro-magnetic limit of the machine. This is achieved by combining performance enhancing strategies such as the use of an outer rotor, the use of CoFe laminations and the adoption of a high performance stator arrangement (double star, double layer winding layout) into a structured methodology, that details the achieved improvements step by step. A main point to highlight is the PM demagnetisation analysis illustrated in Section 3.5.3, which resulted in achieving an optimum arrangement of the full-Halbach array used.

The final results presented in this final section of the chapter, show the excellent performance achievable by the motor in question. From Table 3.14, it can be observed that the application requirements of Table 3.1 for the FrEnv have already been reached. As discussed later in Section 6.2.3, to the author's knowledge, no such torque density values have ever been published for a DD, stand-alone, electrical machine. The final thought given in Part C of Section 2.5 also holds for the GT motor, where obviously the assumed variable V_{air} replaces the assumed variable V_{wat} of Section 2.5.

Chapter 4
The Thermal Management Technique

In electrical machines, a higher torque/force density can usually be achieved by increasing the current density in the windings. However, the resulting increase in copper losses leads to higher temperatures in the coils, especially in the centre of the slots where the thermal resistance to the ambient/cooling surfaces is highest.

In this chapter a novel technique [17, 47] is presented in which a higher thermal conductivity path between the centre of the slot and the cooling arrangement is created, thus increasing the heat flow away from the slot centre. Lumped parameter thermal models are built and used along with FE analysis to investigate the effectiveness of the proposed technique. The lumped parameter models are also used for optimizing the high conductivity path for maximum air-gap shear stress and to obtain a compromise between the reduced slot area and the improved temperature distribution.

This chapter is thus concerned with proposing and investigating an innovative way to improve and extend the thermal limit of electrical machines. The technique is first presented in terms of the TLPM motor of Chapter 2 with its stator jacket arrangement and then also applied to the GT motor and its forced air cooling arrangement. The advantages gained by the implementation of this technique are compared and presented, with main focus being on the reduction of hot-spot temperatures in the windings of the machines.

4.1 Introduction

In general, the need for improvement in terms of size, efficiency and costs of electrical machines is a main issue which electrical machine designers have to consider through all the design stages. This is especially true for aerospace applications such as presented in Section 1.2.1 and Section 1.3.1, where torque/force density, fault tolerance and reliability are of vital importance.

Despite the vastness of the range of electrical machines available today, in general all machines are subject to the constraints imposed by the materials (copper, insulation, soft and hard magnetic materials) from which their main components are constructed [46]. The constraints can be considered to fall into two main categories, namely the electro-magnetic limit and the thermal limit. These two limits quantify what force/torque can be obtained from a particular machine.

In the previous chapters, the main focus has been on the optimisation of the electro-magnetic limit (and how to maximise it), however it was also seen how the thermal limit which is related to the cooling arrangement sets the maximum J_{pk} at which a machine can operate safely. In steady state, this limit typically lies below the electro-magnetic limit and hence extending the thermal limit by adequate cooling automatically results in machines that can operate at higher current loadings, thus achieving a higher torque/force for the same machine mass.

As mentioned in Section 2.3, a convenient way to improve the thermal limit through fluid cooling for electrical machines is by the use of stator jackets such as shown in Figure 2.7. This is however a non-optimal way of heat removal as a considerable temperature gradient exists between the outer stator surface and the winding hot-spots in the centre of the slots and in the end-windings. To this end, direct cooling solutions can be adopted such as oil-spray cooling [131] and directly cooled conductors [132], however, the complexity of such arrangements is only justifiable in large machines. An effective method to achieve better temperature distribution in the slots is to introduce a low thermal resistance path between the winding hot-spots and the cooling arrangement.

4.2 Concept of the thermal improvement technique

Considering the TLPM motor of Figure 2.3, then as for any other electrical machine, it can be stated that temperature builds up mostly towards the centre of the slot as this is the point where the thermal resistance to the ambient/cooling fluid is highest.

Figure 4.1a illustrates a slot of the previously designed, TLPM motor, where the total copper area dependant on K_{fill}, can generally reach high values (>0.6) for pre-formed coils [52]. In between the individual conductors, there is usually some type of varnish or potting compound to provide mechanical integrity, adequate insulation, an improved thermal conductivity and protection against ingress of foreign particles. A slot wall liner is also often required to provide insulation to ground unless suitably thick, conductor wire insulation is adopted.

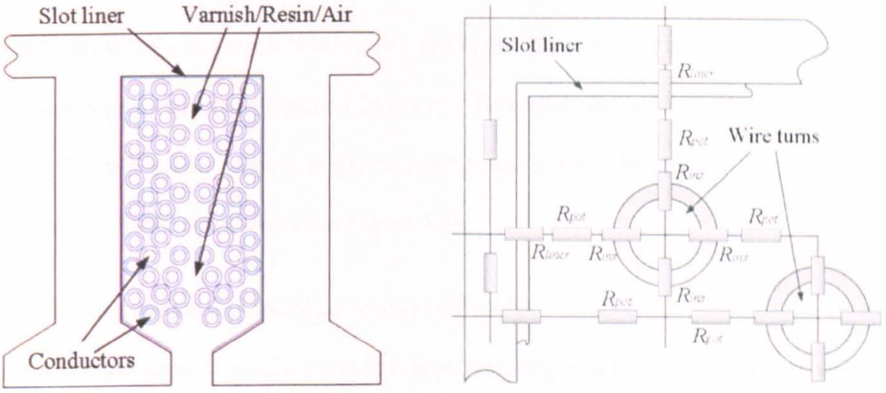

a) Typical motor slot

b) Representative thermal reluctance network

Figure 4.1 The TLPM motor slot area

As illustrated in the representative thermal resistance network of Figure 4.1b, where R_{pot}, R_{ins} and R_{liner} represent the thermal resistances of the potting compound, the copper insulation and the slot liner respectively, the total effective thermal resistance to the conductors' P_{cu} can be quite significant, especially in the central slot section which leads to winding hot-spots. This can result in a k_{eq} that is relatively poor compared to that of copper k_{cu}.

However, by inserting a heat flow path (HP) such as shown in Figure 4.2a, the thermal resistance of the dominant heat conduction path is reduced. This achieves an enhanced k_{eq} from the centre of the slot towards the outer walls, which should result in a better distribution of heat over the slot area and also in an overall reduction of peak hot-spot temperatures.

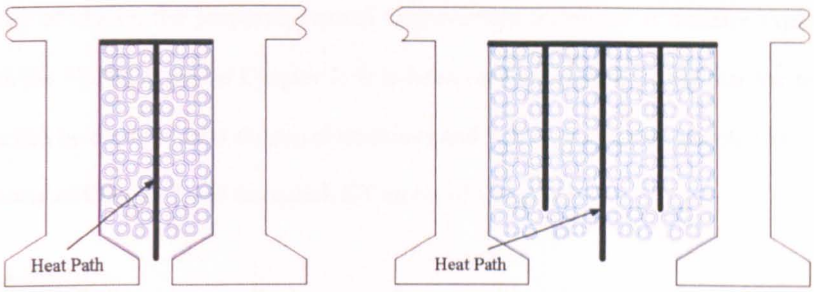

a) HP for TLPM motor slot b) HP for wide, shallow slots

Figure 4.2 Proposed HPs

The conceptual geometry shown in Figure 4.2a, is proposed taking into account the geometry of the TLPM motor of Chapter 2. As shown further on, the narrow, deep nature of the slots of this particular machine results in the HP having a large effect on the thermal performance of the machine due to the large, relative distance of the hot-spot from the back iron. For machines with a considerable T_{sl} and small relative slot depth, the effect of the HP will be less significant if the same design as shown in Figure 4.2a is kept. Therefore, for configurations with large slot width to slot depth aspect ratios it might be appropriate to consider an alternative design such as the multi-finned HP shape shown in Figure 4.2b.

The negative implications of introducing this path, whose structural definitions are shown in Figure 4.3, are the smaller winding window area, resulting in a higher winding resistance and consequently higher copper losses for the same electrical loading at a given temperature and any additional eddy current losses in the HP itself. The material to be used for the heat flow path ideally needs to have a high thermal conductivity and a low effective electrical conductivity. This can be easily achieved through segmentation.

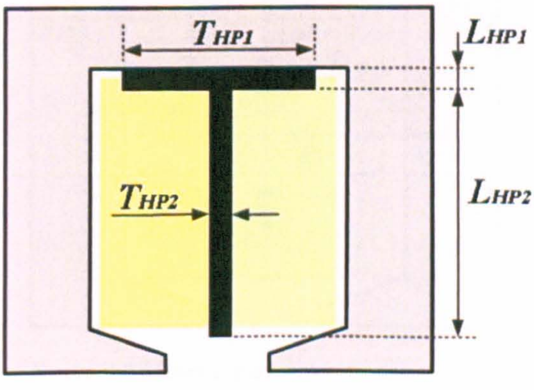

Figure 4.3 Structural definitions of the HP

For reasons of clarity, the proposed thermal improvement technique is initially explained in relation to the TLPM motor of Chapter 2. It is however important to stress that the proposed technique can be used for most electrical machines and will be eventually adopted for both the tubular motor of Chapter 2 and the radial, GT motor of Chapter 3.

4.3 Modelling

Lumped parameter, thermal network models of one slot pitch of the TLPM motor are built, one without the HP (as original) and one with the HP. The models are intended to be used at the design stage where geometric iteration is made. A FE model is also constructed for comparison and to justify the assumptions made.

4.3.1 Lumped parameter model without HP

The lumped parameter model shown in Figure 2.9 is used in conjunction with the temperature analysis presented in Appendix B.2.2, to quickly estimate the temperature distribution in one slot pitch section of the TLPM motor without a HP. The analysis is constrained with the assumptions listed in Section 2.3.2 and Section 2.2.1.2. As a first approximation, the hot-spots are assumed to be at the central nodes at height R_{hc} and K_{fill} is assumed as 0.5. A more accurate temperature distribution can be achieved simply by including more nodes in the network.

4.3.2 Lumped parameter model with HP

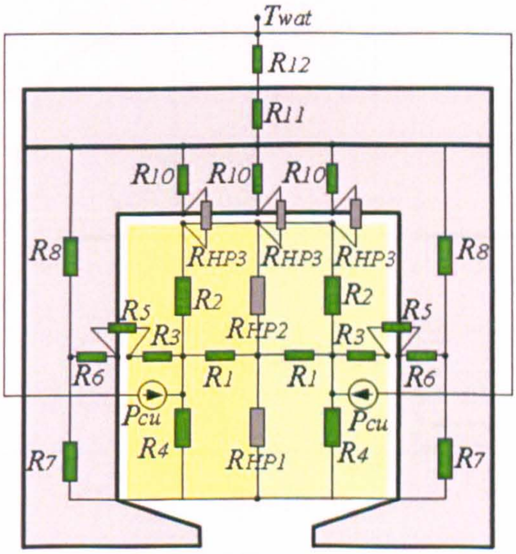

Figure 4.4 Lumped parameter model with HP

The thermal improvement technique involves the insertion of a piece of thermal conductive material (the HP shown in Figure 4.3) into the slot. The resulting lumped parameter network is shown in Figure 4.4, where it can be seen that R_{HP1}, R_{HP2} and R_{HP3} represent the HP itself. The thermal resistances of the model are given in Appendix B.2.3.

4.3.3 Initial verification exercise

Assuming a high thermal conductivity of the HP, then from Figure 4.4 it is clear that a low thermal resistance path has been created along the centre of the slot. The HP is practically acting as a thermal 'short-circuit', through which the heat generated by the copper losses is encouraged to flow towards the stator cooling arrangement.

Initial verification tests to confirm the general effectiveness of this technique are done. The two models of Figure 2.9 and Figure 4.4 are tested considering the P_{cu_tot} of the TLPM motor at steady state, for a constant thrust force (i.e. equal linear A_{rms} and J_{pk}) as shown in Figure 2.18a. For Figure 4.4 an initial design of $T_{HP2} \approx 0.1T_{sl}$ and $L_{HP2} = (R_t - R_{in})$ is considered. Figure 4.5 compares the results, where it is immediately clear that the peak hot-spot temperature in the winding has decreased considerably (≈110°C compared to ≈180°C), thus confirming the effectiveness of this technique in terms of peak slot temperature reduction.

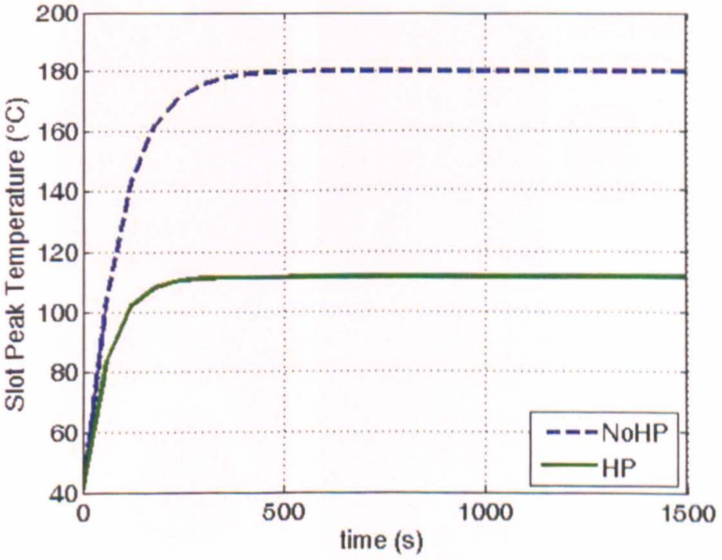

Figure 4.5 Analytical models: first comparisons

4.3.4 FE modelling

A more accurate approach to thermal modelling of the slot area is achieved using numerical methods. An electro-magnetic/thermal FE software package is used to model the slot of the TLPM motor. The same conditions and assumptions as used to obtain the results of Figure 4.5 are applied to the FE models. The slot area (assuming same K_{fill} as above) is modelled as one piece of conducting material (copper) with k_{eq} as calculated using (B.17). A thermal boundary dependant on h_{cv} as derived from (B.14) and with the same initial temperature as above is applied at the ducts of the water jacket.

Figure 4.6 compares the slot temperature distribution for the model with and without the HP, at a steady state condition. It is worth noting that apart from the lower peak slot temperature and the more even temperature distribution, the temperature in the back iron and housing are also lower, when the HP is present. This reflects the lower P_{cu_tot} due to the reduced net winding temperature. Figure 4.7 compares the peak temperatures from the lumped parameter network models with those of the FE models. The results from both models show a reasonable similarity which validates the analytical model, again confirming the effectiveness of the HP in the slot.

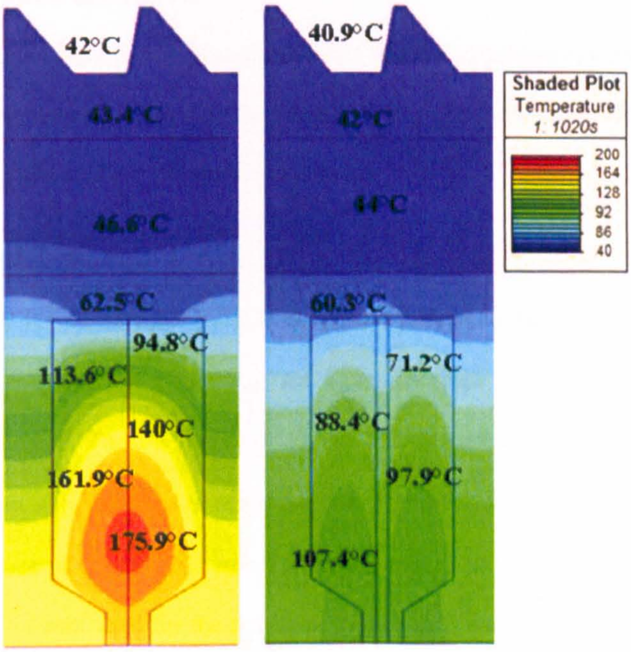

Figure 4.6 FE models: First comparisons

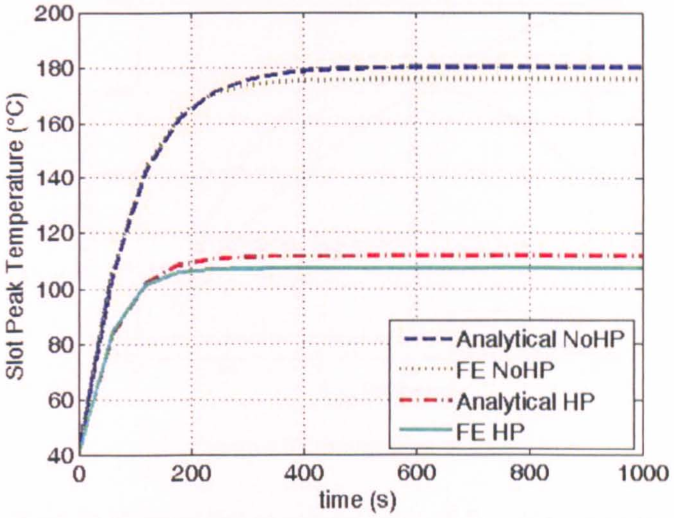

Figure 4.7 Analytical vs. FE models: First comparisons

4.4 Design and optimisation

The results shown in Figure 4.5 - Figure 4.7 confirm that a thermal improvement does occur with the insertion of the HP in the slot. A combination of FE and analytical models is then used to investigate various designs of the shape and thickness of the HP, in an attempt to optimize to the most effective geometry.

4.4.1 Geometry and dimensions

Considering Figure 4.2a, it can be visually deduced that the parameter that has the main effect on the thermal performance is the HP thickness T_{HP2} which results in a trade-off between the winding area available and the HP thermal resistance.

4.4.1.1 The HP thickness T_{HP2}

In general, the thicker the HP, the lower is its thermal resistance. However a thicker HP takes up more space, thus increasing the P_{cu}. An optimum value exists and is selected by an optimisation procedure. The FE model of Figure 2.17 is tested for various values of T_{HP2}, where for each test J_{pk} is adjusted to achieve a peak hot-spot temperature in the slot of 180°C. Due to the presence of the HP, this safe T_{max} is maintained with values of J_{pk} that are much higher than the $16A/mm^2$ used for the results of Figure 2.18 and therefore P_{cu_tot} is also much higher. Figure 4.8 plots the TLPM motor generated output force and P_{cu_tot} for increasing values of the thickness of T_{HP2}, for a constant $T_{sl} = 11.35mm$.

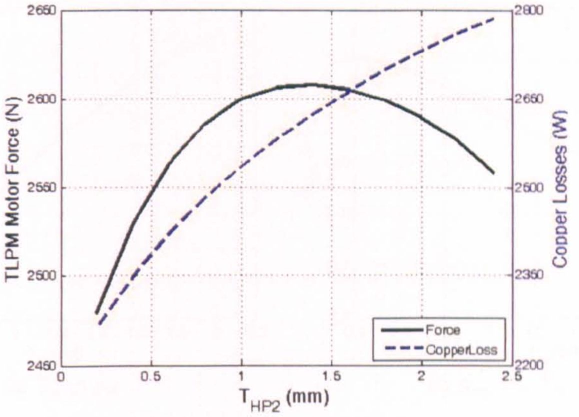

Figure 4.8 Optimisation of T_{HP2}

In Figure 4.8, it can be observed that an optimal value of T_{HP2} of approximately 1.2mm exists. As mentioned, the generated F_{lin} is increasing, because the thicker HP is permitting higher current loadings to be used. Beyond the optimal value, the increasing copper losses due to the reducing copper area result in a reduction in the current density allowed for the T_{max} = 180°C constraint and F_{lin} starts decreasing again.

In an effort to understand the optimal HP thickness as a function of the slot width, a study of the relationship between the optimal T_{HP2} and T_{sl} is conducted. The analytical model is used to find the optimum value of T_{HP2} that results in the maximum current loading possible whilst still 'respecting' the T_{max} limit, for different values of T_{sl}. Figure 4.9a shows the resulting relationship in a per-unit system, where the optimal T_{sl} as found in Chapter 2 is taken as 1*pu*. It can be observed how for relatively small slot width values, the optimal T_{HP2} exhibits a linear increase relative to T_{sl}. As T_{sl} increases (for the same slot height) the relative impact of the HP decreases and the radial heat transfer path through the conductors and resin to the back iron becomes more dominant.

This relationship between T_{HP2} and T_{sl}, also has a direct effect on the maximum permissible A_{rms} (and consequently δ_g) that can be used. Using the results of Figure 4.9a, the respective current loadings are plotted in *pu* values in Figure 4.9b, where A_{rms} is taken as 1*pu* when T_{sl} = 1*pu*. It can be observed that as T_{sl} increases, and for an optimum HP width, the maximum A_{rms} achievable, exhibits decay and does not remain constant. In essence this points to an alternative HP configuration along the lines of the one shown in Figure 4.2b.

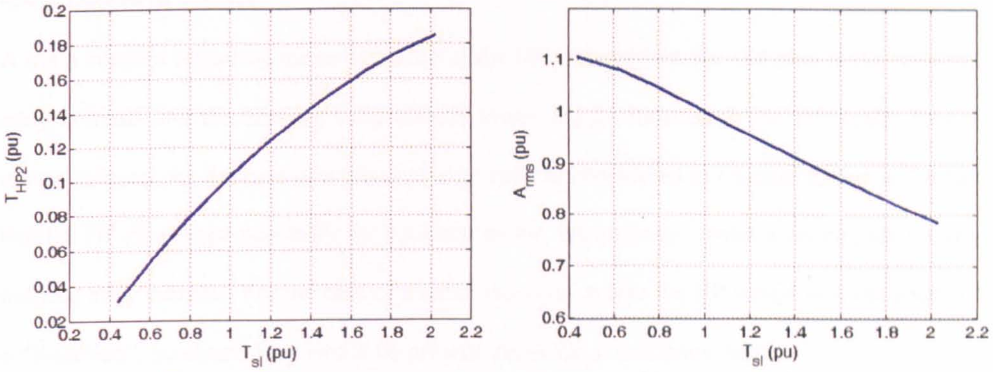

a) T_{HP2} vs. T_{sl} in *pu* b) A_{rms} vs. T_{sl} in *pu*

Figure 4.9 Optimisation of T_{HP2} relative to T_{sl}

4.4.1.2 The HP length L_{HP2}

Considering Figure 4.3 and Figure 4.4, it can be observed that optimisation of the HP length L_{HP2} resides in the fact that it need only be long enough to 'thermally short-circuit' the point of the highest peak temperature with the stator back iron at R_t. A visual observation of the slot temperature distribution shown in Figure 4.6, illustrates that the main hot-spot of the winding is located at approximately half way between R_{hc} and R_{tipa}. Thus setting L_{HP2} to approximately $\frac{3}{4}(R_t - R_{in})$, one can theoretically achieve the required thermal improvement whilst minimizing the loss of copper area. However, if this theoretical optimal length is applied, in practice it will not result in any relative advantages as the pre-formed coil window would still have the same dimensions, irrespective of L_{HP2} (the optimal thickness $T_{HP2} \approx 1mm$). Considering the above, then the length L_{HP2} is taken as (R_t - R_{in}), i.e. the whole slot depth.

4.4.1.3 The dimensions T_{HP1} and L_{HP1}

From Figure 4.6, it can be observed how the thickness L_{HP1} and the span T_{HP1} are reduced to zero. This is because theoretically these two HP dimensions do not have any significant effect on the reduction of the dominant thermal resistance. But in practice one needs as much surface area as possible to be in contact with the inside of the slot wall at R_t, thus finite values of these two parameters need to be set. The main consideration here is to achieve maximum contact between the surface of the HP and the slot wall at R_t, whilst keeping the material volume to a minimum. By practical experiment, optimum values are found to be $T_{HP1} = T_{sl}$ and $L_{HP1} \approx \frac{1}{2}T_{HP2}$, thus achieving a reliable contact area and overall robustness of the HP.

4.4.2 Losses in the HP

A main concern regarding the solid nature of the HP inserted into the slot area is the resulting eddy currents and the ensuing eddy current losses P_{ed_HP}, induced in the HP itself. This is mostly relevant for the case of a tubular motor such as considered in Chapter 2, due to the fact that the HP ring shape necessary for a tubular motor, intrinsically creates a return path for any induced eddy currents. For the case of a radial machine, where the HP would take the shape of a "T-section", no closed loop would be present, resulting in minimum losses.

A. Loss verification

For a ring shaped HP such as shown in Figure 4.11a, the P_{ed_HP} is mainly generated due to the same flux that links the windings, which is made up of the magnet flux and the armature flux. These losses can be described by (5.1) where Ψ_{HP} is the flux linked by the HP, ρ_{Al} is the electrical resistivity of the HP material and L_{HP} and A_{HP} are the mean circumference and the cross-sectional area of the HP respectively.

$$P_{ed\_HP} = \frac{A_{HP}(\Psi_{HP} \times \omega_{el})^2}{\rho_{AL} \times L_{HP}} \tag{5.1}$$

Assuming the same conditions taken to achieve the results of Figure 4.6, the FE model is used to investigate these eddy currents effects. Figure 4.10 compares the P_{ed_HP} induced in one HP for two synchronous frequencies for the maximum, permissible J_{pk}. By comparison to Figure 4.8, it is clear that P_{ed_HP} is considerably high, especially for higher values of f_s. In practice, this would almost completely nullify the thermal advantage gained by the insertion of the HP.

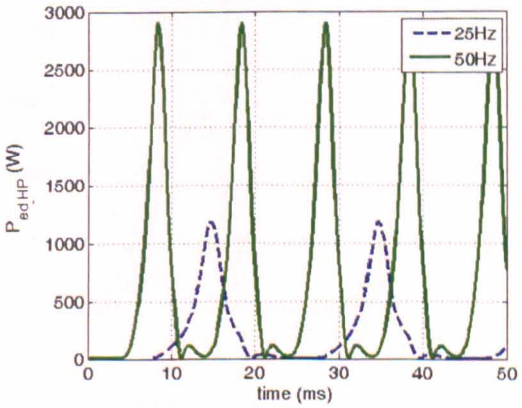

Figure 4.10 P_{ed_HP} at full load

B. Proposed solution

This loss can however be drastically reduced by 'opening' the conductive path travelled by these eddy currents. This can be achieved by the use of slitting in the HPs. An investigation on this approach is conducted. A single slot set-up is modelled in 3D for different slitting configurations and the results compared.

Figure 4.11 shows the proposed HPs and highlights the modifications implemented. Figure 4.11a shows the original HP as a solid ring of aluminium, implemented for the tests highlighted in Section 4.3 and Section 4.4.1. The variation HP2 shown in Figure 4.11b incorporates slitting that completely 'cuts' or 'opens' the flux path. The last proposed HP3 shown in Figure 4.11c has only a partial cut, i.e. the slit does not open circuit the eddy currents path completely. Such a configuration as shown in Figure 4.11c would greatly facilitate manufacturing procedures and maintain a good level of robustness. It is important to note that for reasons of clarity and visualisation, the slits are shown much larger than what is required in practice.


a) HP1: Solid b) HP2: Slit c) HP3: Partial slit

Figure 4.11 Proposed HPs for P_{ed_HP} reduction

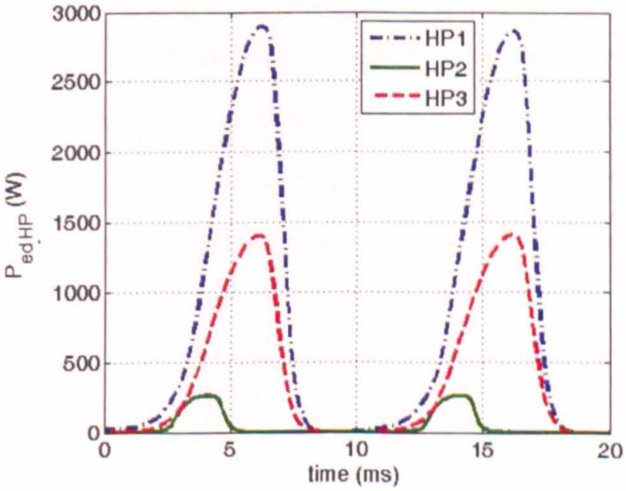

Figure 4.12 Minimisation of P_{ed_HP} via slitting

The different HP models are tested with similar conditions being kept for each test. Figure 4.12 compares the P_{ed_HP} for the proposed HPs at 50Hz, showing the effectiveness of the slitting method to reduce the flow of eddy currents. Minimum losses are obviously achieved when the slits open circuit the current flow path completely such as in the model HP2. A combination of one 'complete' slit and two 'non-complete' slits is therefore suggested, resulting in good mechanical robustness, high thermal properties and low P_{ed_HP}.

4.5 Implementation of the technique

In this section, the thermal management technique is implemented on the motors presented and designed in Chapter 2 - Chapter 3 in order to achieve an understanding of the potential advantages that can be gained by its utilisation.

4.5.1 The TLPM motor

The concept and the analytical/simulation validation of the thermal management technique have been presented in the previous sections, relative to the TLPM motor of Chapter 2. This means that the procedure to implement such a technique on the TLPM motor has automatically already been outlined. In fact, the improvement in terms of thermal behaviour that results from the implementation of the HP is shown in Figure 4.5 - Figure 4.7. Therefore, in this section only a brief re-cap of the implementation procedure is given, after which the resulting advantages in terms of the QI parameters of Section 2.2 are illustrated.

A. Design

The final model results of the TLPM motor without the HP are presented in Figure 2.18 and Table 2.5. Using the optimisation procedures presented in Section 4.4, an optimal shape, geometry and composition for the HP is found. The FE model shown in Figure 2.17 is then equipped with such an HP and this is represented in Figure 4.13. The thermal model of Figure 4.4 is used to identify the maximum J_{pk} that satisfies the thermal limit of 180°C and the TLPM motor model is run at this new current loading value. The main geometrical dimensions of the TLPM motor are given in Table 2.4, while the optimal dimensions of the implemented HP are given below in Table 4.1.

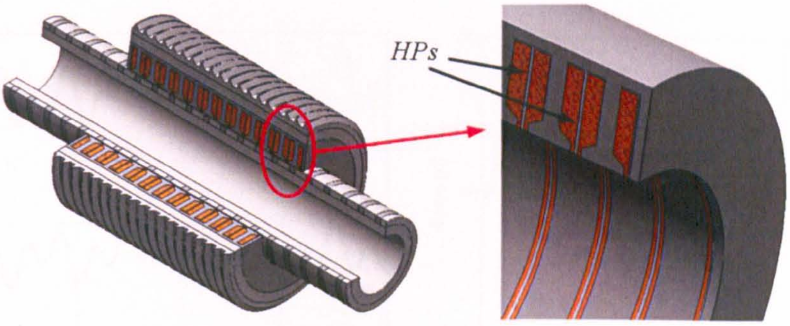

Figure 4.13 TLPM motor: final FE model with HPs

T_{HP1} (mm)	11.35
T_{HP2} (mm)	1
L_{HP1} (mm)	0.5
L_{HP2} (mm)	23.95

Table 4.1 TLPM motor: optimal HP dimensions

B. Results and discussion

Figure 4.14 compares the performance of the TLPM motor without the HP (at $J_{pk} = 16A/mm^2$ as given in Figure 2.18) with the results of when the HP is implemented (at $J_{pk} = 25A/mm^2$ as found from Figure 4.4).

The force capability of the two models is compared in Figure 4.14a, where the effect of the higher electric loading due to the insertion of the HP can be easily observed. The HP implementation has little or no effect on F_{cog} and on the back-EMF quality, as shown in Figure 4.14b, and Figure 4.14c – Figure 4.14d respectively.

Figure 4.14e shows a slightly lower force capability for the HP model which is mainly due to the P_{ed_HP} effect, however this is important only for higher J_{pk} values that exceed the rated values of the application. Figure 4.14e also illustrates the different operating points of the machine (according to the thermal limitation of T_{max}). As explained previously, when the HP is implemented, the TLPM motor operates safely at a $J_{pk} = 25A/mm^2$. The reduced force capability due to the P_{ed_HP} gives rise to the results shown in Figure 4.14f, which also shows that the reduced performance is only important for higher values of J_{pk}.

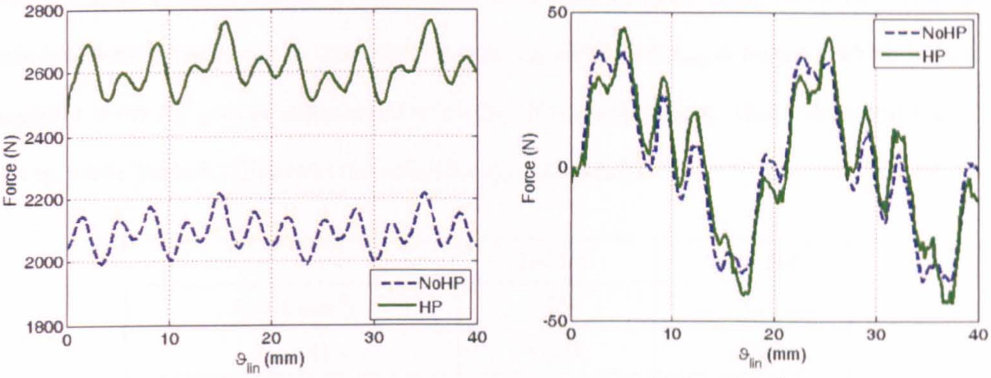

a) Force b) Cogging force

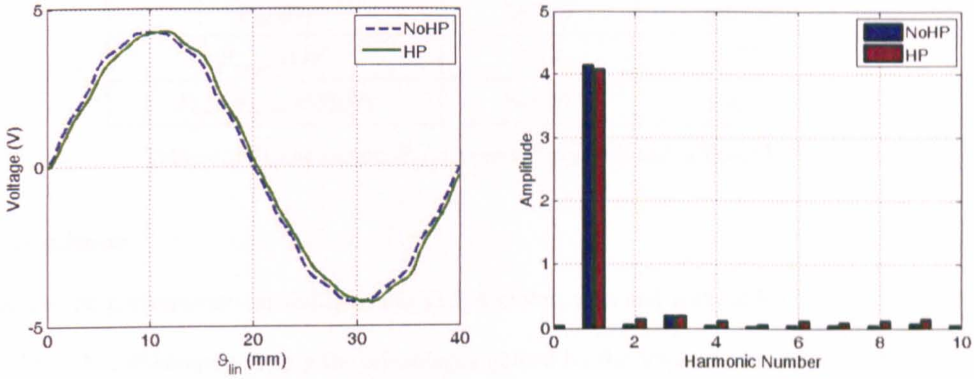

c) Back-EMF d) FFT of Back-EMF

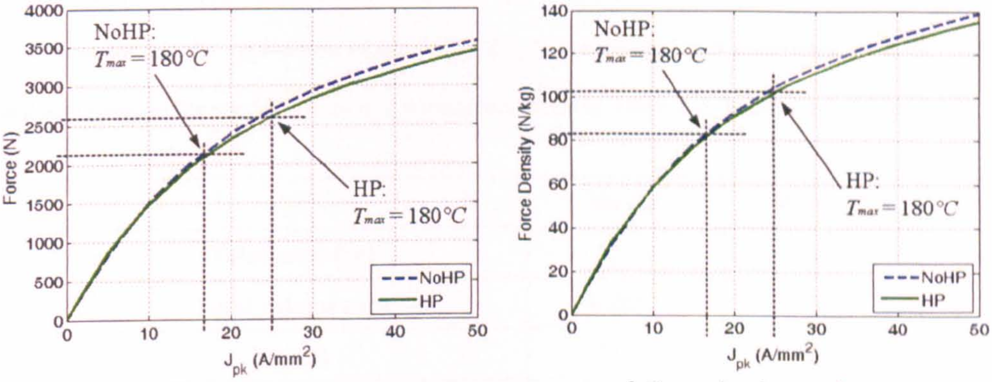

e) Force vs. J_{pk} f) Force density vs. J_{pk}

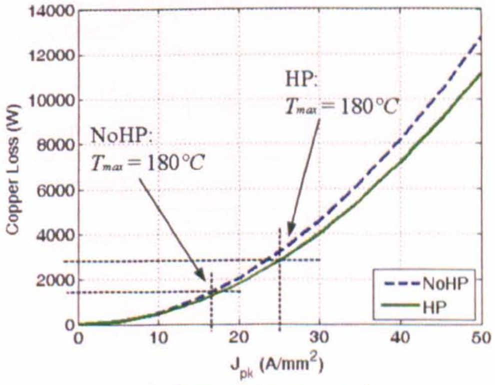

g) Copper losses vs. J_{pk}

Figure 4.14 TLPM motor: performance with and without HP

Another issue of the technique is that the HP itself takes up space from the normal winding window, which means that to maintain the same J_{pk}, a reduced A_{rms} is required which in turn means a lower P_{cu_tot} to be experienced when the HP is implemented. This is shown in Figure 4.14g, while Table 4.2 illustrates this effect for $J_{pk} = 25A/mm^2$.

	No HP	With HP
J_{pk} (A/mm^2)	25	25
I_{rms} (A)	48.54	42.65
A_{rms} (kA/m)	134.1	117.82
F_{lin} (N)	2690.5	2607.8
P_{cu_tot} (kW)	3.18	2.78
F_{lin} / P_{cu_tot} (N/kW)	846.07	936.4

Table 4.2 TLPM motor: P_{cu_tot} comparison with and without HP

C. Conclusion

The overall performance capability of the TLPM motor, with and without the HP is presented in Table 4.3, illustrating clearly the advantages gained by the implementation of the thermal management technique for the TLPM motor. Considering all the above, it is decided that TLPM motor for the application of Section 1.2.1, is constructed and assembled with the HP and according to the specifications and parameters given in Table 2.4, Table 4.1 and Table 4.3.

	No HP	With HP
Total mass (kg)	25.79	25.55
Total volume (m^3)	0.0057	0.0057
I_{rms} (A)	31.07	42.65
A_{rms} (kA/m)	85.83	117.82
J_{rms} (A/mm^2)	11.31	17.68
T_{wat} (°C)	40	40
Mean of F_{lin} (N)	2093.5	2607.8
δ_g (kN/m^2)	35.3	43.96
F_{rip} (%)	11.08	11.46
P_{cu_tot} (kW)	1.3	2.78
Force density (N/kg)	81.14	102.1
Force density (kN/m^3)	367	457.5

Table 4.3 TLPM motor: performance chart with and without HP

4.5.2 The GT motor

It is important to note that whilst for most electric machines the main limiting hot-spots are usually located in the end-windings [133, 134], for tubular machines (with no end-windings) such as the TLPM motor of Chapter 2, the winding hot-spots in the slots practically define the thermal limit of the machine and thus the maximum allowable current density and the resulting maximum output force. However, a HP could technically be also adopted in rotational machines with end-windings, where it would be more practical to adopt for a pre-formed coil, concentrated wound machine such as the GT motor presented in Chapter 3. This would help provide a better thermal path to the winding losses and although the hot-spot would still be in the end-winding this would be reduced with respect to the case of not adopting a low resistance thermal path.

There exist some main differences for the implementation of the HP technique to the GT motor when compared to the implementation for the TLPM motor, namely

1) The nature of the thermal problem

   While for the TLPM motor, the final temperatures are measured for a steady state condition, the duty cycle of Figure 3.20a implies that for the GT motor it becomes a transient problem. Due to this, the optimal shape of the HP is first achieved assuming a steady state condition and then the final comparisons are done by comparing the temperature results for the motor operating under the mentioned duty cycle.

2) The cooling arrangement

   The TLPM motor employs a fluid cooling arrangement, which system has been proven in the previous section to benefit a lot from the HP technique. The thermal management of the GT motor instead relies on forced air cooling, thus it is important to verify whether any considerable advantages are achieved by the implementation of the HP and to what extent these advantages can be improved.

4.5.2.1 Lumped parameter model with HP

Starting from the thermal model of the GT motor shown in Figure 3.27, a HP with structural dimensions as illustrated in Figure 4.3 is implemented. Due to the required higher thermal performance, for the GT motor, the material used for the HP was decided to be copper as this material has a higher thermal conductivity, however with a higher mass density. As the ratio of total HP mass to total machine mass is very small (not so, for the TLPM motor), then the disadvantage of the higher mass density of copper is considered negligible. The new thermal model is shown in Figure 4.15, where it can be seen that R_{HP1}, R_{HP2} and R_{HP3} represent the HP itself. The thermal resistances of the model are given in Appendix B.3.3.

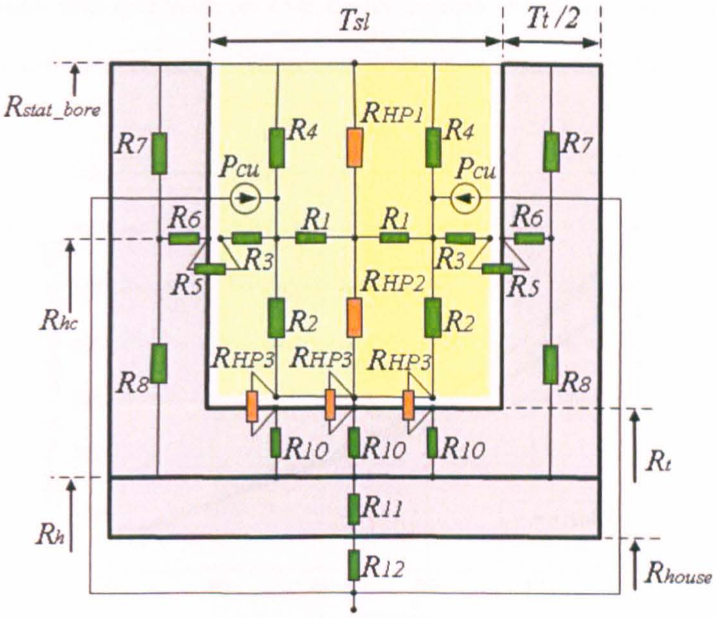

Figure 4.15 GT motor: lumped parameter model with HP

4.5.2.2 Initial verification exercise

The generic analysis for HP dimensions presented in Section 4.4.1 is repeated for a slot of the GT motor, which results in an initial design of $T_{HP2} \approx 0.1T_{sl}$ and $L_{HP2} = (R_{stat\_bore} - R_t)$ to be considered. This results in a value of T_{HP2} that it is approximately $1mm$, which gives the extra advantage related to the fact that any thickness smaller than that would considerably reduce mechanical robustness and complicate manufacturing procedures. It is important to consider these issues even at the initial design stage as such problems might offset any thermal advantage gained by the implementation of the HP.

The validity of the HP technique for the GT motor application is investigated by assuming a steady state condition for various values of electric loading. The thermal model of Figure 3.27 (model without HP) is used to predict the hot-spot temperature in the slot after 60 seconds of operation with the P_{cu} due to each of the J_{pk} values considered. The same operating conditions mentioned above are then applied to the thermal model with the HP shown in Figure 4.15.

Figure 4.16 compares the results of these tests, where it is immediately clear that especially for higher values of J_{pk} an important improvement in terms of temperature can be achieved. At $J_{pk} = 36A/mm^2$, a temperature decrease of approximately 12% is registered. It is important to note that the absolute temperature values (shown on the y-axis, for $J_{pk} > 20A/mm^2$) are so high due to the 60 seconds time span given (as a worst case scenario, to simulate steady state). In reality the GT motor will never exceed 9 – 10 seconds of operation at such high electric loadings.

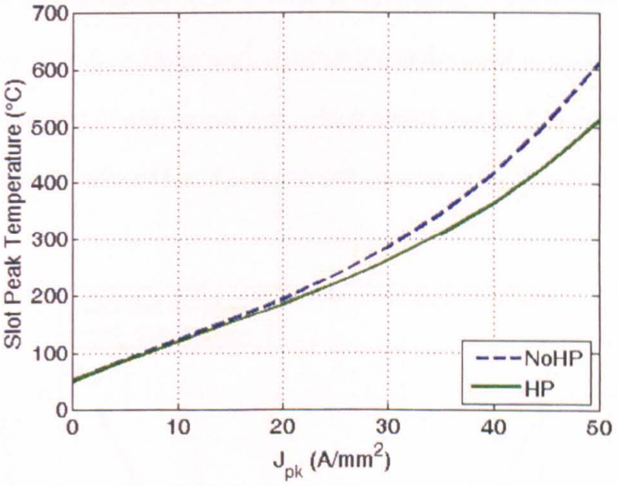

Figure 4.16 GT motor: initial verification exercise results

From this verification exercise, it can be immediately observed how the thermal advantages related to the use of the HP are much less for the GT motor application, then for the TLPM motor. This is mainly due to the difference in the cooling arrangements and the short time span of the tests. The fluid-cooled, water jacket arrangement of the TLPM motor results in the parameter h_{cv} to be dependent on the flow V_{wat}. The thermal management of the TLPM motor can thus be assumed to be a thermal conduction problem. For the air cooled arrangement used for the GT motor the convection parameter is dependent on the air-flow and thus h_{cv} is much lower here, resulting in a reduced potential of the high conductivity thermal path.

4.5.2.3 Optimisation of the HP dimensions

The same optimisation procedures as outlined in Section 4.4.1 are applied to the HP. The most important parameter that has the highest effect in terms of thermal performance on the arrangement is again the HP thickness T_{HP2}. A similar exercise to the one presented in Section 4.4.1.1 is applied to the GT motor thermal model. Various values of T_{HP2} are implemented in the thermal model of Figure 4.15 and the hot-spot temperature is recorded for the resulting J_{pk} that achieves the $7kNm$ requirement. The main difference from the TLPM motor optimisation procedures is that the temperature and the ensuing performance (for each iteration) is measured after 15 seconds (a rough reflection of the peak load requirement from the duty cycle in Figure 3.20a). Figure 4.17 plots the hot-spot temperatures of the GT motor for increasing values of the thickness of T_{HP2}, for a constant slot width T_{sl}. In the plot below, it is important to note that each value of temperature corresponds to the shown J_{pk} value that achieves the $7kNm$ torque requirement. It is shown that an optimal value of T_{HP2} exists at approximately $1.1mm$, which achieves the $7kNm$ with $J_{pk} = 38.5A/mm^2$. Another important point to note is that J_{pk} is the ratio of the current to the area of one copper turn, which means that as T_{HP2} is increased the area of copper is automatically reduced (i.e. K_{fill} is reduced because of the smaller winding area).

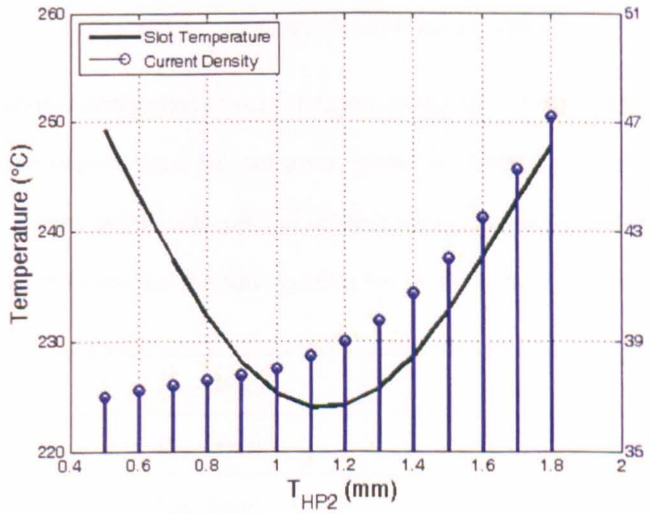

Figure 4.17 GT motor: optimisation of T_{HP2}

The same approach as presented in Section 4.4.12 and Section 4.4.1.3 for the optimisation of the other HP dimensions is taken. Thus the length L_{HP2} is assumed to be $(R_{stat\_bore} - R_t)$, and the dimensions T_{HP1} and L_{HP1} are assumed to be $T_{HP1} = T_{sl}$, and $L_{HP1} \approx \frac{1}{2} T_{HP2}$ respectively.

4.5.2.4 Implementation

In an effort to understand the effect of the thermal technique on the GT motor design, the HP described above is implemented on the GT motor model and the ensuing results evaluated.

A. Design

The final model results of the GT motor without the HP are presented in Figure 3.40 (for the plots labelled as full-Halbach), and Table 3.14. Using the optimisation procedures presented in Section 4.5.2.3, an optimal shape, geometry and composition for the HP is found. The FE model shown in Figure 3.38, is then equipped with such an HP and this is represented in Figure 4.18.

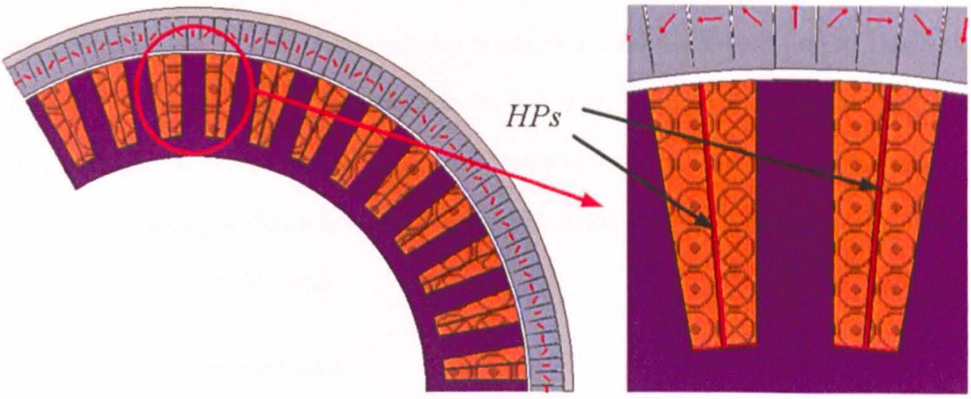

Figure 4.18 GT motor: final FE model with HPs

The main geometrical dimensions of the GT motor are given in Table 3.13, while the optimal dimensions of the implemented HP are given below in Table 4.4. From Figure 4.17, the optimal T_{HP2} is $1.1mm$ but for the sake of manufacturing simplicity and tolerances, T_{HP2} is taken as $1mm$, which means that the new J_{pk} value for the GT motor is $38A/mm^2$.

T_{HP1} (*mm*)	12.28
T_{HP2} (*mm*)	1
L_{HP1} (*mm*)	0.5
L_{HP2} (*mm*)	49.5

Table 4.4 GT motor: optimal HP dimensions

B. Results and discussions

Figure 4.19 compares the performance of the GT motor without the HP (at J_{pk} = 36*A/mm*^{2} as given in Figure 3.40 for the plots labelled as full-Halbach) with the results of when the HP is implemented (at J_{pk} = 38*A/mm*^{2} as found from Figure 4.15). As for Section 4.5.2.3, the time limit for recording temperature is again assumed to be 15 seconds.

The torque capability of the two models is compared in Figure 4.19a, where it can be seen that for the same values of J_{pk} there is a very small decrease in torque when the HP is implemented. As mentioned before, with the insertion of the HP, there is less area for copper which automatically increases J_{pk} and lowers P_{cu_tot}. This and the fact that J_{pk} is only increased from 36 to 38*A/mm*^{2} (due to the temperature limit) contribute towards the small reduction in torque seen in Figure 4.19a. The HP implementation results in a small improvement for F_{cog} shown in Figure 4.19b, but has virtually no effect on the back-EMF quality as can be seen in Figure 4.19c and Figure 4.19d. The lower P_{cu_tot} (for the same values of J_{pk}) due to the smaller window available for winding is shown in Figure 4.19e, which is due to the same reasoning as indicated in Table 4.2 for the TLPM motor.

C. Transient thermal performance

The thermal model of Figure 4.15 is used in conjunction with Figure 3.28 and the torque requirements shown in Figure 3.20a to verify the thermal performance of the machine when subjected to the transient duty cycle given for the application.

Figure 4.19f compares the thermal results of the model without the HP (shown in Figure 3.45) to that achieved from the machine model with the HP. The explanation behind the shape of thermal performance is already presented in Section 3.5.5. As can be observed from Figure 4.19f, a decrease of approximately 30°*C*, in the hot-spot temperatures at the end of the duty cycle (1860 seconds) is achieved when the GT motor is designed with the HP technique. Approximately the same temperature reduction is observed at 2060 seconds when the aircraft has finished its take-off run and is air-borne.

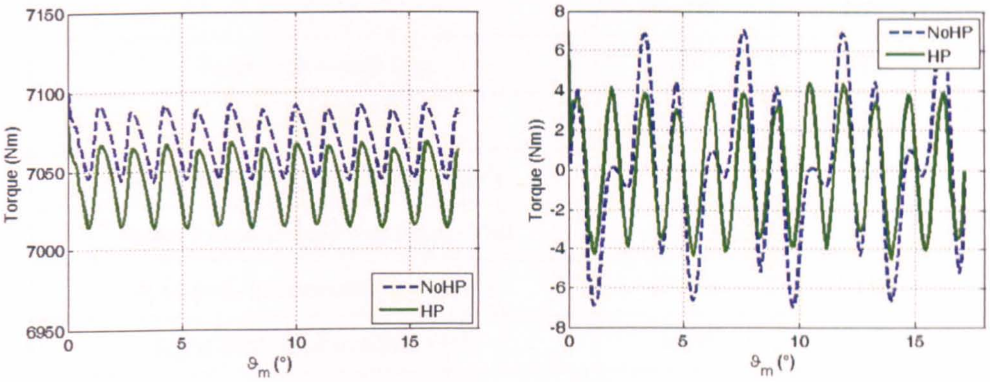

a) Torques b) Cogging torques

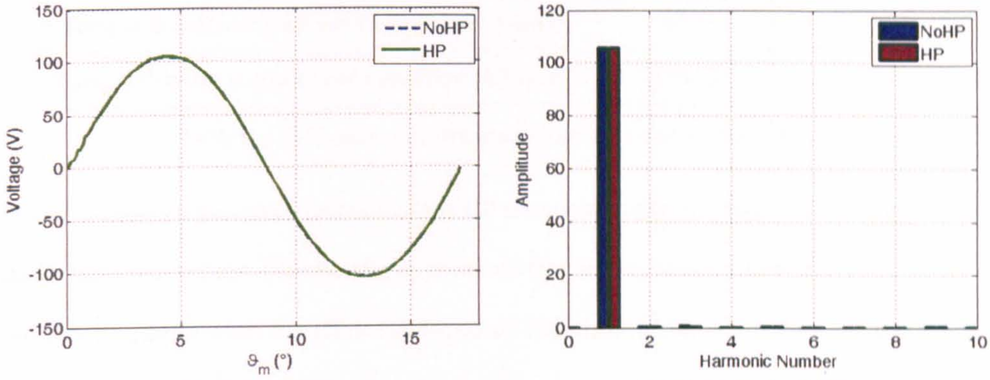

c) Back-EMFs d) FFT of Back-EMFs

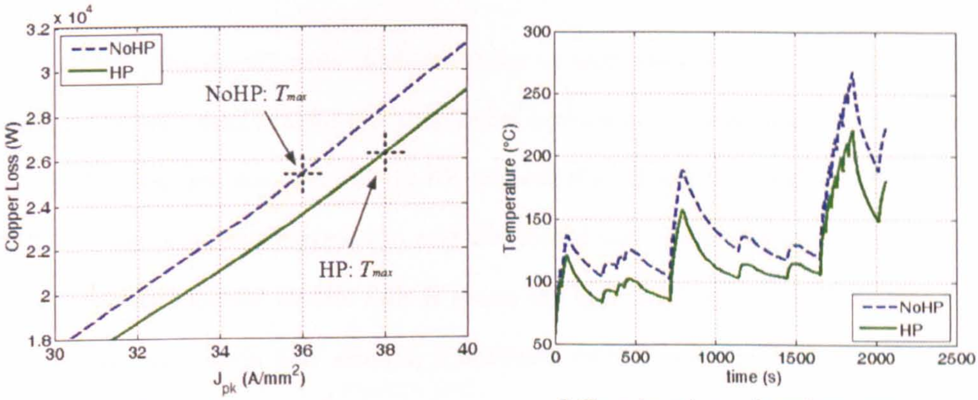

e) Copper losses vs. J_{pk} f) Transient thermal performance

Figure 4.19 GT motor: performance with and without HP

D. Conclusion

The performance capability of the GT motor, with and without the HP (for the peak load conditions) is presented and compared in tabulated form in Table 4.5, which illustrates (this can also be perceived from Figure 4.19) that little or no gain in terms of electro-magnetic performance of the machine is obtained with the implementation of the HP. The main reasons for this are the air cooled arrangement and the transient nature of the problem.

	No HP	HP
Total active mass (*kg*)	108	108.8
Total volume (m^3)	0.0254	0.0254
J_{pk} at peak load condition (A/mm^2)	36	38
Mean T at peak load condition (*Nm*)	7069.3	7049.6
δ_g at peak load condition (kN/m^2)	176.44	175.95
T_{rip} at peak load condition (%)	0.59	0.7
P_{cu_tot} at peak load condition (*kW*)	25.31	26.26
Torque density at peak load condition (*Nm/kg*)	65.5	64.79
Torque density at peak load condition (kNm/m^3)	278.32	277.54

Table 4.5 GT motor: performance chart with and without HP

From the above, a perceived function of the HP technique is that it is much more effective for steady state applications. However for applications that operate on a transient cycle, advantages can still be gained when the HP is implemented especially if the whole duty cycle operates over a considerable time period.

This advantage (for the GT motor application) can be appreciated in Figure 4.19f, which as mentioned before results in a hot-spot temperature decrease of approximately 13%. However Figure 4.19f illustrates that even with the HP, temperatures can still reach high values such as 225°*C*. At this point, it is important to note the relative lack of accuracy synonymous with lumped parameter thermal models such as shown in Figure 3.27 and Figure 4.15. Also for these models, as a worst case scenario, a minimum stator housing thickness of 10*mm* is assumed.

Further reductions in the motor temperature can be achieved by improving the effective h_{cv} by introducing stator fins [102], such as shown in Figure 5.23 and improving the surface air velocity V_{air}. This is part of the on-going, GT project, where detailed thermal design and analysis, using computational fluid dynamics (CFD) techniques is being done. Figure 4.20a shows the air flow path in a slot pitch of the GT motor, modelled using CFD analysis where the integration of the stator fins can be observed, while Figure 4.20b illustrates the temperature distribution over the whole set-up.

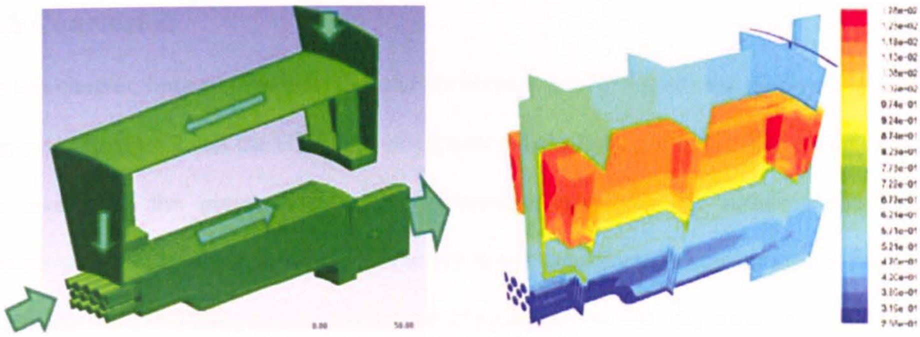

a) Fluid zones b) Temperature contours

Figure 4.20 GT motor: CFD analysis

A comparison of the transient operation, with and without the HP, using CFD analysis is shown in Figure 4.21, where for tests with the same operating conditions as those used in achieving the results shown in Figure 4.19f, a reduction of approximately 27 °*C* is found when the HP is implemented. A good similarity between the CFD results of Figure 4.21 and the lumped parameter, analytical model results of Figure 4.19f can be observed, which validates the worthiness of the analytical model. The difference in the absolute values of temperatures is of course due to the effects of the stator fins (not modelled for Figure 4.19f). The maximum temperature reached in Figure 4.21 (with the HP) is 213 °*C* which shows that a 'safe' operating temperature has been reached.

Considering all the above, it is decided that GT motor for the application of Section 1.3.1, is constructed and assembled with the HP and according to the specifications and parameters given in Table 3.13, Table 4.4 and Table 4.5.

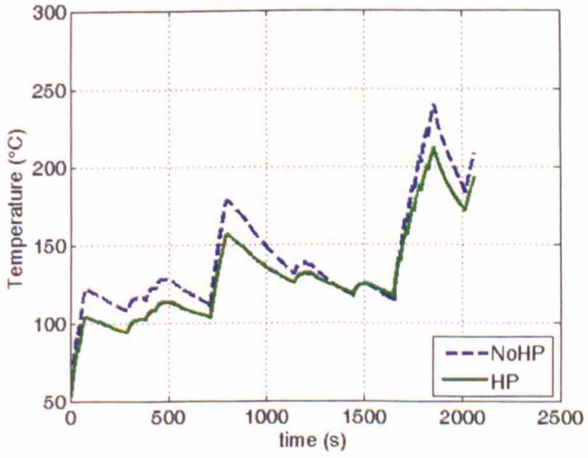

Figure 4.21 GT motor: CFD analysis performance comparison

4.6 Conclusion

In this chapter, lumped parameter thermal networks to model a tooth-slot section of the TLPM motor of Chapter 2 and the GT motor of Chapter 3 have been presented. The models are used to investigate the proposed thermal improvement technique for reducing the hot-spot temperature in the phase windings of the respective machines. Results from the models are compared with FE analysis to confirm the adequateness of the analytical models and more importantly the thermal improvement technique. It is shown that by this technique a reduction of approximately 40% in the slot hot-spot temperature of the TLPM motor and approximately 13% for the GT motor can be achieved. In the case of the TLPM motor this means that a considerably higher J_{pk} can be used to improve performance whilst still 'respecting' the thermal limit of the machine. For the GT motor only a small increase in the current loading is possible which still results in achieving a 'safer' thermal performance.

From all this, a perceived characteristic of this technique is that it is considerably more effective when implemented for machines that are fitted with a fluid cooled arrangement, as long as it is at a relatively lower temperature. Clearly, the higher the temperature difference, the more heat flux can be conducted. Overall, the results presented in this chapter, validate and justify the implementation of the thermal management technique for both applications.

Chapter 5
Manufacturing, Construction and Experimental Validation

This chapter deals with all the manufacturing and experimental aspects of the work conducted and is divided into three main parts. The first part of the chapter is concerned with the experimental verification of the thermal management technique of Chapter 4. The specialised set-up that is constructed to confirm the technique's general worthiness is presented with an explanation of all its attributes and purposes. The tests done are presented and the results are then used to compare with the modelling results of Chapter 4.

The second part deals with the TLPM motor of Chapter 2. Traditionally, manufacturing of tubular machines is very difficult and costly. The major aspects of the construction procedures, used for the implementation of the TLPM motor are thus presented, including a brief overview of the test-rig onto which the TLPM motor is assembled. Finally the experimental results obtained from the rig are compared to the modelling results of Chapter 2 and Chapter 4 (with respect to the TLPM motor). The same methodology is then used to present the manufacturing and the testing done for the GT motor of Chapter 3.

5.1 The thermal management technique

The thermal management technique presented in [47], is shown in Chapter 4 to be able to improve the thermal and electro-magnetic performance of electrical machines by considerable factors. As seen in Section 4.5.1, this is especially true for systems that benefit from a fluid cooling arrangement and operate mainly in steady state such as the TLPM motor of Chapter 2, whilst reduced gains are achieved for other cooling systems such as for the GT motor of Chapter 3. In order to confirm and experimentally validate the mentioned improvements, a specialised, instrumented rig is set up. It is important to note that the HP technique in Chapter 4 was mainly evolved relative to the TLPM motor. A test set-up, designed to emulate one slot pitch of the TLPM motor is presented in the next sections.

5.1.1 The instrumented set-up

The experimental validation of the HP technique can be performed by comparing the thermal distribution in the slot area (such as in Figure 4.6) with and without the HP. To achieve this, a purposely built instrumented set-up (consisting of an axially insulated, double layer, single slot arrangement, its corresponding housing and a cooling arrangement) is used. The set-up can be assembled with or without the HP in order to achieve the required comparisons. The set-up and its assembly procedure is explained below for when the HP is present. To obtain the HP-less version, the exact same procedure as below is applied with the obvious exclusion of the HP.

Figure 5.1a shows a photo of the aluminium HP, which clearly exhibits the slitting, described in Section 4.4.2. The nature of the TLPM motor winding configuration dictates that the coils be pre-manufactured. More on the manufacturing procedures of these coils, shown in Figure 5.1b is presented and investigated later in Section 5.2.1.1. The HP, the pre-formed coils (with a distribution of thermocouples as illustrated in Figure 5.2) and the two stator teeth (making up one slot of the TLPM motor) shown in Figure 5.1c are assembled into the water-cooled housing, illustrated in Figure 5.1d. As explained later in Section 5.2.1.2, the whole set-up is designed with very small geometric tolerances while applying positive interference tolerances where possible.

The pre-formed coils and the tubular nature of the set-up enable the components of Figure 5.1c to be assembled under appropriate pressure, thus ensuring a reliable contact between the various components to be achieved. The complete instrumented set-up with a number of thermocouples to monitor the temperature distribution is shown in Figure 5.1e. Thermal insulation in the mover bore (empty for this set-up) is achieved by inserting a thermally resistive material.

a) The HP b) The pre-formed coils

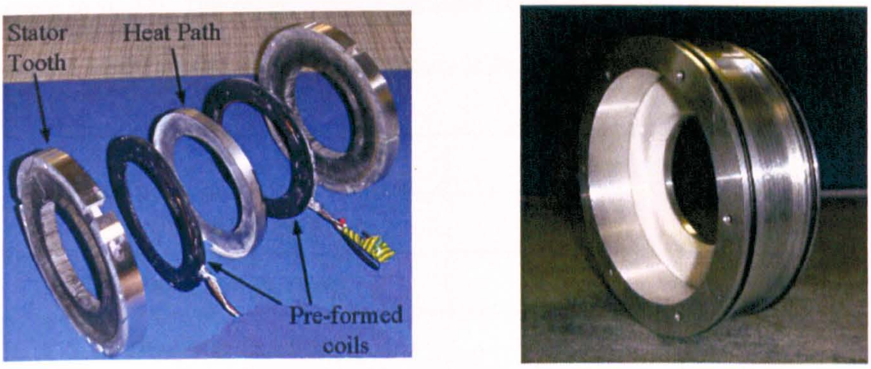

c) 'Exploded' view of slot with HP d) Stator housing with water channel

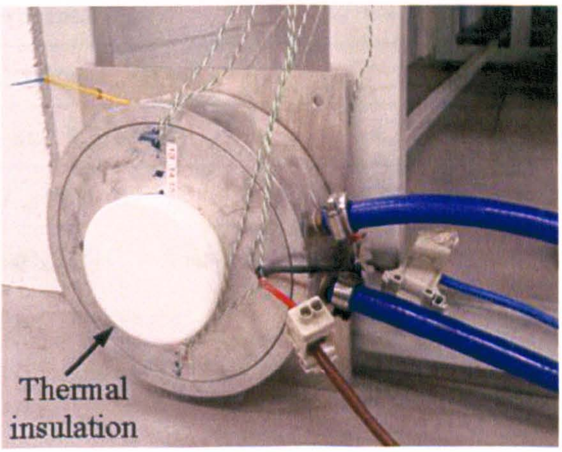

e) The complete instrumented set-up

Figure 5.1 HP technique: the instrumented set-up hardware

Electrical insulation in the slot area is achieved by the use of an appropriate thickness of wire insulation and thin slot liner. The use of high performance, ultra-thin, polyimide material as liner could also facilitate assembly procedures in the actual machine. In case of machines where the two coils in the same slot belong to the same phase (i.e. single layer winding) no additional insulation is needed apart from the same slot liner that would be adopted had the HP not been used.

The design details of the experimental set-up are tabulated in Table 5.1, which reflects the TLPM motor and HP parameters shown in Table 2.4 and Table 4.1 respectively. In the final thought of Section 2.5, it is mentioned that K_{fill} for all modelling purposes is assumed as 0.5. From the instrumented set-up explained above, experimental values for K_{fill} with and without the HP are found and are shown in Table 5.1 Experimental values of the equivalent slot thermal conductivity k_{eq} are also achieved. For modelling purposes, this value is calculated according to (B.17). The experimentally obtained values of K_{fill} and k_{eq} are recorded and as shown later can be used to improve the accuracy of the analytical and numerical models.

	No HP	**HP**
Slot width T_{sl} (*mm*)	11.35	11.35
Slot depth R_t - R_{in} (*mm*)	24.45	24.45
HP thickness T_{HP2} (*mm*)	/	1
Assumed modelling K_{fill}	0.5	
Experimental K_{fill}	0.477	0.448
Assumed modelling k_{eq} (*W/mK*)	3.756	
Experimental k_{eq} (*W/mK*)	4.33	4.33
T_{wat} (°C)	40	40

Table 5.1 HP technique: data of the experimental set-up

5.1.2 Tests and results

A first experiment without a HP in the slot area is conducted, followed by a similar test with the HP included. The coolant temperature is kept constant at 40°C. As previously mentioned, thermocouples are placed strategically in the coils to be able to monitor the temperature distribution in the slot area. The temperature sensors monitor the distribution by measuring the temperature of the points in the coils as shown in Figure 5.2. The point C_c in Figure 5.2a indicates the geometric point where according to Figure 4.6, the maximum temperature hot-spot is predicted to be located, when the HP is not present. For Figure 5.2b, the points C_{1_HP} - C_{6_HP} are located in the same places as C_1 - C_6 but indicate that the HP is present.

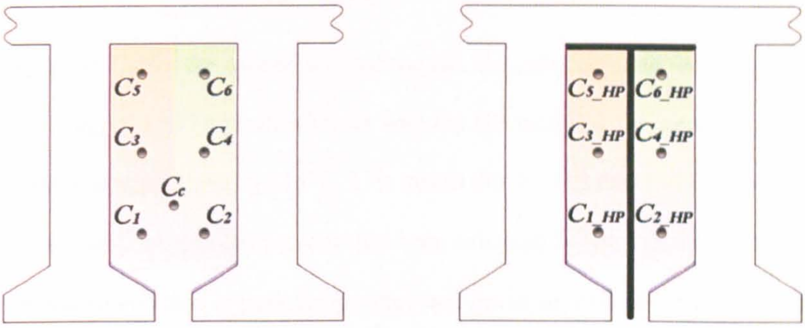

a) No HP b) HP

Figure 5.2 HP technique: monitoring the temperature distribution

As explained in [17, 47], these tests are done using a DC supply, which as stated in [47, 133] ensures that only the copper loss P_{cu}, has an effect on the thermal performance of the set-up. Starting from zero, the DC supply is increased in steps and the temperature distribution recorded for each step. Each measurement is recorded after the appropriate time has been allowed for the temperature to level out to a steady state value.

The temperature results obtained from these two tests are plotted against J_{pk} in Figure 5.3. The use of a dc supply means that for Figure 5.3, J_{pk} is derived by using $I_{pk} = (I_{dc} * \sqrt{2})$, where I_{dc} is the dc, test current. For reasons of clarity, only the temperatures of C_{1_HP} and C_{2_HP} are compared to C_1 and C_2 respectively, these being the points where the temperature is highest. The slight difference between the temperatures of C_1 and C_2 and C_{1_HP} and C_{2_HP} can be attributed to manufacturing tolerances, inaccuracy of sensor placement and any non-uniformity of coil build (i.e. coils cross-section not exactly rotationally symmetric).

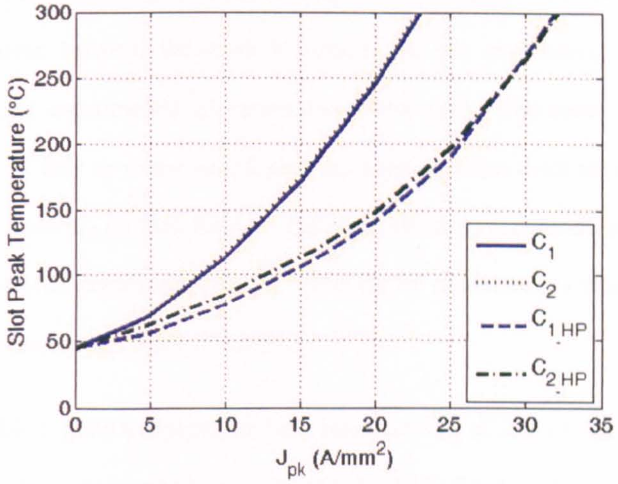

Figure 5.3 HP technique: experimental results

Considering point C_2, for the case of without the HP, the safe operating temperature of 180°C is reached at a J_{pk} of 15.37A/mm^2, whereas with the HP included, the same J_{pk} yields a peak slot temperature of approximately 115°C. This means that for this experimental test a reduction of ≈36% in the slot hot-spot temperature has been achieved, when the HP is included in the slot. The predicted decrease in peak temperature and deviation from the mean when the HP is adopted is thus experimentally validated.

5.1.3 Conclusion

Figure 5.4 compares the analytical and FE results presented in Section 4.3 to the results of the experimental, instrumented set-up presented in Figure 5.3.

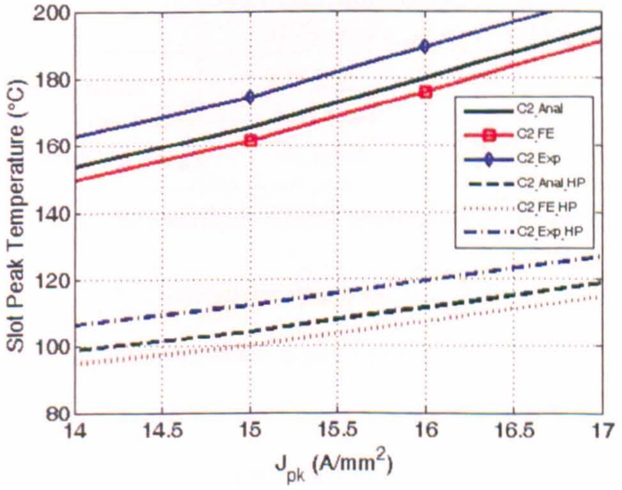

Figure 5.4 HP technique: analytical vs. FE vs. experimental result comparison

For reasons of clarity and visualisation, the comparison of Figure 5.4 is done only for the point C_2. The difference between the models' results and the experimental results is due to manufacturing and experimental tolerances and to the coarse discretisation of the resistance thermal model, as well as to the simplifying assumptions taken with regards to K_{fill} and k_{eq}. Considering the point C_{2_HP}, then for $J_{pk} = 16A/mm^2$, the analytical model predicts a result that is 6.62% less than the experimental results, while the FE model results in a temperature that is lower than the experimental one by 10.05%.

As shown in Table 5.1, the analytical model is based on a k_{eq} of 3.756*W/mK* as calculated using (B.17), whereas the experimental k_{eq} was found to be 4.332*W/mK*. In terms of K_{fill}, the assumed value for modelling is taken as 0.5, while from a practical point of view it is found to be 0.47 when the HP is not implemented and 0.448 for when the HP is present.

As a fine tuning exercise, the experimental values of K_{fill} and k_{eq} are applied to the analytical and FE models and the models tested for the critical value of copper density of $J_{pk} = 16A/mm^2$. At this loading and with the newly adjusted values of K_{fill} and k_{eq} it is found that the models' prediction errors become 3.1% for the analytical model and 5.67% for the FE model. Table 5.2 compares the prediction errors for when the values of K_{fill} and k_{eq} are assumed, to the prediction errors when the values are adjusted according to experimental values. This exercise indicates the effect that the values of K_{fill} and k_{eq} can have on the accuracy of the models.

	Models' prediction error (%)	
	With modelling values of K_{fill} and k_{eq}	**With experimental values of K_{fill} and k_{eq}**
Analytical model	6.62	3.1
FE model	10.05	5.67

Table 5.2 HP technique: models' temperature prediction errors

As a final exercise, the analytical model is used to calculate the optimal value of k_{eq} that results in the best improvement of the analytical model relative to the experimental results. The best improved agreement between the resistance network and experimental results can be achieved, if an adjusted k_{eq} of 4.87*W/mK* for the analytical model is used.

5.2 The TLPM motor

In order to validate the modelling results of the TLPM motor shown in Figure 4.14 and tabulated in Table 4.3, a prototype machine is built and tested on a specialised test-rig in the laboratories of the UoN. The construction and the testing of the prototype machine are addressed in this section.

5.2.1 Manufacturing and construction

Traditionally the nature of tubular motors results in their manufacturing and construction to be very difficult and somewhat expensive. In order to build up the TLPM motor of Chapter 2, specific construction and assembly procedures are proposed and tested. Where appropriate, various materials and different assembly techniques are investigated. The manufacturing parameters and geometrical dimensions of the TLPM motor are given in Table 2.4, Table 4.1 and Table 4.3. The design procedures shown below are all done relative to these parameters and dimensions.

5.2.1.1 The coils

The nature of the TLPM motor dictates that the coils be pre-manufactured. The toroid shape of the coils permits the coils to be wound individually (under tension to increase K_{fill}). Traditionally this can be achieved by manufacturing a specific coil former usually made of some type of mild steel and then winding the coil directly on it. However considering the high thermal performance that is required from the TLPM motor, it was decided to impregnate the wound coils with a thermally conductive, potting compound which also exhibits good electrical insulation properties. In order to prevent the impregnated coil from sticking to the inside walls of the former during the compound curing period, a lining of the plastic material known as Polytetrafluoroethylene (PTFE), is used. The whole setup is shown in Figure 5.5, where Figure 5.5a shows an exploded view of the coil former assembly and Figure 5.5b shows a cross-sectional view of the assembled former. From Figure 5.5b it can be perceived, how the coil is first wound, then impregnated via the holes bored on purpose to inject the compound (in its liquid form) and then cured at room temperature or in an oven. When cured, the former is taken apart and a coil, such as shown in Figure 5.1b is produced.

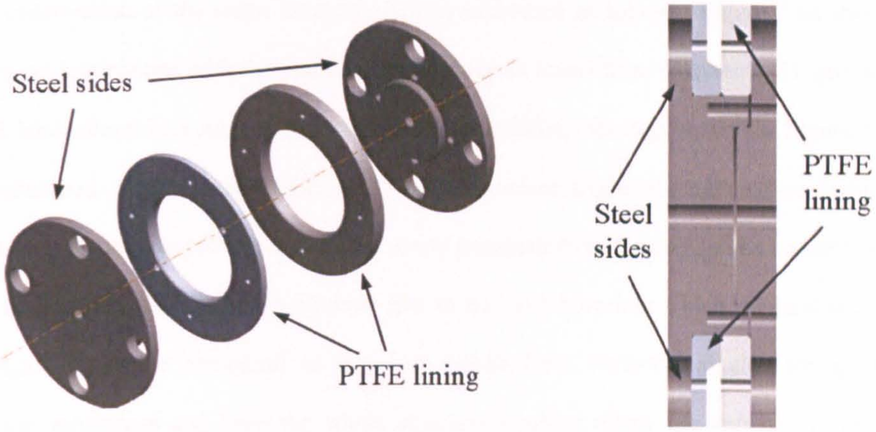

a) Exploded view b) Cross sectional view

Figure 5.5 TLPM motor: the coil former assembly

The geometrical tolerances of the assembly above are highly critical as they determine the overall dimensions of the pre-formed coils. For the reasons illustrated by the stator assembly diagram of Figure 5.7a, the coils need to fit as best as possible in the space allocated to them.

5.2.1.2 The stator assembly

The most time consuming and difficult part of the construction of the TLPM motor is represented by the construction and assembly of the stator. The challenging factor is that for a good electro-magnetic performance, the laminations of a tubular machine need to be in the axial direction and not radial like in a rotational machine. While the nature of rotational machines and even that of standard, linear machines makes the implementation of the stator laminations a relatively easy task, in the case of a tubular motor the building and attaching of the axial stator laminations is much more complicated and requires careful manufacturing and assembly planning.

A convenient and easy way how to circumvent the problem is to construct the stator core out of soft magnetic composites (SMC) materials [135, 136], which give the possibility of manufacturing complicated stator structures whilst still maintaining an acceptable electro-magnetic performance [137]. However, these materials cannot reach the level of electro-magnetic performance that can compete with standard SiFe laminations. Thus for a high performance application such as that of Section 1.2.1, it is advised to utilise standard laminations, even when considering the assembly complexity they entail.

The construction of the stator assembly is thus addressed as follows. Figure 5.6a shows the ready cut laminations with the optimum dimensions as found from Chapter 2. To position the axial laminations in a tubular form, the stator aluminium housing shown in Figure 5.6b is manufactured. The three axial slots on the outside surface area of the housing are included as these slots are used to provide a path for the coil terminals from the coils to the connection box. The housing has a series of longitudinal slits in its inner bore into which the laminations are slid (as a 'sunshine' structure) as shown in Figure 5.6c. Varnish and glue are applied to increase robustness and keep the whole structure together. Once the varnish is cured, the structure of Figure 5.6c is then cut axially into the stator 'rings', shown in Figure 5.6d.

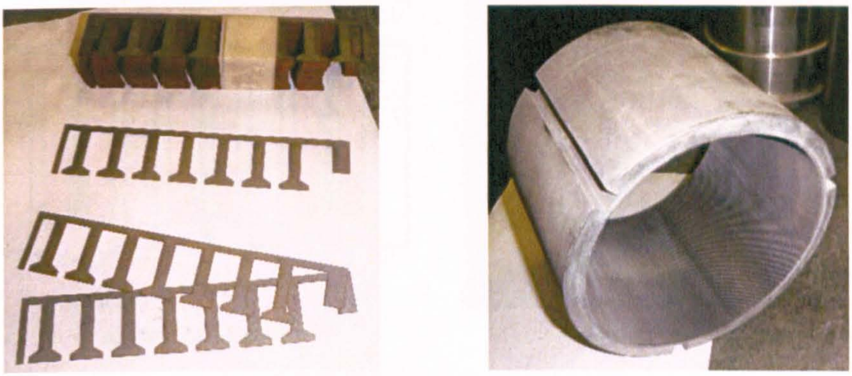

a) Stator laminations b) Stator housing

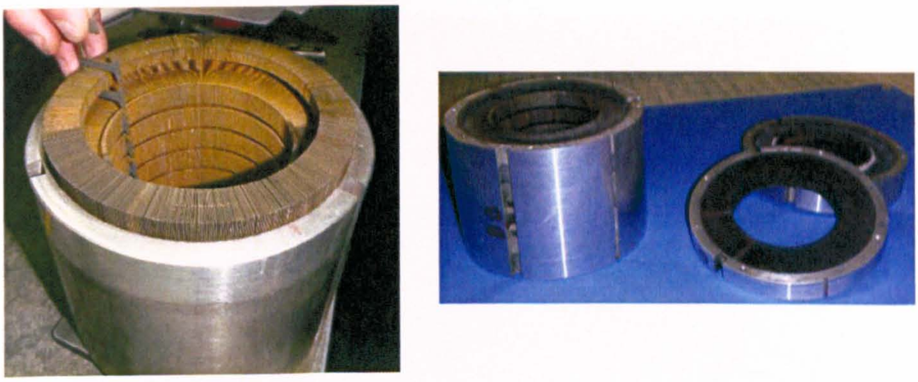

c) Stator housing with laminations d) Stator 'rings'

Figure 5.6 TLPM motor: stator assembly components

The stator 'rings' of Figure 5.6d and the manufactured HPs (shown in Figure 5.1a) can then be used to re-assemble the stator in a similar manner to the 'exploded' view shown in Figure 5.1c. A more general illustration of the re-assembly concept is shown in Figure 5.7a, which stresses the importance of having good contact between all the surfaces for thermal purposes.

The ability to conduct heat away from the coils depends heavily on this contact between the various component surfaces. Due to this, the geometrical dimensions of all the components are highly critical. For example, as mentioned in Section 5.2.1.1, the dimensions of the coil former assembly shown in Figure 5.5, determine the size of the coils. Appropriate gauges are created to measure and confirm each component and make sure that everything fits as best as possible. The complete re-assembled stator housing with all the coils and HPs inside as shown in Figure 5.7b, is then fit (with a positive interference) into a pre-manufactured stator water-jacket, whose material is aluminium. The final stator assembly is illustrated in Figure 5.8.

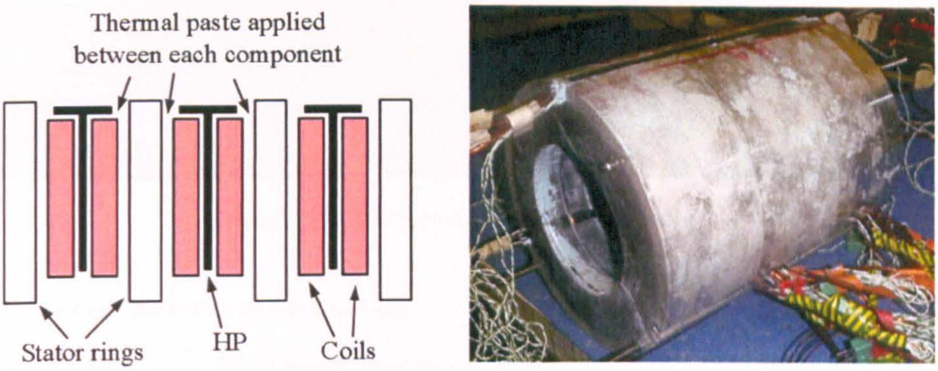

a) General structure b) Re-assembled housing

Figure 5.7 TLPM motor: re-assembly of housing

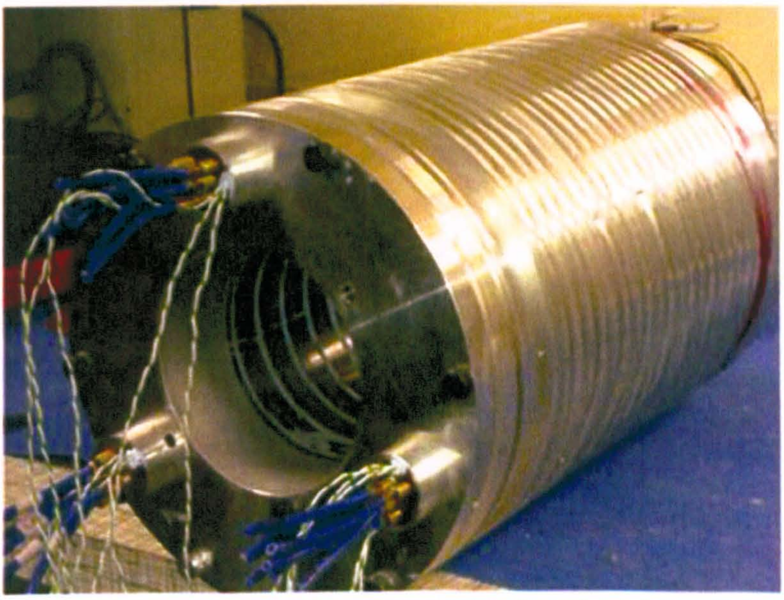

Figure 5.8 TLPM motor: final stator assembly with water-jacket

5.2.1.3 The mover assembly

For an IPM configuration such as shown in Figure 2.3, the mover consists of the axially magnetised PMs, the ferromagnetic flux focusing pieces and the non-ferromagnetic support tube. The PMs and the pieces are simply slid onto the support tube and Figure 5.9 illustrates the complete mover assembly including the force transmission shafts.

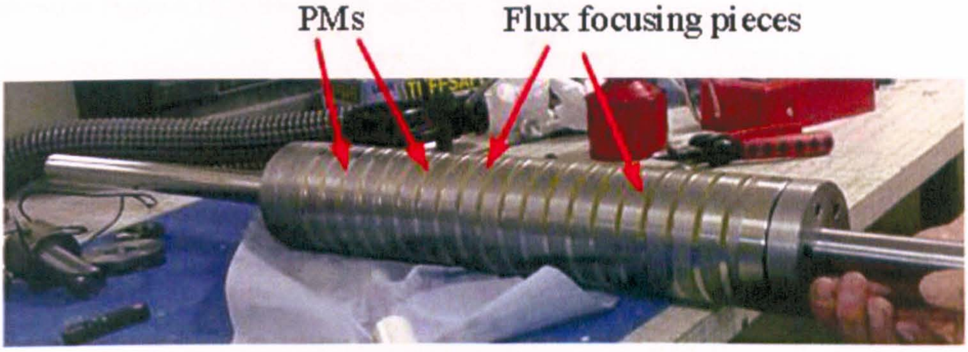

Figure 5.9 TLPM motor: final mover assembly

5.2.1.4 General assembly and the test-rig

A cross-sectional view of the motor assembly is shown in Figure 5.10a, where the various components mentioned above can be observed. The whole motor is assembled on a test-bed that includes linear bearing guides, support plates and a load actuator for testing purposes. A general view of the motor test-bed is shown in Figure 5.10b.

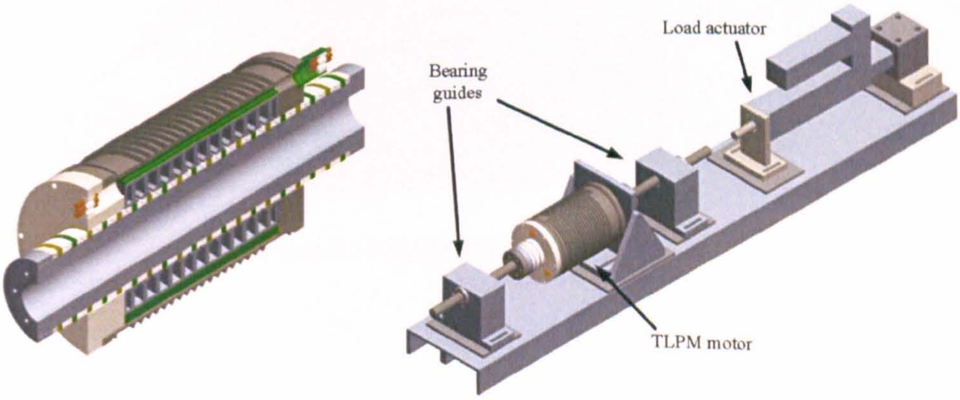

a) Motor assembly

b) Test-bed

Figure 5.10 TLPM motor: assembly structures

The load actuator is an industrial, 40*kW* EMA, capable of peak force loads up to 17.8*kN* with a maximum stroke of 300*mm* at a maximum linear velocity of 313*mm/s*. These performance parameters ensure that a complete set of tests can be done for the TLPM motor.

A high performance, water-cooled, 100*kW*, matrix converter drive, designed for aerospace applications at the UoN [138-140], is used to drive the TLPM motor. The complete test-rig is shown in Figure 5.11. A linear force cell with a measurement accuracy of 1% is used for linear thrust force measurements.

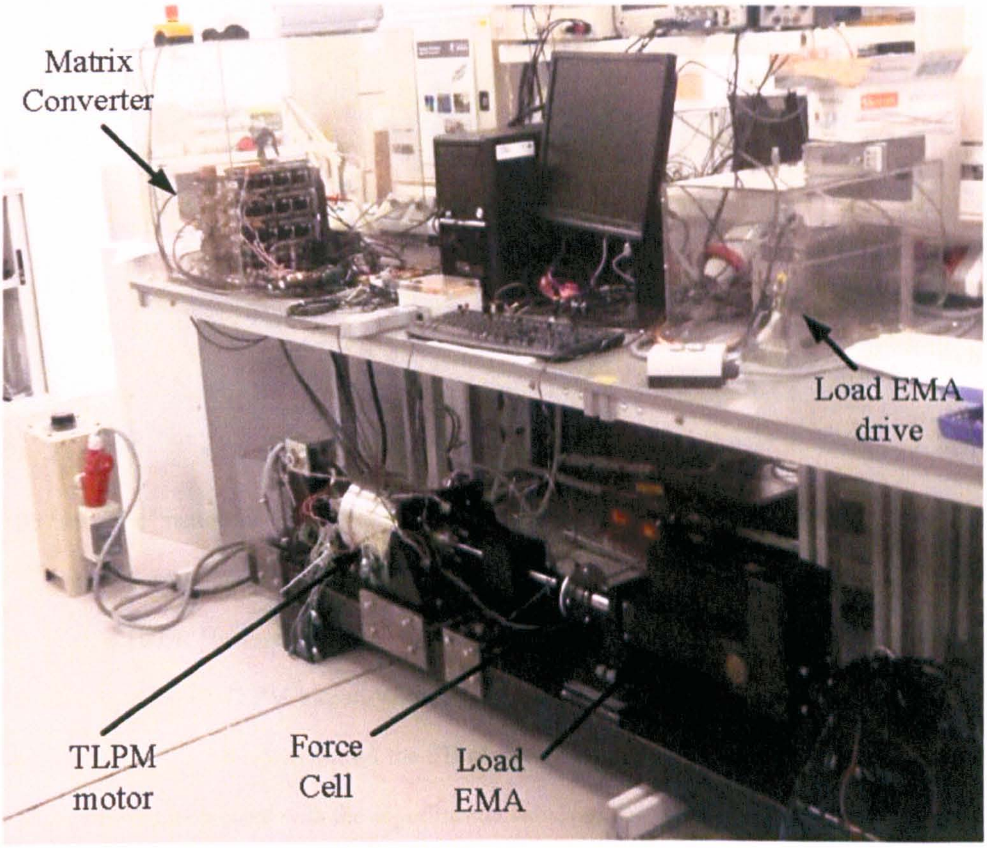

Figure 5.11 TLPM motor: complete test-rig

5.2.2 The stator lamination fill factor K_{lam}

A perceived disadvantage related to the 'sunshine' structure (shown in Figure 5.6c) with which the stator of the TLPM motor is assembled is the resulting empty space in between the laminations. This is illustrated in Figure 5.12 which shows a representative and simplified, end view of the stator of the TLPM motor, where for reasons of clarity, the mentioned spaces between the laminations are exaggerated. For the built motor, it is found that the ratio of the total lamination material to the total stator area available is 73.27%. This ratio is thus defined as the stator lamination fill factor K_{lam}.

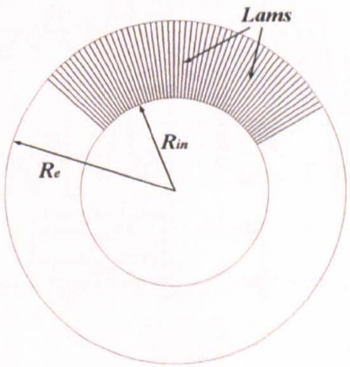

Figure 5.12 TLPM motor: definition of K_{lam}

The 'sunshine' nature of the TLPM motor makes it very difficult to implement the effect of K_{lam} into the FE models presented in Chapter 2 and Chapter 4, for which K_{lam} is always assumed as 100%. However this can be implemented into the models by assuming a standard, linear version of the TLPM motor, where l_{ax} is equal to the circumference of the stator inner bore (i.e. $2\pi R_{in}$). Figure 5.13 shows the FE model of the linear version of the TLPM motor, which is also implemented with the experimental values of K_{fill} and k_{eq} given in Table 5.1.

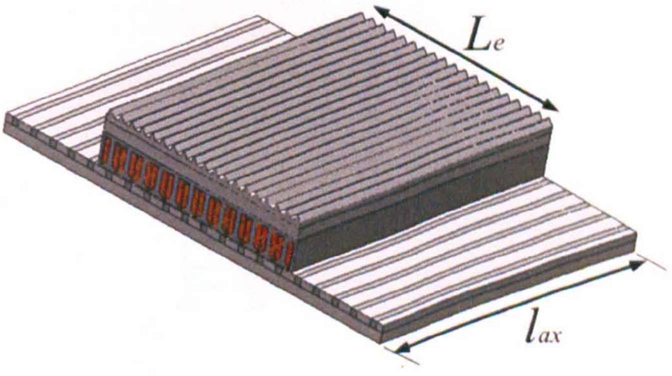

Figure 5.13 TLPM motor: FE model to consider K_{lam}

Figure 5.14 compares the results of the more realistic, linear version (K_{lam} = 0.73 and K_{fill} = 0.448) to the 'original' tubular results (K_{lam} = 1) shown in Figure 4.14. As can be observed from Figure 5.14a, for J_{pk} =25A/mm^2 there is a reduction of approximately 16% in the force capability. The cogging force F_{cog} and the back-EMF quality are basically the same, for both cases. Figure 5.14e and Figure 5.14f reconfirm the effect of K_{lam} on the force performance of the machine, where for Figure 5.14f the mass of the machine is calculated considering the fact that the stator mass is only 73.27% of the 'original' stator mass.

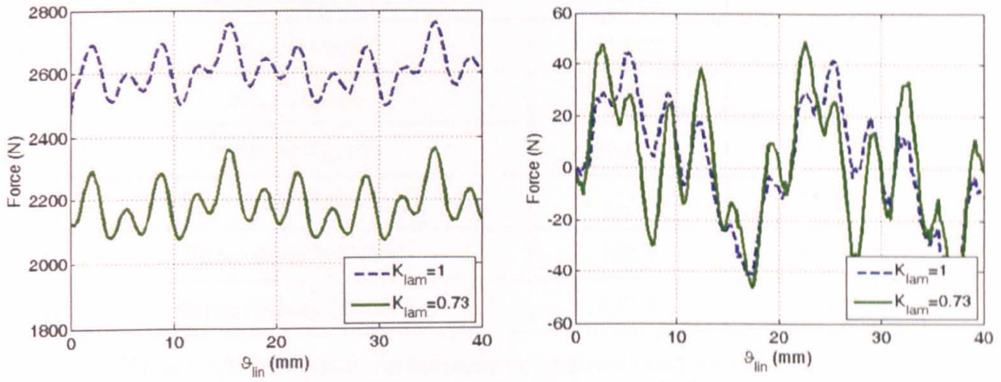

a) Force b) Cogging force

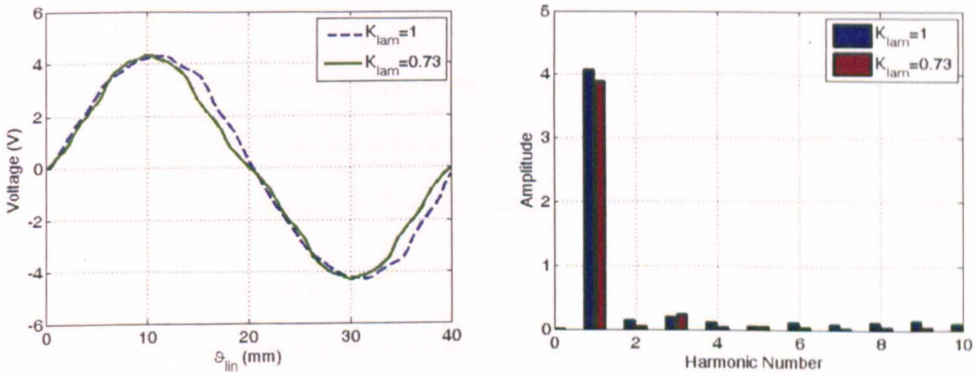

c) Back-EMF d) FFT of Back-EMF

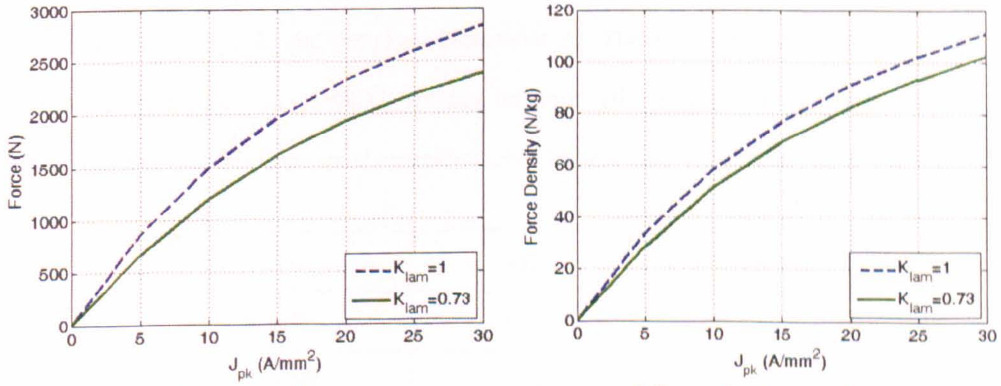

e) Force vs. J_{pk} f) Force density vs. J_{pk}

Figure 5.14 TLPM motor: performance comparison considering K_{lam}

Table 5.3 tabulates and compares the results considering K_{lam} = 0.73, to the TLPM results tabulated in Table 4.3, where it can be observed that the final predicted values of F_{lin} and force density for the TLPM motor are 2184.2*N* and 93.46*N/kg* respectively. Considering all the above, then it is to these realistic values (with K_{lam} = 0.73 and K_{fill} = 0.448) that the experimental results of the following sections will be compared to.

	$K_{lam} = 1$	$K_{lam} = 0.73$
Total mass (*kg*)	25.55	23.37
Total volume (m^3)	0.0057	0.0057
A_{rms} (*kA/m*)	117.82	105.6
J_{rms} (A/mm^2)	17.68	17.68
Mean of F_{lin} (*N*)	2607.8	2184.2
δ_g (kN/m^2)	43.96	36.82
Force density (*N/kg*)	102.1	93.46
Force density (kN/m^3)	457.5	383.2

Table 5.3 TLPM motor: performance comparison chart considering K_{lam}

5.2.3 Tests and results

A series of tests are done on the experimental rig of Figure 5.11, in order to validate the TLPM motor performance and compare the experimental results to the modelling results as given in Figure 5.14 (plots labelled as K_{lam} = 0.73) and tabulated in Table 5.3.

5.2.3.1 Measurable parameters

Having the assembled motor and rig permits the measurement of certain parameters that are critical to the operation of the machine. Table 5.4 compares the predicted and measured values of the phase resistance R_a and the phase inductance L_a. These parameters are measured at a reference temperature T_{wat} of 40°C. As can be observed, good similarity exists for both parameters with prediction errors of approximately 13% and 5.66% for R_a and L_a respectively.

	FE	**Experimental**
R_a (Ω)	0.51	0.59
L_a (*mH*)	10.6	10

Table 5.4 TLPM motor: measurable parameters comparison

Considering that the predicted value of R_a is calculated by considering P_{cu_tot} in relation to I^2, where I is the RMS phase current, then for this parameter, the error due to K_{lam} is not significant. However it is also true that the FE analysis does not take into account the length and the resistance of the inter-phase and connection leads, which could be the main contributing factor in the prediction error of R_a.

5.2.3.2 No load back-EMF

The importance of the back-EMF quality is already addressed in the presentation of the QI parameters in Section 2.2. In order to measure this parameter, the TLPM motor windings are left on open circuit and the load actuator is used as a prime mover to smoothly translate the mover of the TLPM motor at a constant, required speed of 100*mm/s*. The back-EMF is observed and recorded via a high bandwidth oscilloscope, in order to measure as much as detail as possible.

Figure 5.15a shows the measured signal and also compares it to the predicted back-EMF. Figure 5.15b compares the harmonic spectra of the measured back-EMF to the FE-predicted wave-form. From the figures, it can be observed that the measured back-EMF is very similar to the predicted one. The FE induced voltage is slightly higher than the measured waveform and this can also be observed from the slightly higher value of the fundamental in Figure 5.15b. The slight difference between the signals can be safely attributed to experimental tolerance.

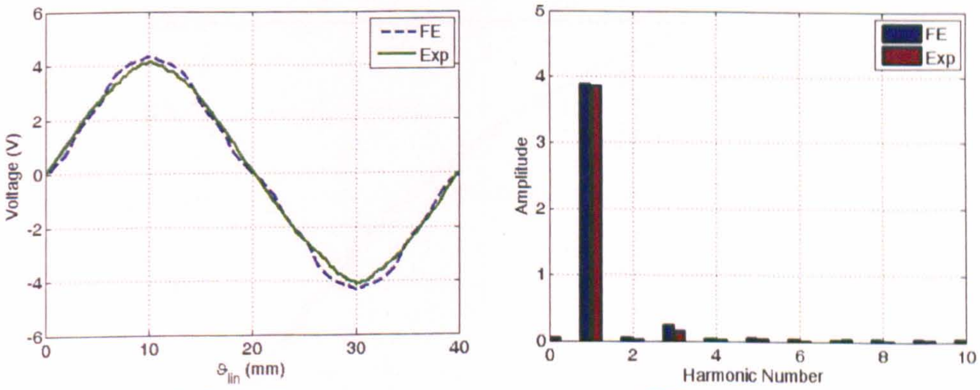

a) Back-EMF b) FFT of back-EMF

Figure 5.15 TLPM motor: back-EMF comparison

5.2.3.3 Force capability

One of the main points of interest of this experimental section is the force/torque capability of the machine. As seen in Chapter 2 and Section 4.5.1, for the case of the TLPM motor, high emphasis is placed on the force and force density capability of the machine.

In order to measure the force capability of the TLPM motor, a suitable control strategy making use of a precise position loop, is designed and implemented in the matrix converter controller. The load EMA is controlled via current loop control to maintain a specific load. The design and optimisation of the control goes beyond the scope of this work and so is not included in the thesis. The linear force cell, shown in Figure 5.11 is used to obtain values of the linear force generated. The tests are done for increasing values of the peak phase current I_{pk}. Figure 5.16 shows the results of the experimental tests and also compares the experimental values to the predicted results shown in Figure 5.14e. It is important to note that for the last experimental value (i.e. at $I_{pk} = 59.76A$), the test is done for a very short period of time as at this current value J_{pk} is more than $25A/mm^2$ and thus the thermal limits of the motor are exceeded.

As can be observed from Figure 5.16, a very good similarity between the predicted and measured results is achieved, which validates the FE model and the considered K_{lam} effect. Any remaining prediction errors can be safely attributed to inaccuracies in measurement due to the load cell tolerance, human error and manufacturing tolerances.

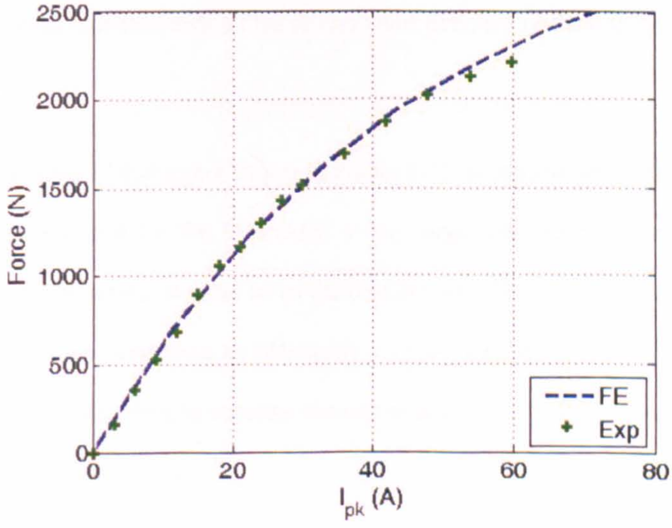

Figure 5.16 TLPM motor: force capability comparison

5.2.3.4 Force constant

The results shown in Figure 5.16 can be used to plot the predicted and measured values of the force constant K_F. Figure 5.17 illustrates and compares the FE and experimental results, where it can be observed that for the rated value of $J_{pk} = 25A/mm^2$ (i.e. $I_{pk} = 54.05A$) the error between the FE and experimental results is approximately 2.48%.

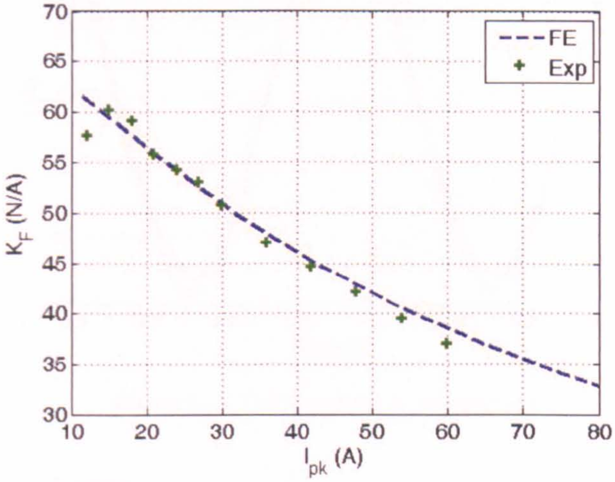

Figure 5.17 TLPM motor: K_F comparison

5.2.3.5 Fault tolerance

As for all aerospace applications, it is important to assess the fault tolerance performance of the machine. The term fault tolerant remains at best vague and depends on the particular application, however a simplistic measure of the parameter can be achieved by considering the performance of the machine with all the phases short circuited (reflecting the EMC concept of Section 3.5.4).

The FE model of the TLPM motor shown in Figure 5.13 is used to achieve the predicted I_{sc}. It is important to note that for the FE model, a very large time window is required to obtain reliable short circuit values, in order to let the required variable reach a steady state value. The experimental tests are performed by physically shorting all three phases of the TLPM motor and then using the load EMA to translate the mover at a V_{lin} of 100*mm/s*, with a current probe to measure the experimental I_{sc}.

The results of the FE model and the experimental test are compared in Figure 5.18, where the similarity between the two wave-forms can be observed, with a small overestimation error exhibited by the FE waveform.

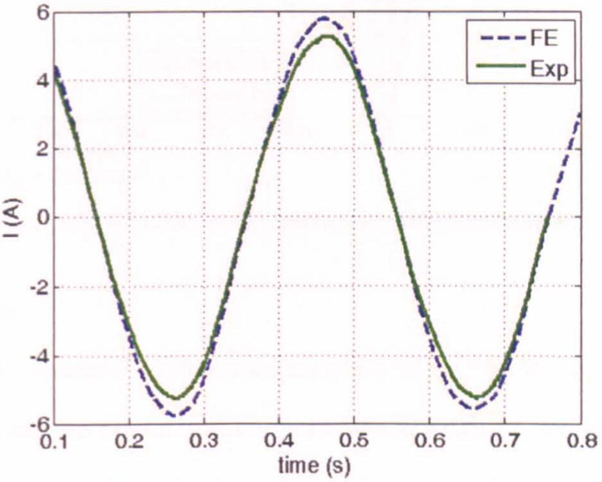

Figure 5.18 TLPM motor: I_{sc} comparison

5.2.3.6 Thermal performance

As shown in Figure 5.7 and Figure 5.8, the TLPM motor is equipped with a number of thermocouples, so as to be able to monitor and record the operating temperatures in various parts of the machine. Each coil of the machine has a thermocouple that is placed in the same location as the point C_{2_HP} of Figure 5.2, thus ensuring a temperature measurement at the hottest spot in the coil. For the tests whose results are shown in Figure 5.16 , one coil per phase is chosen and its thermal performance monitored.

Figure 5.19a illustrates the hot-spot temperature of one of the three phases for $J_{pk} = 20A/mm^2$, while Figure 5.19b shows the same for the rated, steady state value of $J_{pk} = 25A/mm^2$. These tests are done with an initial $T_{wat} = 40°C$ and $V_{wat} = 1m/s$. It can be observed in Figure 5.19b, that the experimentally measured, phase temperature settles to a temperature of approximately 190°C. Considering that the copper used for the motor windings has an insulation class that is rated at 220°C, and the thermal paste used for potting is also rated at 220°C, then this can be considered as a safe temperature. Further reduction in temperature can be achieved by simply increasing V_{wat} or decreasing T_{wat}.

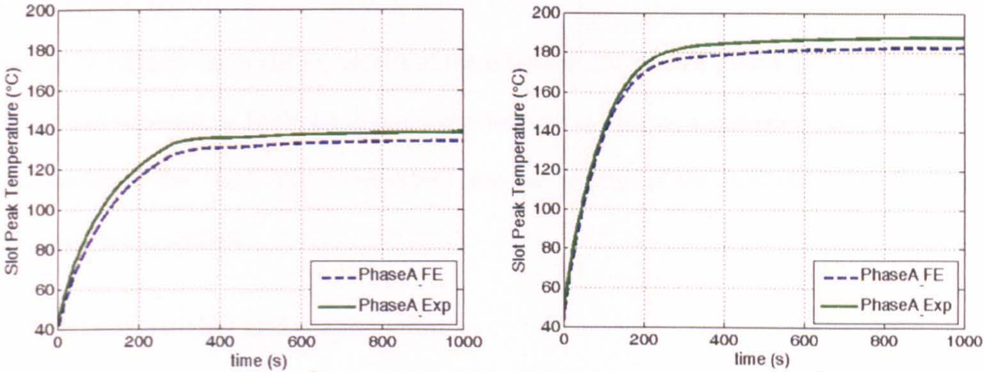

a) $J_{pk} = 20A/mm^2$ b) $J_{pk} = 25A/mm^2$

Figure 5.19 TLPM motor: thermal performance comparison

5.2.4 Conclusion

The experimentally measured, performance capability of the TLPM motor is presented and compared to the predicted capability in tabulated form in Table 5.5, for which the FE models are adjusted with the experimental values of K_{lam}, K_{fill} and k_{eq}. The results are shown for the rated condition of $J_{pk} = 25A/mm^2$. The performance chart clearly illustrates the similarities between the models' and the prototype's results, while also highlighting the excellent force density performance achieved. As mentioned in Section 2.5 and discussed later in the concluding chapter, these values compare excellently with results published in available literature. All this confirms a successful and satisfactory implementation of the TLPM motor for the application mentioned in Section 1.2.1.

	FE	**Experimental**
R_a (Ω)	0.51	0.59
L_a (mH)	10.6	10
A_{rms} (kA/m)	105.6	
J_{rms} (A/mm^2)	17.68	
T_{max} (°C)	180	188.89
F_{lin} (N)	2184.2	2128.5
δ_g (kN/m^2)	36.82	35.88
Force density (N/kg)	93.46	91.5
Force density (kN/m^3)	383.2	381.42

Table 5.5 TLPM motor: final performance chart

5.3 The GT motor

In order to validate the modelling results of the GT motor shown in Figure 4.19 (plots labelled as HP) and tabulated in Table 4.5, a prototype machine is built on a specialised test-rig in the laboratories of the UoN. The construction and the testing of the prototype machine are addressed in this section.

5.3.1 Manufacturing and construction

In order to build up the GT motor of Chapter 3, specific construction and assembly procedures are proposed and tested. Where appropriate, various materials and different assembly techniques are investigated. The manufacturing parameters and geometrical dimensions of the GT motor are given in Table 3.13, Table 4.4 and Table 4.5. The design procedures shown below are all done relative to these parameters and dimensions.

5.3.1.1 The coils

As stated in Section 3.5.2, the GT motor is designed to operate with a double star configuration that utilises a double layer arrangement of concentrated wound coils. This means that the coils can be manufactured prior to assembly.

A. Towards the best K_{fill}

The possibility to pre-manufacture the coils allows a convenient degree of freedom in the search for the best K_{fill} possible. This is done by manufacturing a set of dummy slots with the exact shape and dimensions of the GT motor slot and then winding different sizes and different shapes of wires, in order to find the experimental K_{fill} associated with each test. A general 'look-up' table of K_{fill} vs. wire size/shape is thus achieved.

Figure 5.20a shows one of the manufactured dummy slots, while Figure 5.20b and Figure 5.20c show cut-away sections of these dummy slots, so as to reveal the fill achieved for round and flat copper wire respectively. From these tests, it is observed that the best results in terms of K_{fill} are achieved by the use flat copper wire such as those shown in Figure 5.20c.

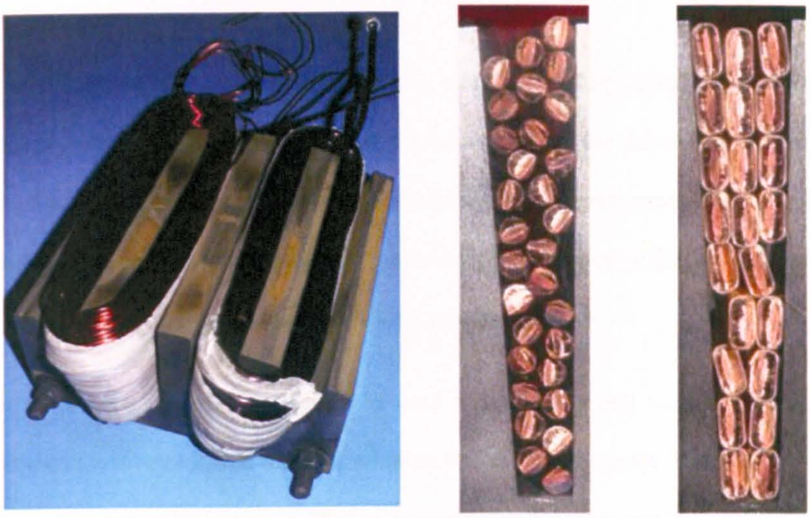

a) Dummy slot b) Round copper c) Flat copper

Figure 5.20 GT motor: K_{fill} tests

The experimental winding tests with the flat copper wire result in considerably high values of K_{fill} to be achieved, mainly because of the better distribution in the slot area that flat wire can give. Due to the presence of the HP in the slot, two different values of K_{fill} can be quoted for the GT motor with each one being valid according to its particular definition of K_{fill}.

The first value is for when considering the ratio of the total copper area (i.e. A_{1cop} * N) to the area actually available for copper. This is shown in the left hand slot of Figure 5.21, where the K_{fill} achieved is 67%. In the case of considering the ratio of the total copper area to the total slot area, then as shown in the right hand slot of Figure 5.21, the value of K_{fill} reached is 62%.

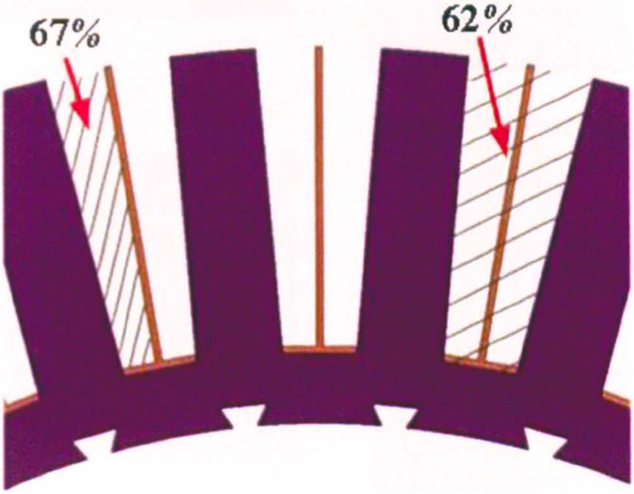

Figure 5.21 GT motor: K_{fill} results

B. Manufacturing the coils

As for the TLPM motor coils, it is decided to manufacture the coils and then utilise high thermally conductive paste as a potting compound to enhance the thermal performance of the machine. To achieve this, a similar concept to the coil former arrangement shown in Figure 5.5 is applied with the obvious difference that the new former must cater for concentrated, axially-wound coils and not the toroid-shaped coils of a tubular machine.

In order to do this, a specialised former is used to produce a coil such as shown in Figure 5.22a. The coil is then removed from the winding former and put in the 'shaping' mould shown in Figure 5.22b. A pressure of up to $2kg/cm^2$ is applied to the sides and the top of the coil so as to achieve the desired dimensions. At this point, the whole set-up is varnished and then heat-cured, such that the coil retains its particular shape, even after removal from the mould. When the varnish has set, the varnished coil is put into the next mould (shown in Figure 5.22c) along with HPs on each side, while thermal paste is applied to all the surfaces of the set-up. A curing time for the thermal paste is once again observed, at the end of which a coil, complete with HPs on each side as shown in Figure 5.22d is produced.

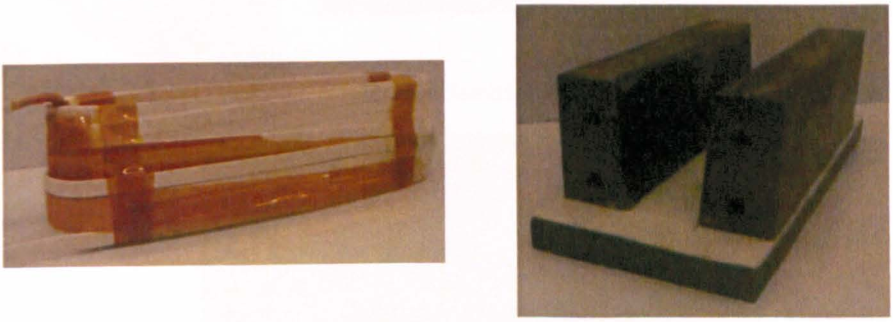

a) Wound coil b) Shaping and varnishing mould

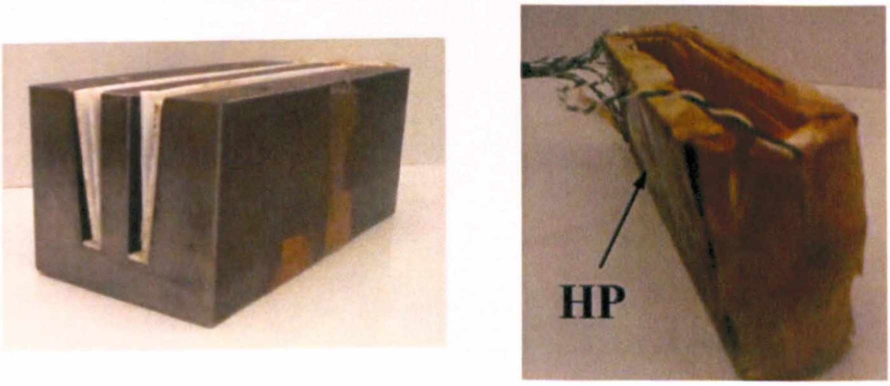

c) Thermal paste mould d) Finished coil

Figure 5.22 GT motor: coil manufacturing

5.3.1.2 The stator assembly

A stator housing (henceforth called the stator shell) incorporating cooling fins to aid in the general thermal performance of the machine is manufactured. This is shown in Figure 5.23a. In order to achieve high mechanical integrity, the CoFe laminations shown in Figure 5.23b are locked to the stator shell by the insertion of a series of copper keys, as shown in Figure 5.23c.

The function of these keys is twofold, firstly they serve for mechanical robustness in terms of the reaction torque on the stator and secondly they enhance the operation of the HP technique, by reducing the thermal path between the bottom of the slot and the cooling fins of the stator shell. It is important to note that thermal paste is applied between all the surfaces of all the components of the stator assembly. A general view of the assembly is shown in Figure 5.23d, illustrating the concept of the locking keys.

a) Stator shell with fins b) CoFe laminations c) Locking keys

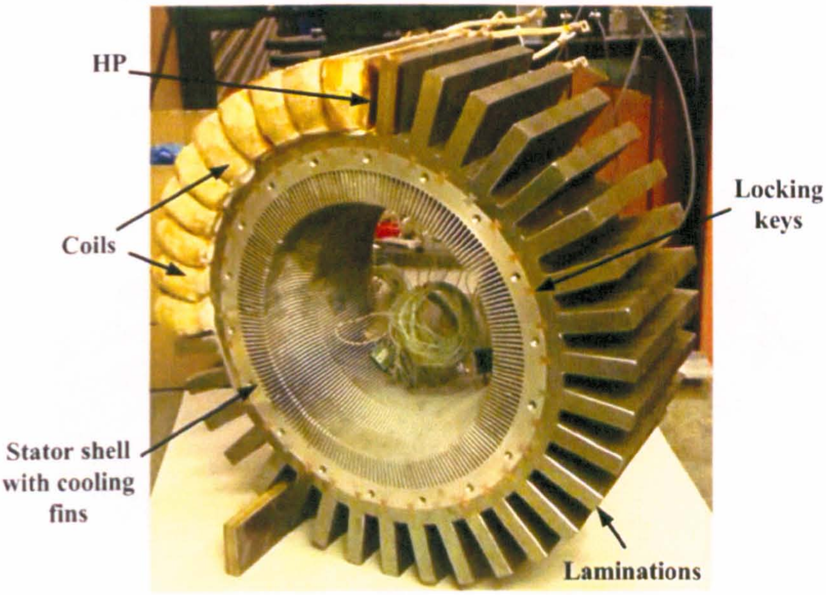

d) Stator assembly

Figure 5.23 GT motor: final stator assembly

5.3.1.3 The rotor assembly

For a machine topology such as shown in Figure 3.38, the outer rotor of the GT motor consists of the PMs, the necessary yoke (henceforth called rotor shell) and any supporting accessories such as the torque transmitting, rotor disk. The PMs are assembled into the rotor shell and held together by the use of high performance glue. Figure 5.24a shows the complete rotor assembly, while Figure 5.24b shows a close up of the PM, full-Halbach array.


a) Assembly b) PMs

Figure 5.24 GT motor: final rotor assembly

5.3.1.4 General assembly and the test-rig

A cross-sectional view of the GT motor assembly is shown in Figure 5.25a, while an exploded view is given in Figure 5.25b. The various components mentioned above can be observed. Considering the mass, the magnetic strength and at the same time the physical fragility of the PMs etc… then to assemble the rotor to the stator, a specialised jig is manufactured in order to assemble the components safely and with the necessary accuracy and concentricity.

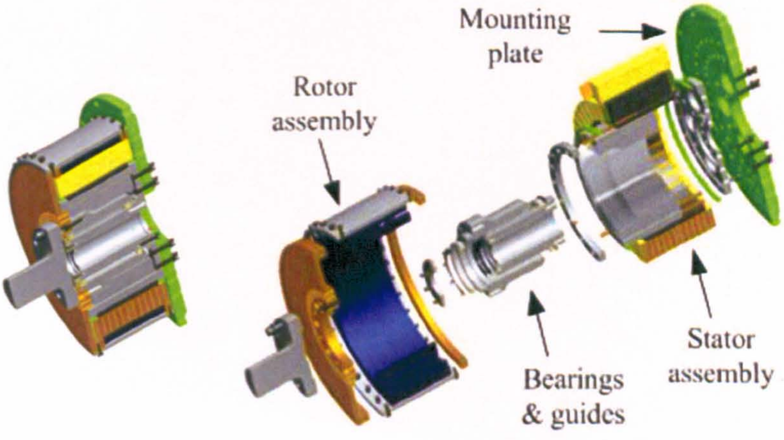

a) Cross-sectional view b) Exploded cross-sectional view

Figure 5.25 GT motor: final motor assembly

The complete motor assembly, which is shown in Figure 5.26, is then assembled on a specialised, heavily instrumented test-rig. Figure 5.27 shows a picture of the general assembly diagram of the test-bed, which includes the GT motor itself, a load induction motor (IM), a gear-box and a torque transducer for measurement purposes.

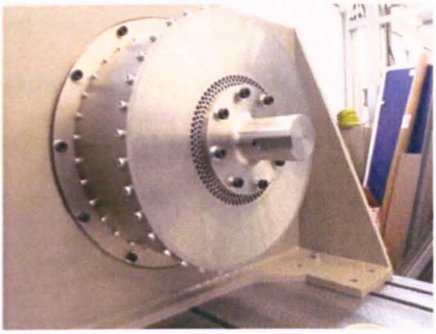

Figure 5.26 GT motor: final prototype

The load IM is a standard, industrial, 110*kW* IM, capable of up to 900*Nm* continuous loads. Due to the obvious difference between the torque capabilities of the load IM and the GT motor, a foot-mounted, planetary gear-box is implemented between them. The ratio of the output to input shafts of the gear-box is 14.88:1, which is enough to compensate between the peak load of 7*kNm* of the GT motor and the 900*Nm* rating of the IM. As regards torque measurements, a rotary torque transducer is included in the test-bed. The transducer is capable of monitoring loads up to 10*kNm* with an accuracy of 0.1%.

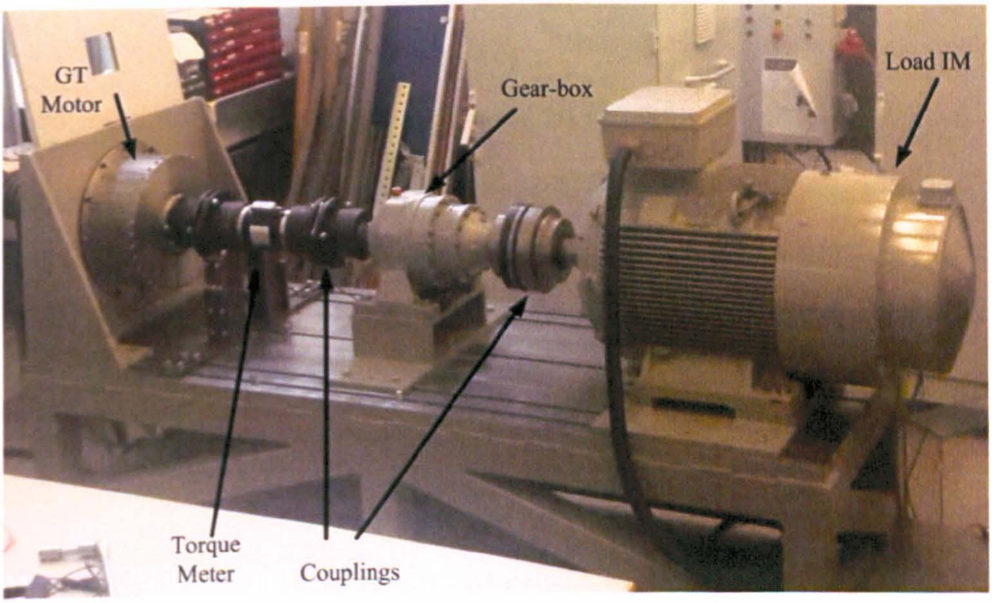

Figure 5.27 GT motor: test-bed

5.3.2 FE 3D verification

Prior to the actual experimental testing of the GT motor, it is decided to build a complete, 3D model of the proposed, GT motor so as to achieve the most accurate results possible with numerical modelling, which can then be used for comparison with experimental results.

The importance of 3D modelling arises from the fact that 2D models do not consider the consequences due to the end-winding effects or the fringing effects at the end of the stack length. These are important because the magnetic flux paths of a motor at the ends of a motor are always different than those in the central part. For 2D modelling, the FE analysis is usually carried out for an assumed plane in this central part. Figure 5.28 shows the 3D, FE model of the GT motor, where it can be observed that the end-windings are assumed to be of cylindrical shape with a radius of approximately half a slot pitch. Figure 5.29 compares the results of the 3D model with those of the 2D model presented in Figure 4.19 (plots labelled as HP).

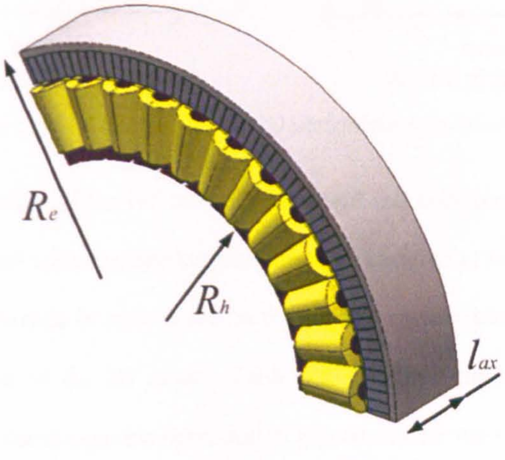

Figure 5.28 GT motor: 3D, FE model

The torque capability of the two models is compared in Figure 5.29a, where it can be seen that a mean decrease of approximately 2.6% in the torque performance is registered. Figure 5.29b illustrates the slightly higher T_{cog} that results from the 3D model. The differences between the results of the 2D and 3D models shown in Figure 5.29a and Figure 5.29b are due to the 3D effects mentioned above. An increase in T_{rip} is observed when the 3D effects are taken into consideration. Figure 5.29c plots the phase back-EMFs of the two models for a rotational speed of 121.1rpm. From Figure 5.29c and Figure 5.29d, it can be observed how the phase back-EMF remains virtually the same for both models.

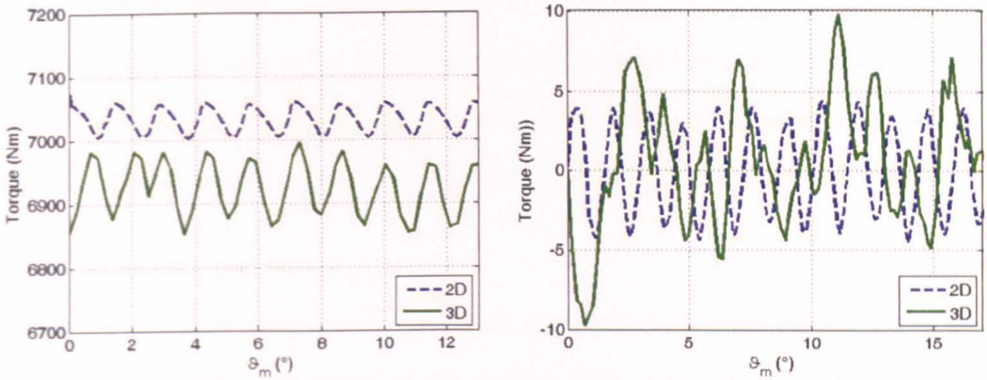

a) Torques b) Cogging torques

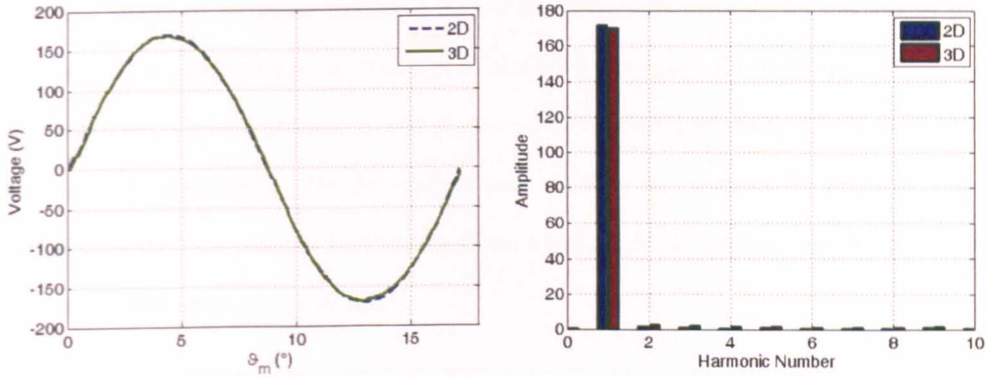

c) Phase back-EMFs d) FFT of Back-EMFs

Figure 5.29 GT motor: 2D vs. 3D performance comparisons

The performance capability of the GT motor is presented and compared in tabulated form in Table 5.6, where the total volume considers also the space required (17*mm*) at each end for the end windings. The difference in mass is due to the slight overestimation in the calculation of the end-winding weight of the 2D model. Table 5.6 illustrates the similarity between the results, thus validating the design and optimisation procedures for the GT motor, presented in this thesis.

	2D	**3D**
Total active mass (*kg*)	108.8	108.5
Total volume (m^3)	0.0311	0.0311
Mean *T* at peak load condition (*Nm*)	7049.6	6979.4
δ_g at peak load condition (kN/m^2)	175.95	174.2
Peak of T_{cog} (*Nm*)	4.2	9.77
T_{rip} at peak load condition (%)	0.7	3.31
Torque density at peak load condition (*Nm/kg*)	64.79	64.33
Torque density at peak load condition (kNm/m^3)	226.68	224.42

Table 5.6 GT motor: 2D vs. 3D performance comparison chart

5.3.3 Tests and results

A series of tests are done on the experimental rig of Figure 5.27, in order to validate the GT motor performance and compare the experimental results to the modelling results as given in Figure 4.19 (plots labelled as HP), Figure 5.29 and tabulated in Table 4.5 and Table 5.6.

5.3.3.1 Measurable parameters

Having the assembled motor and rig permits the measurement of certain parameters that are critical to the operation and control of the machine. Table 5.7 compares the predicted and measured values of the phase resistance R_a and the phase inductance L_a for one star of the machine. These parameters are measured at an ambient temperature. As can be observed, good similarity exists for both parameters with prediction errors of approximately 4.18% and 6.59% for R_a and L_a respectively. The FE analysis does not take into account the length and the resistance of the inter-phase and connection leads, which could be the main contributing factor in the prediction errors of R_a and L_a.

	FE	**Experimental**
R_a (Ω)	0.215	0.224
L_a (mH)	4	4.282

Table 5.7 GT motor: measurable parameters comparison

5.3.3.2 No load back-EMF

In order to measure the no load back-EMF of the GT motor, the phase windings are left on open circuit and the load IM is used as a prime mover to spin the rotor of the GT motor at a constant speed of $80.8rpm$. The back-EMF is observed and recorded via a high bandwidth oscilloscope, in order to measure as much as detail as possible. Figure 5.30a shows the measured signal and also compares it to the predicted 2D and 3D back-EMFs. Figure 5.30b compares the harmonic spectra of the measured back-EMF to the FE-predicted wave-forms. From the figures, it can be observed that the measured back-EMF is very similar to the predicted one. The FE induced voltage is slightly higher than the measured waveform and this can also be observed from the slightly higher value of the fundamental in Figure 5.30b. The slight difference between the signals can be safely attributed to experimental and manufacturing tolerance.

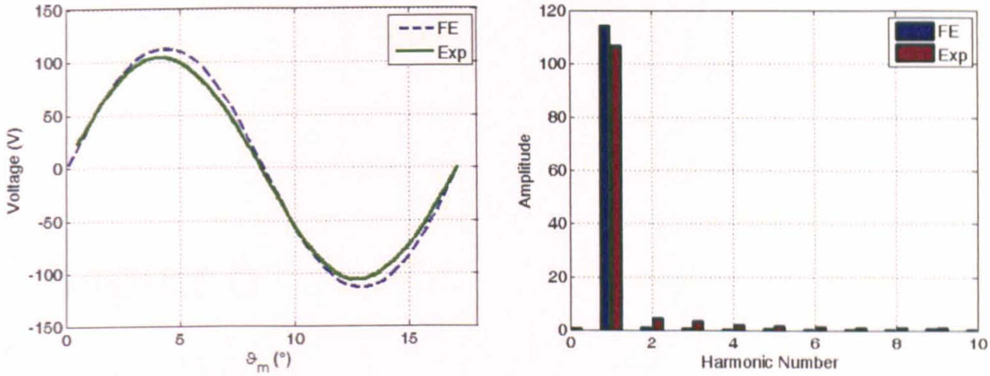

a) Back-EMF b) FFT of back-EMF

Figure 5.30 GT motor: back-EMF comparison

5.3.4 Conclusion

The performance chart shown in Table 5.6 clearly illustrates and highlights the excellent torque density performance achieved. As mentioned in Section 3.6 and discussed later in the concluding chapter, such torque density values are unprecedented in the available literature, which could make the GT motor a point of reference for future research.

One of the main points to address in the immediate future is the completion of the experimental validation of the GT motor. At the time of writing of this thesis, the power electronics and the control for the load IM motor is completed and operational. This permits to perform all the no load tests such as shown in Figure 5.30 and Table 5.7. In fact, these preliminary tests show a clear similarity between the modelling and the prototype results, which is a good indication of the validity of the models used to predict the performance of the GT motor.

On the other hand, the control and power electronics for the GT motor itself is still under construction which means that no experimental results in terms of the load conditions are available at the time of submission of this thesis. However, this lack of experimental data does not mean that the GT motor project for the application of Section 1.3.1 is in any way, lagging behind its pre-set time schedule or general project plan, but only indicates that the thesis submission deadline has been reached. It is projected to have the complete test results in the very near future.

Chapter 6
Conclusion

The implementation of DD systems (where no mechanical gearing or connections between the machine and its load is required) is a very attractive solution for environments where reliability requirements are very important, such as for the aerospace industry. To implement such solutions (without any mechanical advantages), electrical machines with high torque/force density are required. This boils down to the ability to maximise the peak shear stress the device can produce as well as the peak shear stress in relation to the current loading, i.e. both the electro-magnetic and thermal limits. At times these two objectives are conflicting and optimisation strategies specific to the particular application can be required. The work presented in this thesis has been focused on extending the capabilities of high performance, electrical machines, especially in terms of torque/force density capabilities.

DD solutions for the applications of Section 1.2.1 and Section 1.3.1 have been presented, showing excellent torque and force performances. Considering the case of the GT motor, the peak torque density performances are unprecedented. These DD solutions are achieved by employing novel electro-magnetic and thermal management structures and optimisation procedures, as presented in this thesis. Conclusions, discussions, validations and observations were presented throughout all the stages of this work, thus this final chapter is mainly concerned with providing a brief outline of the general conclusions and 'points to note', that emerged during the course of this work. Some ideas for future work are also included.

6.1 The TLPM motor

The feasibility of using a TLPM motor instead of a mechanically geared EMA for the application described in Section 1.2.1, has been investigated in this work. As previously mentioned, the successful implementation of a DD solution such as the TLPM motor depends on achieving satisfactory performance capabilities for the available space and maximum permissible mass.

6.1.1 General overview

In general, it can be concluded that the work presented in this thesis, has tried to achieve the goal of a high, force density capability by addressing and pushing the boundaries set by the electro-magnetic and thermal limits of the machine.

As shown in Chapter 2, satisfactory electro-magnetic performance is achieved by the selection of the best possible configurations in terms of winding arrangements, slot/pole combinations and geometrical dimensioning. For the available space envelope, a number of parameters have been investigated, via the use of analytical and FE models, in order to achieve the best performing machine topology. The electro-magnetic analytical models which were derived for both SMPM and IPM configurations can be used as tools for design procedures that require much iteration while still being very time efficient. The FE models which have been shown by experimental measurements to be highly accurate can then be used to finalise the designs.

A new approach to improve the thermal performance of electrical machines by minimising the thermal resistance has been proposed, investigated and validated in this thesis. The concept of this novel, thermal management technique was presented in Chapter 4. The lumped parameter analytical models are highly efficient tools that can be used to drastically minimise computational time.

The thermal performance of the TLPM motor which is dependent on its fluid cooling arrangement was enhanced by adopting this thermal management technique. The resulting benefits from its implementation were investigated in Section 4.5.1, where it was shown how the resulting decrease in slot hot-spot temperature could be used to increase the current loading to higher values, thus improving the force density performance of the machine.

The predicted results for the TLPM motor are shown in Figure 4.14 and tabulated in Table 4.3, with more realistic results that consider the effect of K_{lam} shown in Figure 5.14 and Table 5.3. To validate the modelling results, a prototype machine was built and tested. Section 5.2 addresses the construction and manufacturing procedures used for the building of the prototype. In Section 5.2.2, it was shown how the 'sunshine' structure adopted for the construction of the stator of the TLPM motor, inevitably results in a 'loss' of soft magnetic material that automatically reduces the magnetic flux available for the production of the required force. Regarding this, an interesting point for future investigation might be the comparison between the performances of a 'sunshine' structure stator and that of a machine made from SMC material. This would confirm whether the effect of K_{lam} is preferable to the inherent, reduced performance potential of the SMC material.

Section 5.2 also illustrates the experimental tests done, which show that when the effects of K_{lam}, K_{fill} and k_{eq} are considered in the FE models, excellent similarity between the modelling results and the measured results is achieved. In fact with the FE models equipped with the experimentally measured values of these parameters, the prediction errors of the models are minimal, again confirming the value of the modelling structures presented in this thesis.

6.1.2 General conclusions

The performance capabilities of the prototype, TLPM motor for the rated current loading are tabulated below in Table 6.1. The mass and volume values are shown as including the presence of both active and non-active components.

	TLPM motor
F_{lin} (*kN*)	2128.5
Mass (*kg*)	23.26
Stator volume (*cm^3*)	5600
δ_g (*kN/m^2*)	35.88
Force density (*N/kg*)	91.51
Force density (*N/cm^3*)	0.38

Table 6.1 Simplified TLPM motor performance chart

The excellent performance of the TLPM motor in terms of its force density performance relative to other high performance, tubular machines can be appreciated more clearly from Table 6.2. This comparison chart tabulates the topology, the mode of operation and the force-to-volume performance of a number of PM, linear motors referenced in literature. Unfortunately it is virtually impossible to include and compare the force density performance in terms of the force-to-mass ratio as this type of information is not readily available in the referenced publications.

	Topology		**Operation**	**Force density** (*N/cm*^{3})
	PMs	**Air-gap**		
Bianchi et al. [84]	SMPM	Single	Continuous	0.35
Bianchi et al. [84]	IPM	Single	Continuous	0.25
Wang et al. [66]	Quasi-Halbach	Single	Continuous	0.43
TLPM motor	IPM	Single	Continuous	0.38
Danson et al. [79]	SMPM	Double	Continuous	0.35
Cavarec et al. [87]	IPM	Multi	Continuous	1
Ziegler et al. [88]	SMPM	Multi	Pulsed	4.8

Table 6.2 Force density comparison chart

From Table 6.2, it can be observed that apart from the multi air-gap technologies (which however state their performances relative to the active volume and not to the total volume of the machine), then only the quasi-Halbach motor exceeds the TLPM motor's performance in terms of force-to-volume ratio. It is however important to point out that as seen in Section 3.5.3, this type of PM configuration is burdened with extra complexity, cost and demagnetisation issues; issues which for the TLPM motor are non-existent. The same is valid for the complexity and mechanical issues synonymous with the double and multi air-gap technologies.

In relation to all this, it can be said that the relative simplicity, the low cost and the general robustness qualities, inherent for the TLPM motor are added benefits of this machine. This indicates the quality of the design methodologies proposed in this thesis.

6.2 The GT motor

The design, optimisation and implementation of a PMSM with an out-runner and a full-Halbach array on the rotor, as a DD solution for the application of Section 1.3.1 has been investigated in this thesis. The successful implementation of such a DD solution depends on achieving satisfactory performance capabilities for the available space and maximum permissible mass.

6.2.1 General overview

As for the TLPM motor, the goal to achieve the best performance has been addressed by pushing the electro-magnetic and thermal boundaries of the proposed machine. A history of the evolution of the GT motor and the applied design methodologies is given in Chapter 3, where it is seen how for the available space envelope, various techniques to enhance the electro-magnetic limit are proposed and investigated.

In order to achieve the required performance level, an innovative methodology that combines a series of performance enhancing strategies into a well-defined structure was proposed and investigated in Chapter 3. The methodology starts off from an initial design (obtained from the initial trade-off studies) and then applies a number of performance improvement techniques in a logical 'journey' towards the optimum electro-magnetic design. As can be observed in Section 3.3 and Section 3.5, the methodology investigates a sequence of techniques (such as the use of an outer rotor, the use of CoFe laminations, the use of Halbach arrays and the use of open slots) , where for each step it manages to 'build up' on the advantages of the previous technique.

However, the flexible nature of the methodology also permits the 'real-time' intertwining of 'particular application oriented' strategies such as the investigation and adoption of a high performance stator arrangement (double star, double layer winding layout) of Section 3.5.2 and the PM demagnetisation analysis of Section 3.5.3. The detailed PM demagnetisation analysis and the innovative solution for the practical implementation of a full-Halbach array are also points to highlight in favour of the design procedures with which the GT motor was realised.

The thermal performance of the GT motor which is dependent on the forced air arrangement (designed in parallel to the electro-magnetic design) is also enhanced by the thermal management technique of Chapter 4. The fact that the GT motor operation is constrained by a transient duty cycle (i.e. the motor never actually reaches steady state) and the nature of the cooling arrangement resulted in that the benefits of the HP technique for the GT motor are much reduced relative to the case of the TLPM motor. However, the importance of this technique for the GT motor was illustrated in Figure 4.19f and Figure 4.21, which prove that the implementation of the HP technique results in achieving a final slot hot-spot temperature that 'respects' the thermal limits set by the insulation and the material properties.

As discussed previously, at the time of writing, not all the experimental data is available for the GT motor. Due to this the load condition results of the FE models were verified by comparing to the results of a final, 3D model. Figure 5.29 and Table 5.6 compare the performance results of the two models, which show excellent similarity and thus confirm the value of the modelling structures presented for the realisation of the GT motor.

6.2.3 General conclusions

Considering all the above, then it is appropriate to state that the proposed GT motor is an innovative solution for the aircraft taxiing application with all the intrinsic advantages, brought about by the directly driven, drive-train. It is estimated that a 4-5% reduction in fuel burning and carbon emissions can be achieved by the introduction of such a motor onto a modern aircraft such as described in Section 1.3.1, with other inherent advantages being the lower noise pollution in airports and the reduction of wear on the landing gear brakes.

This thesis has shown the feasibility of manufacturing such an electrical machine and has presented a clearly defined, design methodology to achieve the required performances. With the implementation of the mentioned procedures, an excellent peak torque density performance was achieved. The final results of the proposed motor are shown in Table 6.3, which indicates a torque-to-mass and torque-to-volume performance capabilities of approximately $64.33Nm/kg$ and $224.42kNm/m^3$ respectively.

	GT motor
T (Nm)	6979.4
Mass (kg)	108.5
Volume (m^3)	0.0311
δ_g (kN/m^2)	174.2
Torque density (Nm/kg)	64.33
Torque density (kNm/m^3)	224.42

Table 6.3 Simplified GT motor performance chart

It is important to point out that due to thermal limitations, these values are for a peak load condition, the duration of which never lasts more than 20 seconds. However, it is also true that to the author's knowledge, based on the research done during the course of this thesis and on the consulted literature, no such values of torque density (whether peak or continuous) have been reported in literature before, making the proposed, GT motor a considerable technological achievement and a possible point of reference for future research.

6.3 Major contributions to research

The major contributions to technical research for high performance, DD machines, developed during the course of this research program and thesis can be listed as follows.

1) Accurate, electro-magnetic, analytical and numerical FE models are presented for both the TLPM motor and the GT motor. The models have been shown to achieve minimum prediction errors with reasonable time penalties, resulting in the possibility of heavy iteration during optimisation to achieve the optimal designs.
2) Accurate, thermal, analytical and numerical FE models, which result in the possibility of constant monitoring of thermal performance during the electro-magnetic iteration processes mentioned in 1).
3) An innovative methodology that investigates the use of performance enhancement techniques in an organised and logical structure, resulting in excellent improvements of the torque density. The methodology was applied to the design of the GT motor, where it was seen how it is possible to combine the proposed structure with more 'application-oriented' strategies in order to achieve an optimum design.

4) A detailed, demagnetisation analysis procedure for Halbach arrays. Using this procedure an innovative, practical solution for full-Halbach arrays was conceived which virtually eliminates the possibility of demagnetisation while still enjoying the benefits synonymous with full-Halbach arrays
5) A novel, thermal management technique for electrical machines that addresses thermal hot-spot issues by minimising the thermal resistance between the hot-spot and the cooling arrangement. A parametric solution was first investigated resulting in a research output that can be applied universally for any type of electrical machine, thermal application. The technique was shown to be extremely advantageous when applied for machines that have fluid cooling arrangements and operate mainly in steady state such as the TLPM motor, while reduced benefits (benefits nonetheless) can be achieved for other types of cooling arrangements and operating conditions.

The research presented in this thesis has also resulted in a number of published works in peer reviewed journals [47, 141] and conference proceedings [17, 30, 56, 89, 142, 143], one of which [142] also resulted in achieving the best paper award of its respective conference. It is also projected that with the completion of the experimental work concerning the GT motor, a number of papers will be submitted for publication within the next few months.

6.4 Future work

Apart from the obvious, experimental validation of the GT motor once the test-rig is completely assembled, there are several other areas that can be identified as interesting targets for future research.

1) Investigations of alternative designs of the TLPM motor in an effort to improve the force-to-mass performance capability. This might consider the use of double or multi air-gap technologies with special focus on
    a. reducing the complexity associated with such topologies.
    b. diminishing the extra mass due to the non-active components (such as bearings and guides) synonymous with multi air-gap technologies.

2) Development of an automated, design environment that interfaces the various electromagnetic and thermal models presented in this thesis. This would help reduce even more the time required for generating the optimal design of the required machines.
3) An investigation on the effects of K_{lam} for tubular machines. Would a SMC material with its reduced performance or a solid soft magnetic material with all its iron losses actually perform better than a stator 'sunshine' structure that intrinsically includes an inevitable loss of lamination material?
4) An investigation looking at the possible improvement of the HP technique which might be achieved by looking at different materials that could be used. An extremely interesting option would be to investigate the use of phase change materials. This type of material could also be utilised and investigated for replacing the traditional potting of end-windings that use standard thermal potting compounds.
5) A second generation, GT motor (already on-going) with focus on
    a. possible measures to further improve torque density performance
    b. the ability for it to be integrated into the main landing gear of an aircraft.
6) Studies to investigate the system integration mentioned in 5),
    a. detailed mechanical analyses that consider all the vibrations and shocks related to aircraft taxiing operation.
    b. detailed thermal analyses that consider the effects of adjacent components (such as the aircraft brakes).
7) Development of techniques to improve the manufacturability of pre-formed coils.

Appendix A
Modelling: Electro-magnetic

A.1 Basic electro-magnetic definitions

For the simple, magnetic circuit shown in Figure A.1, the basic definitions are given in (A.1-A.4), where H_c is the coercive force of the PM, $\mathfrak{R}_m$ and $\mathfrak{R}_g$ are the reluctances of the PM and the air-gap respectively and A_m and A_g are the cross-sectional areas of the PM and the air-gap respectively. Assuming that the magnetic steel is infinitely permeable, then it can be said that only the PM and the air-gap have a reluctance and thus the air-gap flux ϕ_g is simply the source MMF divided by the sum of these two reluctances.

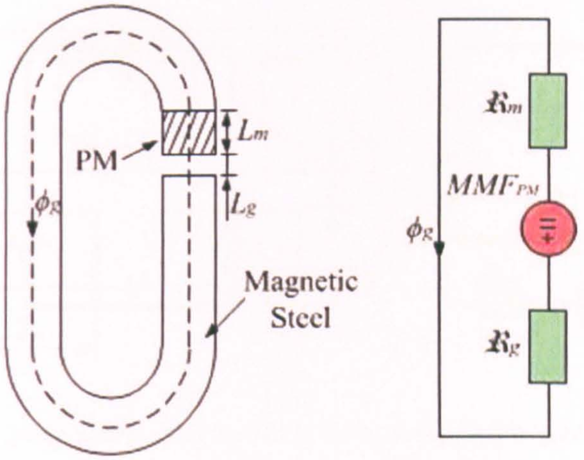

Figure A.1 Simple electro-magnetic circuit

$$MMF_{PM} = L_m \times H_c \tag{A.1}$$

$$\mathfrak{R}_m = \frac{L_m}{\mu_0 \mu_{rrec} A_m} \tag{A.2}$$

$$\mathfrak{R}_g = \frac{L_g}{\mu_0 A_g} \tag{A.3}$$

$$\phi_g = B_g A_g = \frac{MMF_{PM}}{\mathfrak{R}_m + \mathfrak{R}_g} \tag{A.4}$$

A.2 TLPM Motor: the SMPM configuration

Considering the structure of a TLPM motor with a SMPM configuration such as shown in Figure 2.2 and considering the assumptions listed in Section 2.2.1.1, then the no-load air-gap flux density B_g as described by (2.6) can be derived as follows.

One pole pitch of the TLPM motor of Figure 2.2 can be depicted as in Figure A.2, which shows the magnetic structure of the set-up and its equivalent reluctance network and where $\Re_m$' represents the leakage flux in the air-gap.

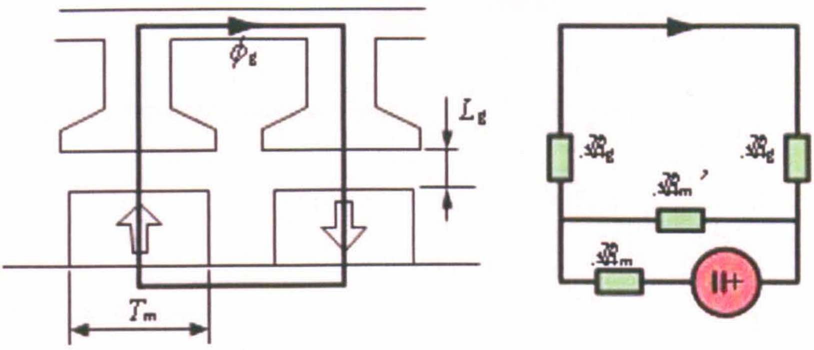

Figure A.2 One pole pitch of the TLPM motor with a SMPM configuration

The cross-sectional area A_m of one PM is

$$A_m = \pi T_m (R_m + R_r) \tag{A.5}$$

Substituting into (A.2), then

$$\Re_m = \frac{L_m}{\mu_0 \mu_{rrec} \times \pi T_m (R_m + R_r)} \tag{A.6}$$

The area of the air-gap A_g, through which the flux due to only one PM flows, is

$$A_g = \pi T_m (R_{in} + R_m) \tag{A.7}$$

Substituting into (A.3), then

$$\Re_g = \frac{L_g}{\mu_0 \times \pi T_m (R_{in} + R_m)} \tag{A.8}$$

The residual flux ϕ_{rem} of one PM is given in (A.9) where B_{rem} is the PM remnant flux density.

$$\phi_{rem} = B_{rem} A_m = B_{rem} \times \pi T_m (R_m + R_r) \tag{A.9}$$

Thus, considering Figure A.3 and assuming $\Re_m' = \Re_m$ the total air-gap flux ϕ_g over one pole pitch can be described by (A.10).

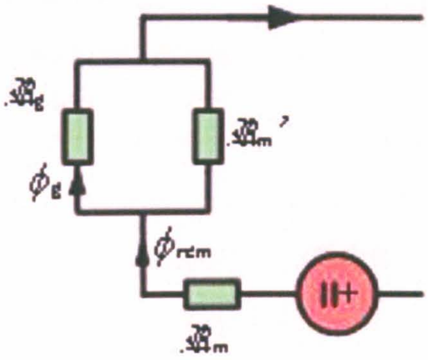

Figure A.3 Simplified magnetic network of the TLPM motor with SMPMs

$$\phi_g = \phi_{rem} \times \frac{\Re_m}{\Re_m + \Re_g} \qquad (A.10)$$

Substituting (A.6), (A.8) and (A.9) into (A.10) and rearranging

$$\phi_g = B_{rem} \pi T_m (R_m + R_r) \times \frac{L_m(R_{in} + R_m)}{L_m(R_{in} + R_m) + \mu_{rrec} L_g (R_m + R_r)} \qquad (A.11)$$

Substituting for (A.11) and (A.7), the no-load flux density B_g is as described in (A.12)

$$B_g = \frac{\phi_g}{A_g} = B_{rem} \times \frac{1}{\frac{(R_{in} + R_m)}{(R_m + R_r)} + \left(\frac{\mu_{rrec}}{L_m}\right) L_g} \qquad (A.12)$$

A.3 TLPM Motor: the IPM Configuration

Considering the structure of a TLPM motor with an IPM configuration such as shown in Figure 2.3 and considering the assumptions listed in Section 2.2.1.1, then the no-load air-gap flux density B_g as described by (2.8) can be derived as follows.

One pole pitch of the TLPM motor of Figure 2.3 can be depicted as in Figure A.4, which shows the magnetic structure of the set-up and its equivalent reluctance network and where $\mathfrak{R}_m$' represents the leakage flux in the air-gap. The extra length X_g allows for any fringing at the ends of the PMs to be included in the calculations. Assuming that $X_g = L_g$, then this gives rise to the term $2\mathfrak{R}_g$ as shown in the magnetic network.

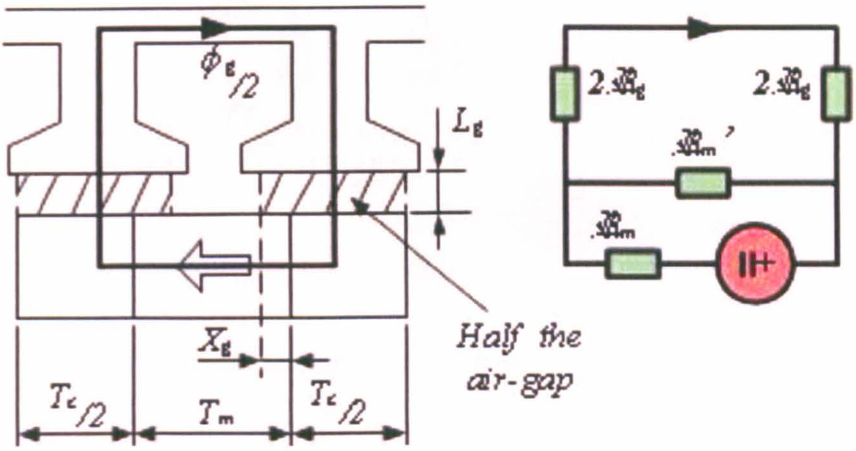

Figure A.4 One pole pitch of the TLPM motor with an IPM configuration

The cross-sectional area A_m of the PM through which the PM flux ϕ_{rem} flows is

$$A_m = \pi(R_m^2 - R_h^2) \tag{A.13}$$

Substituting into (A.2), then

$$\mathfrak{R}_m = \frac{T_m}{\mu_0 \mu_{rrec} \times \pi(R_m^2 - R_h^2)} \tag{A.14}$$

Letting $T_c = (T_p - T_m)$, then the total area of the air-gap A_g, over one pole pitch (i.e. combining the two shaded areas) is

$$A_g = \pi \frac{T_c}{2}(R_{in} + R_m) \tag{A.15}$$

and substituting into (A.3), then

$$\Re_g = \frac{L_g}{\mu_0 \times \pi \frac{T_c}{2}(R_{in} + R_m)} \tag{A.16}$$

The residual flux ϕ_{rem} of one PM is given in (A.17) where B_{rem} is the PM remnant flux density.

$$\phi_{rem} = B_{rem}A_m = B_{rem} \times \pi(R_m^2 - R_h^2) \tag{A.17}$$

Thus, considering Figure A.5 and assuming $\Re_m' = \Re_m$ the total air-gap flux ϕ_g over one pole pitch can be described by (A.18)

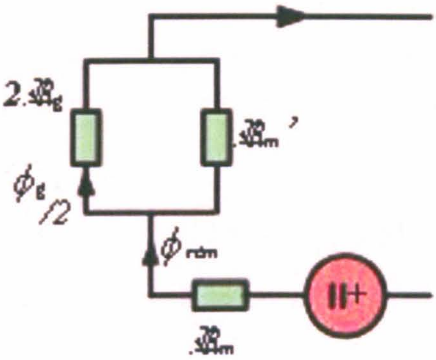

Figure A.5 Simplified magnetic network of the TLPM motor with IPMs

$$\phi_g = 2\phi_{rem} \times \frac{\Re_m}{\Re_m + 2\Re_g} \tag{A.18}$$

Substituting (A.14), (A.16) and (A.17) into (A.18) and rearranging

$$\phi_g = 2\pi B_{rem}(R_m^2 - R_h^2) \times \frac{T_m \frac{T_c}{2}(R_{in} + R_m)}{T_m \frac{T_c}{2}(R_{in} + R_m) + 2\mu_{rrec}L_g(R_m^2 - R_h^2)} \tag{A.19}$$

Substituting for (A.19) and (A.15), the no-load flux density B_g is as described in (A.20)

$$B_g = B_{rem} \times \frac{\frac{T_m}{\mu_{rrec}}(R_m^2 - R_h^2)}{L_g(R_m^2 - R_h^2) + \left(\frac{T_m}{\mu_{rrec}}\right)\left(\frac{T_c}{4}\right)(R_{in} + R_m)} \tag{A.20}$$

A.4 GT Motor: demagnetisation analysis

Starting from (3.2) in Section 3.5.3.2, then the equivalent demagnetisation proximity field in terms of H can be obtained as follows.

The PM flux density field $\underline{B}$ can be described by (A.21) where $\underline{M}$ is the vector mentioned in (3.2), $\underline{H}$ is the energy field, $\underline{H_c}$ is the PM coercive force and μ_0 is the permeability of free space.

$$\underline{B} = \mu_0(\underline{H} + \underline{M}) = \mu_0\left(\underline{H} - \underline{H_c}\right) \qquad (A.21)$$

Let M be the norm of the vector $\underline{M}$, and

$$\underline{M}/_M \equiv \underline{m} \qquad (A.22)$$

then

$$\underline{B} = \mu_0(\underline{H} + \underline{M}) = \mu_0(\underline{H} - H_c\underline{m}) \qquad (A.23)$$

Therefore

$$\underline{B} \cdot \underline{m} = \mu_0(\underline{H} \cdot \underline{m} - H_c) \qquad (A.24)$$

Considering that

$$B_m \equiv \underline{B} \cdot \underline{m} \quad \text{and} \quad H_m \equiv \underline{H} \cdot \underline{m} \qquad (A.25)$$

then

$$B_m(H_m) = \mu_0(H_m - H_c) \qquad (A.26)$$

Considering H_{demag} as the PM material demagnetisation value in terms of H, then letting

$$B_{demag} \equiv B_m(H_{demag}) = \mu_0(H_{demag} - H_c) \qquad (A.27)$$

and substituting (A.24) and (A.27) into (3.2), and taking care to set ($H_{demag} < H_c$), then the demagnetisation proximity field H_{prox} can be expressed as

$$H_{prox} = H_{demag} - \underline{H} \cdot \underline{M}/_M \qquad (A.28)$$

A.5 GT Motor: short circuit analysis

For a PM machine such as shown in Figure 3.38, the voltages in the *d-axis* and *q-axis*, V_d and V_q can be described by (A.29) and (A.30) respectively, where R_{ph} is the resistance of one phase, ϕ_m is the PM flux, L_{ph} is the phase self-inductance of the motor, ω is the rotating velocity and I_d and I_q are the currents along their respective axes.

$$V_d = R_{ph}I_d - L_{ph}\omega I_q \qquad (A.29)$$

$$V_q = R_{ph}I_q + L_{ph}\omega I_d + \omega\phi_m \qquad (A.30)$$

Assuming a short circuit along all the phases, then $V_d = V_q = 0$, thus

$$I_d = -\frac{L_{ph}\omega^2\phi_m}{R_{ph}^2 + L_{ph}^2\omega^2} \qquad (A.31)$$

$$I_q = -\frac{R_{ph}\omega\phi_m}{R_{ph}^2 + L_{ph}^2\omega^2} \qquad (A.32)$$

And considering that

$$\lim_{\omega\to\infty} I_{sc} = \lim_{\omega\to\infty}\sqrt{I_d^2 + I_q^2} \qquad (A.33)$$

Then

$$\lim_{\omega\to\infty} I_{sc} = {}^{\phi_m}\!/_{L_{ph}} \qquad (A.34)$$

From the above, the braking torque T_{sc} can be described by (A.35), where P is the number of pole pairs and I_{q_sc} is the generated short circuit current in the *q-axis*.

$$T_{sc} = -\frac{3}{2} \times P \times \phi_m I_{q\_sc} \qquad (A.35)$$

Appendix B
Modelling: Electrical and thermal

B.1 TLPM motor: natural cooling

Considering the structure of the stator of a TLPM motor such as shown in Figure 2.2 and Figure 2.3 and considering the assumptions listed in Section 2.2.1.2, then total copper loss P_{cu_tot} as described by (2.10) can be derived as follows.

Considering assumption 3) of Section 2.2.1.2, then the average length of copper wire L_{1turn}, used to achieve a complete turn is

$$L_{1turn} = \pi(R_{in} + R_t) \tag{B.1}$$

The total, average length of copper used per coil L_{1coil} is

$$L_{1coil} = N \times L_{1turn} = \pi N(R_{in} + R_t) \tag{B.2}$$

And one phase of the double layer machines is made up of 8 coils, thus

$$L_{1phase} = 8\pi N(R_{in} + R_t) \tag{B.3}$$

Let A_{slot} be the area of one slot, then the cross-sectional area of one copper wire is

$$A_{1cop} = \frac{A_{slot} \times K_{fill}}{2N} = \frac{T_{sl}(R_t - R_{in})K_{fill}}{2N} \tag{B.4}$$

The phase current I_{rms} is related to the copper current density J_{rms} by

$$I_{rms} = J_{rms} \times A_{1cop} = J_{rms} \times \frac{T_{sl}(R_t - R_{in})K_{fill}}{2N} \tag{B.5}$$

Such that

$$I_{rms}^2 = J_{rms}^2 \times \frac{{T_{sl}}^2 {K_{fill}}^2 (R_t - R_{in})^2}{4N^2} \tag{B.6}$$

Copper loss is as described by (B.7) where ρ_{cu} is the electrical resistivity of copper, L is the total length of copper used and A is the cross-sectional area of the copper.

$$P_{cu} = I^2 R = I^2 \frac{\rho_{cu} L}{A} \tag{B.7}$$

Thus the copper loss generated by one phase of the machine is

$$P_{cu\_1phase} = I_{rms}^2 \frac{\rho_{cu} \times L_{1phase}}{A_{1cop}} \qquad (B.8)$$

And the total copper loss generated by the whole machine is

$$P_{cu\_tot} = 3 \times I_{rms}^2 \frac{\rho_{cu} \times L_{1phase}}{A_{1cop}} \qquad (B.9)$$

Substituting (B.3), (B.4) and (B.6) into (B.9) and rearranging, then P_{cu_tot} is

$$P_{cu\_tot} = \frac{\pi}{2} \times \rho_{cu} N_{slots} \times J_{rms}^2 \times T_{sl} K_{fill} (R_t - R_{in})(R_t + R_{in}) \qquad (B.10)$$

B.2 TLPM motor: fluid cooling

In order to achieve the electrical models presented in Section 2.3.2, the mechanical and thermo-dynamic behaviour of the water-jacket must be investigated. This is done in order to achieve an analytical expression for the highly important convection heat transfer coefficient h_{cv} due to the flow of the coolant in the water-jacket.

B.2.1 Design of the water-jacket

Considering Figure 2.8, then the hydraulic diameter of the water-jacket d_h is as given in (B.11) where P_h is the perimeter of the ducts in contact with water and A_h is the hydraulic cross-sectional area of the coolant flow.

$$d_h = \frac{4A_h}{P_h} \qquad (B.11)$$

The Reynolds number R_{ey} of the system can then be found from (B.12) where v_{sc} is the kinematic viscosity of the water-based fluid.

$$R_{ey} = \frac{d_h V_{wat}}{v_{sc}} \qquad (B.12)$$

From [106], the Prundtl number P_r of water at 40°C is 4.34. Assuming this value for the water-based fluid, then as stated in [107], when $P_r \geq 1.5$, the Nusselt number N_u of the system can be calculated from (B.13), where l_{wat} is the peripheral length along the ducts through which the coolant fluid flows.

$$N_u = 0.012\left(R_{ey}^{0.87} - 280\right) \times P_r^{0.4}\left(1 + \sqrt[3]{\left(\frac{d_h}{l_{wat}}\right)^2}\right) \qquad (B.13)$$

Thus, the convection heat transfer coefficient h_{cv} due to the flow of the coolant in the water-jacket, is as described by (B.14) where k_{wat} is the thermal conductivity of water.

$$h_{cv} = \frac{k_{wat} N_u}{d_h} \qquad (B.14)$$

B.2.2 The lumped parameter thermal model

Consider a rectangular volume as shown in Figure B.1a and a segment of an annulus as in Figure B.1b of a thermally conductive material where A is the cross-sectional area through which the heat is conducted. For these two general shapes, the basic equations that describe their respective thermal resistances are as given in (B.15) and (B.16), where k is the thermal conductivity of the material used.

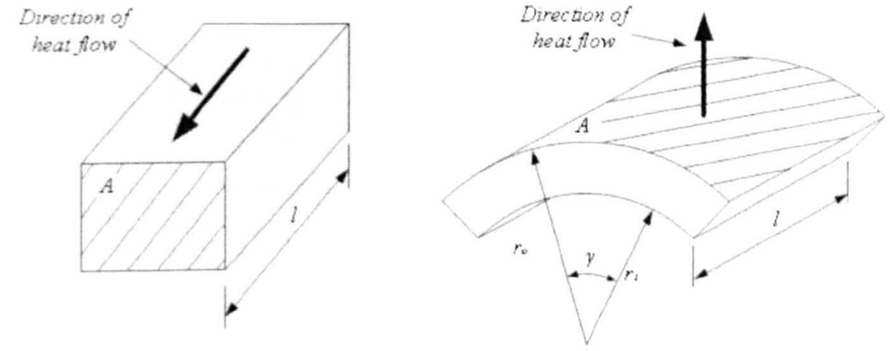

a) Rectangular volume

b) Annulus segment

Figure B.1 Basic shapes for thermal modelling

$$R_{rect} = \frac{l}{kA} \tag{B.15}$$

$$R_{ann} = \frac{\ln(^{r_o}/_{r_i})}{k\gamma l} \tag{B.16}$$

Starting from (B.15) and (B.16) and considering the geometry of the lumped parameter thermal model shown in Figure 2.9, then the thermal resistance R_1 – R_{12} are as given by (B.18) – (B.30), where k_{Al}, k_{Fe}, k_{cu} and k_{lin} are the thermal conductivities of aluminium, silicon steel, copper and slot liner insulation material respectively and T_{lin} is the thickness of the slot liner.

The term k_{eq} represents an equivalent thermal conductivity of the windings, which is dependent on a number of components and their properties such as K_{fill}, the copper insulation, the impregnating compound etc.... Assuming that the copper insulation has the same thermal properties as the impregnation compound and that a good impregnation is achieved, then using an 'area weighted approach', k_{eq} can be simplistically computed from (B.17), where k_{res} is the equivalent thermal conductivity of the impregnating compound.

$$k_{eq} = \frac{k_{cu} k_{res}}{\left(k_{res} K_{fill}\right) + \left(1 - K_{fill}\right) k_{cu}} \tag{B.17}$$

$$R_1 = \frac{T_{sl}}{3\pi \times k_{eq} \times \left[(R_t - T_{lin})^2 - R_{tipa}^2\right]} \tag{B.18}$$

$$R_2 = \frac{\ln\left(\frac{R_t - T_{lin}}{R_{hc}}\right)}{\frac{2\pi}{3} \times k_{eq} \times T_{sl}} \tag{B.19}$$

$$R_3 = {}^{R_1}/_{2} \tag{B.21}$$

$$R_4 = \frac{\ln\left(\frac{R_{hc}}{R_{tipa}}\right)}{\frac{2\pi}{3} \times k_{eq} \times T_{sl}} \tag{B.22}$$

$$R_5 = \frac{T_{lin}}{k_{lin} \times \pi\left(R_t^2 - R_{tipa}^2\right)} \tag{B.23}$$

$$R_6 = \frac{T_t}{2\pi \times k_{Fe} \times (R_e^2 - R_{in}^2)} \tag{B.24}$$

$$R_7 = \frac{\ln\left({}^{R_{hc}}/_{R_{in}}\right)}{\pi \times k_{Fe} \times T_t} \tag{B.25}$$

$$R_8 = \frac{\ln\left({}^{R_e}/_{R_{hc}}\right)}{\pi \times k_{Fe} \times T_t} \tag{B.26}$$

$$R_9 = \frac{\ln\left({}^{R_t}/_{(R_t - T_{lin})}\right)}{\frac{2\pi}{3} \times k_{lin} \times T_{sl}} \tag{B.27}$$

$$R_{10} = \frac{\ln\left({}^{R_e}/_{R_t}\right)}{\frac{2\pi}{3} \times k_{Fe} \times T_{sl}} \tag{B.28}$$

$$R_{11} = \frac{\ln\left({}^{R_{wat}}/_{R_e}\right)}{\pi \times k_{Al} \times T_s} \tag{B.29}$$

$$R_{12} = \frac{1}{2\pi \times R_{wat} \times T_s \times h_{cv}} \tag{B.30}$$

Using (B.18) – (B.30) to set the values of the thermal resistances and setting a specific winding temperature, the copper loss that is relative to that temperature can be found from the model. The copper density J_{rms} relative to that copper loss can then be found from (B.31).

$$P_{cu} = \pi \times T_{sl} R_{hc} K_{fill} \times \rho_{cu}\left(R_t - R_{tipa}\right) J_{rms}^2 \qquad (B.31)$$

The same (B.31) can also be used to identify the maximum J_{rms} for safe operation of the machine. Considering a maximum winding temperature T_{max} for safe operation, then the maximum copper loss that ensures safe operation can be achieved. Using (B.31) the maximum J_{rms} that ensures a winding temperature below T_{max} is calculated.

B.2.3 The lumped parameter thermal model with HP

For the model with the HP as shown in Figure 4.4, the same analysis and procedures given in Appendix B.2.2 can be used. The main differences result from the thermal resistances of the HP. If the material used for the HP has a thermal conductivity k_{Al}, then the thermal resistances are as described by (B.32) - (B.36). From (B.36) and Figure 4.4, it can be noted that R_{HP3} represents the thickness L_{HP1} plus the thickness of the liner at the slot wall.

$$R_1 = \frac{(2T_{sl} - 3T_{HP2})}{6\pi \times k_{eq} \times \left[(R_t - T_{lin} - L_{HP1})^2 - R_{tipa}^2\right]} \qquad (B.32)$$

$$R_2 = \frac{\ln\left(\frac{(R_t - T_{lin} - L_{HP1})}{R_{hc}}\right)}{\frac{2\pi}{3} \times k_{eq} \times T_{sl}} \qquad (B.33)$$

$$R_{HP1} = \frac{\ln\left(\frac{R_{hc}}{R_{tipa}}\right)}{2\pi \times k_{Al} \times T_{HP2}} \qquad (B.34)$$

$$R_{HP2} = \frac{\ln\left(\frac{(R_t - T_{lin} - L_{HP1})}{R_{hc}}\right)}{2\pi \times k_{Al} \times T_{HP2}} \qquad (B.35)$$

$$R_{HP3} = \frac{\ln\left(\frac{R_t - T_{lin}}{(R_t - T_{lin} - L_{HP1})}\right)}{\frac{2\pi}{3} \times k_{Al} \times T_{HP1}} + \frac{\ln\left(\frac{R_t}{(R_t - T_{lin})}\right)}{\frac{2\pi}{3} \times k_{lin} \times T_{sl}} \qquad (B.36)$$

B.3 GT motor: thermal modelling

For the thermal modelling of the GT motor, the basic principles as described by (B.15) and (B.16) are also applied. For the following derivations, k_{Al}, k_{CoFe}, k_{cu} and k_{lin} are the thermal conductivities of aluminium, CoFe steel, copper and slot liner insulation material respectively. The term k_{eq} represents an equivalent thermal conductivity of the windings and is as described by (B.17). As can be observed in Figure 3.4 and Figure 3.27 the term T_{lin} is the thickness of the slot liner, T_{sl} is the slot width, T_s is the slot pitch, T_t is the tooth thickness and R_{wat}, R_{hc}, R_t, R_{stat_bore} and R_{house} are the defining radii.

B.3.1 Single layer model

Considering the geometry of the lumped parameter thermal model shown in Figure 3.4, then the thermal resistance R_1 – R_{10} are as given by (B.37) – (B.46). The thermal resistance R_{11} is mainly dependant on the velocity of the cooling air V_{air}.

$$R_1 = \frac{T_{sl}}{2 \times k_{eq} \times l_{ax} \times \left[R_{stat\_bore} - (R_t + T_{lin})\right]} \qquad (B.37)$$

$$R_2 = \frac{\ln\left(\frac{R_{hc}}{R_t + T_{lin}}\right)}{k_{eq} \times T_{sl} \times \left[R_{hc} - (R_t + T_{lin})\right]} \qquad (B.38)$$

$$R_3 = \frac{\ln\left(\frac{R_{stat\_bore}}{R_{hc}}\right)}{k_{eq} \times T_{sl} \times \left[R_{stat\_bore} - R_{hc}\right]} \qquad (B.39)$$

$$R_4 = \frac{\ln\left(\frac{R_t + T_{lin}}{R_t}\right)}{k_{lin} \times T_{sl} \times T_{lin}} \qquad (B.40)$$

$$R_5 = \frac{T_{lin}}{k_{lin} \times l_{ax} \times \left[R_{stat\_bore} - R_t\right]} \qquad (B.41)$$

$$R_6 = \frac{T_t}{2k_{CoFe} \times l_{ax} \times \left[R_{stat\_bore} - R_h\right]} \qquad (B.42)$$

$$R_7 = \frac{2 \times \ln\left({R_{stat\_bore}}/{R_{hc}}\right)}{k_{CoFe} \times T_t \times \left[R_{stat\_bore} - R_{hc}\right]} \qquad (B.43)$$

$$R_8 = \frac{2 \times \ln\left({}^{R_{hc}}/_{R_h}\right)}{k_{CoFe} \times T_t \times [R_{hc} - R_h]} \tag{B.44}$$

$$R_9 = \frac{\ln\left({}^{R_t}/_{R_h}\right)}{k_{CoFe} \times T_{sl} \times [R_t - R_h]} \tag{B.45}$$

$$R_{10} = \frac{\ln\left({}^{R_h}/_{R_{house}}\right)}{k_{Al} \times T_s \times [R_h - R_{house}]} \tag{B.46}$$

B.3.2 Double layer model

Considering the geometry of the lumped parameter thermal model shown in Figure 3.27, then the thermal resistance R_1 – R_{11} are as given by (B.47) – (B.57). The thermal resistance R_{12} is mainly dependant on the velocity of the cooling air V_{air}.

$$R_1 = \frac{T_{sl}}{3 \times k_{eq} \times l_{ax} \times \left[R_{stat\_bore} - (R_t + T_{lin})\right]} \tag{B.47}$$

$$R_2 = \frac{3 \times \ln\left(\frac{R_{hc}}{R_t + T_{lin}}\right)}{k_{eq} \times T_{sl} \times [R_{hc} - (R_t + T_{lin})]} \tag{B.48}$$

$$R_3 = {}^{R_1}/_2 \tag{B.49}$$

$$R_4 = \frac{3 \times \ln\left(\frac{R_{stat\_bore}}{R_{hc}}\right)}{k_{eq} \times T_{sl} \times \left[R_{stat\_bore} - R_{hc}\right]} \tag{B.50}$$

$$R_5 = \frac{T_{lin}}{k_{lin} \times l_{ax} \times \left[R_{stat\_bore} - R_t\right]} \tag{B.51}$$

$$R_6 = \frac{T_t}{2k_{CoFe} \times l_{ax} \times \left[R_{stat\_bore} - R_h\right]} \tag{B.52}$$

$$R_7 = \frac{2 \times \ln\left({}^{R_{stat\_bore}}/_{R_{hc}}\right)}{k_{CoFe} \times T_t \times \left[R_{stat\_bore} - R_{hc}\right]} \tag{B.53}$$

$$R_8 = \frac{2 \times \ln\left({}^{R_{hc}}/_{R_h}\right)}{k_{CoFe} \times T_t \times [R_{hc} - R_h]} \tag{B.54}$$

$$R_9 = \frac{3 \times \ln\left(\frac{R_t + T_{lin}}{R_t}\right)}{k_{lin} \times T_{sl} \times T_{lin}} \qquad (B.55)$$

$$R_{10} = \frac{3 \times \ln\left(\frac{R_t}{R_h}\right)}{k_{CoFe} \times T_{sl} \times [R_t - R_h]} \qquad (B.56)$$

$$R_{11} = \frac{\ln\left({R_h}/{R_{house}}\right)}{k_{Al} \times T_s \times [R_h - R_{house}]} \qquad (B.57)$$

B.3.3 Double layer model with HP

For the GT motor, double layer, thermal model with the HP as shown in Figure 4.15, the same analysis and procedures given in Appendix B.3.2 can be used. The main differences result from the thermal resistances of the HP. If the material used for the HP has a thermal conductivity k_{cu}, then the thermal resistances are as described by (B.58) - (B.62). From (B.62), it can be noted that R_{HP3} represents the thickness L_{HP1} plus the thickness of the liner at the slot wall.

$$R_1 = \frac{(2T_{sl} - 3T_{HP2})}{6k_{eq} \times l_{ax} \times \left[R_{stat\_bore} - (R_t + T_{lin} + L_{HP1})\right]} \qquad (B.58)$$

$$R_2 = \frac{3 \times \ln\left(\frac{R_{hc}}{R_t + T_{lin} + L_{HP1}}\right)}{k_{eq} \times T_{sl} \times [R_{hc} - (R_t + T_{lin} + L_{HP1})]} \qquad (B.59)$$

$$R_{HP1} = \frac{\ln\left(\frac{R_{stat\_bore}}{R_{hc}}\right)}{k_{cu} \times T_{HP2} \times \left[R_{stat\_bore} - R_{hc}\right]} \qquad (B.60)$$

$$R_{HP2} = \frac{\ln\left(\frac{R_{hc}}{(R_t + T_{lin} + L_{HP1})}\right)}{k_{cu} \times T_{HP2} \times [R_{hc} - (R_t + T_{lin} + L_{HP1})]} \qquad (B.61)$$

$$R_{HP3} = \frac{\ln\left(\frac{(R_t + T_{lin} + L_{HP1})}{(R_t + T_{lin})}\right)}{k_{cu} \times \frac{T_{HP1}}{3} \times L_{HP1}} + \frac{\ln\left(\frac{R_t + T_{lin}}{R_t}\right)}{k_{lin} \times \frac{T_{sl}}{3} \times T_{lin}} \qquad (B.62)$$

REFERENCES

[1] R. I. Jones, "The More Electric Aircraft: the past and the future?," in *Electrical Machines and Systems for the More Electric Aircraft (Ref. No. 1999/180), IEE Colloquium on*, 1999, pp. 1/1-1/4.

[2] J. A. Rosero, J. A. Ortega, E. Aldabas, and L. Romeral, "Moving towards a more electric aircraft," *Aerospace and Electronic Systems Magazine, IEEE*, vol. 22, pp. 3-9, 2007.

[3] J. A. Weimer, "The role of electric machines and drives in the more electric aircraft," in *Electric Machines and Drives Conference, 2003. IEMDC'03. IEEE International*, 2003, pp. 11-15 vol.1.

[4] A. Boglietti, A. Cavagnino, A. Tenconi, and S. Vaschetto, "The safety critical electric machines and drives in the more electric aircraft: A survey," in *Industrial Electronics, 2009. IECON '09. 35th Annual Conference of IEEE*, 2009, pp. 2587-2594.

[5] Safran. Electric green taxiing: a promising new aircraft system. Available: http://www.lebourget2011.com/news/electric-green-taxiing-a-promising-new-aircraft-system

[6] A. Radun, "Generating with the switched reluctance motor," in *Applied Power Electronics Conference and Exposition, 1994. APEC '94. Conference Proceedings 1994., Ninth Annual*, 1994, pp. 41-47 vol.1.

[7] G. M. Raimondi, T. Sawata, M. Holme, A. Barton, G. White, J. Coles, P. H. Mellor, and N. Sidell, "Aircraft embedded generation systems," in *Power Electronics, Machines and Drives, 2002. International Conference on (Conf. Publ. No. 487)*, 2002, pp. 217-222.

[8] P. A. Robson, K. J. Bradley, P. Wheeler, J. Clare, L. de Lillo, C. Gerada, S. J. Pickering, D. Lampard, C. K. Goh, G. Towers, and C. Whitley, "The impact of matrix converter technology on motor design for an integrated flight control surface actuation system," in *Electric Machines and Drives Conference, 2003. IEMDC'03. IEEE International*, 2003, pp. 1321-1327 vol.2.

[9] C. Gerada and K. J. Bradley, "Integrated PM Machine Design for an Aircraft EMA," *Industrial Electronics, IEEE Transactions on*, vol. 55, pp. 3300-3306, 2008.

[10] A. G. Jack, B. C. Mecrow, and J. Haylock, "A comparative study of permanent magnet and switched reluctance motors for high performance fault tolerant applications," in *Industry Applications Conference, 1995. Thirtieth IAS Annual Meeting, IAS '95., Conference Record of the 1995 IEEE*, 1995, pp. 734-740 vol.1.

[11] A. Boglietti, A. Cavagnino, D. Staton, M. Shanel, M. Mueller, and C. Mejuto, "Evolution and Modern Approaches for Thermal Analysis of Electrical Machines," *Industrial Electronics, IEEE Transactions on*, vol. 56, pp. 871-882, 2009.

[12] R. Crowder, *Electric Drives and Electromechanical Systems*. Oxford, UK: Elsevier, 2006.

[13] C. Gerada, K. Bradley, C. Whitley, and G. Towers, "Integrated Machine design for Electro Mechanical Actuation," in *Industrial Electronics, 2007. ISIE 2007. IEEE International Symposium on*, 2007, pp. 1305-1310.

[14] A. Garcia, J. Cusido, J. A. Rosero, J. A. Ortega, and L. Romeral, "Reliable electro-mechanical actuators in aircraft," *Aerospace and Electronic Systems Magazine, IEEE*, vol. 23, pp. 19-25, 2008.

[15] S. E. Lyshevski, "Electromechanical flight actuators for advanced flight vehicles," *Aerospace and Electronic Systems, IEEE Transactions on*, vol. 35, pp. 511-518, 1999.

[16] S. E. Lyshevski, V. A. Skormin, and R. D. Colgren, "High-torque density integrated electro-mechanical flight actuators," *Aerospace and Electronic Systems, IEEE Transactions on,* vol. 38, pp. 174-182, 2002.

[17] M. Galea, C. Gerada, T. Raminosoa, and P. Wheeler, "Design of a high force density tubular permanent magnet motor," in *Electrical Machines (ICEM), 2010 XIX International Conference on,* 2010, pp. 1-6.

[18] G. W. McLean, "Review of recent progress in linear motors," *Electric Power Applications, IEE Proceedings B,* vol. 135, pp. 380-416, 1988.

[19] E. s. C. Sky. (2008, Clean Sky Joint Technology Initiative. Available: http://www.cleansky.eu/

[20] M. Christmann, S. Seemann, and P. Janker, "Innovative approaches to electromechanical flight control actuators and systems," in *Recent Advances in Aerospace Actuation Systems and Components*, ed. Toulouse, France, 2010.

[21] S. Seemann, M. Christmann, and P. Janker, "Control and monitoring concept for a fault-tolerant electromechanical actuation system," presented at the Recent Advances in Aerospace Actuation Systems and Components, Toulouse, France, 2012.

[22] M. Rottach, C. Gerada, T. Hamiti, and P. Wheeler, "Fault-tolerant Electrical Machine Design within a Rotorcraft Actuation Drive System Optimisation," in *Power Electronics, Machines and Drives (PEMD), 2012 6th IET Conference on* 2012.

[23] J. G. Leishman, *Principles of Helicopter Aerodynamics*, 2nd ed. New York: Cambridge University Press, 2006.

[24] P. H. Mellor, S. G. Burrow, T. Sawata, and M. Holme, "A wide-speed-range hybrid variable-reluctance/permanent-magnet generator for future embedded aircraft generation systems," *Industry Applications, IEEE Transactions on,* vol. 41, pp. 551-556, 2005.

[25] J. E. McNamara, "Electrically Driven Environmental Control System," *Aerospace and Electronic Systems, IEEE Transactions on,* vol. AES-20, pp. 257-260, 1984.

[26] J. W. Mildice, I. G. Hansen, K. E. Schreiner, and M. E. Roth, "Variable-speed induction motor drives for aircraft environmental control compressors," in *Energy Conversion Engineering Conference, 1996. IECEC 96., Proceedings of the 31st Intersociety,* 1996, pp. 209-214 vol.1.

[27] P. J. Masson, D. S. Soban, E. Upton, J. E. Pienkos, and C. A. Luongo, "HTS motors in aircraft propulsion: design considerations," *Applied Superconductivity, IEEE Transactions on,* vol. 15, pp. 2218-2221, 2005.

[28] R. E. Colyer, "Progress in electrically-propelled aircraft," in *Electrical Machines and Power Electronics, 2007. ACEMP '07. International Aegean Conference on,* 2007, pp. 357-362.

[29] S. Messier-Bugatti-Dowty. Messier-Bugatti's "Green Taxiing" Solutions for Smarter Ground Operations. Available: http://www.safranmbd.com/actualites/actu-et-communiques-de-presse/article/messier-bugatti-s-green-taxiing?lang=en

[30] T. Raminosoa, T. Hamiti, M. Galea, and C. Gerada, "Feasibility and electromagnetic design of direct drive wheel actuator for green taxiing," in *Energy Conversion Congress and Exposition (ECCE), 2011 IEEE,* 2011, pp. 2798-2804.

[31] J. F. Gieras and M. Wing, *Permanent Magnet Motor Technology: Design and Applications.* New York, USA: Marcel Dekker Inc., 2002.

[32] N. Bianchi, S. Bolognani, and M. D. Pre, "Design and Tests of a Fault-Tolerant Five-phase Permanent Magnet Motor," in *Power Electronics Specialists Conference, 2006. PESC '06. 37th IEEE,* 2006, pp. 1-8.

[33] T. Raminosoa, C. Gerada, and N. Othman, "Rating issues in fault tolerant PMSM," in *Electric Machines and Drives Conference, 2009. IEMDC '09. IEEE International*, 2009, pp. 1592-1599.

[34] C. Gerada, *Lecture Notes: Advanced AC Drives*. University of Nottingham, 2009.

[35] M. J. Melfi, S. Evon, and R. McElveen, "Permanent magnet motors for power density and energy savings in industrial applications," in *Pulp and Paper Industry Technical Conference, 2008. PPIC 2008. Conference Record of 2008 54th Annual*, 2008, pp. 218-225.

[36] A. M. El-Refaie and T. M. Jahns, "Comparison of synchronous PM machine types for wide constant-power speed range operation," in *Industry Applications Conference, 2005. Fourtieth IAS Annual Meeting. Conference Record of the 2005*, 2005, pp. 1015-1022 Vol. 2.

[37] A. Vagati, G. Pellegrino, and P. Guglielmi, "Comparison between SPM and IPM motor drives for EV application," in *Electrical Machines (ICEM), 2010 XIX International Conference on*, 2010, pp. 1-6.

[38] F. Charih, F. Dubas, C. Espanet, and D. Chamagne, "Performances comparison of PM machines with different rotor topologies and similar slot and pole numbers," in *Power Electronics, Electrical Drives, Automation and Motion (SPEEDAM), 2012 International Symposium on*, 2012, pp. 56-59.

[39] L. Ling, L. Weiguo, and D. Manfeng, "Two high speed brushless DC motors of different rotor configuration," in *TENCON 2010 - 2010 IEEE Region 10 Conference*, 2010, pp. 54-58.

[40] A. R. Munoz, F. Liang, and M. W. Degner, "Evaluation of Interior PM and Surface PM Synchronous machines with distributed and concentrated windings," in *Industrial Electronics, 2008. IECON 2008. 34th Annual Conference of IEEE*, 2008, pp. 1189-1193.

[41] Z. P. Xia, Z. Q. Zhu, L. J. Wu, and G. W. Jewell, "Comparison of radial vibration forces in 10-pole/12-slot fractional slot surface-mounted and interior PM brushless AC machines," in *Electrical Machines (ICEM), 2010 XIX International Conference on*, 2010, pp. 1-6.

[42] D. Gerada, A. Mebarki, R. P. Mokhadkar, N. L. Brown, and C. Gerada, "Design issues of high-speed permanent magnet machines for high-temperature applications," in *Electric Machines and Drives Conference, 2009. IEMDC '09. IEEE International*, 2009, pp. 1036-1042.

[43] T. Raminosoa, C. Gerada, N. Othman, and L. D. Lillo, "Rotor losses in fault-tolerant permanent magnet synchronous machines," *Electric Power Applications, IET*, vol. 5, pp. 75-88, 2011.

[44] S. A. Nasar, I. Boldea, and L. E. Unnewehr, *Permanent Magnet, Reluctance and Self-Synchronous Motors*. Florida, USA: CRC Press, 1993.

[45] P. Giangrande, "Position Sensorless Control of Linear Permanent Magnet Motors using High Frequency Injection Strategies," PhD, Dipartimento Ingegneria Elettrica, Politecnico di Bari, Italy, 2012.

[46] A. Hughes, *Electric motors and drives: fundumentals, types and applications*, 3rd ed. Oxford: Newnes, 2006.

[47] M. Galea, C. Gerada, T. Raminosoa, and P. Wheeler, "A Thermal Improvement Technique for the Phase Windings of Electrical Machines," *Industry Applications, IEEE Transactions on*, vol. 48, pp. 79-87, 2012.

[48] M. Galea, "Air-gap Shear Stress Analysis," University of Nottingham, Internal Report, Nottingham2010.

[49] T. Raminosoa, C. Gerada, and N. Othman, "Performance comparison of fault tolerant PM machine for static load holding application," in *Electric Machines and Drives Conference, 2009. IEMDC '09. IEEE International*, 2009, pp. 1729-1735.

[50] A. M. El-Refaie, "Fractional-Slot Concentrated-Windings Synchronous Permanent Magnet Machines: Opportunities and Challenges," *Industrial Electronics, IEEE Transactions on,* vol. 57, pp. 107-121, 2010.

[51] R. Wrobel and P. H. Mellor, "Design Considerations of a Direct Drive Brushless Machine With Concentrated Windings," *Energy Conversion, IEEE Transactions on,* vol. 23, pp. 1-8, 2008.

[52] R. Wrobel, P. H. Mellor, N. McNeill, and D. A. Staton, "Thermal Performance of an Open-Slot Modular-Wound Machine With External Rotor," *Energy Conversion, IEEE Transactions on,* vol. 25, pp. 403-411, 2010.

[53] G. Pellegrino, A. Vagati, P. Guglielmi, and B. Boazzo, "Performance Comparison Between Surface-Mounted and Interior PM Motor Drives for Electric Vehicle Application," *Industrial Electronics, IEEE Transactions on,* vol. 59, pp. 803-811, 2012.

[54] D. Ishak, Z. Q. Zhu, and D. Howe, "Permanent-magnet brushless machines with unequal tooth widths and similar slot and pole numbers," *Industry Applications, IEEE Transactions on,* vol. 41, pp. 584-590, 2005.

[55] C. Qian, L. Guohai, G. Wensheng, and Z. Wenxiang, "A New Fault-Tolerant Permanent-Magnet Machine for Electric Vehicle Applications," *Magnetics, IEEE Transactions on,* vol. 47, pp. 4183-4186, 2011.

[56] M. Galea, C. Gerada, and T. Hamiti, "Design Considerations for an Outer Rotor, Field Wound, Flux Switching Machine," in *Electrical Machines (ICEM), 2012 XX International Conference on,* Marseille, France, 2012.

[57] F. Meier, "Permanent-Magnet Synchronous Machines with Non-Overlapping Concentrated Windings for Low-Speed Direct-Drive Application," PhD Thesis, School of Electrical Engineering, Royal Institute of Technology of Stockholm, Sweden, 2008.

[58] Z. Q. Zhu and D. Howe, "Halbach permanent magnet machines and applications: a review," *Electric Power Applications, IEE Proceedings -,* vol. 148, pp. 299-308, 2001.

[59] B. C. Mecrow, A. G. Jack, D. J. Atkinson, S. R. Green, G. J. Atkinson, A. King, and B. Green, "Design and testing of a four-phase fault-tolerant permanent-magnet machine for an engine fuel pump," *Energy Conversion, IEEE Transactions on,* vol. 19, pp. 671-678, 2004.

[60] P. H. Mellor and R. Wrobel, "Optimization of a Multipolar Permanent-Magnet Rotor Comprising Two Arc Segments per Pole," *Industry Applications, IEEE Transactions on,* vol. 43, pp. 942-951, 2007.

[61] Z. Q. Zhu, Z. P. Xia, K. Atallah, G. W. Jewell, and D. Howe, "Novel permanent magnet machines using Halbach cylinders," in *Power Electronics and Motion Control Conference, 2000. Proceedings. IPEMC 2000. The Third International,* 2000, pp. 903-908 vol.2.

[62] W. Jiabin and D. Howe, "Tubular modular permanent-magnet machines equipped with quasi-Halbach magnetized magnets-part I: magnetic field distribution, EMF, and thrust force," *Magnetics, IEEE Transactions on,* vol. 41, pp. 2470-2478, 2005.

[63] S. Dwari, L. Parsa, and K. J. Karimi, "Design and analysis of Halbach array permanent magnet motor for high acceleration applications," in *Electric Machines and Drives Conference, 2009. IEMDC '09. IEEE International,* 2009, pp. 1100-1104.

[64] W. Jiabin and D. Howe, "Tubular modular permanent-magnet machines equipped with quasi-Halbach magnetized magnets-part II: armature reaction and design optimization," *Magnetics, IEEE Transactions on,* vol. 41, pp. 2479-2489, 2005.

[65] J. Wang, G. W. Jewell, and D. Howe, "Design optimisation and comparison of tubular permanent magnet machine topologies," *Electric Power Applications, IEE Proceedings -*, vol. 148, pp. 456-464, 2001.

[66] W. Jiabin, W. Weiya, and K. Atallah, "A Linear Permanent-Magnet Motor for Active Vehicle Suspension," *Vehicular Technology, IEEE Transactions on*, vol. 60, pp. 55-63, 2011.

[67] J. Wang, W. Wang, K. Atallah, and D. Howe, "Demagnetization Assessment for Three-Phase Tubular Brushless Permanent-Magnet Machines," *Magnetics, IEEE Transactions on*, vol. 44, pp. 2195-2203, 2008.

[68] J. F. Gieras and Z. J. Piech, *Linear Synchronous Motors: Transportation and Automation Systems*: CRC Press LLC, 2000.

[69] K. J. Meessen, J. J. H. Paulides, and E. A. Lomonova, "Modeling and Experimental Verification of a Tubular Actuator for 20-g Acceleration in a Pick-and-Place Application," *Industry Applications, IEEE Transactions on*, vol. 46, pp. 1891-1898, 2010.

[70] L. Young Jin, L. Jin Woo, C. Hyun Cheol, K. Kyung Wan, and L. Kwon Soon, "Positioning Control of Linear Motor-Based Container Transfer System with Varying Weight," in *Future Generation Communication and Networking Symposia, 2008. FGCNS '08. Second International Conference on*, 2008, pp. 17-22.

[71] W. C. Gan and N. C. Cheung, "Development and control of a low-cost linear variable-reluctance motor for precision manufacturing automation," *Mechatronics, IEEE/ASME Transactions on*, vol. 8, pp. 326-333, 2003.

[72] W. R. Cawthorne, P. Famouri, C. Jingdong, N. N. Clark, T. I. McDaniel, R. J. Atkinson, S. Nandkumar, C. M. Atkinson, and S. Petreanu, "Development of a linear alternator-engine for hybrid electric vehicle applications," *Vehicular Technology, IEEE Transactions on*, vol. 48, pp. 1797-1802, 1999.

[73] R. Thornton, "The future of maglev," in *Electrical Machines and Systems, 2007. ICEMS. International Conference on*, 2007, pp. 1950-1954.

[74] Y. Luguang, "Development and Application of the Maglev Transportation System," *Applied Superconductivity, IEEE Transactions on*, vol. 18, pp. 92-99, 2008.

[75] L. Hong Sun and R. Krishnan, "Ropeless Elevator With Linear Switched Reluctance Motor Drive Actuation Systems," *Industrial Electronics, IEEE Transactions on*, vol. 54, pp. 2209-2218, 2007.

[76] A. Onat, E. Kazan, N. Takahashi, D. Miyagi, Y. Komatsu, and S. Markon, "Design and Implementation of a Linear Motor for Multicar Elevators," *Mechatronics, IEEE/ASME Transactions on*, vol. 15, pp. 685-693, 2010.

[77] K. Park, E. P. Hong, and K. H. Lee, "Development of a linear motor for compressors of household refrigerators," in *Linear Drives for Industry Applications (LDIA), 2001 The 3rd International Symposium on* Nagano, Japan, 2001, pp. 283-286.

[78] W. Jiabin, M. West, D. Howe, H. Z. D. La Parra, and W. M. Arshad, "Design and Experimental Verification of a Linear Permanent Magnet Generator for a Free-Piston Energy Converter," *Energy Conversion, IEEE Transactions on*, vol. 22, pp. 299-306, 2007.

[79] D. M. Joseph and W. A. Cronje, "Design and Analysis of a Double-Sided Tubular Linear Synchronous Generator with Particular Application to Wave-Energy Conversion," in *Power Engineering Society Conference and Exposition in Africa, 2007. PowerAfrica '07. IEEE*, 2007, pp. 1-8.

[80] S. Kuznetsov and D. Marriott, "High Velocity Linear Induction Launcher with Exit-Edge Compensation for Testing of Aerospace Components," in *Electromagnetic Launch Technology, 2008 14th Symposium on*, 2008, pp. 1-8.

[81] H. Robertson, R. N. Lt Cdr Matt Bolton, and R. N. Lt Mick Thomson, "An advanced linear motor system for electromagnetic launch: development and opportunities," in *Pulsed Power symposium, 2005. The IEE (Reg. No. 2005/11070)*, 2005, pp. 29/1-29/6.

[82] H. Shuanghui, T. Zili, and H. Minghui, "A decentralized linear motor for electromagnetic aircraft launch system," in *Consumer Electronics, Communications and Networks (CECNet), 2011 International Conference on*, 2011, pp. 3813-3818.

[83] G. Stumberger, D. Zarko, M. Timur Aydemir, and T. A. Lipo, "Design and comparison of linear synchronous motor and linear induction motor for electromagnetic aircraft launch system," in *Electric Machines and Drives Conference, 2003. IEMDC'03. IEEE International*, 2003, pp. 494-500 vol.1.

[84] N. Bianchi, S. Bolognani, D. D. Corte, and F. Tonel, "Tubular linear permanent magnet motors: an overall comparison," *Industry Applications, IEEE Transactions on*, vol. 39, pp. 466-475, 2003.

[85] J. F. Eastham, "Novel synchronous machines: linear and disc," *Electric Power Applications, IEE Proceedings B*, vol. 137, pp. 49-58, 1990.

[86] P. E. Cavarec, H. Ben Ahmed, and B. Multon, "Force density improvements from increasing the number of airgap surfaces in synchronous linear actuators," *Electric Power Applications, IEE Proceedings -*, vol. 150, pp. 106-116, 2003.

[87] P. E. Cavarec, H. B. Ahmed, and B. Multon, "New multi-rod linear actuator for direct-drive, wide mechanical bandpass applications," *Industry Applications, IEEE Transactions on*, vol. 39, pp. 961-970, 2003.

[88] N. Ziegler, D. Matt, J. Jac, T. Martire, and P. Enrici, "High force linear actuator for an aeronautical application. Association with a fault tolerant converter," in *Electrical Machines and Power Electronics, 2007. ACEMP '07. International Aegean Conference on*, 2007, pp. 76-80.

[89] M. Galea, C. Gerada, T. Raminosoa, and P. W. Wheeler, "Considerations for the design of a tubular motor for an aerospace application," in *Electrical Machines and Systems (ICEMS), 2011 International Conference on*, 2011, pp. 1-6.

[90] C. Gerada, K. Bradley, C. Whitley, and G. Towers, "High Torque Density PM Machines for High Performance Operation," in *Industrial Electronics Society, 2007. IECON 2007. 33rd Annual Conference of the IEEE*, 2007, pp. 210-215.

[91] J. Cros, P. Viarouge, and C. Gelinas, "Design of PM brushless motors using iron-resin composites for automotive applications," in *Industry Applications Conference, 1998. Thirty-Third IAS Annual Meeting. The 1998 IEEE*, 1998, pp. 5-11 vol.1.

[92] A. G. Jack, B. C. Mecrow, P. G. Dickinson, D. Stephenson, J. S. Burdess, J. N. Fawcett, and T. Evans, "Permanent magnet machines with powdered iron cores and pre-pressed windings," in *Industry Applications Conference, 1999. Thirty-Fourth IAS Annual Meeting. Conference Record of the 1999 IEEE*, 1999, pp. 97-103 vol.1.

[93] N. Bianchi and S. Bolognani, "Design techniques for reducing the cogging torque in surface-mounted PM motors," *Industry Applications, IEEE Transactions on*, vol. 38, pp. 1259-1265, 2002.

[94] M. Barcaro, N. Bianchi, and F. Magnussen, "Analysis and Tests of a Dual Three-Phase 12-Slot 10-Pole Permanent-Magnet Motor," *Industry Applications, IEEE Transactions on*, vol. 46, pp. 2355-2362, 2010.

[95] N. Bianchi, S. Bolognani, M. D. Pre, and G. Grezzani, "Design considerations for fractional-slot winding configurations of synchronous machines," *Industry Applications, IEEE Transactions on*, vol. 42, pp. 997-1006, 2006.

[96] N. Bianchi and M. Dai Pre, "Use of the star of slots in designing fractional-slot single-layer synchronous motors," *Electric Power Applications, IEE Proceedings -*, vol. 153, pp. 459-466, 2006.

[97] J. Cros and P. Viarouge, "Synthesis of high performance PM motors with concentrated windings," *Energy Conversion, IEEE Transactions on,* vol. 17, pp. 248-253, 2002.

[98] M. M. Liwschitz, "Distribution Factors and Pitch Factors of the Harmonics of a Fractional-Slot Winding," *American Institute of Electrical Engineers, Transactions of the,* vol. 62, pp. 664-666, 1943.

[99] P. Salminen, M. Niemela, J. Pyrhonen, and J. Mantere, "High-torque low-torque-ripple fractional-slot PM-motors," in *Electric Machines and Drives, 2005 IEEE International Conference on*, 2005, pp. 144-148.

[100] L. Kung, U. Bikle, O. Popp, and R. Jakoby, "Improvement of the cooling performance of symmetrically self-ventilated induction machines in the 2-15 MW range," in *Electric Machines and Drives Conference, 2001. IEMDC 2001. IEEE International*, 2001, pp. 673-680.

[101] A. Boglietti, A. Cavagnino, M. Lazzari, and M. Pastorelli, "A simplified thermal model for variable-speed self-cooled industrial induction motor," *Industry Applications, IEEE Transactions on,* vol. 39, pp. 945-952, 2003.

[102] G. M. Gilson, T. Raminosoa, S. J. Pickering, C. Gerada, and D. B. Hann, "A combined electromagnetic and thermal optimisation of an aerospace electric motor," in *Electrical Machines (ICEM), 2010 XIX International Conference on*, 2010, pp. 1-7.

[103] B. Yazicioglu and H. Yuncu, "A correlation for optimum fin spacing of vertically-based rectangular fin arrays subjected to natural convection heat transfer," *Thermal, Science and Technology, Journal of,* pp. 99-105, 2009.

[104] J. Mugglestone, S. J. Pickering, and D. Lampard, "Effect of geometric changes on the flow and heat transfer in the end region of a TEFC induction motor," in *Electrical Machines and Drives, 1999. Ninth International Conference on (Conf. Publ. No. 468)*, 1999, pp. 40-44.

[105] S. Pickering, F. Thovex, P. Wheeler, and K. Bradley, "Thermal Design of an Integrated Motor Drive," in *IEEE Industrial Electronics, IECON 2006 - 32nd Annual Conference on*, 2006, pp. 4794-4799.

[106] B. Funieru and A. Binder, "Thermal design of a permanent magnet motor used for gearless railway traction," in *Industrial Electronics, 2008. IECON 2008. 34th Annual Conference of IEEE*, 2008, pp. 2061-2066.

[107] C. Kral, A. Haumer, and T. Bauml, "Thermal Model and Behavior of a Totally-Enclosed-Water-Cooled Squirrel-Cage Induction Machine for Traction Applications," *Industrial Electronics, IEEE Transactions on,* vol. 55, pp. 3555-3565, 2008.

[108] P. H. Mellor, D. Roberts, and D. R. Turner, "Lumped parameter thermal model for electrical machines of TEFC design," *Electric Power Applications, IEE Proceedings B,* vol. 138, pp. 205-218, 1991.

[109] A. Boglietti, A. Cavagnino, and D. Staton, "Determination of Critical Parameters in Electrical Machine Thermal Models," *Industry Applications, IEEE Transactions on,* vol. 44, pp. 1150-1159, 2008.

[110] W. Jiabin, D. Howe, and G. W. Jewell, "Fringing in tubular permanent-magnet Machines: part II. Cogging force and its minimization," *Magnetics, IEEE Transactions on,* vol. 39, pp. 3517-3522, 2003.

[111] J. Wang, M. Inoue, Y. Amara, and D. Howe, "Cogging-force-reduction techniques for linear permanent-magnet machines," *Electric Power Applications, IEE Proceedings -*, vol. 152, pp. 731-738, 2005.

[112] L. Touzhu and G. Slemon, "Reduction of cogging torque in permanent magnet motors," *Magnetics, IEEE Transactions on,* vol. 24, pp. 2901-2903, 1988.

[113] Z. Q. Zhu, Z. P. Xia, D. Howe, and P. H. Mellor, "Reduction of cogging force in slotless linear permanent magnet motors," *Electric Power Applications, IEE Proceedings* -, vol. 144, pp. 277-282, 1997.

[114] T. Raminosoa and C. Gerada, "WP3.7 - Nottingham Annual Report October 2010," University of Nottingham2010.

[115] A. Cavagnino, M. Lazzari, F. Profumo, and A. Tenconi, "A comparison between the axial flux and the radial flux structures for PM synchronous motors," *Industry Applications, IEEE Transactions on,* vol. 38, pp. 1517-1524, 2002.

[116] H. Surong, L. Jian, F. Leonardi, and T. A. Lipo, "A comparison of power density for axial flux machines based on general purpose sizing equations," *Energy Conversion, IEEE Transactions on,* vol. 14, pp. 185-192, 1999.

[117] EMERF, "Lamination Steels Third Edition," S. Sprague, Ed., ed. New York, USA, 2007.

[118] D. Ishak, Z. Q. Zhu, and D. Howe, "Comparative study of permanent magnet brushless motors with all teeth and alternative teeth windings," in *Power Electronics, Machines and Drives, 2004. (PEMD 2004). Second International Conference on (Conf. Publ. No. 498),* 2004, pp. 834-839 Vol.2.

[119] T. Hamiti, C. Gerada, and M. Galea, "WP3.7 - Nottingham Annual Report November 2011," 2011.

[120] M. Galea, T. Hamiti, C. Gerada, Z. Xu, and S. Pickering, "WP3.7 - Nottingham Annual Report November 2012," 2012.

[121] P. Salminen, "Fractional Slot Permanent Magnet Synchronous Motor for Low Speed Applications," PhD Thesis, Lappeenranta University of Technology, Finland, 2004.

[122] M. Andriollo, G. Bettanini, G. Martinelli, A. Morini, and A. Tortella, "Analysis of Double-Star Permanent-Magnet Synchronous Generators by a General Decoupled d-q Model," *Industry Applications, IEEE Transactions on,* vol. 45, pp. 1416-1424, 2009.

[123] F. Terrien and M. F. Benkhoris, "Analysis of double star motor drives for electrical propulsion," in *Electrical Machines and Drives, 1999. Ninth International Conference on (Conf. Publ. No. 468),* 1999, pp. 90-94.

[124] R. H. Nelson and P. C. Krause, "Induction Machine Analysis for Arbitrary Displacement Between Multiple Winding Sets," *Power Apparatus and Systems, IEEE Transactions on,* vol. PAS-93, pp. 841-848, 1974.

[125] K. Marouani, F. Khoucha, L. Baghli, D. Hadiouche, and A. Kheloui, "Study and harmonic analysis of SVPWM techniques for VSI-Fed double-star induction motor drive," in *Control & Automation, 2007. MED '07. Mediterranean Conference on,* 2007, pp. 1-6.

[126] R. Smith and J. M. Layton, "Harmonic elimination in polyphase machines by graded windings," *Electrical Engineers, Proceedings of the Institution of,* vol. 110, pp. 1640-1648, 1963.

[127] T. M. Jahns, G. B. Kliman, and T. W. Neumann, "Interior Permanent-Magnet Synchronous Motors for Adjustable-Speed Drives," *Industry Applications, IEEE Transactions on,* vol. IA-22, pp. 738-747, 1986.

[128] S. Kallio, J. Karttunen, M. Andriollo, P. Peltoniemi, and P. Silventoinen, "Finite element based phase-variable model in the analysis of double-star permanent magnet synchronous machines," in *Power Electronics, Electrical Drives, Automation and Motion (SPEEDAM), 2012 International Symposium on,* 2012, pp. 1462-1467.

[129] N. Bianchi, S. Bolognani, A. Consoli, T. M. Jahns, R. D. Lorenz, E. C. Lovelace, S. Morimoto, and A. Vagati, "Design, Analysis and Control of Interior PM Synchronous Machines," in *Industry Applications Society Annual Meeting, 2004. The 2004 IEEE,* Seattle, USA, 2004.

[130] C. Infolytica. (2010, Demagnetization of Permanent Magnets. Available: http://www.infolytica.com/secured/customer/elite/livedocs/

[131] K. M. Takami and J. Mahmoudi, "A new apparatus for mitigating the hot spot problem in large power transformers using Ants algorithm," in *Power Engineering Society Conference and Exposition in Africa, 2007. PowerAfrica '07. IEEE*, 2007, pp. 1-8.

[132] C. H. Holley and H. D. Taylor, "Direct Cooling of Turbine-Generator Field Windings," *Power Apparatus and Systems, Part III. Transactions of the American Institute of Electrical Engineers*, vol. 73, pp. 542-550, 1954.

[133] A. Boglietti, A. Cavagnino, D. A. Staton, M. Popescu, C. Cossar, and M. I. McGilp, "End Space Heat Transfer Coefficient Determination for Different Induction Motor Enclosure Types," *Industry Applications, IEEE Transactions on*, vol. 45, pp. 929-937, 2009.

[134] C. Micallef, S. J. Pickering, K. A. Simmons, and K. J. Bradley, "An alternative cooling arrangement for the end region of a totally enclosed fan cooled (TEFC) induction motor," in *Power Electronics, Machines and Drives, 2008. PEMD 2008. 4th IET Conference on*, 2008, pp. 305-309.

[135] Y. G. Guo, J. G. Zhu, P. A. Watterson, and W. Wu, "Comparative study of 3D flux electrical machines with soft magnetic composite cores," in *Industry Applications Conference, 2002. 37th IAS Annual Meeting. Conference Record of the*, 2002, pp. 1147-1154 vol.2.

[136] G. Youguang, Z. Jianguo, L. Haiyan, L. Zhiwei, and L. Yongjian, "Core Loss Calculation for Soft Magnetic Composite Electrical Machines," *Magnetics, IEEE Transactions on*, vol. 48, pp. 3112-3115, 2012.

[137] M. Popescu, T. Jokinen, E. Demeter, and V. Navrapescu, "Magnetic materials in design and construction of electrical motors," in *Electrotechnical Conference, 1998. MELECON 98., 9th Mediterranean*, 1998, pp. 125-128 vol.1.

[138] L. De Lillo, L. Empringham, M. Schulz, and P. Wheeler, "A high power density SiC-JFET-based matrix converter," in *Power Electronics and Applications (EPE 2011), Proceedings of the 2011-14th European Conference on*, 2011, pp. 1-8.

[139] L. Empringham, P. Wheeler, and J. Clare, "Power density improvement and robust commutation for a 100 kW Si-SiC matrix converter," in *Power Electronics and Applications, 2009. EPE '09. 13th European Conference on*, 2009, pp. 1-8.

[140] P. W. Wheeler, J. Rodriguez, J. C. Clare, L. Empringham, and A. Weinstein, "Matrix converters: a technology review," *Industrial Electronics, IEEE Transactions on*, vol. 49, pp. 276-288, 2002.

[141] T. Raminosoa, C. Gerada, and M. Galea, "Design Considerations for a Fault-Tolerant Flux-Switching Permanent-Magnet Machine," *Industrial Electronics, IEEE Transactions on*, vol. 58, pp. 2818-2825, 2011.

[142] M. Galea, G. Buticchi, L. Empringham, L. De Lillo, and C. Gerada, "Considerations for Manufacturing and Experimental Validation of a PM, Tubular Motor for a Matrix Converter Driven Aerospace Application," in *The 9th International Symposium on Linear Drives and Industrial Automation, LDIA2013*, Hangzhou, China, 2013.

[143] M. Galea, T. Hamiti, and C. Gerada, "Torque density improvements for high performance machines," in *Electric Machines & Drives Conference (IEMDC), 2013 IEEE International*, 2013, pp. 1066-1073.